A method for validation of GIA models using sea-level data with applications to Hudson Bay and SW Fennoscandia

Dissertation

zur Erlangung des Grades eines
Doktors der Naturwissenschaften

am Fachbereich Geowissenschaften der Freien Universität Berlin
angefertigt am Deutschen GeoForschungszentrum GFZ, Potsdam

vorgelegt von

Milena Latinović

Berlin, 2020

Autor:	Milena Latinović
Erstgutachter:	Prof. Dr. Maik Thomas
Zweitgutachter:	Prof. Dr. Giorgio Spada (University of Bologna)
Datum der Einreichung:	04.09.2020
Datum der Disputation:	25.02.2021

Declaration of Authorship

I, Milena Latinović, declare that this thesis titled, "A method for validation of GIA models using sea-level data with applications to Hudson Bay and SW Fennoscandia" and the work presented in it are my own. I confirm that:

- This work was done wholly or mainly while in candidature for a research degree at the Freie Universität Berlin.
- Where any part of this dissertation has previously been submitted for a degree or any other qualification at the Freie Universität Berlin, or any other institution, this has been clearly stated.
- Where I have consulted the published work of others, this is always clearly attributed.
- Where I have quoted from the work of others, the source is always given. With the exception of such quotations, this thesis is entirely my own work.
- I have acknowledged all main sources of help.
- Where the thesis is based on work done by myself jointly with others, I have made clear exactly what was done by others and what I have contributed myself.

Signature:

Date: 05.03.2021

"*An expert is a person who has made all the mistakes which can be made, in a narrow field.*"

Niels Bohr

Abstract

Glacial isostatic adjustment (GIA) is the ongoing response of the viscoelastic solid Earth, oceans and the gravitational field to the previous burden of the ice loads. The Earth's surface was once covered with massive ice sheets, and melting of these ice sheets is still reshaping coastlines and affecting sea-level. To reconstruct former sea level and be able to predict future changes, it is necessary to constrain the rheological properties of the Earth's structure. Widely used data to constrain Earth's interior are sea-level indicators. In the first part of the thesis, we propose a statistical method that quantifies a relationship between the sea-level indicator and a relative sea level in order to compare it to GIA predictions. A statistical method is based on consideration of spatial and temporal probability density functions, derived from the age and elevation of each indicator. This method allows a more rigorous approach to validation with sea-level data and possibility to include low-quality data. We verified method performance in the Hudson Bay, Canada as a test run before applying it to the SW Fennoscandia.

SW Fennoscandia identifies as an area where lateral heterogeneity is likely to exist. The south-western part of Fennoscandia lies on the crustal boundary called the Trans-European Suture Zone (TESZ), or the Tornquist Zone. GIA models have two representations of Earth's structure; radially symmetric (1D), where the rheology only varies vertically, and lateral or 3D variations of viscosity structure.

In this thesis, we compare glacial isostatic adjustment reconstructions with both representations of the rheology. Results from the 1D model show variations in the viscosity structure between the area near to the centre of the former ice sheet and the areas at the margin of the ice sheet. Hence, we verify the importance of including lateral variations in GIA models in this region. Application of 3D models displays the sensitivity of model parameters to crustal deformation. German Baltic coast yields thinner lithosphere than TESZ region and near-centre region. Additionally, in the TESZ region, we notice a steep increase in viscosity of the asthenosphere and upper-mantle. Furthermore, we compared two different global ice histories (ICE5G and ICE6G_C) and concluded that the marginal areas are more sensitive to different deglaciations, and we propose to use regional ice histories to constrain GIA models better. Apart from the new statistical method, this study sets a ground for future GIA studies in complex tectonic regions and demonstrates the importance of including laterally heterogeneous Earth structure in GIA models.

Zusammenfassung

Glazial isostatische Anpassung oder Deformation (GIA) beschreibt die fortdauernde Reaktion des viskoelastischen Teils des Erdkörpers, der Ozeane sowie des Gravitationsfeldes auf die ehemalige Belastung durch große Eisschilde. Die Erdoberfläche war einst von gigantischen Eismassen bedeckt. Das Schmelzen dieser Eismassen beeinflusst bis heute Küstenverläufe und den Meeresspiegel. Um die Meeresspiegel der Vergangenheit zu bestimmen und zukünftige Veränderung vorherzusagen, ist es notwendig, die rheologischen Eigenschaften der Erde in den entsprechenden Modellen einzuschränken. Dies geschieht häufig anhand von Meeresspiegel-Indikatoren.

Im ersten Teil der vorliegenden Dissertation stellen wir eine statistische Methode vor, die den Zusammenhang zwischen Meeresspiegel-Indikatoren und dem relativen Meeresspiegel quantifiziert, und vergleichen die Ergebnisse mit GIA-Vorhersagen. Das Modell basiert auf räumlich und zeitlich aufgelösten Wahrscheinlichkeitsdichtefunktionen, die sich aus dem Alter und der Elevation der einzelnen Indikatoren ableiten. Dies erlaubt eine rigorosere Validierung anhand von Daten zum Meeresspiegel und kann zusätzlich auch mit Datensätzen schlechterer Qualität umgehen. Die Genauigkeit dieser Methode prüfen wir anhand von Daten in der Hudson Bay und Kanada, bevor wir sie anschließend auf Daten von SW-Fennoskandia anwenden.

SW-Fennoskandia ist ein Gebiet, in dem laterale Heterogenität mit hoher Wahrscheinlichkeit existiert. Der südwestliche Teil von Fennoskandia liegt in einem plattentektonischen Grenzbereich, der sogenannten Tornquistzone. GIA Modelle nutzen entweder ein radialsymmetrisches (und daher effektiv eindimensionales) Erdmodell, in der die rheologischen Eigenschaften sich lediglich vertikal verändern, oder ein drei-dimensionales Erdmodell mit drei-dimensional variierender Viskosität.

In dieser Arbeit vergleichen wir Modelle der glazialen isostatischen Anpassung auf Basis der beiden Darstellungen der Rheologie. Die Ergebnisse des eindimensionalen Modells zeigen Unterschiede in der Viskositätsstruktur zwischen dem Zentrum des ehemaligen Eisschildes und dessen Rand. Dies zeigt, dass es wichtig ist, laterale Variationen in den GIA Modellen für SW-Fennoskandia zu integrieren. Die Anwendung des dreidimensionalen Modells bestätigt die Sensitivität der Modellparameter für Krustendeformationen. An der deutschen Ostseeküste ist die Lithosphäre weniger dick als in der Tornquistzone und in zentrumsnahen Regionen. Zusätzlich ist in der Tornquistzone ein starker Anstieg der Viskosität der Asthenosphäre und des oberen Erdmantels zu beobachten. Darüber hinaus vergleichen wir zwei verschiedene globale Eisschild-Rekonstruktionen (ICE5G und ICE6G_C) und stellen fest, dass die Randgebiete empfindlicher auf verschiedene Deglaziationen reagieren. Daher

schlagen wir, vor regionale Eisschild-Rekonstruktionen zu nutzen, um GIA-Modelle besser justieren zu können. Neben der neuen verwendeten statistischen Methode legt die vorliegende Dissertation den Grundstein für die Anwendung von GIA-Modellen in tektonisch komplexen Gebieten und zeigt wie wichtig es ist, lateral heterogene Erdstrukturen in das verwendete Modell einzubinden.

Acknowledgements

This thesis was not a one-person work, and I would like to express my gratitude for all the support and assistance I got during this period. I would like to express my sincere gratitude to my supervisors Maik Thomas and Volker Klemann, for giving me this opportunity in the first place. I would like to thank Maik for his insightful guidance, support, and endless patience. When talking about patience, special thanks go to Volker Klemann, without whom this thesis would be hardly possible. Volker's guidance through all the ups and downs was crucial, as well as commitment and knowledge on the topic.

I am deeply grateful to Chris Irrgang, Meike Bagge and Johannes Petereit for their help and support. All of them taught me a lot and helped pass technical obstacles and learn new things. I would also like to thank the rest of my colleagues from sections 1.3 and 4.4 at GFZ; numerous interesting coffee talks lead to new ideas and insights. Special thanks to Theresa Blume on her support at the very end.

Of course, the whole GFZ volleyball team was unbelievable support and source of laughter and great friendship. Special thanks go to my friends Dunja Mitrović and Goran and Pedja Babarogić for their excellent design skills and help with figures. I thank my best friends Manar, Aleenah and Carli for always supporting me. Last but not the least, I thank my family and friends in Serbia and my partner Vedran for always pushing me to go forward. Mama, tata ovo je za vas.

The complete research work was carried out at the German Research Centre for Geosciences (GFZ). The study was embedded in the project PalMod (FKZ:01LP1503A) funded by the Federal Ministry of Education and Science (BMBF) under the framework programme "Research for Sustainable Development" (FONA).

Contents

List of Figures

List of Tables

List of Abbreviations

BP	**B**efore **P**resent
GIA	**G**lacial **I**sostatic **A**djustment
GIS	**G**renland **I**ce **S**heet
GPS	**G**lobal **P**ositioning **S**ystem
IPCC	**I**ntergovernmental **P**anel for **C**limate **C**hange
IRTS	**I**nverse **R**elaxation **T**ime **S**pectrum
LIS	**L**aurentide **I**ce **S**heet
LGM	**L**ast **G**lacial **M**aximum
MIS	**M**arine **I**sotope **S**tage
MOM	**M**ethod **O**f **M**oments
ML	**M**aximum **L**ikelihood
MSL	**M**ean **S**ea **L**evel
OSL	**O**pritcally **S**imulated **L**uminescence
PDF	**P**robability **D**ensity **F**unction
PREM	**P**reliminary **R**eference **E**arth **M**odel
PWM	**P**robability **W**eighted **M**oments
RSL	**R**elative **S**ea **L**evel
SLI	**S**ea **L**evel **I**ndicator
SLIP	**S**ea **L**evel **I**ndex **P**oint
SLR	**S**atellite **L**aser **R**anging
VAM	**VA**lidation**M**ethod
VILMA	**VI**scoelastic **L**ithosphere and **MA**ntle **M**odel

Dedicated to my family

1

Introduction

1.1 Understanding sea-level change

Sea-level change has affected and will continue to affect the life of humankind in many ways. It is estimated that today, one-third of the human population lives in the vicinity of the coastline (Matti et al., 2016). For its majority, knowledge about whether or not sea level will rise enough to jeopardize their households is of utmost importance. Apart from the direct threat to human settlements, sea-level rise is affecting the coastal habitats of birds, fish and plants. It can cause flooding of wetlands, devastating erosion and the pollution of agricultural soil and aquifers with salt (Woodworth and Blackman, 2004; Lemke et al., 2007). Furthermore, higher sea levels increase vulnerability to extreme events such as storm surges, causing significant environmental, social and economic issues. The main contributors to sea-level rise are thermal expansion of the oceans, melting of the glaciers and ice caps and loss of Greenland and Antarctica's ice sheets (Lemke et al., 2007).

To better understand present changes in sea level and climate in general, we look at how the Earth responded to changing conditions. Based on the Milanković theory of ice ages, Earth's climate has periods of global cooling and warming due to variations in the Earth's orbit around the sun (Milanković, 1969). Milutin Milanković (who worked on this theory for 30 years) assumed that the shape of Earth's orbit changes from near-circular to elliptical, affecting the intensity of solar radiation in Northern Atmosphere (Wilson et al., 2000). Periods with a lower amount of solar radiation reaching the surface, causing more moderate

temperatures and onsetting glaciation, are therefore termed *glacials*. During these periods, massive ice sheets were formed in North America (Laurentide Ice Sheet), northern Europe and Asia (Eurasian Ice Sheet) and in Antarctica, Patagonia and Himalaya (Figure 1.1).

Approximately 26 ka before present (BP), Earth's ice sheet coverage reached maximum ex-

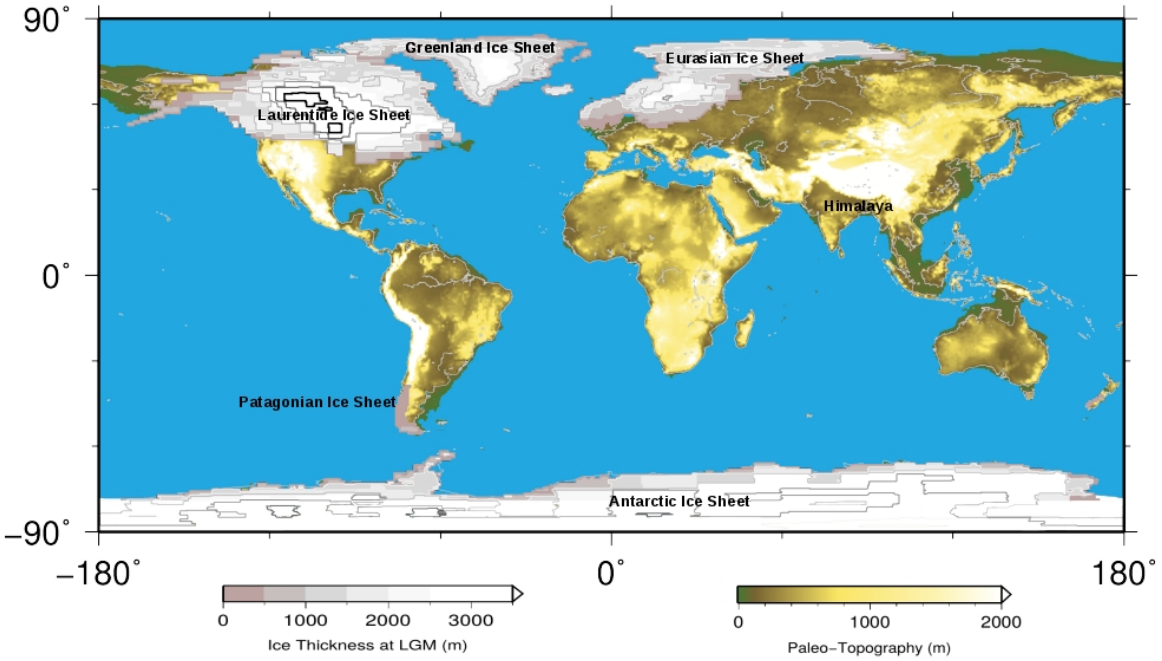

FIGURE 1.1: Ice sheets at the Last Glacial Maximum worldwide, around 21,000 years ago from ICE-5G data (Peltier, 2004a). Image courtesy Meike Bagge.

tent (Peltier and Fairbanks, 2006). From this period, defined as the Last Glacial Maximum (LGM), deglaciation started which lasted until ∼10 ka BP, causing variations in sea level across the globe. Earth entered a period with warmer surface temperatures and retreating ice sheets called *interglacial*. Relative sea level (RSL) in regions distant from glaciation centres (usually referred to as far-field) rose ∼120-130 m since LGM due to the inflow of melt-water from 50 million km^3 land-based ice (Khan et al., 2015; Peltier and Fairbanks, 2006). Regions in the vicinity to former centres of major ice sheets (near-field) experienced a drop in RSL as a consequence of the solid Earth uplift by hundreds of meters (Peltier, 1998a; Whitehouse, 2018). This phenomenon is characterized as Glacial Isostatic Adjustment (GIA), deformation of the solid Earth as a response to ice loading and unloading, and it is an ongoing process (Milne and Shennan, 2013).

1.2 Development of Glacial Isostatic Adjustment research

During glacial periods, forming of ice sheets caused a crustal depression displacing the mantle beneath and forming a peripheral bulge around the ice extent (Figure 1.2 (a)) (Wilson et al., 2000). Subsidence went on until a mantle mass, equivalent to the amount of loaded ice, was displaced, resulting in crust deformation of several hundreds of meters (Steffen and Wu, 2011). After the LGM, when deglaciation started, the reverse process took place, uplift started in depressed areas, and subsidence occurred on peripheral bulges (Figure 1.2(b)). But the rebound is slower than the melting of ice caps due to the high viscosity of the

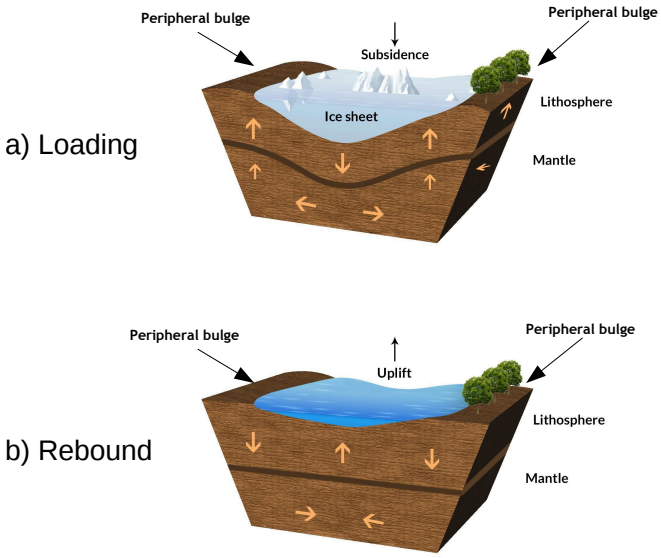

FIGURE 1.2: Solid Earth deformation due to GIA. (a) Loaded crust subsides, and peripheral bulges flex up. (b) Solid Earth is rebounding after the loss of ice sheet mass and peripheral bulges are collapsing.

Earth's mantle which hinders the mantle transport. Thus, the GIA process is still ongoing in areas that were once covered with several kilometres of ice. Scandinavia and Canada are experiencing the uplift at a rate of ∼10 mm a $^{-1}$ (Lidberg et al., 2010; Whitehouse, 2018) and they will continue to uplift by another few thousands of years (Walcott, 1972b). In terms of Earth's timescale, GIA is a rapid process, and sea level change of ∼130 m since LGM can be easily observed in the timespan of modern human civilization. First known description of GIA consequences is dated from 1491, where residents of a town Östhamman on the coast of the Baltic Sea were forced to relocate the whole town because they could not reach the harbour anymore (Ekman, 2009). It was estimated that this area was subject to

2 m rebound since the harbour was built in the 1100s, and this record is considered to be a first documented record of GIA (Ekman, 2009). The first scientific proof was presented by Swedish geophysicist and the geologist Andreas Celsius in 1743, but he found that the sea level was falling at rate of 1.4 cm/yr and not that the cause was a land uplift. Scientists a few generations after him (Playfair, 1802; Lyell, 1835) concluded that changes in sea level were caused due to the land uplift by observing different regions in the world. They concluded that if it would be a drop in sea level, it should be uniform everywhere, but based on different observations, sea level varied from region to region, thus indicating the change in land elevation. Finally, in 1865, the British geologist Thomas Jamieson brought a new theory and first hypothesis about GIA, where he determined that enormous amount of sea ice had caused the observed land depression in Scandinavia, North America, and Scotland (Jamieson, 1865).

Over another few decades in the late 19th and early 20th century, scientists made significant contributions to the GIA field and set a ground for a contemporary GIA studies (Whitehouse, 2018). The first estimate of the mantle viscosity was done by Haskell (1935) who calculated $\sim 10^{21}$ Pa s for the upper mantle, usually referred to as "Haskell" viscosity average. Fast forward to 1970s and the beginning of GIA models as we know today, Farrell and Clark (1976) introduced the "Sea-level equation" (SLE), the foundation of most modern GIA models. SLE is an integral equation primarily used to calculate relative sea level (RSL) changes based on load-induced variations of height in sea surface and seafloor governed by redistribution of ice and water (Spada, 2017; Whitehouse, 2018). We define RSL as a distance between geoid, which is an averaged height of a sea surface over several decades and the solid Earth surface (Shennan et al., 2015). RSL can be presented as:

$$S = N - U\,. \tag{1.1}$$

Where S is RSL, N is absolute sea level or elevation of the sea surface from the centre of mass of the solid Earth and U is a vertical displacement or height of the solid surface of the Earth (Spada, 2017; Whitehouse, 2018). Changes in sea level (S) are clearly affected by changes of U and N. They are determined by the viscoelastic response of the solid Earth due to the time variable surface loading and calculated with the integral sea-level equation. Elaborate theoretical representation of the SLE can be found in many studies, starting from Farrell and Clark (1976) and later in Peltier and Andrews (1976); Peltier (1999); Mitrovica and Milne (2003); Lambeck et al. (2003); Spada (2017). Two largest uncertainties in GIA modelling are paleo ice sheet reconstruction and rheological properties of solid Earth (rheology) (Mitrovica and Milne, 2003; Whitehouse, 2018). They can be calculated using an iterative approach on SLE to constrain the thickness of past global ice sheets and viscosity profile of the mantle using available sea-level data (Spada, 2017).

1.3 Numerical modeling of Glacial Isostatic Adjustment

To numerically model the GIA process, it is necessary to consider solid Earth viscosity structure, changes in global ocean and paleo ice sheet reconstructions (Mitrovica and Milne, 2003). In most GIA studies, the Earth is commonly represented with spherically symmetric Maxwell viscoelastic models (Peltier, 1976). These models are structured from several layers that include specific lithosphere thickness, upper-mantle and lower-mantle layers with different viscosity, where the border between mantles is at a depth of 670 km (coinciding with seismic discontinuity) (Stockamp et al., 2016). The thickness of the lithosphere controls the wavelength of the deformation, and the viscosity structure of the mantle is responsible for the rate of the deformation (Whitehouse, 2018). Models represented with layers are referred to as one-dimensional models (1D) because they do not consider lateral variations in Earth properties (Mitrovica and Milne, 2003).

With the development of geodetic techniques such as satellite missions and the Global

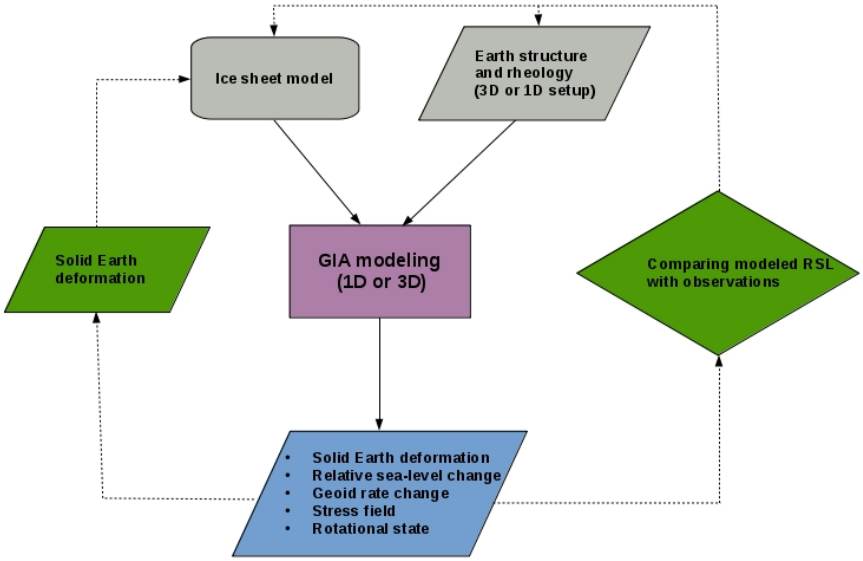

FIGURE 1.3: Diagram of GIA modelling structure. Inputs of the model are Earth structure and rheology, layered approach in case of 1D models or, e.g. inferring viscosity from seismic tomography models for 3D models. Outputs of the model are compared to observations for future tuning of the model. Diagram adapted from Whitehouse (2018)

Positioning System (GPS), it became clear that the viscosity distribution does not vary only with depth but also horizontally (van der Wal et al., 2015). Lateral variation in viscosity structure is investigated for a couple of decades now (Sabadini et al., 1986; Wu et al.,

1998b; Martinec, 2000; Latychev et al., 2005). With advance in computational power, GIA spherical models started to consider three-dimensional Earth structure since 2000s (Milne et al., 2004; Whitehouse et al., 2006; Klemann et al., 2008; van der Wal et al., 2013; Milne, 2015), commonly referred to as 3D models. However, it is still debatable whether they give better results than 1D models, apart from demanding extensive computational power, in 3D models, the mantle is still not constrained enough to make models precise (Milne, 2015).

As mentioned before, the GIA model output depends on two inputs; the rheology of the Earth and the global ice-sheet history. The latter describes global changes in surface load due to the melting water and the ice movement (Steffen and Wu, 2011; Whitehouse, 2018). Numerical ice models are often used to infer past ice-sheet reconstructions (Whitehouse, 2018). According to Steffen and Wu (2011), there are two types of ice-sheet models. The first one uses a priori GIA output that is fitted to the available data, and a second one is based on thermo-dynamical ice-sheet models that are constrained with geological data. Most commonly used models in GIA studies are global ICE-NG models developed by Peltier and co-authors (Tushingham and Peltier, 1991; Peltier, 1993, 2004b; Peltier et al., 2015). Another group of global models has been developed by Nakada and Lambeck (1987) and Lambeck et al. (2003). Fully coupled ice-sheet and GIA models are done to produce self-consistent ice-sheet and sea-level reconstructions (Gomez et al., 2012, 2013; De Boer et al., 2014; Konrad et al., 2014; Pollard et al., 2017, e.g.). Several studies include many ice-history models and vary Earth model parameters (Gowan et al., 2016; Vestøl et al., 2019, e.g.). In this study, we do not vary the glaciation history as it is not the scope of this thesis, but consider the last glacial cycle according to ICE5G and ICE6G_C glaciation histories (Peltier, 2004b; Peltier et al., 2015). We analyse results from both 1D and 3D GIA models. We use the spectral-finite element model VILMA (VIscoelastic Lithosphere and MAntle model) (Martinec, 2000; Hagedoorn et al., 2007; Klemann et al., 2008, 2015). VILMA 1D model uses the previously mentioned layered model with vertical changes in viscosity. Earth structure for VILMA model is obtained with a conventional method that relates seismic velocity structure (from seismic tomography) to mantle temperature, and by using scaling laws it is converted to viscosity structure (Ivins and Sammis, 1995).

1.4 Sea-level data

Over the decades, as the GIA modelling advanced so did techniques for observing changes significant for GIA studies. Different observations can be used to constrain model parameters such as rheology and ice sheet history (Spada, 2017). Modern geodetic techniques, such as GNSS, VLBI, SAR, airborne- and satellite-altimetry and satellite gravimetry are used to observe changes in Earth rotation and Earth surface motion and Earth's gravity

field, caused by ongoing redistribution of mass of ice, ocean water and mantle (Wahr and Davis, 2013). Geological records, tide gauges and altimetry are used to determine RSL or changes in RSL. Geological records can be dated back to several 100,000 years while geodetic techniques, even though reliable and precise, only cover the last few decades. Different observations have different sensitivities; RSL data is useful for estimation of upper mantle viscosity and is dependent on the glaciation history. However, it is not so sensitive to deep-mantle viscosity (below 1800 km depth) (Wahr and Davis, 2013; Paulson et al., 2007). Some geodetic data is sensitive to lower mantle viscosity and retreat of ice sheets; therefore, a combination of geological data and geodetic techniques can improve constraints of GIA models (Wahr and Davis, 2013). In this study, we focus solely on geological data and means

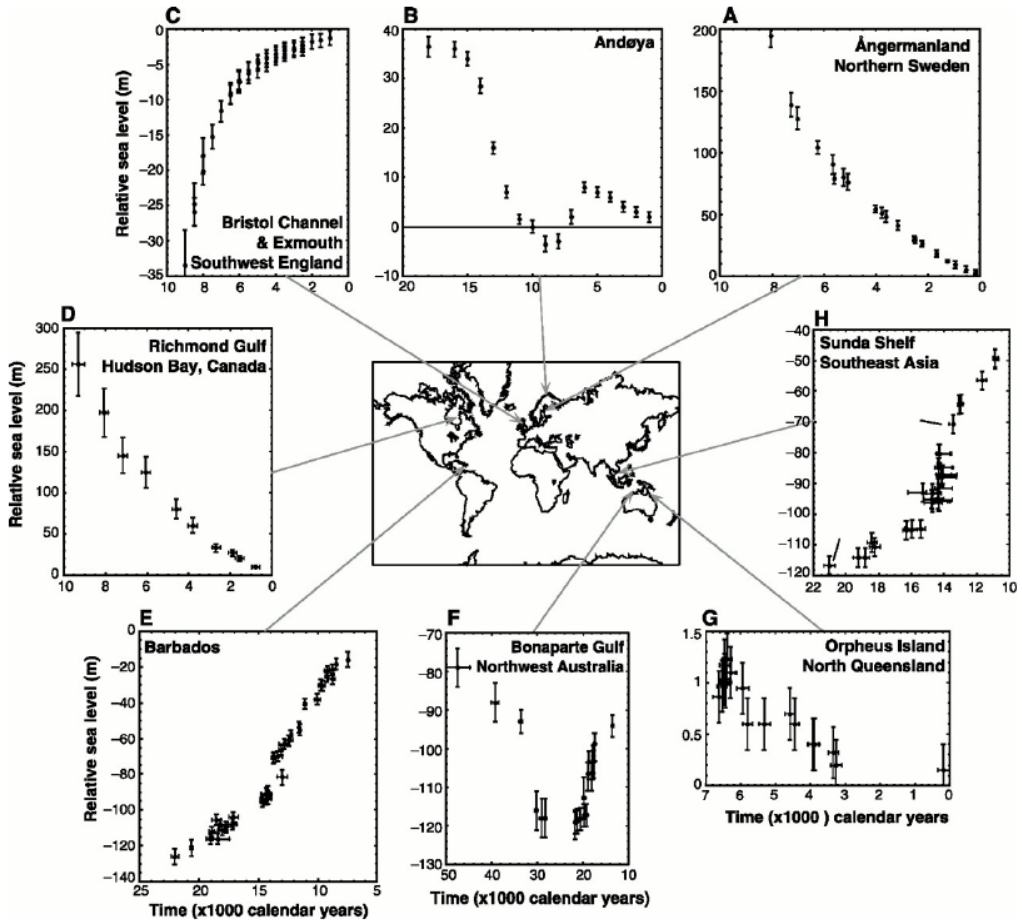

FIGURE 1.4: Reconstruction of past sea level using a variety of geological indicators. Figure from Lambeck and Chappell (2001).

to use them to constrain GIA models. Therefore more attention is given to the description and classification of geological data. Figure 1.4 shows examples of reconstructed RSL from different far-field and near-field locations, and depending on the location, either rise or fall of RSL is detected (Lambeck and Chappell, 2001). Geological data is considered to be any feature that was influenced or formed by a change of paleo sea level (Shennan et al., 2015). A common term for this kind of data is a sea-level indicator (SLI). The important word here

is an indicator, stating that SLIs are only providing the indicative meaning of former RSL since the elevation of SLI is relative to the crust (land) and a location of SLI, which does not always coincide with former sea surface (Shennan et al., 2015). Therefore, RSL needs to be inferred from SLI's elevation, usually by comparing it to its modern analogue (elevation of indicator's natural habitat concerning present sea level) (Shennan et al., 2015; Hibbert et al., 2016). SLIs that contain the location (geographical coordinates), age (measured by any dating technique), elevation and tendency (increase or decrease of sea level) and indicating the position or band-limited range of sea level, are referred to as sea-level index points (SLIPs). Less precise SLIs are limiting points that can give only maximum sea level (upper limit), usually found in freshwater inland and at or above past high-tide level (such as dead barnacles for example), and SLIs that are found in fully marine environments that give only minimum sea level (lower limit) (Shennan et al., 2015). So SLIs can be limiting points to paleo RSL or, as SLIPs, can provide a finite range.

Geological data can be classified in a few mayor types; *coastal sediments, coastal caves and sinkholes, geomorphological indicators, coral reefs, archaeological and biological data* (Shennan et al., 2015). *Coastal sediments* contain deposits of different organic materials that provide information about diverse processes such as lake stages and marine or terrestrial processes (retreat or deformation of shorelines) (Stockamp et al., 2016). *Coastal caves and sinkholes* are formed by groundwater, whose elevation is controlled by sea level, meaning that vertical movements of groundwater are governed by sea-level change (Van Hengstum et al., 2015). Structures that are formed in caves and sinkholes such as sediments and speleothems, serve as SLIs (Van Hengstum et al., 2015). Landforms like marine terraces, beach ridges, shore platforms and other coastal features that were formed during RSL fall, are *geomorphological indicators* (Kelsey, 2015). In the case of RSL rise, geomorphological features experience erosion or are buried by sediments, and as such are not valid as indicators. RSL is usually related to tidal range and elevation of geomorphological feature from a reference water level (Kelsey, 2015). *Coral reefs* are good indicators of sea level because they can be classified based on the sea-level depths of their living positions today (Yokoyama and Esat, 2015; Hibbert et al., 2016). Hence, dead corals can be related to past sea levels (Hibbert et al., 2016). Archaeological evidence of the ancient world in the Mediterranean and Atlantic Europe, for example, gives an interesting insight into the behavior of former sea level (Morhange and Marriner, 2015). *Bioindicators* like mussels and other marine organisms are fixed to *archaeological indicators*, so the combination of these two features is what makes SLIs. Examples of *archaeological indicators* are old harbours and drowned coastal cities covered with attached biological fauna that can be radiocarbon dated, and they are considered to be precise SLIPs. In other cases, they can serve as limiting points (Morhange and Marriner, 2015).

Due to this variety and abundance of geological data collected and investigated in past 100

yrs, it became highly important to use databases for easier manipulation of data in sea-level studies, and with the appearance of numerous databases, there is a need for standardization of data formats (Hijma et al., 2015). Standardization of the data was first suggested by van der Plassche (1986) in International Geological Correlation Program (IGCP) project 61, and it was followed by several IGCP projects afterwards (Shennan and Horton, 2002; Engelhart and Horton, 2012; Milne, 2015; Khan et al., 2015). Hijma et al. (2015) published a protocol for a sea-level geological database, including information on how to collect data from different geomorphological environments, how to interpret indicative meaning, reported age and location, and in general how to structure a database. Düsterhus et al. (2016) gives an overview of current problems as well as a list of regional databases. The special issue in the Quaternary Science Reviews journal provides a standardized global synthesis of regional RSL data that follows consistent reporting protocol (Khan et al., 2019). In the first part of this study, we use data compiled by Art Dyke (unpublished) in Hudson Bay, Canada (full list of data in Appendix B). For SW Fennoscandia, we use data provided by different authors (Appendix C).

1.5 Present state of studies on the interpretation of SLIs

Whitehouse (2018) stated that there is a need for a new strategy to infer GIA constraints from independent data since the precision and coverage of data-sets are constantly improving. Most of the studies use the basic goodness of fit to determine the degree of fit between the sea-level indicators and the predicted RSL from the GIA model (e.g., Tushingham and Peltier, 1991; Steffen and Kaufmann, 2005; Whitehouse et al., 2012; Melini and Spada, 2019). A limited number of studies developed statistical reconstructions of the indicative meaning of SLIs to treat uncertainties in elevation and age: Wolf et al. (2006) and Klemann and Wolf (2007) used fuzzy logic to formulate a classification scheme of the deposition conditions, which served for systematic interpretation of limiting points as well as index points. Kopp et al. (2009) suggested a censored normal distribution for limiting points to derive the posterior probability distribution of sea level and ice volume and applied this to reconstructions during the last interglacial based on SLIs. This approach was followed by Khan et al. (2015). Several studies analyse the indicative meaning of Last Interglacial in situ fossil corals using the modern living range of the same species (Deschamps et al., 2012). A most recent thorough study on corals is done by Hibbert et al. (2016), where authors in detail analysed fossil corals depth habitat to evaluate sea-level reconstructions and generated a Uranium-Thorium (U-Th) dated fossil corals database. Lorscheid (2017) related samples found on coastal deposits to the formation of specific landforms for the period the Marine Isotopic

Stage (MIS) 5e between ca. 128 and 116 ka in the Western Mediterranean. Vacchi et al. (2018) assembled a database of SLIs from the eastern coast of Canada, from Hudson Bay to the border with the USA, and applied an empirical-Bayesian spatio-temporal statistical method based on Kopp et al. (2009) to reconstruct former RSL change in this area. In his approach Vacchi et al. (2018) only considered SLIPs and no limiting points.
Probably the most comprehensive book about sea-level studies is "Handbook of Sea-Level Research" edited by Shennan et al. (2015). In Chapter 31 of this book Kemp and Telford (2015) explain transfer functions used for paleoenvironmental reconstructions and state five basic assumptions; 1) present-day geological data is related to their environment; 2) geological data has a linear relationship to another ecological factor; 3) modern analogue data and fossil data have the same relationship with the environment (if they are similar in composition); 4) numerical methods for sea-level reconstructions are accurate and unbiased; 5) sea-level indicator's location was not changed since the dated period. In this study, we apply these assumptions to determine the indicative meaning of SLIs. A statistical method developed in this study carefully considers the probability distribution of age and elevation, where, on latter, we apply the two-parameter gamma distribution in some cases. The two-parameter gamma distribution is often used in hydrology studies (e.g., Bobee and Ashkar, 1991; Yue et al., 2001), but this is the first time to be used to derive the probability density function of the elevation of sea-level data. We also combine existing methods to derive elevation probability of different data types (e.g., Hibbert et al., 2016; Caron et al., 2018), which are explained in Chapter 2.

1.6 Research questions and objectives

Scientists are researching land uplift or GIA since the beginning of the 18th-century (Steffen and Wu, 2011). Data collected since then include geological records and modern observations like tide gauges, satellite, GPS, absolute and relative gravity measurements. Modern observations and geological records have significant differences in accuracy and time-span they are covering. Recent records provide accurate and reliable information, but only for the last decades, while geological records date back over 10 000 years. GIA models are applied to correct geodetic observables for the resulting linear trends in surface motion, geoid and sea level, to reconstruct former sea-level variability during the last glacial cycle and to be coupled to Earth system models. They are mainly constrained by sea level reconstructions based on geological records (Milne et al., 2005; Bradley et al., 2011; Engelhart et al., 2011). GIA research advanced during the last decades, and different Earth models are developed. The spectral method, for which the Earth model is only radially stratified and is linearly viscoelastic, is refereed as 1D model (e.g., Mitrovica and Peltier, 1993; Fjeldskaar, 1994; Wieczerkowski et al., 1999; Kaufmann and Lambeck, 2002; Fleming et al., 2003;

Milne et al., 2004). The more realistic 3D Earth model accounts for lateral heterogeneity or non-linear rheology using spectral or spatial Finite-element methods (e.g., Martinec, 2000; Kaufmann and Wu, 2002; Latychev et al., 2005; Klemann et al., 2008; van der Wal et al., 2015). 3D models require more computational resources. For efficient ensemble runs, it is therefore necessary to determine if they give significantly different results from 1D-model approximations (Steffen and Wu, 2011).

This study is a part of PalMod program, German climate modelling initiative funded by the Federal Ministry of Education and Science to understand climate system dynamics and variability during the last glacial cycle. GIA models in this study are provided by Meike Bagge, who is a part of the PalMod working group WG 1.4. The task of this working group is to investigate the key processes of the solid Earth while other groups are working on the ice sheet dynamics. The decision not to vary ice distribution was made at the beginning of this study. Hence, the emphasis of this study is on developing a more advanced statistical method for considering different types of SLIs and its resulting impact when resolving the viscoelastic structure of the solid Earth in response to glacial loading. The study follows three main research questions:

RQ1: How can different types of sea-level indicators be rigorously combined to constrain GIA model-based reconstructions?

RQ2: To which degree does a 1D viscosity structure fit SLI based reconstructions of the former sea level in SW Fennoscandia?

RQ3: Is the GIA reconstruction for SW Fennoscandia compatible with geodynamic and tectonic constraints of the Earth structure?

The monographic dissertation contains six chapters. In Chapter 2, we present a new statistical method to analyse different types of sea-level indicators (SLIs) jointly for the validation of the GIA model reconstructions of former sea-level variability. In order to discuss this method, in Chapter 3, we apply it to the Hudson Bay region, Canada, as a test study. In Chapters 4 and 5, the method is transferred to Fennoscandia, which next to NE Canada is the second prominent region of GIA (Steffen and Wu, 2011). In Chapter 6, we discuss results from the study and future work.

2

A statistical method for validation of relative sea-level reconstructions

The performance of GIA models needs to be validated to constrain the radial or lateral profile of the Earth's mantle, and there is a need for an appropriate validation strategy (Whitehouse, 2018). Relative sea-level (RSL), as one of the outputs from GIA models (Figure 1.3), is a quantity that can be compared to sea-level indicators (see Sec. 1.4.). Majority of studies are using a basic approach to validate GIA models against sea-level data by applying a goodness of fit (Tushingham and Peltier, 1991; Steffen and Kaufmann, 2005; Whitehouse et al., 2012; Melini and Spada, 2019, e.g.). A few studies apply statistical reconstructions in order to treat uncertainties in age and elevation (Kopp et al., 2009; Khan et al., 2015; Vacchi et al., 2018).

Here, we propose a statistical method which is based on Bayes' statistics which we call VAlidation Method (VAM). The main goal of VAM is to constrain GIA reconstructions also in regions where data is not of a high quality.

We split the problem into respective probability density functions (PDFs) representing the information in elevation and dating, which enables us to consider different data types without defining a weighting scheme. For each data type, a tailored distribution is selected based on an indicative meaning of a sample and the dating technique. Combination of probability density functions such as the two-parameter gamma distribution presents an innovative approach to the statistical reconstruction of RSL based on observational data. Derived PDFs are combined into joint probability functions and conditioned concerning RSL predictions

from the GIA model.
Data types are classified as SLIP, upper and lower limiting point, and an elevation PDF is derived based on these types. Dating techniques used in this study, on which age distribution is based, are described in Section 2.2 of this Chapter.
To be able to apply VAM on RSL data, it is required that each data point has relevant information for further processing. Information such as position, age (including details on dating techniques), description of the sample and quantification of measurement uncertainty, and of course its elevation regarding a present-day RSL. Even though large effort has been made by several authors to establish guidelines for reporting the data (Düsterhus et al., 2016; Hijma et al., 2015), there are still numerous data points that were collected before these efforts, and sometimes, are the only available data in certain regions. Quite often, these outdated samples need to be re-calibrated and re-investigated. Insufficient information provided by the database can cause difficulty to determine whether the sample is a SLIP or a limiting point. In addition, inadequate use of calibration curve can cause possible error in the reported age of the sample.
In this study we use data from the German Research Centre for Geosciences (GFZ) database that contains more than 8000 points from different sources and this inconsistent reporting needs to be taken into account before processing the data.

2.1 Elevation probability density function

Depending on the interpretation of SLIs elevation from the database (or literature where data was published), we distinguish between SLIs that are limiting points, thus only providing upper or lower limit of the sea level, and SLIs that give a range of the former sea level, thus can be related to the modern analogue. Modern analogue is a technique used to reconstruct past oceanographic properties such as salinity, temperature and sea level by quantifying proxy records in terms of modern oceanographic conditions, assuming that the conditions have not changed significantly over time (Kucera, 2016).

2.1.1 Elevation probability of sea-level index points (SLIPs) using gamma distribution

SLIPs are considered to be biological samples found in the living positions, such as dead corals and shells still attached to the solid surface and geomorphological features whose formation can be related to the present day formation (beach ridges, marine terraces, coral reef terraces...) (Hibbert et al., 2016; Lorscheid, 2017). SLIPs are providing indicative ranges of former RSL, and we assume that these ranges have a distribution that often deviates from the normal distribution.

One of the main objectives of VAM, developed in this study, is to identify a suitable distribution that can represent an elevation distribution. We show one example of a modern analogue distribution of selected shells used in this study that are evidently exponential in Fig.2.1. Thus, confirm that normal distribution is not applicable to the indicators that are presenting living conditions of the samples related to RSL, such as corals or shells still attached to the original location. The most commonly used distribution in geophysics and hydrology is the two-parameter gamma distribution (Yue et al., 2001; Bobee and Ashkar, 1991; Clarke, 1980; Mathier et al., 1992).

The two-parameter gamma distribution is always positively skewed which makes it suitable for representation of numerous geophysical variables with positive values such as rainfall, floods, hydraulic conductivity, or in case of this study, frequency of tides, waves and shallow water environment. The general assumption of the gamma distribution is that it is a distribution of a sum of independent but identically distributed random variables, which we relate to, for example, unique tidal wave, or one shell sample.

Two parameters specifying the gamma distribution are the shape parameter k and the scale parameter θ. Parameter k determines if the shape of the distribution appears as exponential (k=1), bell-shaped (k>1), or as a shape of inverse letter J (k<1) (Koutsoyiannis, 2008). The shape parameter k is often denoted by α. The second parameter θ, determines the scale of the distribution, but inverse scale, or rate parameter $\beta := 1/\theta$ is usually used. To estimate these parameters, most common are the Method of Moments (MOM), Maximum Likelihood (ML) and Probability Weighted Moments (PWM) (Gamage et al., 2013). In this study, we use two methods, MOM and ML. MOM was adopted for estimation of tides and waves due to its simplicity, assuming that each tidal wave has same shape and scale, and we calculate parameters one time and use them for iterations to estimate PDF of each sample. We adopted the ML method for distribution of living shells and corals, where we claim that each variable is stochastically independent and has different shape parameter. Thus, we calculate both parameters repeatedly for each sample, meaning that each SLI has a different distribution. Several studies argue that MOM method is more bias than ML in a case of large samples and that estimates calculated by MOM are outside of the parameter space (e.g., Kliche et al., 2008; Johnson et al., 2014). Therefore we decided on applying ML for the estimation of parameters of living samples due to the more extensive data set. At the same time, we found MOM suitable for the smaller sample size when estimating parameters for tides and waves. Furthermore, MOM yields consistent estimators, and as mentioned, we assumed that tide and wave propagation has an equivalent Gamma distribution.

In MOM the scale and rate parameters are related to the mean value, μ, and variance σ^2 of the considered distribution:

$$\mu = \alpha\beta \tag{2.1}$$

$$\sigma^2 = \alpha\beta^2 . \tag{2.2}$$

Here σ is variance or standard deviation and μ is mean value of parameters of the distribution. From equations (2.1) and (2.2) and replacing μ and σ^2 with sample estimates $\bar{x}$ and s^2 respectively to be consistent with the notation in the literature, we get estimators of gamma parameters:

$$\hat{\alpha} = \frac{\bar{x}^2}{s^2} \tag{2.3}$$

$$\hat{\beta} = \frac{s^2}{\bar{x}} . \tag{2.4}$$

Second applied method is ML (e.g., Moran, 1969):

$$s = \ln\left(\frac{1}{N}\sum_{i=1}^{N} x_i\right) - \frac{1}{N}\sum_{i=1}^{N} \ln\left(x_i\right) . \tag{2.5}$$

Where independent and identically distributed random variables are $i = 1, 2..., N$. From here estimator of shape parameter $\hat{\alpha}$ is approximately

$$\hat{\alpha} \simeq \frac{3 - s + \sqrt{(s-3)^2 + 24s}}{12s} \tag{2.6}$$

and estimator of rate parameter $\hat{\beta}$ is

$$\hat{\beta} = \frac{\hat{\alpha}}{N} . \tag{2.7}$$

Finally, when we have estimated shape and scale parameters, $\hat{\alpha}$ and $\hat{\beta}$, we can proceed to the definition of the PDF of the two-parameter gamma distribution:

$$f(\bar{x}) = \frac{\hat{\beta}^{\alpha}}{\Gamma(\hat{\alpha})} \left(\bar{x}\right)^{\hat{\alpha}-1} e^{-\bar{x}\hat{\beta}} . \tag{2.8}$$

PDF in eq. (2.8) is a continuous distribution where it is assumed that parameters $\hat{\alpha}$,$\hat{\beta}$>0 and $\bar{x} \geq 0$. We investigate if the two-parameter gamma distribution is appropriate for sea-level data by applying it to four different shell types presented in Fig. 2.1 which is demonstrated in Chapter 3.

2.1.2 Elevation probability of limiting points

We apply a different approach for samples defined as limiting points because upper or lower limiting points only provide maximum or minimum bound of former RSL. For example, we

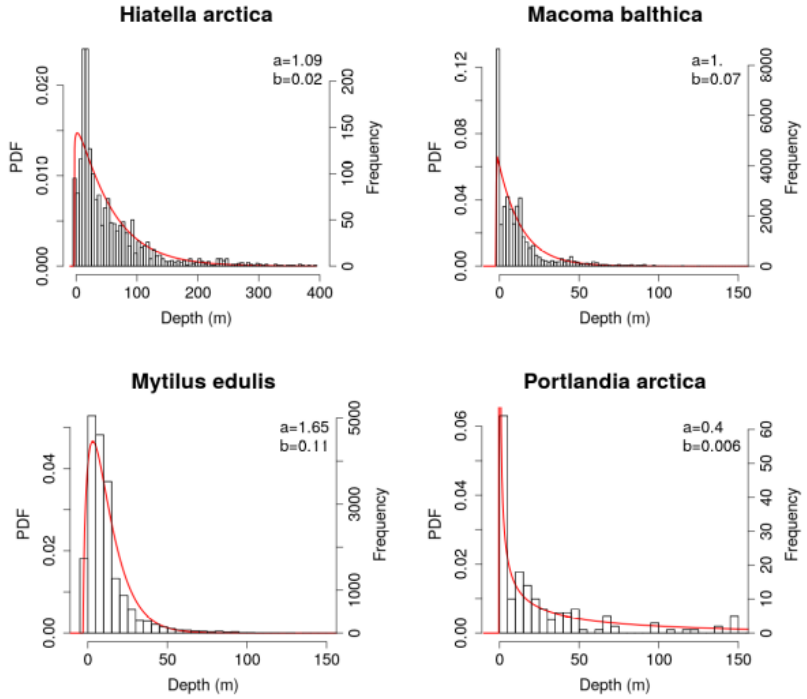

FIGURE 2.1: Water-depth distribution for samples of selected shell types extracted from OBIS (2017) which are related to, and fit of respective gamma distribution (red curve).

have marine samples that can only tell us a lowest possible elevation of former sea level, while terrestrial samples are indicating a highest possible elevation of former RSL. We based this approach on Caron et al. (2018) and we limit the bounds of former RSL with predictions provided by the GIA model and get elevation PDF as uniform distribution over assigned bound. In order to get a distribution we need to have a range of parameters, and we need to estimate maximum parameter values in case of lower limit points, and minimum parameter values for upper limit points. Caron et al. (2018) constrained data set with prediction models, and we follow this approach. If, for example, we are validating and comparing model ensemble with 30 members, maximum and minimum predictions from 30 values will serve as constraints of limiting points.

$$x_i = \begin{Bmatrix} h_{\text{SLI}} : h_{\text{max\_model}}, & \text{lower limiting points} \\ h_{\text{min\_model}} : h_{\text{SLI}}, & \text{upper limiting points} \end{Bmatrix} \tag{2.9}$$

Here h_{SLI} is an elevation value of SLI from a database and $h_{\text{min\_model}}$ and $h_{\text{max\_model}}$ are minimal and maximal RSL modeled predictions for the location and year given by the SLI. The constrained data set will result in uniform probability density function (PDF).

2.1.3 Measurement uncertainties

Measurement uncertainties of each SLI can include different variables such as water depth error, leveling error, drilling offset, tidal error, sample thickness and others. We account measurement uncertainties as a normal distribution, i.e.,

$$g(x|x_m, \sigma) \;=\; \frac{1}{\sqrt{2\,\pi\,\sigma^2}}\, e^{\frac{-(x-x_m)^2}{2\sigma^2}}\,, \tag{2.10}$$

where

$$\sigma \;=\; \sqrt{(\sigma_{\mathrm{SLI}})^2} \tag{2.11}$$

represents sum of reported errors in the database. Assuming that observational errors and the depth distribution are represented as independent random variables, their combination is represented by a convolution of the two distributions

$$p_h(x) \;=\; (f \,*\, g)(x) \;=\; \int_{-\infty}^{\infty} f(y)\, g(x-y)\, dy\,. \tag{2.12}$$

For its calculation we apply the Fourier transformation - which means the convolution is replaced by the product of the two Fourier transformed distribution functions. Furthermore, in case of homogeneous, normal and gamma distribution, there exist analytical expression.

2.2 Age probability density function

A process used to find out how old is an object or event is called *chronological dating*. There are several dating methods mainly classified by two criteria: *relative* and *absolute* dating. While relative dating can only determine the order of certain events, absolute dating can provide absolute age, hence more commonly used in geology, paleontology and archaeology. In this study we use absolute criteria, that mainly consists of radiometric dating methods, and we will focus on their definition, and the reason behind it is that most of the sea-level data is dated with radiometric dating methods.

Radiometric dating has a long history since its invention in 1905 by Ernest Rutherford and its first publication by Boltwood (1907). A basic principle is a measurement of a fixed decay rate of radioactive isotopes that naturally occur in wide range of materials. Rocks, organic material or other objects in nature often contain isotopes. Isotopes are unstable radioactive elements that are always aiming to reach stable state and during this process they release radiation, which is leading to the radioactive decay. Each radioactive isotope has known fixed decay rate that is called half-life (Van Grieken, 1994). Therefore, by determination of the isotope ratio in the sample and knowing the isotope's half life and the ration when

the material of the sample formed, it is possible to determine its age. Radiometric dating techniques vary based on the type of dated organic material. Uranium-lead, potassium-argon, rubidium-strontium, uranium-thorium, samarium-neodymium and radiocarbon dating are some of known radiometric methods (McRae, 1998). Radiocarbon dating is one of the most represented dating in sea-level data, with few exemptions like luminescence dating or a stratigraphic relationship dating. Luminescence dating methods differ from radiometric dating methods in a way that they do not depend on decay of isotopes, but rather indicate the age of a material based on deriving the duration since they were last exposed to light or heat. In this study, we use indicators that are dated with the radiocarbon, one type of luminescence, and the stratigraphic relationship dating. Therefore we explain only those methods in detail.

2.2.1 Radiocarbon dating

Radiocarbon dating, also called carbon-14 dating, is based on a half-life of carbon isotope ^{14}C. The radiocarbon dating has been used for dating of archaeological and geological records since its invention in the 1940s by Willard Libby who was awarded the Nobel Prize in 1960 for it (Libby et al., 1949; Reimer et al., 2013). ^{14}C isotope has a half-life of 5730 $\pm$ 40 years, and it is formed continuously in the upper atmosphere after interaction of cosmic ray neutrons and atmospheric nitrogen (Törnqvist et al., 2015; Analytic, 2019; Higham, 2019). Next, after it combines with oxygen, it enters the global carbon cycle as carbon dioxide, and is incorporated by living beings till their death, when the exchange of carbon with environment stops. A content of ^{14}C isotopes that is left in a dead organic material is used to determine its age (or basically time of death). Radiocarbon dating is limited to 50 – 60,000 years which is equal to ten half-lives. After this period the amount of ^{14}C is very small, and other radiometric techniques have to be used (Reimer et al., 2013).
Fundamental point in radiocarbon dating is that ^{14}C content is not a date but measurement of an isotope ratio - $^{12}C/^{14}C$, and to transfer this ratio into date, it is necessary to apply statistical analysis using a calibration curve (Higham, 2019). A calibration curve is necessary as the ^{14}C content in the atmosphere is variable with the time. Parameters used for this statistical method are collected from precise carbon-14 dating of various samples such as known-age tree rings of oak, fir and sequoia and dating of annual varves counted in lakes for the period up to 12,000 BP (Analytic, 2019). From this period to the period up to 45,000 BP high-precision techniques such as uranium-thorium are used for comparison, and finally, calibration curves are built and are accessible in internationally accepted databases. Present databases contain the following curves: INTCAL13 for northern hemisphere, SHCAL13 for southern hemisphere and MARINE13 for marine environments (Analytic, 2019). The calibration is performed by comparing the ^{14}C age of a sample to a calibration curve and

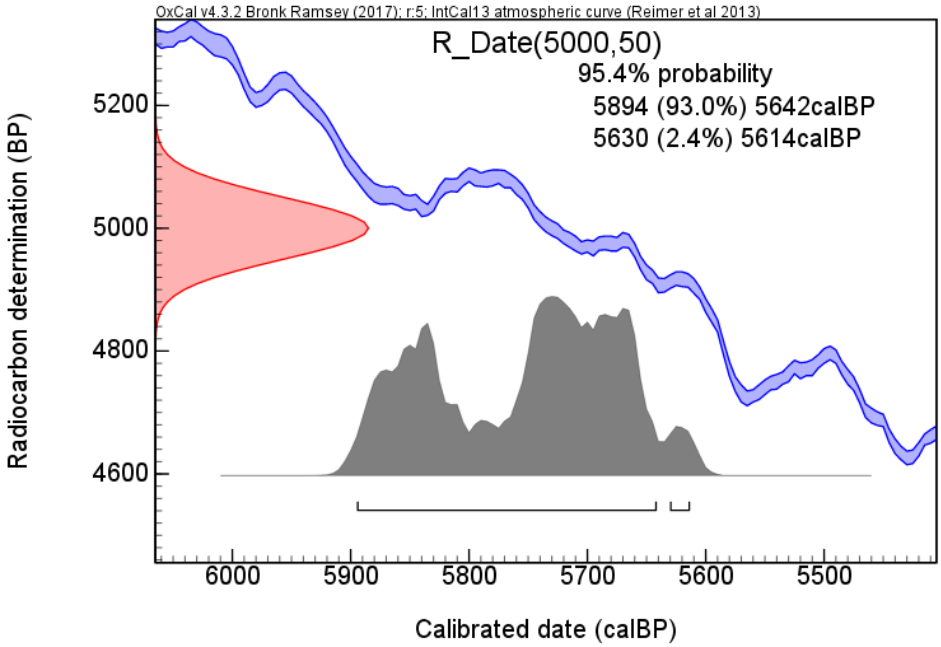

FIGURE 2.2: Example calibration performed with OxCal program for a sample with measured radiocarbon determination of 5000±50 BP (Ramsey, 2017). Blue curves indicate calibration curves INTCAL13; the red curve on the left indicates the dated age of the sample with its determined probability, where a Gaussian (normal) distribution is assumed. The grey histogram shows the posterior probability density function determined by the statistical analysis performed by the calibration program OxCal.

the mathematical basis for it is based on Bayes' theorem (Bronk Ramsey, 2009). The basic equation behind the statistical method is:

$$p(t \mid y) \propto p(y \mid t)p(t) \ , \tag{2.13}$$

where t is the set of parameters measured for calibration curves and y observations or samples that are being calibrated. $p(t)$ is the *prior* or the information about the parameters (selected calibration curve) we have apart from the measurements, $p(y|t)$ is the likelihood for the measurements given a set of parameters, $p(t \mid y)$ is the *posterior probability*, or the likelihood of a particular parameter set given the measurements and the prior. This posterior probability is what we use in our statistical method as an age PDF of radiocarbon dated samples, and it is calculated by the used calibration program. Age of a calibrated sample is expressed in years before 1950, which is a year that depicts present day (before present – BP). In Fig. (2.2) one calibrated example is shown, 5000±50 BP presents dated age of 5000 years before present with 50 years of uncertainty, and calibration gives a likelihood range within 95.4 and 68.2 probabilities, presented as grey area in the figure where peaks are showing higher probability.

2.2.2 Optically stimulated luminescence dating

Optically stimulated luminescence (OSL) dating is a luminescence response of grain to the exposure to the blue light of a wavelength of 470 nm. Grains that have optical properties such as quartz and feldspar can be used for OSL dating. When these types of grains are deposited into the sediments, they are receiving a small dosage of ionizing radiations from the natural decay of radionuclides from the local sediments. The radiation liberates the electrons from their spots in the crystal lattice, and they are after that stored in the defects of the minerals.

After grain's exposure to light or heat, these electrons are recombined with electron holes in the empty lattice spots resulting in a release of the stored energy. Stored energy is photons, whose release is observed as a tiny flux of light called luminescence. The OSL signal is converted to an absorbed radiation dose with a dose-response by matching it to the curve obtained in laboratory conditions. The age of the sample is calculated from the yearly dose of the radiation, acquired from the radionuclide concentrations of the sample and local sediments (Chamberlain, 2018).

2.2.3 Varved deposits

Varved sediments are a sequence of fine layers of sediments that are deposited during one year period. Name varv comes from a Swedish word for layer, and it represents a pair of laminae that are formed in glacial lake sediments during different seasons (Saarnisto and Ojala, 2009). Varved sediment stratigraphy was first introduced by the Swedish geologist De Geer (1884, 1940) and it was later adopted by the Finish geologist Sauramo (1929). Varves can be *glacial*, where the sediments are deposited during the melting of glacial water in spring and summer (Fig. 2.3). Large particles are first to be settled at the bottom of the water body, while the fine clay particles are placed during the winter, thus, resulting in seasonal sedimentation during a single year (Saarnisto and Ojala, 2009). The thickness of varves depends on the distance from the melting glacier/ice-sheet, being thicker closer to the melting glacier. A varve's thickness also varies with the intensity and the velocity of the meltwater, and these variations, as well as their colour, chemical content and texture, are a basis for varve chronology (Saarnisto and Ojala, 2009). *Nonglacial* varves are found in nonglacial lakes and marine environments and are formed by aeolian processes (of Encyclopaedia Britannica, 2011).

Varved sediment stratigraphy has been widely applied in assigning ages in sediments, and with the advancements in sediment sampling and development of image analysis, it is also used to reconstruct past climate changes (Saarnisto and Ojala, 2009).

FIGURE 2.3: Varved deposits attributed to sedimentation in Glacial Lake Missoula, Montana, U.S. Picture taken from of Encyclopaedia Britannica (2011)

2.3 Joint probability density function of age and elevation

The two PDFs representing uncertainties in age and elevation are used to create joint probability densities. Referring to the theory from Tarantola (2005), the joint PDF is equal to the product of two marginal probabilities. With this assumption we can represent the joint PDF as

$$f(t,\, h) \;=\; p_a(t)\, p_h(h)\;. \tag{2.14}$$

where $p_a(t)$ is the age probability density function and $p_h(h)$ is the elevation probability density function. Joint probability can be visualised as a two-dimensional parameter space. One example is presented in Fig. (2.4) with different confidence intervals.

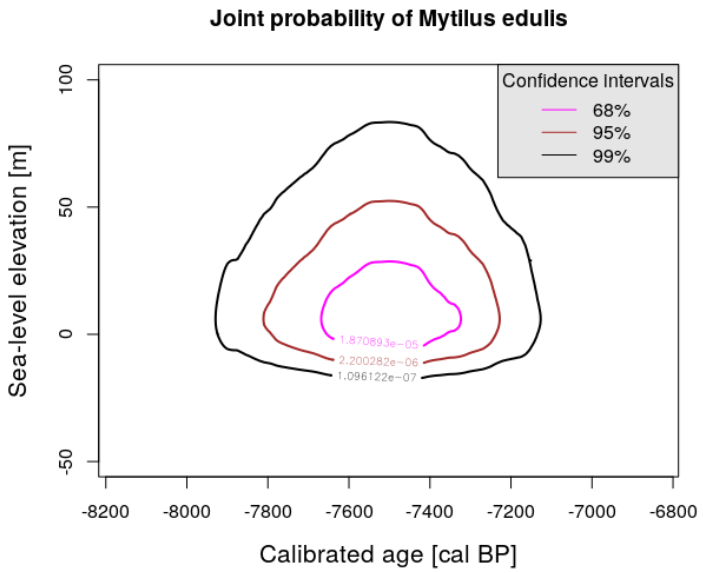

FIGURE 2.4: Confidence level of sea level from *Mytilus edulis* sample (found in living position) as function of elevation and age.

2.4 Evaluation of sea-level reconstructions

In past decades performance of numerical models and computational power have improved significantly (Caron et al., 2018). We are now in the position to perform a larger number of sensitivity experiments using variations of different parameters that are affecting GIA (the ice history, mantle properties, deformational rates...). A larger number of simulations allows statistical significance of uncertainty estimation of each parameter that are specifically problematic in the areas of former ice sheets (Caron et al., 2018). Therefore, models with unlimited ensemble members, constrained with large set of indicators with significant spatial and temporal resolution, can improve understanding of impact of certain parameters on GIA, especially in the regions with dynamical tectonic history (as presented in Chapter 4).
Here, we rigorously constrain derived uncertainties by considering the conditional probability density based on the definition of Tarantola (2005, p. 18). This probability density is a special case of conjunction of probability distributions (in our case elevation and age probability). In other words, we want to 'condition' the joint probability. Thus, if we say that the joint PDF represents application of p_h to p_a, our condition is to get the values where $p_h = p_h(t)$. For the time interval (t_1, t_2) covered by the confidence of p_a, e.g. of 99.5 %, we assume past RSL (h_{RSL}) to change linearly with time:

$$h_m^{\mathrm{RSL}}(t) \;=\; a_m \;+\; b_m\,(t - t_m) \tag{2.15}$$

Here a_m and b_m are respective sea-level elevation and rate of a specific model ensemble member at the location of the considered sample.
Then, the conditional probability based on Tarantola (2005) can be shown to follow:

$$P_{h,t|m} = \int_{t_1}^{t_2} {p_a}^{\mathrm{SLI}}(t)\, p_h^{\mathrm{SLI}}(h_m^{\mathrm{RSL}}(t))\, dt \,. \tag{2.16}$$

2.4.1 Redundancy weights

Collections of sea-level data points are rarely homogeneously distributed over a considered region and time interval, and an interpretation will be biased by the distribution in space and time (see Fig 3.1). Having a larger amount of SLIs dated to approximately same period and being located in close proximity to each other can cause redundancy, and, as such, can bias the result. To address spatio-temporal density and to suppress the consequence of redundant information of considered SLIs, we apply a weighting scheme. Briggs and Tarasov (2013) as well as Love et al. (2016) applied a spatial weighting algorithm to already aggregated curves in order to consider the clustering of curves in specific regions. We apply the redundancy weighting method proposed in Caron et al. (2018) where the cross correlations of the SLIs with respect to the considered model ensemble are taken into account. Therein, for each SLI a redundancy weight

$$w_i = \frac{K}{\sum_{j=1}^{N_{\mathrm{data}}} \rho_{ij}} \tag{2.17}$$

is defined. Here, K is a normalization constant so that

$$\frac{w_i}{\sum_i N_{\mathrm{data}}} = 1 \,, \tag{2.18}$$

N_{data} is the total number of samples. The Pearson correlation coefficient between the ensembles of predictions i and j is represented as

$$\rho_{ij} = \frac{cov(i,j)}{\sigma_i \sigma_j} \,, \tag{2.19}$$

where $cov(i,j)$ is the covariance between two SLIs and σ_i, σ_j are the standard deviations of the two SLIs.

2.4.2 Likelihood of model reconstructions of sea level

After calculating the conditional probability (2.16) for each selected SLI and redundancy weights (2.17), we continue with the conditional probability (2.20) for a whole set of SLIs

for each member of the ensemble we want to validate.

$$P = \bigcap_{i=1}^{N_{\text{data}}} P_i^{w_i} = \prod_{i=1}^{N_{\text{data}}} P_i^{w_i} , \tag{2.20}$$

which is computed as the product of the respective PDFs (Tarantola, 2005). For computational convenience, we consider the logarithm of the probabilty P,

$$\mathcal{L} = \frac{1}{N_{\text{data}}} \sum_{i=1}^{N_{\text{data}}} w_i \ln(P_{\text{sli}_i}) , \tag{2.21}$$

divided by the total number of samples N_{data} as the likelihood($\mathcal{L}$) of the set of SLIs to be represented by one member of the considered model ensemble.
In this study, we do not derive a posterior probability due to insufficient knowledge about the prior, which is fundamental in defining a posterior, but instead base the determination of the highest likelihood on Bayes factors (e.g., Kass and Raftery, 1995), which for two hypothesis we can write as:

$$K_i = \ln(P_i / P_{max}) = \mathcal{L}_i - \mathcal{L}_{max} . \tag{2.22}$$

Here P_{max} is the highest probability reached among ensemble members.

2.5 Summary

The method (VAM) proposed in this study addresses difficulties and uncertainties while using sea-level data, often the only available data, for validation of sea-level reconstructions based on GIA models. The advantage of the statistical method is that it allows usage of data points of "lower" quality such as limiting points. Derivation of probability density functions compensates for the weighting of different data types. Further advantage is a cautious consideration of elevation and dating uncertainties. Innovative aspect of the method is the application of the gamma distribution instead of a regular normal distribution. A gamma distribution is more suitable to depict probability behavior of data with positive skewness, such as a frequency of tides, waves and shallow water environment. The gamma distribution is used for the first time in a statistical reconstruction of a sea level, even though it is often applied in hydrology studies.
We present samples' indicative meaning as joint probability and condition them to model reconstructions, in that way model predictions are rigorously constrained and not merely compared as a spread of values. We discuss redundancy of the samples due to their spatial and temporal distribution. In addition, the statistical method can be applied to validate a model ensemble with unlimited members, which can contribute to estimation of uncertainties of model parameters, especially in areas covered with ice and with the history of dynamic

geologic processes.

To apply VAM, it is necessary to carefully examine individual samples in order to determine appropriate density functions. With the advance in data reporting standardization, to which this study contributes, this step can be facilitated.

3

Application of VAM to Hudson Bay

The Laurentide Ice Sheet (LIS) was the largest ice sheet in the northern hemisphere during the last glacial cycle. The ice sheet (Fig. 1.1) was covering the northern part of the United States and much of Canada with a thickness in some areas of more than 4 km and with a center close to Hudson Bay (Alley et al., 2005). At the end of the LGM, around 20,000 yrs BP, the LIS started to melt. Around 8,500 yrs BP the size of the LIS was just a fraction of its original size due to the enhanced surface radiation in boreal summer during early Holocene and the sea entered Hudson Bay (Clark et al., 1999). Changes in Earth's orbit caused insolation changes. Meaning that larger amounts of solar energy were reaching the surface than today, and these changes ("Milanković forcing") are regarded as the most dominating climate forces during the Quaternary period (Milanković, 1969; Lorenz et al., 2006). During the period from 7,600 yrs BP until final deglaciation of the LIS around 6,800 yrs BP sea level was rising 1 cm yr^{-1} on average (Carlson et al., 2007).

Ice sheets have a large influence on climate change due to several effects; freshwater fluxes from melted ice influence river flows, create underground proglacial lakes, influence thermohaline circulation of the oceans and change sea level (Clark et al., 1999). Also, ice sheet-atmosphere interaction causes winter jet streams from the ice, large anticyclones and storms at the ice-sheet surface (Ganopolski et al., 1998). History of ablation of the LIS is of high importance for future projections of sea-level changes caused by melting of the Greenland ice sheet (GIS), both are terrestrial ice sheets and better understanding of the past climate interactions with the LIS can provide more insights than time-limited modern observations of GIS. (Carlson et al., 2007).

One method to reconstruct paleo-ice sheets is geophysical modelling of GIA (e.g., Tarasov et al., 2012; Peltier et al., 2015; Lambeck et al., 2017). Changes in sea-level are caused by the Earth's rheology and ice history and with an iterative approach in GIA models it is possible to constrain former ice margins with geological records (e.g., Tushingham and Peltier, 1991; Peltier, 1993, 2004b; Peltier et al., 2015). Here we apply statistical method VAM developed in Chapter 2 to validate its performance in constraining the 1D GIA model ensemble with 140 different members in the Hudson Bay region, due to its importance as a region west of the most prominent uplift around 7,600 yrs BP. In the 1D GIA model ensemble, three Earth-structure variability parameters are varied. Parameters are presented in Table 3.1 and the complete list of members is in Appendix A. The model ensemble is explained in more detail in Section 3.3 of this Chapter.

To apply VAM, we use data from a large database of radiocarbon dates over North America compiled by Art Dyke (unpublished). Data can be found in the German Research Centre for Geoscience (GFZ) RSL database where SLIVISU software was used to access and visualize a proper regional subset (Unger et al., 2012, 2018). Many samples from this region are of low quality in terms of new interpretation. Nevertheless they contain important information about sea-level variability. From the database we take four different types of shells into consideration; *Hiatella arctica, Macoma balthica, Portlandia arctica* and *Mytillus edulis*. The database contains in total 160 shells of these four types. Figures 3.1(b) and 3.1(c) summarize the temporal and spatial distribution of SLIs and Fig. 3.1(a) shows the elevation distribution condensing them into a sea-level curve. The relative sea level at 8,000 years BP is shown in Fig. 3.2 since the age of most of selected SLIs is around this period (see Fig. 3.1(b)). From Fig. 3.2 it is visible that the range of RSL is up to 250 m around the coast of Hudson Bay, which coincides with that of the sea-level data shown in Fig. 3.1(a).

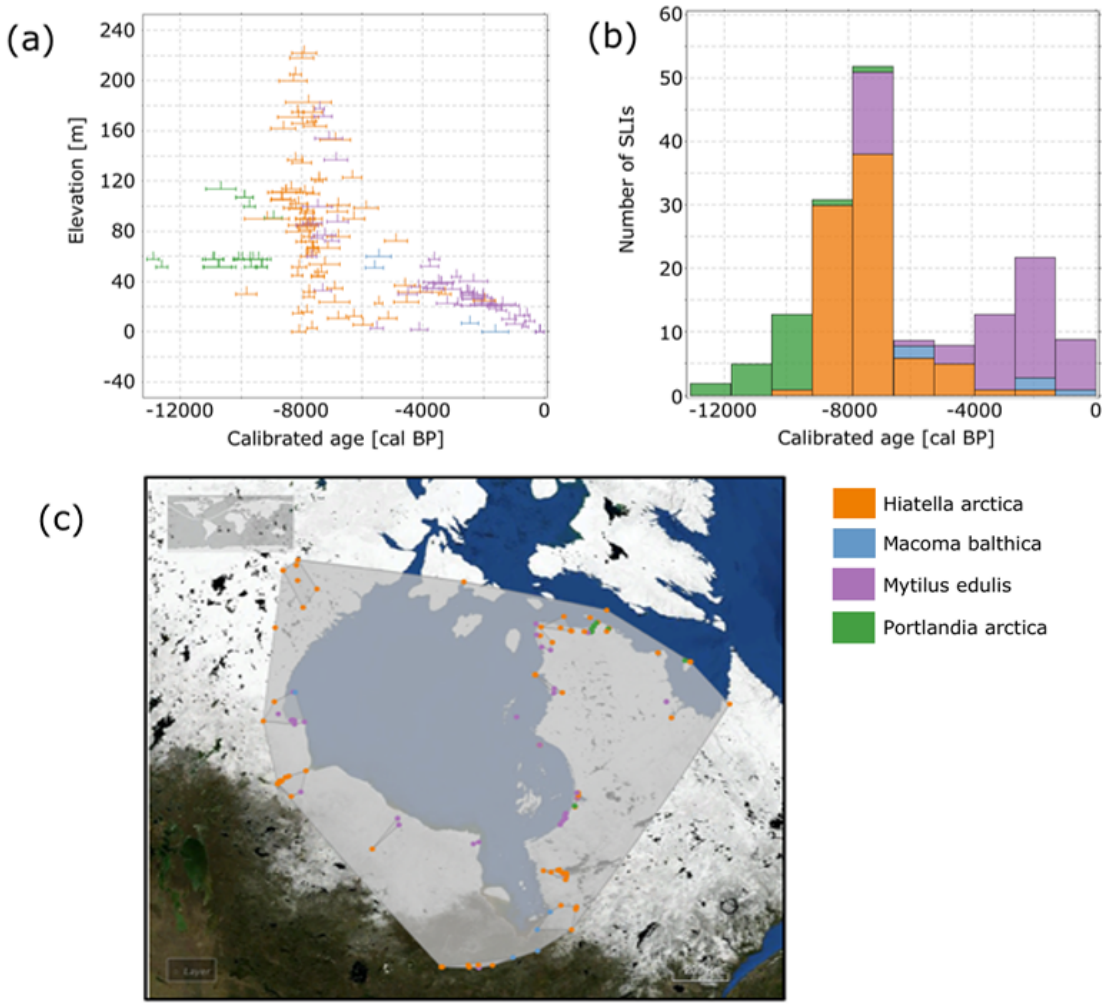

FIGURE 3.1: Spatio temporal distribution of shallow water shells covering the Hudson-Bay region: (a) Sea-level curve of selected SLIs in Hudson Bay. (b) histogram depicting occurrence of selected SLIs in various age periods in Hudson Bay. (c) Map of Hudson Bay with the selected SLIs retrieved from SLIVISU. Colors distinguish selected shells as shown in the color bar on the right. Data output visualized with SLIVISU.

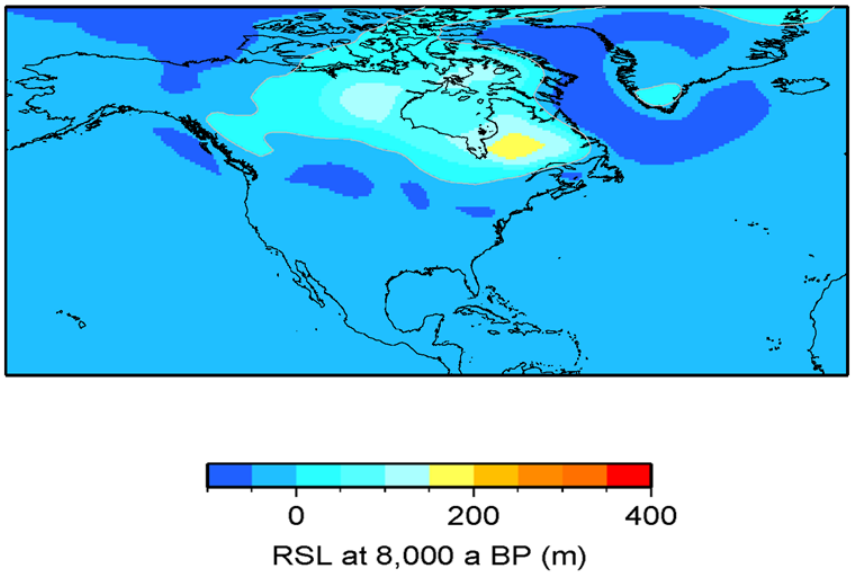

FIGURE 3.2: Relative sea level (RSL) at 8,000 years before present (BP) in the region of Hudson Bay based on mean predictions of the considered model ensemble. On land areas, the RSL follows the vertical displacement. Figure courtesy Meike Bagge.

3.1 Elevation probability density function for considered shell samples

We proceed with the spatio-temporal VAM introduced in Chapter 2. The first step is to calculate the elevation PDF of each SLI based on their indicative meaning interpretation. To classify the data based on the indicative meaning, we consulted original publications of the data that is listed in Appendix B. Tentative re-investigation rated that most of the samples were not found in their living position but were transported. Fragments of shells were dated and related to the formation of beach ridges. Therefore, we consider 152 SLIs as geomorphological SLIPs and relate them to the modern-day analogue of beach ridge formation, while eight samples were found in the living position – seven of *Portlandia arctica*, one of *Mytilus edulis* – which we relate to the present day habitat of mentioned shells.

3.1.1 Shells in living position

We generate elevation PDFs of identified SLIPs as explained in Chapter 2. ML method is used for parameter estimation of shells found in a living position. We acquire present-day information from the Ocean Biogeographical Information System (OBIS) database. The comprehensive OBIS database contains 45 million observations of nearly 120,000 marine species (OBIS, 2017).

Here OBIS data is interpreted as independent data points $x = [x_1, ..., x_n]$ where x_n presents height of each sample in relation to the present RSL from the same density or equally weighted. Thus, after calculating parameters for the gamma distribution ($\hat{\alpha}$, $\hat{\beta}$) using equations (2.5)-(2.7), we continue with the eq. (2.8) that calculates the gamma distribution for each selected sample. The gamma distribution from OBIS data is "shifted" by the observational elevation value of each SLIP, and by this is representing the transfer function $x \mapsto x - h_{\mathrm{SLIP}}$. In Fig. 3.3 one example of the "shifting" is presented. Here, red line depicts elevation of an SLIP with the age error. The modern analogue curve represents the present-day gamma distribution of a species to which selected SLIP is classified. We assume that the distribution of species did not change over time and that their habitat is related to the sea level, meaning that in the past they inhabited equivalent water depths in reference to RSL. Therefore, by "shifting" the present-day distribution of species for an elevation of an SLIP, we relate an SLIP to the modern analogue (Fig. 3.3) and eq. (2.8) now reads:

$$f(\bar{x}) \;=\; \frac{\hat{\beta}^{\alpha}}{\Gamma(\hat{\alpha})}\;(\bar{x} - h_{\mathrm{SLIP}})^{\hat{\alpha}-1}\;e^{-(\bar{x}-h_{\mathrm{SLIP}})\hat{\beta}}\,. \tag{3.1}$$

After taking into account measurement errors of both OBIS data and SLIPs, eq. (2.11)

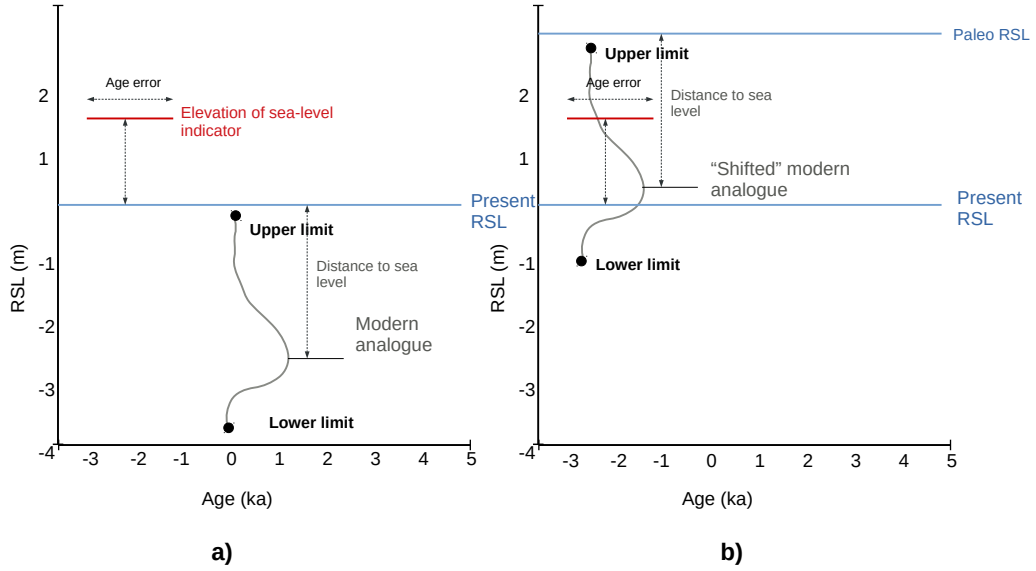

FIGURE 3.3: Example of a calculation of former RSL based on modern analogue. In figure a), modern analogue and elevation of an SLI in reference to present-day RSL are shown. In figure b) modern analogue is "shifted" for the height of SLI from RSL, and paleo RSL is calculated from the "shifted" position.

becomes:

$$\sigma = \sqrt{(\sigma_{\mathrm{O}})^2 + (\sigma_{\mathrm{S}})^2} \tag{3.2}$$

and sums up the uncertainties derived from the leveling of the OBIS data, σ_{O}, and the leveling errors of the geological sample (SLIP), σ_{S}.
Depth distribution of two shell types used in the analysis of the Hudson Bay region is shown in Fig. 2.1. Two shell types that are considered are *Portlandia arctica* and *Mytilus edulis*.

3.1.2 Beach ridges

Next, we continue with the approach with the following samples rated as geomorphological samples and relate former beach ridges to a present-day rate of beach ridge formation in Hudson Bay, based on the assumption that conditions have not changed significantly. For this group of SLIPs, we use MOM for parameter estimation using equations (2.1)-(2.4).
Beach ridges are emergent coastal deposits, formed by storm waves with a maximum altitude at storm wave swash height (SWSH) (Kelsey, 2015). When a wave breaks at the coast and washes up on the beach, moving sediments and biological materials, it is called a swash (Lorscheid, 2017). Repeated swash action forms different geomorphic features such as beach ridges, storm berms and marine terraces (Kelsey, 2015; Lorscheid, 2017). This process is present globally, and all shoreline deposits are related to present or past sea levels, making them suitable for interpretations as SLIs. Beach ridges cannot form above high tide levels or SWSH, meaning if they are located meters above present-day SWSH they are an

apparent document of former sea-level change. In some regions, beach ridges are the only available indicators of previous sea levels (Lorscheid, 2017). But beach ridges are classified as low-grade sea-level indicators due to the wide vertical indicative range because they are formed in different tidal environments (Rovere et al., 2016; Vacchi et al., 2018). Here we want to constrain this range with the gamma distribution proposed in Chapter 2 and, if proven possible, apply this approach to other geomorphic features, also often classified as low-quality SLIs.

We based this approach partly on the theory of Vacchi et al. (2018) who compiled a relative-sea level database in the Hudson Bay region. In his study, he argues that *Mytilus edulis* shells are usually attached to beach ridges since they live in intertidal and shallow environments. Vacchi et al. (2018) were assigning an indicative range of beach ridges to be 3 m + High Tide Level (HAT) and upper limit to be Mean Lower Low Water (MLLW), which represents averaged height of the lowest tide recorded during 19 years at one tidal station. The lower limit of 3 m Vacchi et al. (2018) justify with the reports from the formation of beach ridges in Eastern Canada to be up to this height.
We apply a slightly different approach since the aim of this study is to obtain the probability density function of an indicative meaning of each SLI. Therefore, as a range of the modern analogue elevation, we take tide levels of Hudson Bay and then shift the whole range according to the sample's elevation, instead of assigning a fixed value of 3 m. In this way, we assume that sample's elevation presents an elevation of the beach ridge with the height of SWSH.

We assume that the geomorphological shape of the Hudson Bay did not change substantially since Holocene and, so, do not consider changes in tidal range over time. From the regional tide model of Webb (2014), we find tides to follow a tidal wave entering through the Hudson Strait and travelling anti-clockwise through the bay with reducing amplitude. Accordingly, we divide Hudson Bay into four different high-tide level regions with decreasing amplitude (Fig. 3.7) In the Hudson Strait with high tide level of 4 m, 41 SLIPs are located, in the second region with 2 m, 39 SLIPs, in the third with 1 m, 12 SLIPs, and in the south-east part of Hudson Bay with 0.5 m tides, 56 SLIPs were found. We, again, use the gamma distribution to obtain elevation PDFs (Yue et al., 2001; Bobee and Ashkar, 1991). Distribution range is from the lowest high-tide level to highest high-tide level in the region, "shifted" by h_{SLIP}. In that way in: $x = [x_1, ..., x_n]$, where $x_n = 0.5$ and $x_n = 4$. We apply the same distribution in all four tidal regions, just shift the beginning of the distribution to the corresponding high-tide value (Fig. 3.4). For this gamma distribution, $\hat{\alpha}$ and $\hat{\beta}$ parameters are estimated to follow the shape of the wave frequencies using the MOM approach. Since in OBIS distribution we assign values to have a positive sign for depth, we flipped the

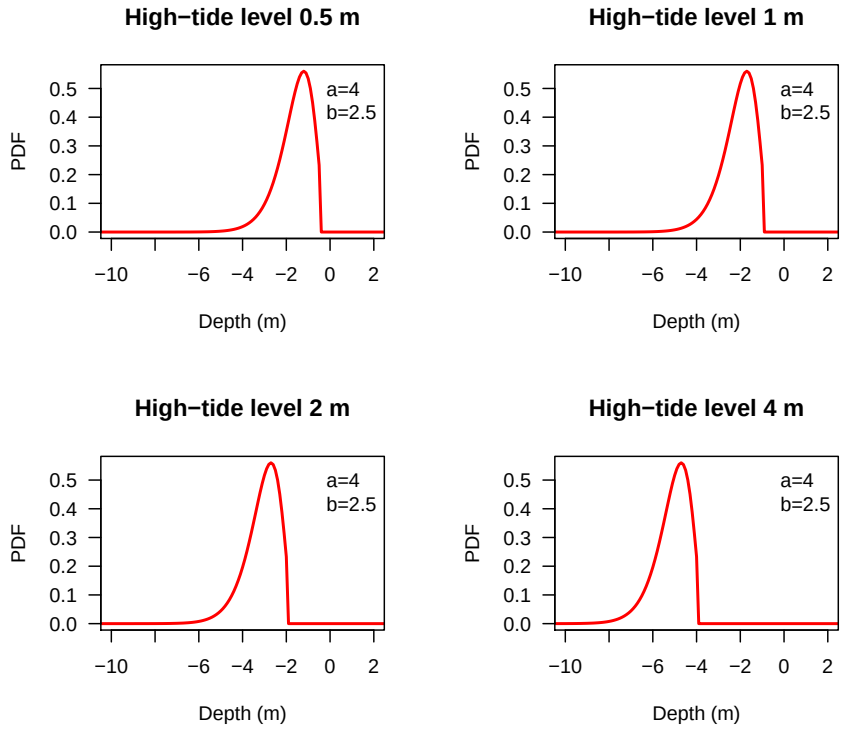

FIGURE 3.4: Gamma distribution of a beach ridge formation distribution based on different high-tide levels in Hudson Bay, Canada

sign in the distribution for elevation to correspond to depth in Fig. 3.4.

3.2 Probability density function for the age of sea-level data

Geological samples used in this study were dated with the Carbon-14 method. ^{14}C ages according to the decay of the radionuclide do not represent calendar years directly due to the variable production rate of ^{14}C in the upper-atmosphere (Reimer et al., 2013). Determination of ^{14}C age is calculated by ratio of $^{14}C/\ ^{12}C$, which depends on ^{14}C production and the conversion of ^{14}C age to calendar years is done with calibration curves (Törnqvist et al., 2015). Here we used the marine curve "Marine13.14" (Reimer et al., 2013) and the calibration software OxCal (Ramsey, 2017) to calibrate ages of considered SLIs. Since they are marine samples, we had to take into account "reservoir effects". The CO_2 exchange between the atmosphere and the ocean leads to a delayed uptake in surface waters (Törnqvist et al., 2015). Due to this effect, called reservoir effect, marine samples will have a lower concentration of ^{14}C than terrestrial samples, having a global average deviation of 400 ^{14}C years (Törnqvist et al., 2015). Butzin et al. (2017a) discussed spatial and temporal variability of the marine

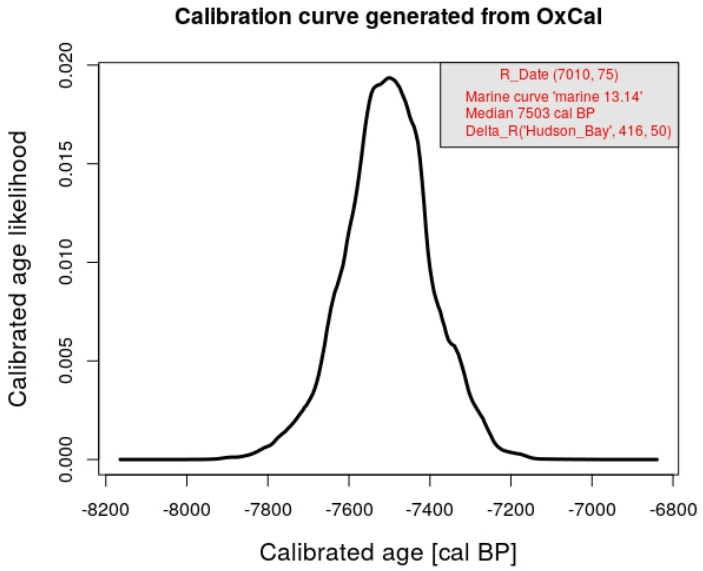

FIGURE 3.5: Calibration curve generated from OxCal output with measured radiocarbon determination of 7010 ± 75 BP (Ramsey, 2017). The marine curve "marine 13.14" was used in the calibration, with the reservoir age correction of 416 ± 50 years.

radiocarbon reservoir age during the last 50,000 years based on ocean circulation modelling. The authors did not focus on small regions like Hudson Bay. Nevertheless their published model results (Butzin et al., 2017b) show some variability. Therein, we find a decrease of reservoir age from about 700 years in the Hudson Strait to about 416 years in Hudson Bay for the last 12,000 years. The time variability amounts to 50 years for this time interval. In some parts near the W and SW shoreline of the Hudson Bay, the basin correction reduces further to 200 years which we do not consider in this study because the selected samples are not located in this region. Art Dyke (Art Dyke, pers. comm.), while gathering data for the database, did marine reservoir age correction for 440 years for those SLIs that were not already corrected in the primarily reported age . So, we first add back 440 years that Art Dyke accounted for, and then we apply the marine curve.

We split our data into two regions, 'Hudson Bay' and 'Hudson Strait' (Fig. 3.7), in which we consider basin corrections for the selected marine shells of 416 ± 50 years and 700 ± 50 years, respectively. The reason for this deviation is the higher sea-ice concentration in the Hudson Strait than in the central Hudson Bay. As sea ice inhibits air-sea $^{14}C_2$ exchange, this leads to lower surface water concentrations and, thus higher ^{14}C ages in the entry of Hudson Bay than in the central bay (Martin Butzin, 2018, pers. comm.). One example of the calibration curve generated for one sample located in the Hudson Bay region is shown in Fig. 3.5. After applying the marine curve for the time range of considered SLIs with the default resolution of 5 years, the posterior probability distribution is calculated by the calibration program as

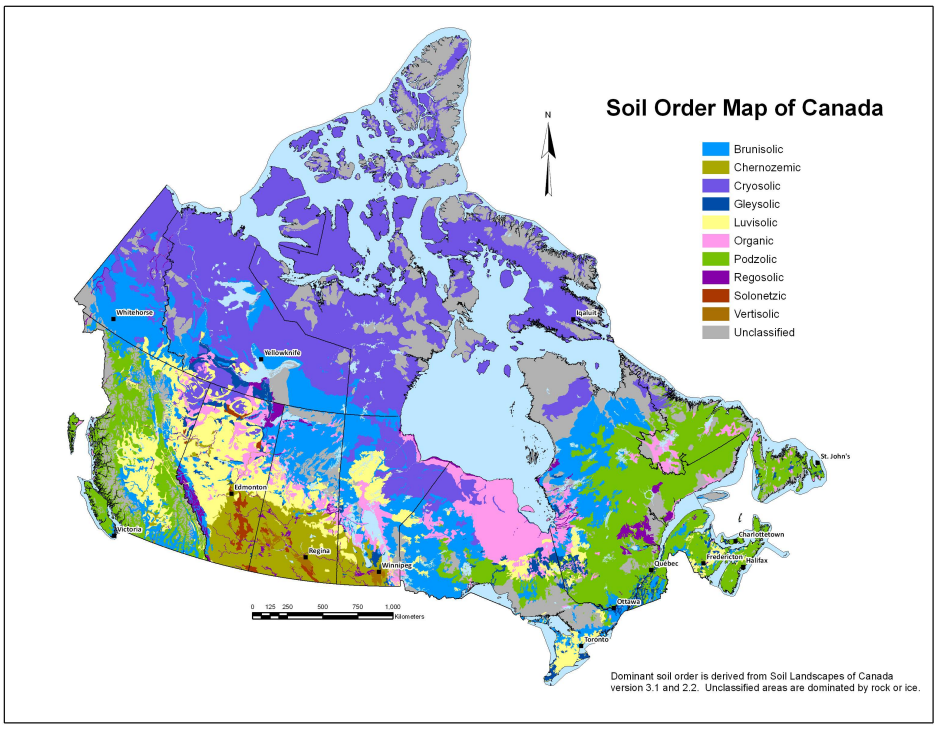

FIGURE 3.6: The image shows the Canadian System of Soil Classification with ten orders. Pink color depicts organic class. Deposit feeders such as *Macoma balthica* are located in this region and are excluded from the study. Image is extracted from Canadian Society of Soil Science (2019).

the age PDF ($pa^{\mathrm{SLI}}(t)$).

A further problem discussed in the literature is the fact that *Portlandia arctica* and *Macoma balthica* are deposit feeders, meaning, they absorb bicarbonate from the rocks they live on, unlike suspension feeders, causing them to appear older by up to 2000 ^{14}C years (England et al., 2013). Therefore, if such SLIs are located in regions where deposits are calcareous, their ^{14}C concentration is affected by an unknown fraction of practically ^{14}C-free carbonate from million years old rock, making them unreliable for chronological reconstructions (England et al., 2013). In Fig. 3.6, we can see the Canadian System of Soil Classification, where a pink region is an organic order (Canadian Society of Soil Science, 2019). In this region, organic soils consist of different types of wetlands, peats, bogs and fen soils, which are mainly fed with surface water emerging from calcareous soils, meaning they are suitable for deposit feeders mentioned above (Godwin et al., 2002). When we compare the organic region in Fig. 3.6 with the location of *Macoma balthica* (blue dots in Fig. 3.1 c)) and *Portlandia arctica* (green dots in Fig. 3.1 c)) locations, we conclude that four samples of *Macoma balthica* type are located in the James Bay, the most southern part of the Hudson Bay. Accordingly, we exclude these four points from the analysis, but other points are taken into account since

they are located outside this region.

3.3 Fit to model predictions

The elevation and age PDFs for each sample we combine into joint PDFs using eq. (2.14). Fig. 2.4 in Chapter 1 shows one example for *Mytilus edulis* found in living position, where we distinguish the confidence intervals of 68%, 95%, and 99%. The asymmetries concerning height and age are visible.

We calculate the conditional probability for each SLI (2.15) taking into account redundancy weights (eq. (2.17) and (2.16)). Redundancy weights are presented in Fig. 3.7, and from there it is clear why it is necessary to apply redundancy weighting, since clusters of indicators are visible, meaning that they are located in close proximity to each other.

For this study, we consider an ensemble of sea-level reconstructions, which was generated in the German Climate Modeling initiative PalMod, and represents the variability in h_{RSL} due to variations in the Earth's structure with respect to lithosphere thickness, upper- and lower-mantle viscosities (Tab. 3.1). We analysed a model ensemble of GIA reconstructions containing 140 different members. For all members, the glaciation history ICE6G_C (Peltier et al., 2015) was applied. The model predictions were calculated with VILMA, Viscoelastic Lithosphere and Mantle model, for modelling of global deformations and gravity changes (Martinec, 2000).

In Fig. 3.8, the results are presented as a 3D scatter plot, where ensemble members with

Table 3.1: List of Earth-structure variability parameters on which the model ensemble is based.

Parameter	**Values**
Lithosphere thickness [km]	60, 80, 100, 120
Upper-mantle viscosity[10^{21} Pa s]	0.1, 0.2, 0.5, 0.8, 1
Lower-mantle viscosity [10^{21} Pa s]	1, 2, 5, 8, 10, 20, 50

better fit have more intense colours. As expected from the large probability intervals, we get a broad spread of acceptable models fitting the considered set of indicators. After examining the likelihoods, we determined the 'best' fit for the model member with lithosphere thickness of 80 km, upper-mantle viscosity of 2×10^{20} Pa s and lower-mantle viscosity of 8×10^{21} Pa s. We calculate Bayes factors with eq. 2.22. Thus, the value 0 is presenting the highest likelihood. In Table 3.2, we present ensemble members with the highest likelihoods. Values of lithosphere thickness are quite uniform in all ensemble members as well as upper-mantle viscosity. The first 27 models with the highest likelihood ($\mathcal{L} < -0.5$) show the same order of magnitude for upper-mantle viscosity. Slight sensitivity is present in lower-mantle viscosity, as we can see a variation in values. Isolating slices of the considered lithosphere thicknesses

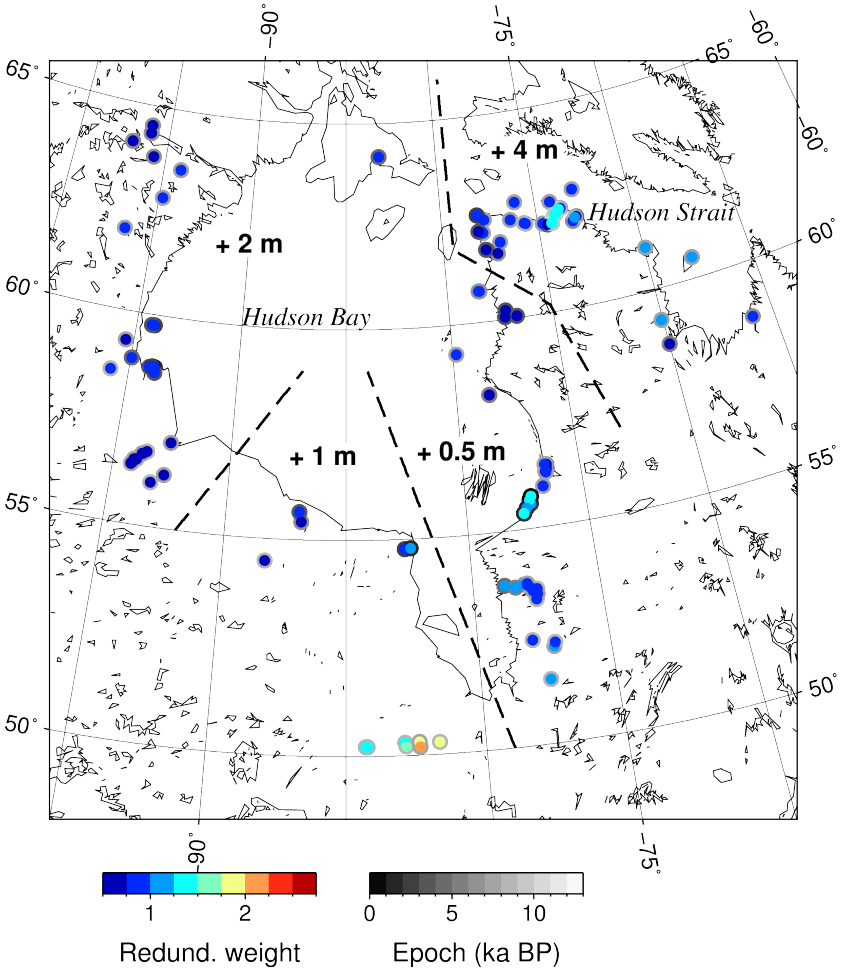

FIGURE 3.7: Redundancy weights for each selected SLI. The colour of the individual circle denotes the considered weight, the shade scale of the epoch around circles denotes the calibrated age of the SLI. An overlap of SLIs could not be avoided. Furthermore, dashed lines are separating the regions of different high-tide levels considered in this study.

TABLE 3.2: Five ensemble members with the highest likelihood values

Lith. thickness [km]	Upper-mantle visc. [10^{21} Pa s]	Lower-mantle visc. [10^{21} Pa s]	Likelihood ($\mathcal{L}$)
80	0.2	8	0
80	0.2	10	-0.002
80	0.1	20	-0.03
80	0.1	10	-0.06
60	0.2	8	-0.08

(Tab. 3.1) are displayed in Fig. 3.9. The contour patterns are showing best fits in the same region, which corresponds to regional values of $0.1 - 0.2 \times 10^{20}$ Pa s for upper-mantle viscosity and values of $8 \times 10^{21} - 2 \times 10^{22}$ Pa s for lower-mantle viscosity, with slightly better fits for ensemble members with lithosphere thickness of 60 and 80 km.

In Fig. 3.10 we show RSL in the Hudson Bay region at 8,000 yrs BP based on mean predictions of ensemble members that displayed the highest likelihood ($\mathcal{L} < -0.5$), counting

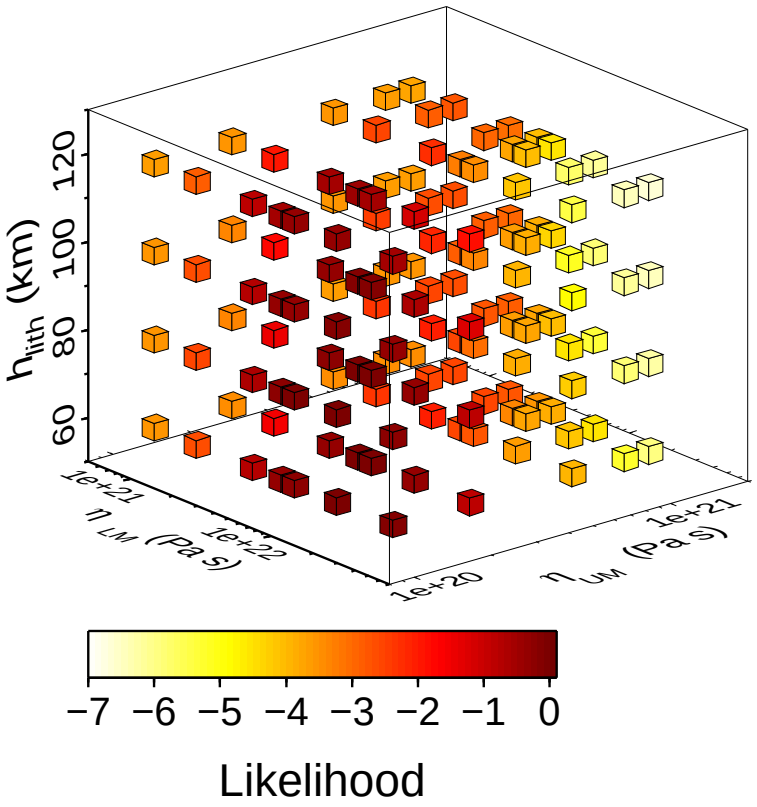

FIGURE 3.8: 3D presentation of model ensemble with 140 members varying in lithosphere thickness (h_{lith}), upper- and lower-mantle viscosities (η_{UM}, η_{LM}). Color scale indicates a likelihood for considered set of shallow-water shells of the Hudson Bay region.

27 members out of 140 to fall into this likelihood, and in Fig. 3.11 we present RSL with the predicted range of these 27 ensemble members. Here we see that maximal difference in predicted values varies up to 100 m in certain regions around the Hudson Bay. If we compare Fig. 3.10 with Fig. 3.1 that depicts RSL based on the whole ensemble, we notice that the constrained ensemble predicts sea level higher than 200 m in the Hudson Bay region and around 300 m in the west and south-east region of the Hudson Bay. In comparison, the mean prediction of the whole ensemble shows ∼100 m lower sea level in the same area.

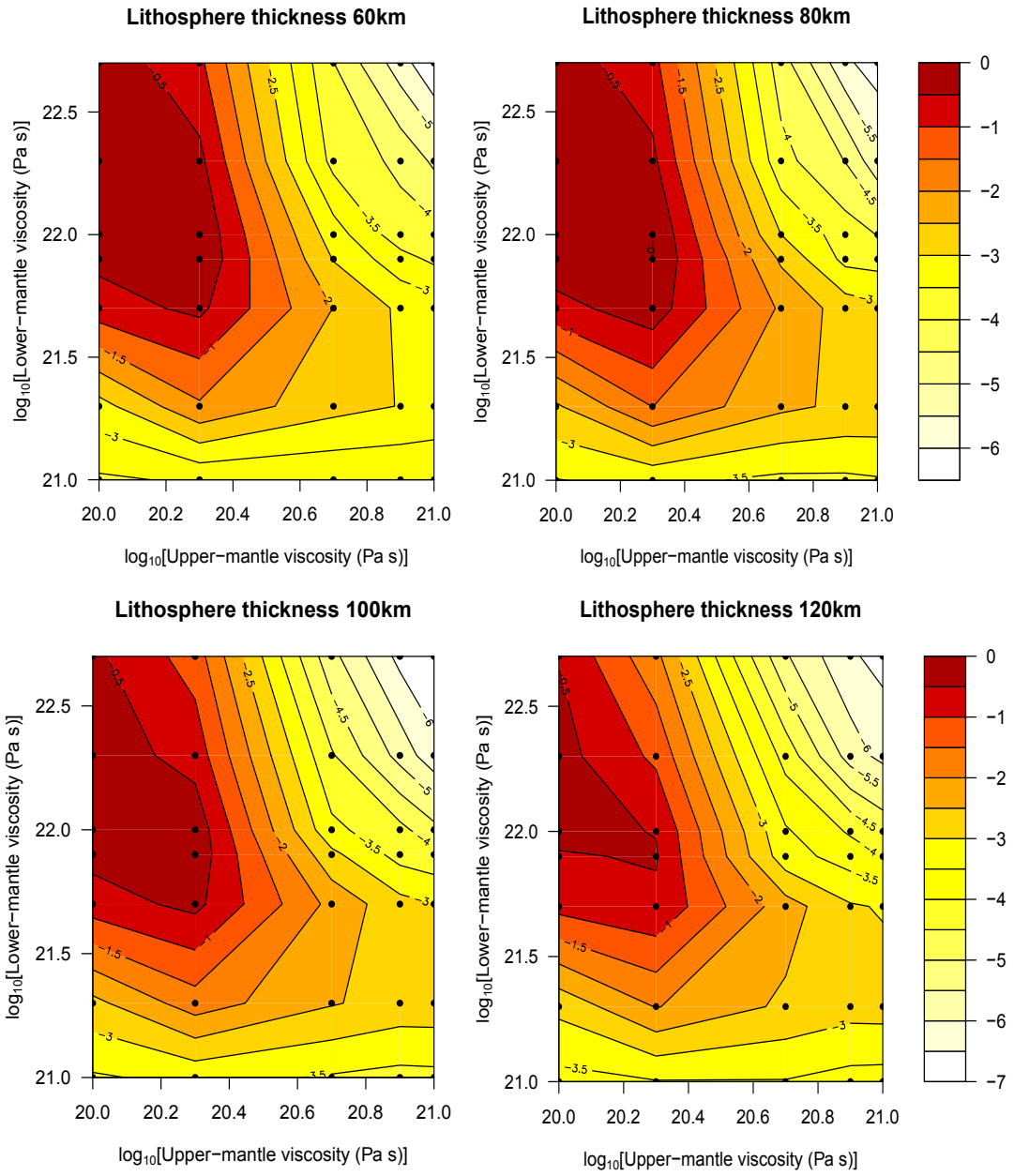

FIGURE 3.9: Model ensemble members' fits as function of upper- and lower-mantle viscosities for considered lithosphere thicknesses for a Hudson Bay region.

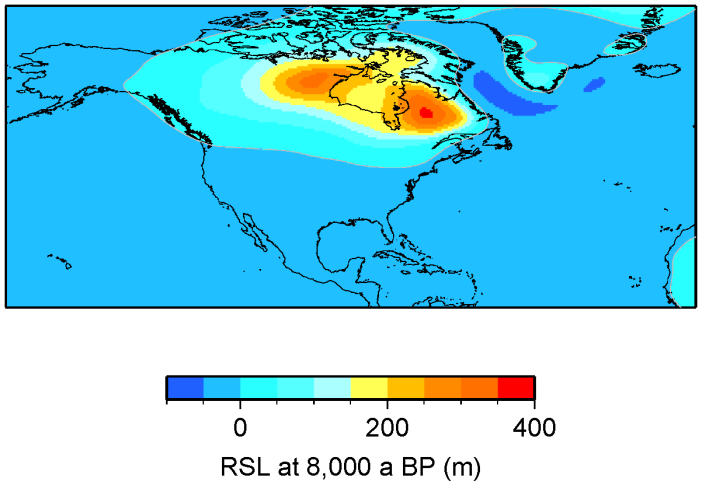

FIGURE 3.10: Relative sea level (RSL) at 8,000 years before present (BP) in the region of Hudson Bay based on mean predictions of considered ensemble that fall in the 0.5 misfit (27 members). Figure provided by Meike Bagge.

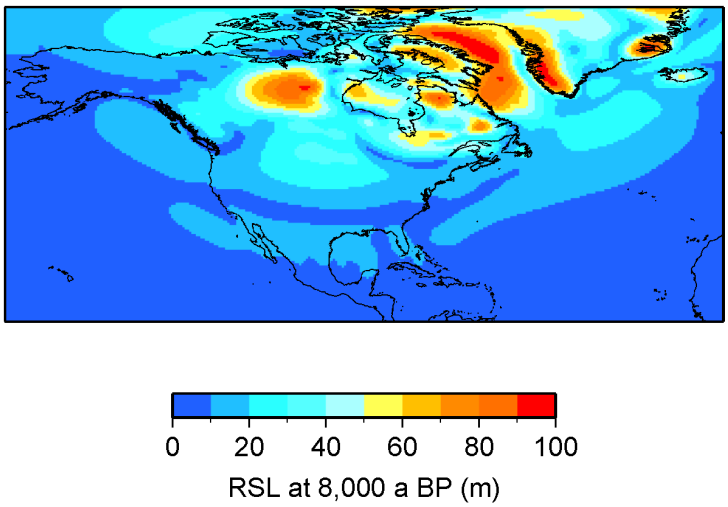

FIGURE 3.11: Relative sea level (RSL) at 8,000 years before present (BP) in the region of Hudson Bay based on a range of predictions of considered ensemble that fall in the 0.5 misfit (27 members). Figure provided by Meike Bagge.

3.4 Summary

We considered a total number of 156 SLIPs covering the Hudson Bay region for the period since 12,000 yrs BP. We focus on four different types of shells found in this region and interpret their indicative meaning in two different ways to show the flexibility of VAM to be applied to different SLI types. Shells found in the living position we relate to the present day living conditions of considered species. In contrast, shells dislocated from their original habitat, we link to geomorphic features they were found on, such as beach ridges. Specific attributes of selected species are taken into consideration, such as deposit-feeding, and spatial and temporal redundancy.

Based on the glaciation history ICE6G_C, we determined best fitting Earth model ensemble members to be represented by upper- and lower-mantle viscosities of $0.1 - 0.2 \times 10^{21}$ Pa s and $8 - 10 \times 10^{21}$ Pa s, respectively. Mantle viscosity structure varies depending on the methods used to infer it as seen in Table 3.3. The consensus in the scientific community is that the upper-mantle viscosity is a multiple of 10^{20} Pa s and the viscosity of the lower-mantle is still poorly constrained, but it is agreed on that it has a considerably higher viscosity than the upper mantle (Kuchar et al., 2019).

In Table 3.3, we present results of different studies that are estimating mantle viscosity for the Hudson Bay region compiled in Wolf et al. (2006) together with three global estimates at the end of the table. Based on the values from previous studies we can conclude that

TABLE 3.3: List of different estimates of mantle viscosity, η_{UM}, η_{LM} from the Hudson Bay region, based on Wolf et al. (2006), complemented by more recent studies and global estimates.

Publication	**Viscosities** [10^{21} **Pa s**]	
	Upper-mantle	Lower-mantle
this study	0.1–0.2	8–20
Nakada (1983)	0.05–0.75	100
Peltier and Andrews (1983)	1	1–3
Nakada and Lambeck (1991)	4–6	20–50
Mitrovica and Peltier (1992)	1	1–3
Han and Wahr (1995)	1	50
Mitrovica and Peltier (1995)	0.5	0.5–3
Cianetti et al. (2002)	1	2
Mitrovica and Forte (2002)	0.39–0.43	6.5–11
Mitrovica and Forte (2004)	0.5	1
Wolf et al. (2006)	0.32	16
Zhao (2013)	0.37	1.9
Lambeck (1998)	0.3	10
Peltier et al. (2015)	0.5	3
Lambeck et al. (2017)	0.35–0.75	8–28

this method underestimates the values of the lower-mantle viscosity. While the majority of studies are estimating lithosphere thickness at 120 km, we found a preference for thinner lithosphere. However, the study was limited by the number of selected samples. Further observations are needed to be included to reach a statistical significance.
Nevertheless, our findings demonstrate that the statistical method VAM allows exploitation of a large number of SLIs that is usually disregarded due to the low-quality. Our method can serve for validation of GIA estimation of RSL change in regions and on time scales where indicators of higher quality are not available. A further advantage of VAM is its possibility to combine different types of sea-level data, as well as to take into account various techniques of dating.

4

Constraining 1D GIA models in SW Fennoscandia with geological data

"Fennoscandia remains the key region for GIA research" is the sentence that repeats over decades in studies dealing with this phenomenon (e.g. Lambeck et al., 1998; Steffen and Wu, 2011). From watermarks in the rocks to satellite-based systems such as the Gravity Recovery and Climate Experiment (GRACE), different techniques and data are used to examine this region. However, geological records remain the primary means to constrain radial profiles of GIA models' structure.

4.1 History of the Baltic Sea

The Baltic Sea is located in the southwestern part of Fennoscandia. The Baltic Sea experienced dynamic and complex changes since LGM, and its present shape was influenced by GIA that was most extensive in the north due to the thickest ice (Bennike and Jensen, 1998). Since the end of the Pleistocene, the Baltic Sea had various lake and sea stages and the current shape of the Baltic is only 3,000 years old (Berglund et al., 2005). First, a large lake formed next to the retreating Fennoscandian ice sheet, then, after the retreat of the ice from south-central Sweden, the Baltic ice lake dropped to sea level and became Yoldia Sea (Björck, 1995). The newly formed sea was named after brackish mollusc that inhabited it. Next, glacial-isostatic uplift was responsible for the formation of the Ancylus lake around 10,600 yrs BP (Eronen, 1983). Finally, the sea flooded today's Straits of Denmark around

8,400 yrs BP and connected Baltic for the second time to the sea. Littorina Sea was named after common periwinkle (a small sea snail) and the Baltic Sea that we know today followed (Björck, 1995). Even though it is one of the most studied regions for GIA during last centuries, these periods of the lake and sea stages are still imprecise. The reason for these uncertainties is simultaneous ongoing GIA in the northern parts of the Baltic Sea, making the regression hard to evaluate. The region of Baltic, where coasts of Ancylus lake became inundated due to the regionally varying sea level is an essential threshold in the geological history of the Baltic Sea, which makes it a crucial region for understanding the formation of the Baltic Sea (Bennike and Jensen, 1998).
Recent studies in Fennoscandia report that rebound triggered by GIA causes sea level rise of 2.1 ± 0.3 mm/year (Milne et al., 2001) and ice load affects seismic and fault instability (Wu et al., 1999). Fennoscandian uplift is monitored since decades by tide gauges, satellite gravimetry, tilt measurements, surface levelling and GPS, and these observations are used to constrain GIA models based on the present-day uplifts (Steffen and Wu, 2011). Present-day observations of this region are comprehensive and include different techniques and projects; SWEPOS® is a network with 21 permanent GPS stations that is functional since 1993, WEGENER program (Working group of European Geo-scientist for the Establishment of Networks for Earth-science Research) uses different geodetic techniques such as SLR and VLBI and includes seismic measurements, tide gauges and absolute gravimetry (Scherneck et al., 2002). The largest GPS network with more than 40 permanent stations is operational since autumn 1993 and is called BIFROST (Baseline Inferences for Fennoscandian Rebound Observations) (Scherneck et al., 2002; Johansson et al., 2002). BIFROST's aim is to measure a crustal deformation in the area of the former Baltic shield in high precision, i.e., parts of millimetres per year (Wahr and Davis, 2013).

4.1.1 Trans-European Suture Zone

Apart from dynamical history due to the land uplift and melting of the ice, the Baltic Sea region also experienced complex tectonic-event changes since the late Paleozoic period. The Southwest Baltic lies on a significant lithospheric boundary and the longest tectonic lineament in Europe, the Trans-European Suture Zone (TESZ). In a tectonic sense, the TESZ divides central Europe; it is a zone that divides the Precambrian East European Craton (EEC) from the Phanerozoic Europa (PE) and spreads from the North Sea to the Black Sea (Fig. 4.1). It contains two linear branches: the Sorgenfrei-Tornquist Zone (STZ) through the northwestern part between Scania (Sweden), Kattegat, and North Jutland (Denmark) and the Teisseyre–Tornquist Zone (TTZ) from the Baltic Sea through Poland and Ukraine to the Black Sea (Janutyte et al., 2015).
The EEC contains three major areas: Fennoscandia with the Baltic Shield, Sarmatia and

Volgo-Uralia (Fig. 4.1) (Knapmeyer-Endrun et al., 2017). The crust and the upper mantle in this region are a result of series of collisions of Fennoscandia and Sarmatia at approximately 1.8-1.7 Ga BP, after which this region has been stable as a paleo-continent Baltica (Bogdanova et al., 2006). Evolution of this region is long and complex, and we will not go into more detail here, sufficient to say, that this complexity inspired a large number of studies (e.g. Heuer et al., 2006, 2007; Geissler et al., 2010; Knapmeyer-Endrun et al., 2017). Hence, the structure of the crust and uppermost mantle have been studied extensively with deep seismic sounding profiles (DSS) (e.g. Eurobridge Seismic Working Group, 1999; Grad et al., 2002; Guterch et al., 1999, 2004; Grad et al., 2006). Results from these studies show large variations in the crust thickness and in the Mohorovicic discontinuity (Moho) depths from 30 km to 50 km, with largest depths in the area of The Southwest Baltic (Knapmeyer-Endrun et al., 2017). We, therefore, identify this area as the most exciting area in Fennoscandia due to its complicated structural history and take it as an excellent example for regions around the world with complex tectonic structures. Aim of the following study is to determinate if it is sufficient to apply a 1D GIA model with constant thickness and mantle properties, or if it is needed to use a 3D model.

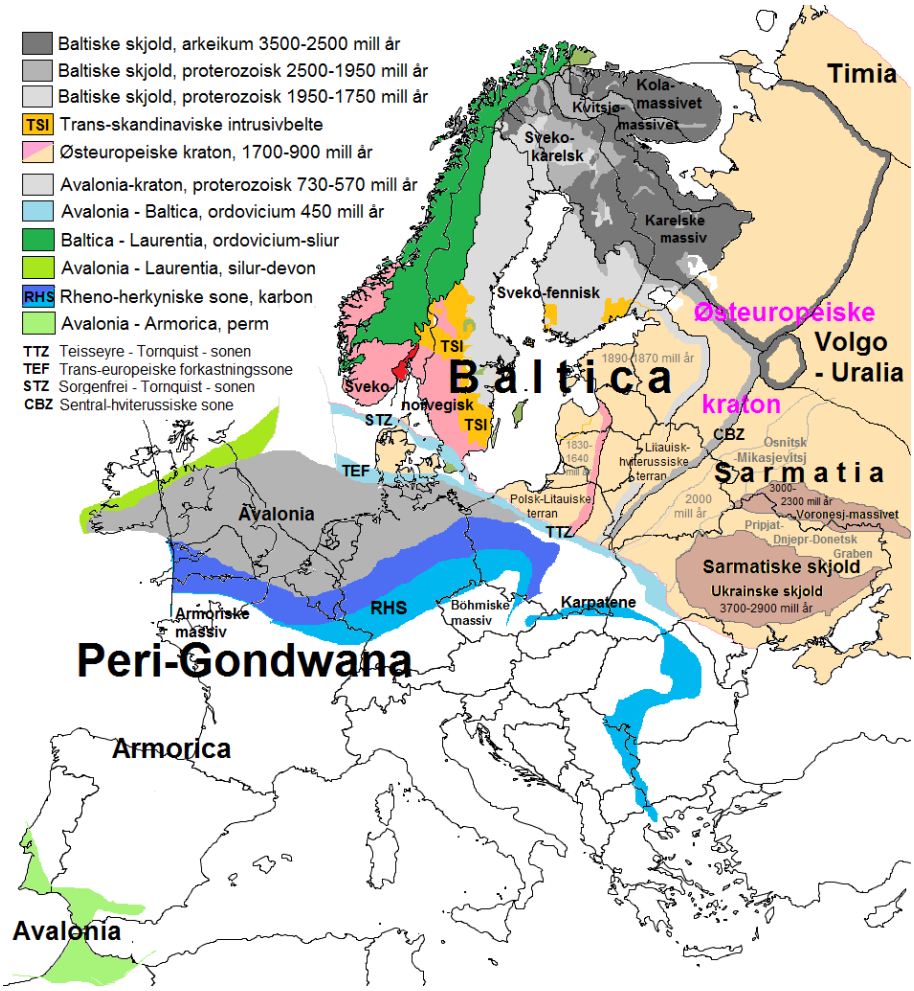

FIGURE 4.1: Geological map of the Northern Europe where parts of the Trans-European Suture Zone are shown in light-blue colour between the North Sea and the Black Sea. Figure taken from Bjørtvedt (2011).

4.2 Methodology and data

The statistical method VAM developed in Chapter 2 is applied to the region of the Southwest Baltic Sea. Data sets are grouped based on the regions in this area. We select five different data sets from the new late Pleistocene-Holocene sea-level database for the Baltic Sea covering this area (Rosentau et al., 2020). The database was compiled in the format suggested by Hijma et al. (2015) and it is stored in Standard Query Language (PostgreSQL), database system provided by the German Research Centre for Geosciences (GFZ) which makes it suitable for visualisation with SLIVISU software (Sea-Level Indicator Visualization, Unger et al. 2012). Data sets from Denmark (Bennike and Jensen, 1998) and a separate analysis of the data from the island Samsø (Hede et al., 2015), NE German Baltic Sea coast (Mecklenburg-West Pomerania) (Lampe et al., 2010) and N Germany (Schleswig-Holstein) (Winn et al., 1986) were chosen from this database (Fig. 4.2). The total number of samples is 514, where 303 samples are from Denmark and 192 from Germany. Additionally, we take data from central Sweden, Ångarmanland (19 samples) as a reliable data because it is located near to the centre of the Fennoscandian ice sheet, and its sea-level record shows consistent sea fall caused by the most significant uplift signal, usually recorded near the centres of former ice sheets (Nordman et al., 2015). We restrict the data to the Littorina Sea period and exclude all data older than 9,000 yrs BP from the database. Reason for this is that the data once located in lakes during the lake stages is not representing the sea level at that epoch. During Ancylus lake stage the lake level was likely higher than sea level during this stage, as it was filled with rivers and melting ice (Bennike and Jensen, 1998).

In the following subsections, indicators are described together with the adjustment of VAM introduced in Chapter 2 based on the data specifications. VAM is first applied to each data-set independently, and the model ensemble member that fits best to each data-set is presented, as well as the whole range of the prediction values. And finally, the best fit for the whole region is calculated, analysed and presented in section 4.7. A whole range of model ensemble predictions is presented and discussed also in section 4.7. As in Chapter 2, here we are using a model ensemble with the same combination of parameters (Tab. 3.1). The ensemble has 140 members, and the glaciation history ICE6G_C (Peltier et al., 2015) is used in the model. Combinations of parameters of each ensemble member are listed in Table A.1 in Appendix A, and member abbreviations are used in figures in this Chapter.

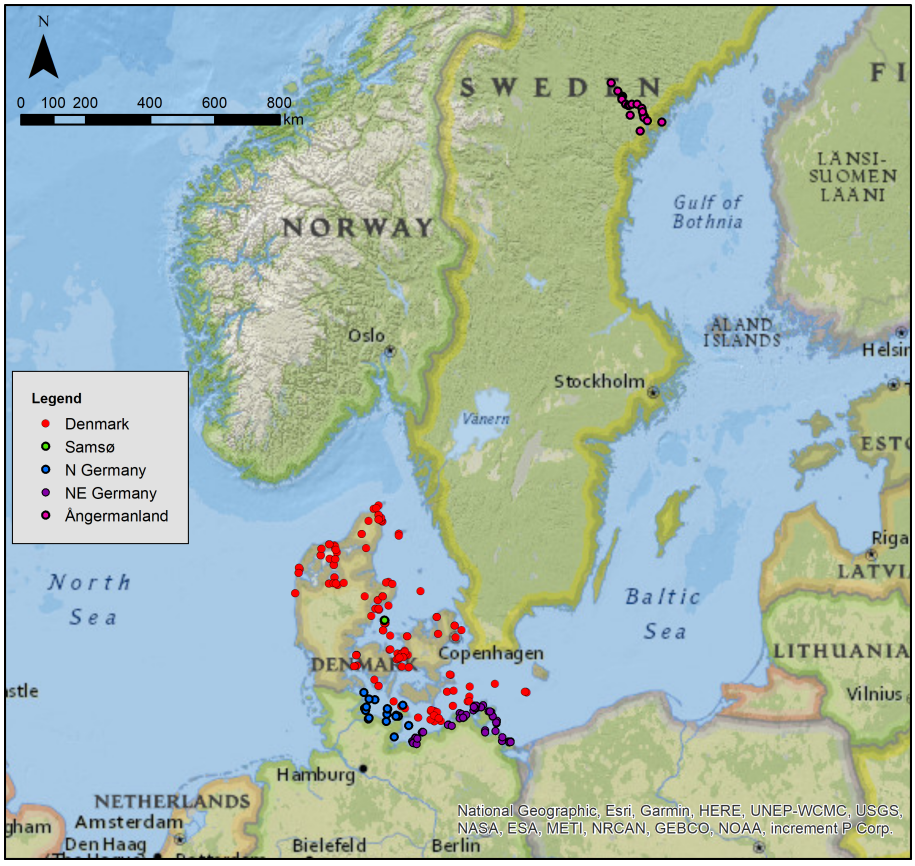

FIGURE 4.2: Region of Fennoscandia with considered SLIs. Data from Denmark is presented as red dots with data from Samsø as light green dots. North German and North East German data are shown as blue and purple dots respectively, and Ångermanland data is in magenta.

4.3 Denmark

Data for Denmark was obtained from two data-sets; the data-set complied by Bennike and Jensen (1998) and the data-set for Samsø by Hede et al. (2015). We divide the data based on the regions and do separate analysis; the study aims to establish if the tectonic structure influences GIA models. Therefore, data from Denmark is divided into three regions; Belt Sea region including Samsø, Arkona Basin and North Jutland with Kattegat. After analysis, RSL predictions from every model member are showing large deviations from observed values in the area of Arkona Basin, as well as in North Jutland (Jylland) with the Kattegat. Reason for it is their location and uncertainties it contributes: Arkona Basin is located at the border of the former Ancylus lake, and mixing of fresh and seawater is challenging to quantify. At the same time, it produces irregular basin age corrections. North Jutland and Kattegat, on the other hand, are connected to the ocean and the SLIs are affected by ocean currents, which leads to significant uncertainties in the estimation of former RSL. Therefore, we excluded these two regions from the study.

4.3.1 Data analysis

To categorise the indicative meaning of the respective samples, we distinguish, according to Chapter 2, SLIPs, upper and lower limiting points. From the total number of 187 samples, 88 are classified as lower limiting points, 85 as upper limiting points, and 14 as the range or SLIPS. Elevation probability for upper and lower limiting points is calculated using uniform probability over the assigned range, as described in Section 2.1.3. Samples identified as SLIPs are related to raised beaches, mainly consisting of radiocarbon-dated wood, twig brunches and cow bones. But, unlike in Hudson Bay study, we do not "shift" the elevation for tides since the Baltic Sea is known to have insignificant tidal ranges. Tides are governed by topography and water basin size, and tides in Baltic Sea depend on waves from the North Sea, but they are limited due to shallow waters and narrow straights, resulting in only a few centimetres changes (Swedish Meteorological and Hydrological Institute, 2017).
Elevation probability is calculated with a gamma distribution (equations (2.1) to (2.4)), and x_i is a range from minimum to maximum value of SLIP's elevation. Data that was radiocarbon dated we calibrate with OxCal software (Ramsey, 2017), having in mind reservoir correction, and extract age PDFs. A separate analysis is done for Samsø data, here we consult the laboratory that was performing dating of samples with OSL method to decide on the age distribution (Lars Nielsen, 2019, pers. comm.)

4.3.2 Kattegat, northern Jutland (Jylland) and Arkona Basin

Indicators found in Kattegat, northern Jutland (Jylland) and Arkona Basin were excluded from this study because their location causes uncertainties in RSL. Jutland is a peninsula that separates the North Sea and Baltic Sea, and Kattegat is located at the entrance of the Baltic Sea, east from Jutland (Fig. 4.3). This region is connected to the ocean, and cyclonic circulation is affecting water levels in this region (Kristiansen and Aas, 2015), making it challenging to model former RSL (Fig. 4.3). Additionally, Kattegat is characterized by shallow waters. As an essential navigation route, sand was pumped from it to safeguard important passage (of Encyclopaedia Britannica, 2012), which adds to the uncertainty of indicators located in this area.

The Arkona Basin is connected to the Belt Sea region and at present-day has a maximum depth of 45 m (Fig. 4.4). The Arkona Basin, as well as the whole Baltic Sea, is a large brackish system. Due to the various lake stages explained in Section 4.1, salinity has varied in this region. During the Littorina Sea (around 8,5 ka BP) seawater entered from Kattegat, developing brackish conditions, especially in the region of Arkona Basin that is connecting the Baltic Sea and the North Sea. Even at present day, there is a quite dynamical mixing of seawater inflow happening in this area (Lass, 2003). The Baltic Sea evolution has been highly

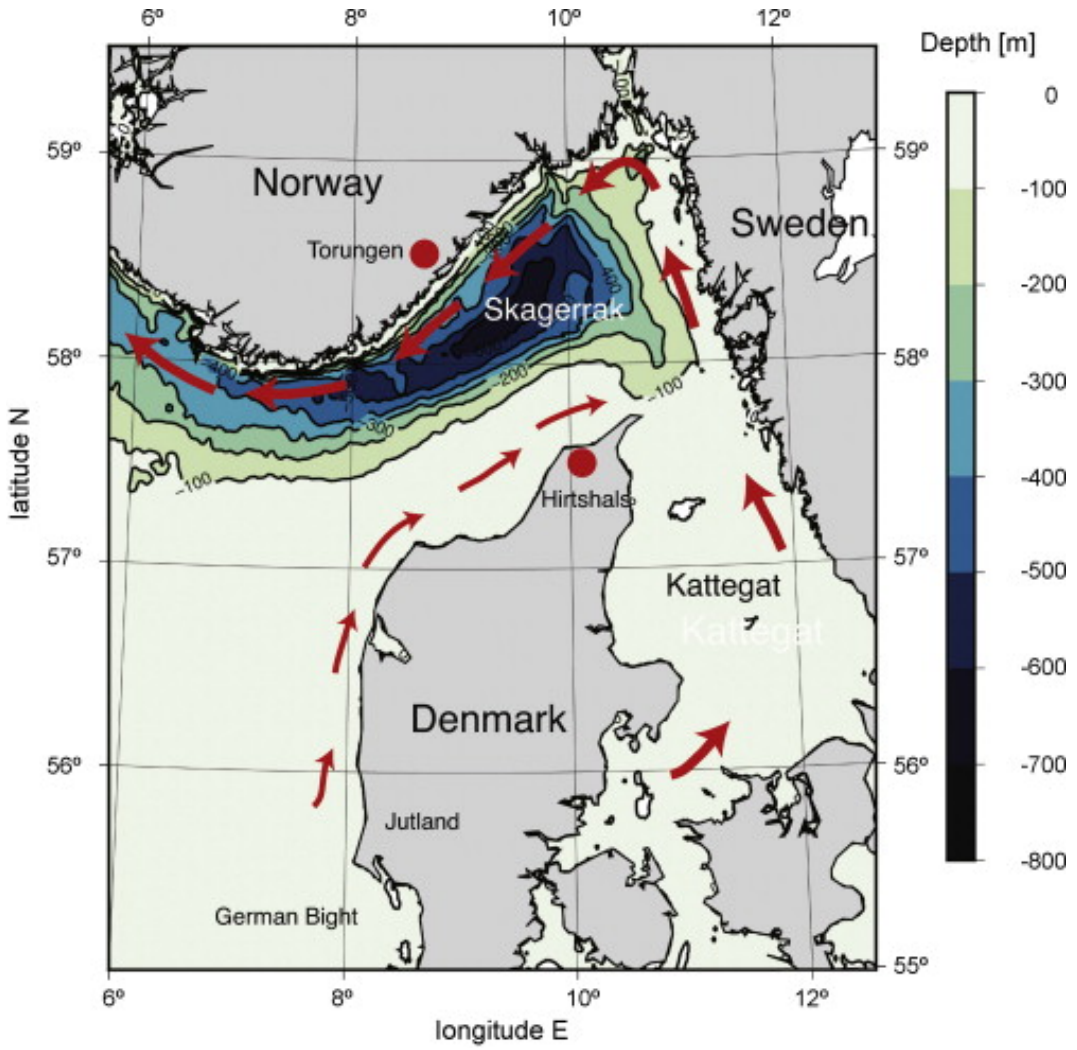

FIGURE 4.3: Currents off the northern Jutland and the Kattegat. Figure from Kristiansen and Aas (2015)

FIGURE 4.4: Location of the Arkona Basin. Figure from Holzhüter (2012)

studied in past decades, and there are still open questions about the age and characteristic of lake stages (Kostecki, 2014). Uncertainties in time-frames of lake stages are leading to the unspecified salinity during the Holocene, which causes difficulties in determining the age of indicators, as the carbon intake varies with the living environment. As explained in Chapter 2, ^{14}C content depends on the environment (marine or atmospheric). Therefore, we decided to exclude indicators from the Arkona Basin. One way to reduce uncertainties in age determination would be to include studies that quantify salinity in this region during the Holocene. Study example that deals with this problem is Ning et al. (2017), but this was beyond the scope of this study. Finally, we present results of 1D and 3D models analysed in the thesis in Appendix D. Models are overestimating SLIs throughout the whole study time for $\sim$ 15 m, and unlike in other regions, overestimation is evident at the present-day as well. Only exceptions are 1D model members in Kattegat and northern Jutland, but the poor performance of 3D models was the deciding reason for excluding this region from the final analyses.

4.3.3 Belt Sea region

Data for Belt Sea region includes 177 radiocarbon-dated samples and additional ten from Samsø, dated with the OSL method. All data in this data-set is published, and detailed information about each sample can be found in Appendix C. The data-set was collected and analysed in last decades by different authors and techniques (Bennike et al., 2017; Bennike and Jensen, 1998). Most of the data come from sedimentary records. Samples were analysed for macro-fossils and remains of plants and animals typical for this region, such as different types of shells, mammal bones or stems from different plants. Authors concluded, based on the size and type of shells, if the water was brackish or marine with higher salinity. For instance, a larger size of the shells indicates marine environment with higher salinity (Bennike et al., 2017).

4.3.3.1 Samsø

Samsø is an island located in the Kattegat Sea in Denmark. A beach ridge system was created by a large amount of sediment from the Pleistocene deposits. Authors of this data-set reconstructed changes in RSL during the past 5,000 yrs (Hede et al., 2015). Data-set contains 11 samples collected from 10 different locations (Tab. 4.1). All samples were dated with OSL method at Nordic Laboratory for Luminescence Dating, Risø National Laboratory in Denmark. Authors used ground-penetrating radar (GPR) to collect the data across a raised beach system. Swale deposits (holes in sediments) have downlapping reflections. Since downlap presents a condensed marine unit mostly, this was identified as an actual sea level at the time of the deposition (Nielsen and Clemmensen, 2009). High tide in this region

reaches only 0.3 m, and it is considered in the error propagation of the sea-level elevation of each point (Hede et al., 2015). Further corrections were made for the burial depth, sampling error, digital elevation model error (DEM) and levelling error which are all summed up in the *sample_error*.

As outlined in Chapter 2, VAM application consists of inferring uncertainties in age and

Table 4.1: List of SLIPs from the Samsø Island (Hede et al., 2015) prefix *cal* represents calibrated values

name	cal_age [BP]	cal_max [BP]	cal_min [BP]	msl [m]	sample_error [m]
NH1	5000	5600	4400	2.1	0.2502
NH2	4500	5100	3900	2.7	0.2502
NH3	3900	4500	3300	1.8	0.2502
NH4a	3300	3900	2700	0.9	0.2502
NH4b	3700	4100	3300	0.9	0.2502
NH5	3530	3900	3100	0.5	0.2502
NH6	2800	3200	2400	0.7	0.2502
NH7	2130	2410	1850	0.4	0.2502
H8	1720	2000	1440	0.1	0.2502
NH9	1220	1420	1020	0	0.2502
NS1	8	14	2	-0.3	0.2502

elevation by defining a join probability and applying it to the 1D model ensemble, as discussed in Chapter 3. Since this data marks RSL at the time of the deposition, we observe these samples as SLIPs and elevation distribution is defined as a gamma distribution between the range of a minimum and maximum elevation of the sample $((msl - sample\_error) : (msl + sample\_error))$, defining the x_i for equation (2.5). The approach follows the ML method for parameter estimation with equations (2.6)–(2.8). Age distribution we calculate as normal distribution after consulting Nordic Laboratory for Luminescence Dating, Risø National Laboratory in Denmark who conducted the dating (Lars Nielsen, 2019, pers. comm.).

After calculation of the joint probability density function by combining age and elevation PDFs (2.14) of all samples in the Belt Sea region, we proceed with the evaluation of the fit to the model prediction in this region. The same model ensemble as in Chapter 2 was used. In Table 4.1 we present, as an example, data from Samsø, (rest of data is presented in Appendix C). Here one sample (NS1) is excluded from the study since it is dated to 8 yrs BP which is used as a present-day reference and cannot be used for model validation. These data give the relation of the sample elevation to the present-day sea level. As explained in

Chapter 2, the likelihood of the set of SLIs is presented as one member of the considered ensemble, and for the Belt Sea region together with Samsø, this member has following viscosity structure; lithosphere thickness 100 km, and 10^{21} Pa s and 5×10^{22} Pa S for upper- and lower-mantle viscosity respectively. This model member abbreviation is m_83. Predictions from all 140 ensemble members, together with the observed samples, are presented in Fig. 4.5 with the best-fitting prediction highlighted. Fig. 4.5 shows considerable variability in model predictions regarding the observed sea-level curve in the period from 8,000 to 6,000 yrs BP with a decreasing tendency towards present-day. Larger variability and observational outliers around 8,000 yrs BP are possibly caused by the Littorina transgression.

FIGURE 4.5: Variability of model ensemble predictions for the region of Belt Sea with Samsø. Black triangles are presenting SLIs and yellow triangles the best fitting ensemble member for this region.

4.4 North East Germany

The data-set from the Baltic Sea coast of the NE Germany (Mecklenburg-West Pomerania) contains 165 samples, and the oldest sample is dated to ca. 8,000 yrs BP. All samples are dated to the period of Littorina Transgression, and like that, suitable for this study. Most of the data was processed and published by Reinhard Lampe over the years (Lampe and Janke,

2004; Lampe et al., 2010). Detailed information about data is in Appendix C. The Baltic coast of NE Germany is an intensively studied area for sea-level change (Lampe et al., 2010). Lake stages dominated its dynamical geological history from the start of the melting of the Fennoscandian ice sheet until ca. 9,000 yrs BP. The water level of the North Sea rose above the Great and the Little Belt (Danish/Swedish straits; here called Belt Sea region) causing the Baltic Sea to become linked to the ocean. During the Littorina transgression (ca. 8,000 yrs BP) sea level was rising rapidly until $\sim 5,000$ yrs BP (Lampe et al., 2010), which is visible from the sea-level curve of this region (Fig. 4.6). Peat layers, basal peats and peat profiles from near-coastal valleys are mainly used for the sea-level reconstruction in this area (Lampe and Janke, 2004; Lampe et al., 2010). The assumption is that peat growth follows the sea-level rise, and it is not affected by groundwaters (Lampe et al., 2010). If the peat growth cannot follow the fast sea-level rise, it gets inundated and cowered with sediments, and in this case, serve as an upper limit of former RSL.

Data is collected with coring techniques and is radiocarbon dated. As mentioned before, the Baltic Sea has a micro-tidal condition, and tidal influence is inconsiderable along the coast of NE Germany. Same as with the data-set from Denmark, here we distinguish three types of samples based on the indicative meaning; upper, lower limiting point and the range. Hence the application of VAM is the same as for the data from Denmark.

After application of VAM, the highest likelihood for this data-set has the model ensemble member (m_59) with 80 km viscosity thickness, 0.5×10^{21} Pa s and 2×10^{21} Pa s for upper and lower mantle viscosity respectively. In Fig. 4.6 we present the variability of all 140 ensemble members and SLI values. Further interpretation of Fig. 4.6 is in section Results of this Chapter.

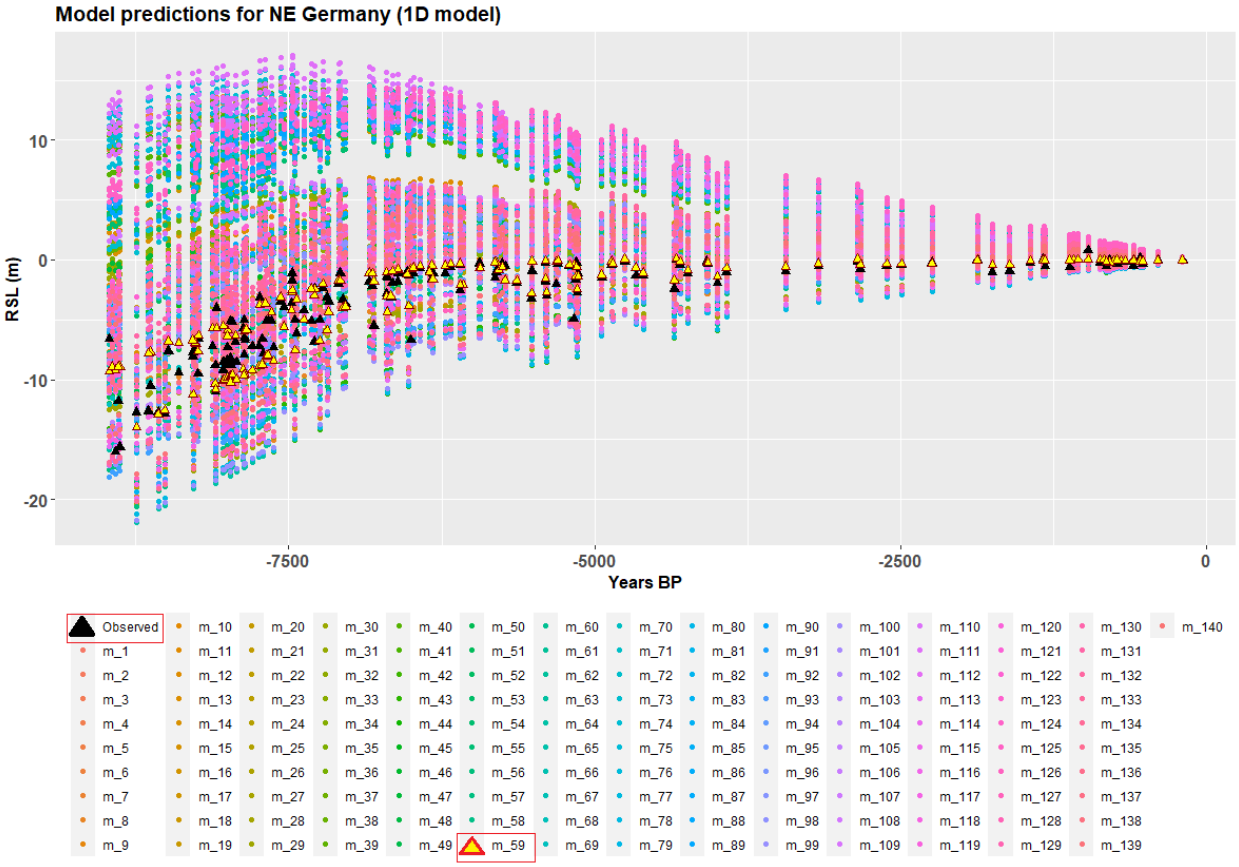

FIGURE 4.6: Variability of model ensemble predictions for the region of North East Germany. Black triangles are presenting SLIs and yellow triangles the best fitting ensemble member for this region.

4.5 North Germany

The North German coast of the Baltic Sea belongs to Schleswig-Holstein region. All samples from this region were collected from sediment cores and radiocarbon dated (Winn et al., 1986). Located in the Kiel, Lübeck and Mecklenburg Bay, all sites for sample extraction were in the water depth up to 35 m below RSL. In this data-set, we also exclude samples older than 9,000 yrs BP because they belong to the Ancylus lake stage. Samples taken into consideration for this study (27 samples) are not direct indicators of sea level but merely the oldest or youngest possible age of marine Littorina Transgression. The exact dating of marina transgression from SLIs is challenging due to the non-deposition or sediment erosion, meaning that sediment deposition was not continuous or it was eroded by younger sediments, making the determination of transgression age limiting (Winn et al., 1986). The VAM application procedure is the same as for Denmark data. After calculating elevation and age PDFs for all samples, we get final best fit for the model member (m_69) to be with viscosity thickness of 80 km, upper-mantle viscosity 0.8×10^{21} Pa s and lower-mantle viscosity 5×10^{22} Pa s (Fig. 4.7).

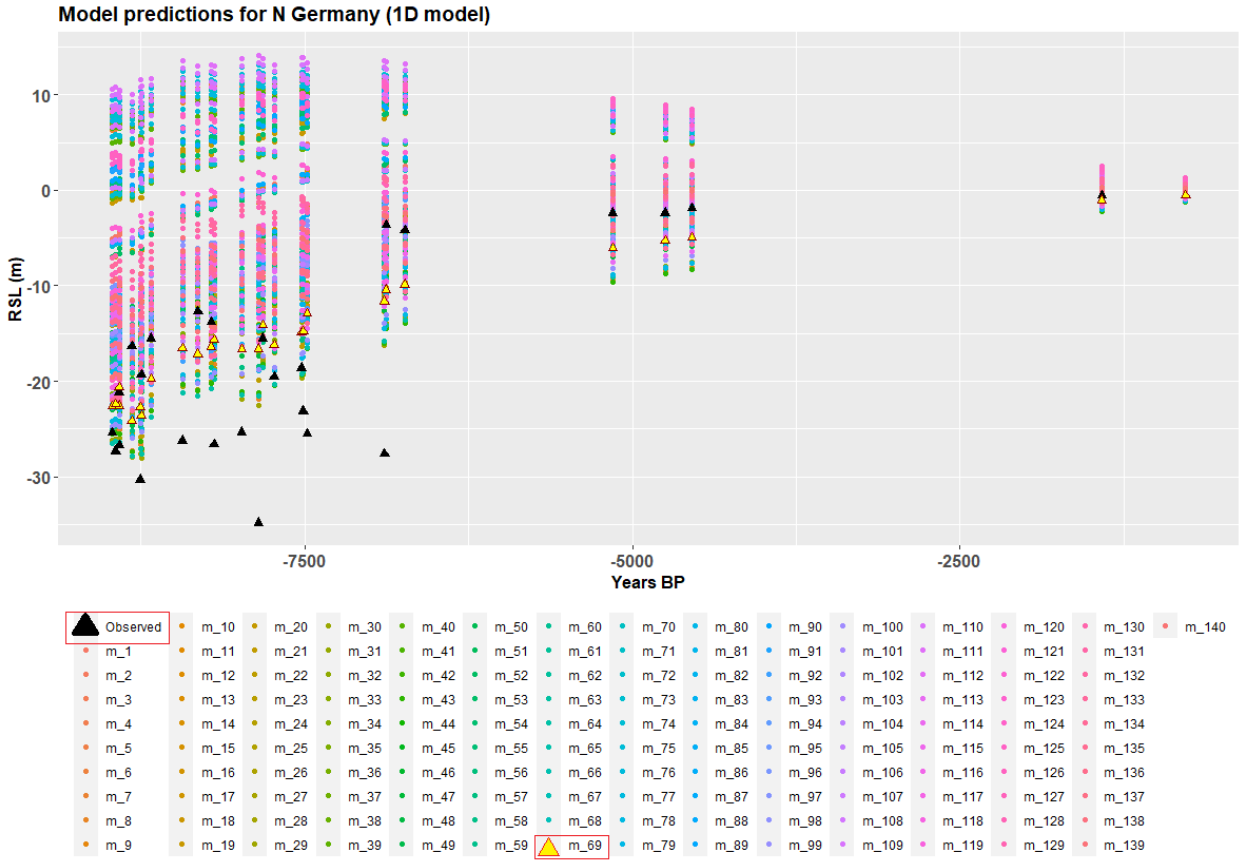

FIGURE 4.7: Variability of model ensemble predictions for the region of North Germany. Black triangles are presenting SLIs and yellow triangles the best fitting ensemble member for this region.

4.6 Ångermanland

The province of Sweden, Ångermanland, has been commonly used as an area of interest in GIA studies (Mitrovica and Peltier, 1993; Peltier and Jiang, 1996; Peltier, 1998b; Fang and Hager, 2002; Mitrovica and Forte, 2002, 2004). Ångermanland data represents a reliable and continuous sea-level record with a dominant sea-level fall. Reason for this is its proximity to the centre of the former ice sheet where crustal rebound rates are the largest (Nordman et al., 2015). Consequently, the Holocene shoreline history of this region has been studied since the early 20th century by reconstruction of shoreline displacement (Lidén, 1913, 1938). We use 19 samples published by Cato (1985, 1987, 1992, 1998). All samples were dated with varved deposits stratigraphy (Nordman et al., 2015). In this study, we use Ångermanland to compare it with results from SW Fennoscandia and get a better perspective of the sensitivity of the model. Varve data we consider as SLIPs, and apply normal distribution for varve chronology which leads us to the best fitting model ensemble member m_78. This ensemble member has parameter values: lithosphere thickness 100 km, upper-mantle viscosity 10^{21} and lower-mantle viscosity 10^{21}. Model predictions are shown in Fig.4.8 and interpreted in

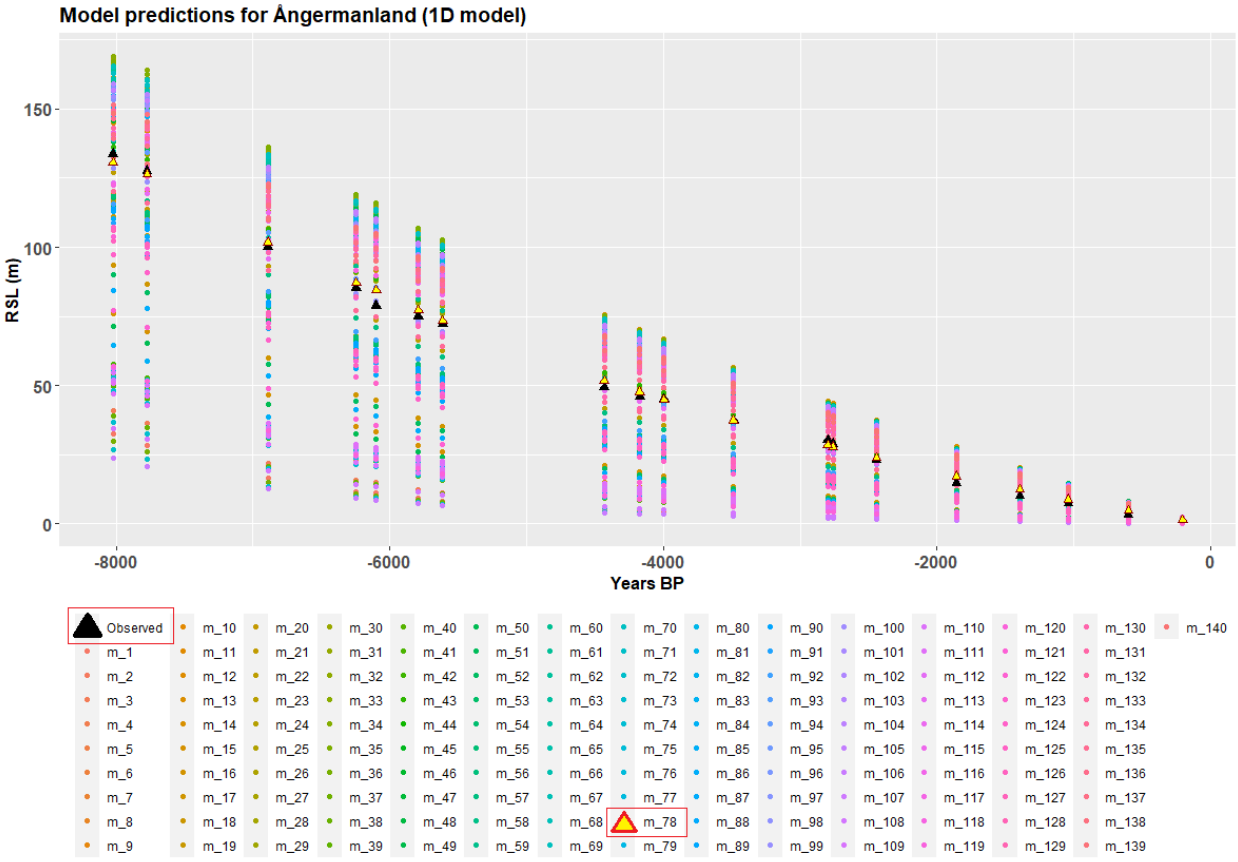

FIGURE 4.8: Variability of model ensemble predictions for the region of Ångermanland. Black triangles are presenting SLIs and yellow triangles the best fitting ensemble member for this region.

Results section of this Chapter.

4.7 Results

In previous sections of this Chapter, we presented four regions that were independently analysed following the VAM presented in Chapter 2. For each data-set we calculate elevation and age probability, and finally joint probability (equations (2.1) – (2.14)). We carefully consider different types of SLIs to select appropriate equations for elevation probability. Data-points from Samsø and Ångermanland yield normal distribution for age probability due to specific dating techniques. We calculate redundancy weights for each SLI based on Caron et al. (2018) (Fig. 4.9). The final step is the determination of the prediction curve closest to observation points, as explained in Section 2.5.

In Figs. 4.5 – 4.8 we see variability of 140 considered ensemble members. Ensemble members have values that are a combination of values from Table 3.1, the order of members, as presented in mentioned figures, is listed in Appendix 2. The first group of 35 model

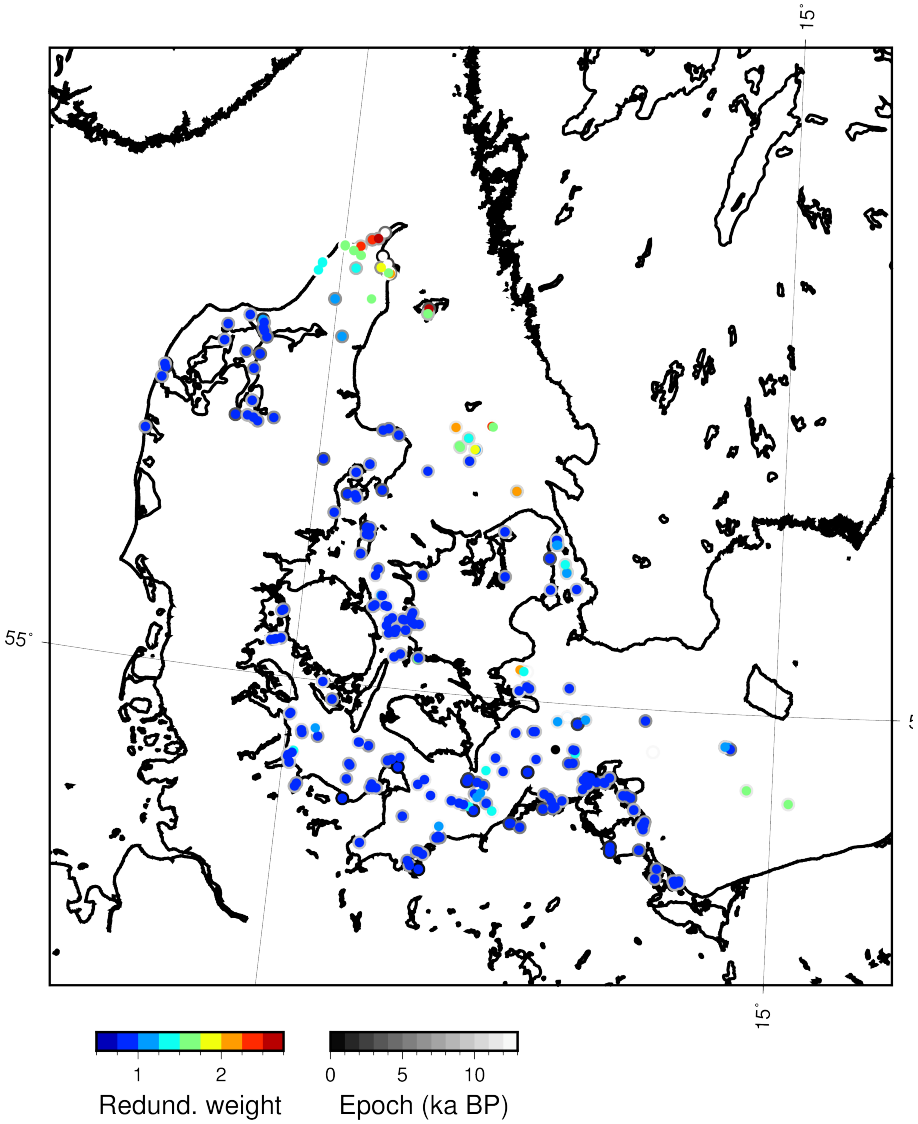

FIGURE 4.9: Redundancy weights for each selected SLI. The colour of the individual circle denotes the considered weight, the shade scale of the epoch around circles denotes the calibrated age of the SLI.

members has a lithosphere thickness of 60 km; the next group has 80 km, then 100 km and the final 35 members have a lithosphere thickness of 120 km. Model predictions vary in the Belt Sea region for around ±30 m around 9 ka BP, best fit and observed values seem to be average values of the model range. Misfit of the predictions is decreasing towards present day, reaching difference of ±2 m. In regions of North East and North Germany, most of the model members are overestimating observations for ∼ 20 m at 9 ka BP and also decreasing to ∼ 2 m close to present day. Ångermanland experienced larger variation in RSL during this period. It dropped from 150 m to around 0 m between 9 ka BP and present day. Therefore the variability of predicted values of RSL is larger. The majority of ensemble members are showing ∼ 150 m lower RSL than observed values, while 20% of model members are overestimating RSL for ∼ 50 m. Variability of predictions around 200 yrs BP is close to 1

m in the region of Ångermanland.

In order to get the likelihood of 1D model members for the whole region of SW Fennoscandia, we apply equations 2.20 and 2.21 on respective PDFs of all four regions. The highest probability for the region of SW Fennoscanida is reached by a model ensemble member m_59 with parameter values: lithosphere thickness 80 km, upper-mantle viscosity 5×10^{20} Pa s and lower-mantle viscosity 2×10^{21} Pa s. In Fig. 4.10 we present plots with four sets of model ensembles, including the VM5a model set from Peltier that has a glaciation history ICE6G_C (Peltier et al., 2015). Best fitting model member for the whole region is depicted with a black line, which is also a best-fitting model member for North and North East Germany. Red dashed line represents VM5a model, the yellow line represents the best-fitting model in the Ångermanland region and, finally, the blue line is delineating best-fitting model in the Belt Sea region. The model performance differs in a couple of meters, especially in the early stage of Littorina transgression, apart from NE Germany, where the VM5 model and best-fitting model member have similar performance around 9 ka BP. All members from our ensemble are giving RSL predictions lower than VM5 in the near field, SW Baltic. In contrast, in the near centre of glaciation, our model is corresponding well or slightly overestimating proxy data, whereas VM5a is exaggerating RSL for $\sim$ 30 m. The model member with the highest likelihood for Ångermanland is unsuitable for the SW Baltic because it is underestimating RSL in each region throughout the whole period, apart from the Belt Sea region in the period of Littorina transgression. For a detailed look we show results as scatter plots (Fig. 4.11) of the model fits for the four considered lithosphere thicknesses and viscosity ranges. It is visible that lower mantle viscosity shows two different favourable regions; one with lower values ($\sim 1 \times 10^{21}$ Pa s) and other with higher ($\sim 2 \times 10^{22}$ Pa s). Lower values are more suitable for the centre of the former ice sheet, and higher values of lower-mantle viscosity are responding better to the near field of the SW Baltic Sea. Lower-mantle viscosity has a more substantial influence on GIA (Ivins and Sammis, 1995), therefore higher sensitivity, suggesting that having a constant value for lower-mantle viscosity does not apply to the whole region. Furthermore, the Belt Sea region shows a preference for a thicker lithosphere than N and NE Germany, which corresponds to the conclusions of TESZ studies, where Jensen and Thybo (2002) state that the Moho topography is strongly varying in the SW Baltic region. Especially in the areas of the TTZ and the STZ which are intersecting beneath the Belt Sea region. Jensen and Thybo (2002) show that the Moho is steeply changing in these zones from a crustal thickness of approximately 32 km to 45 km. Since lithosphere thickness consists of the crust and uppermost solid mantle, and the Moho discontinuity is a border between these two layers, the overall lithosphere thickness in these areas is larger, which is coinciding with our results (USGS, 2020). Based on these results, we conclude that the 1D model member m_59 representing the best fit for the whole region, can reasonably estimate former RSL in

the area of the SW Baltic and Ångermanald for the period between 6 ka BP and present. Before this period, the model is either underestimating or overestimating RSL for $\sim 10-20$ m, which proves that RSL in the Boreal period of Holocene (8.5-6.9 ka BP) is more sensitive to Earth model parameters. As mentioned before, this period is assumed to have a steep rise of sea levels, which could be a cause of a higher variability in RSL prediction (Figs. 4.5 – 4.8).

We present an overview of published 1D structures in this region together with the result from this study in Table 4.2. Column Data-set in Table 4.2 shows which data authors used

TABLE 4.2: Radial profile results for lithosphere thickness, upper-mantle and lower-mantle viscosity from different studies of Fennoscandia, adapted from (Steffen and Wu, 2011). Results from this study are at the end of the table in bold letters.

Study	Lith. thickness [km]	Upper-mantle visc. [10^{20} Pa s]	Lower-mantle visc. [10^{22} Pa s]	Data-set
Steffen et al. (2010)	160	4	2	GRACE
Steffen and Kaufmann (2005)	120	4	10	SLI
Klemann and Wolf (2005)	80	5	0.24	IRTS
Martinec and Wolf (2005)	100	4	0.8	IRTS
Kaufmann and Lambeck (2002)	120	7	2	SLI
Wieczerkowski et al. (1999)	95	4.8	0.59	IRTS
Davis et al. (1999)	156	7.2	2	Tide gauges
Lambeck et al. (1998)	75	3	0.5	SLI
Lambeck et al. (1998)	80	4.5	>0.5	Lake level
This study (all regions)	80	5	0.2 – 1	SLI
Belt Sea region	100	10	5	SLI
North Germany	80	8	5	SLI
North East Germany	80	5	20	SLI
Ångermanland	100	10	0.1	SLI

to derive a radial viscosity profile. Here SLI stands for sea-level indicators, IRTS refers to inverse relaxation-time spectrum and GRACE is a satellite data from the Gravity Recovery

and Climate Experiment (GRACE) (NASA, 2020). From this overview, it is obvious that there is a large deviation in lithospheric thickness in 1D models in Fennoscandia. Based on Martinec and Wolf (2005) the average value is located between 65 and 200 km. Values of lower-mantle viscosity are in general higher by one order of magnitude than upper-mantle viscosity. The difference in data used for constraining GIA models, as well as different ice-sheet history, yields different results for the same region, leading to the conclusion that 3D GIA model could be more suitable for this region.

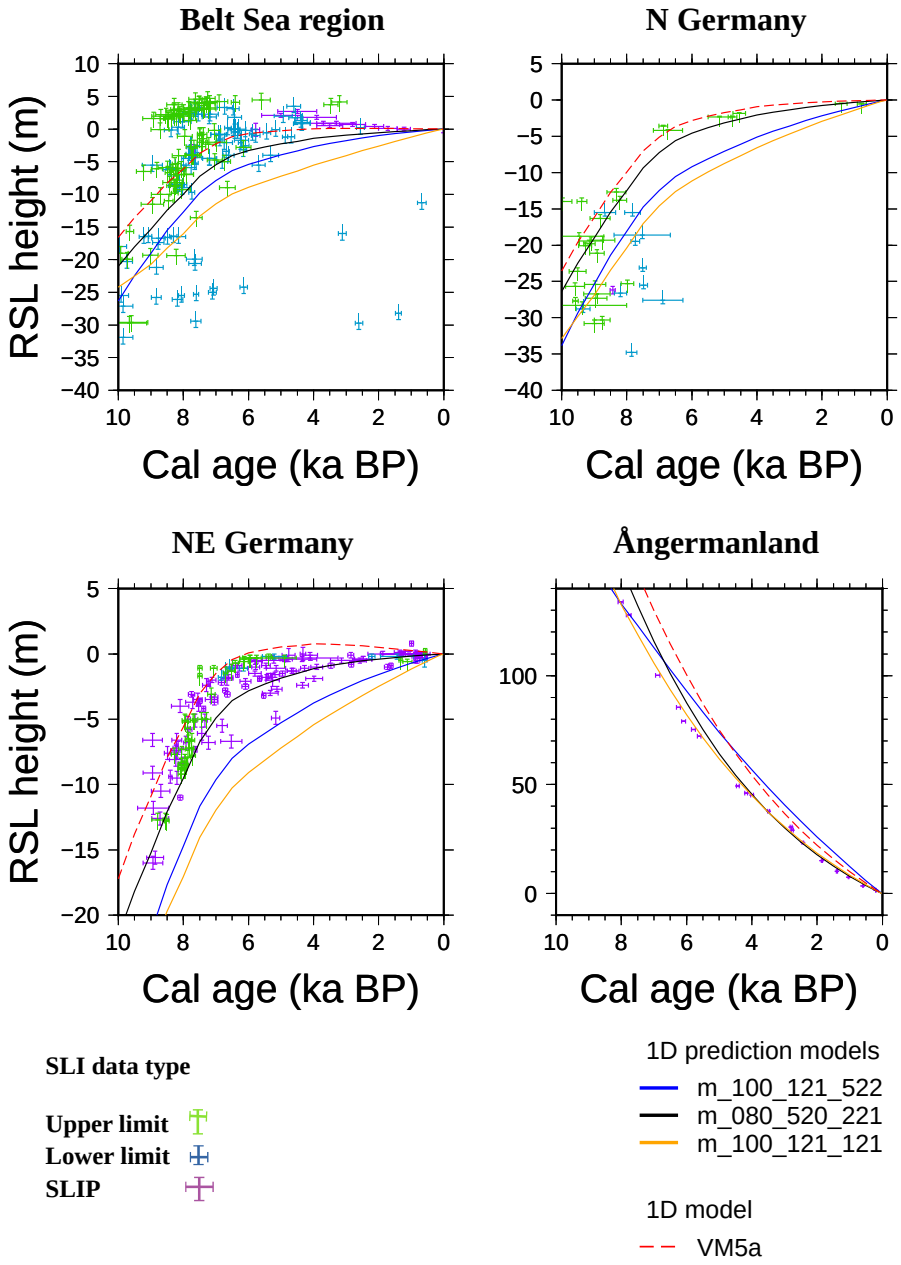

FIGURE 4.10: The best fitting model for each region (orange line for Ångermanland, black for N and NE Germany and blue for Belt Sea region) for the whole region (black line) and VM5a model (red dashed line).

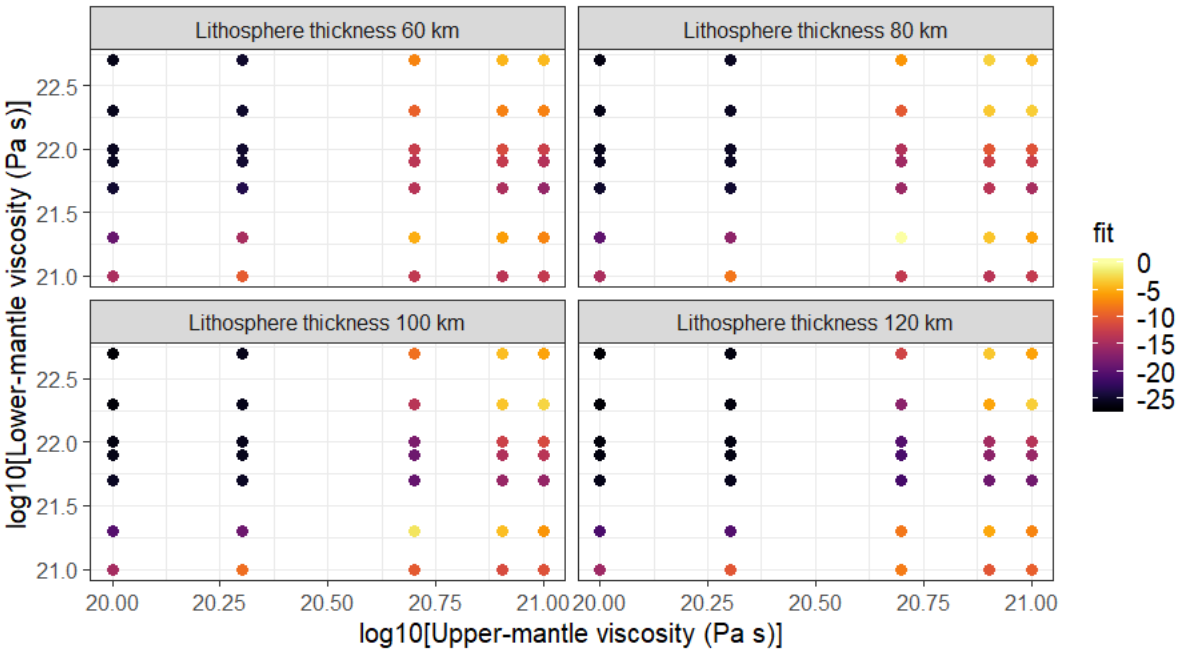

FIGURE 4.11: Model fits for the whole region as a function of upper- and lower-mantle viscosities for considered lithosphere thicknesses.

5

Constraining 3D GIA models in SW Fennoscandia with geological data

GIA research advanced during the last decades and different Earth models were developed. The spectral method, for which the Earth model is only radially stratified and is linearly viscoelastic, is refereed to as 1D model (e.g., Mitrovica and Peltier, 1993; Fjeldskaar, 1994; Wieczerkowski et al., 1999; Kaufmann and Lambeck, 2002; Fleming et al., 2003; Milne et al., 2004). A more realistic 3D Earth model accounts for lateral heterogeneity or non-linear rheology using spectral or spatial finite-element methods (e.g., Martinec, 2000; Kaufmann and Wu, 2002; Latychev et al., 2005; Klemann et al., 2008; van der Wal et al., 2015). 3D models require more computational resources. It is, therefore, beneficial to determine if they provide significantly different results from 1D-model approximations (Steffen and Wu, 2011).

The focus of this Chapter is the analysis of the impact of 3D variability in mantle viscosity on the interpretation of sea-level data. We concentrate on the possible variation in viscosity structure from the Paleozoic central region of Scandinavia to the more Variscan SW European region, discussed in the previous Chapter. The investigation is based on an ensemble of ten global viscosity distributions, which are used to predict sea-level change since the LGM, considering the ICE5G (Peltier, 2004b) and ICE6G_C (Peltier et al., 2015) glaciation histories as forcing.

The majority of models assume that the Earth is a spherically symmetric Maxwell body with radial viscosity profile (Kuchar et al., 2019). However, some studies are applying lateral viscosity variations, especially in regions where seismic tomography models provide evidence

about lateral variations in Earth properties and where there is a variation in tectonics, like, for example, in the area in which we are interested (e.g., Wu et al., 1998a; Kaufmann and Wu, 2002; Whitehouse et al., 2006). Researchers are trying to explain different viscosity inferences in the same regions by applying lateral viscosity contrast (Kuchar et al., 2019). So far, 3D models are showing large deviations in modelled RSL in comparison to 1D approaches. Here we examine how significant these deviations are in the region of SW Fennoscandia and how 3D models can be improved. We validate 3D models with SLIs, using the same set of indicators as in Chapter 4 and applying VAM.

5.1 Model setup

3D models used in this study are provided by Bagge et al. (2020). Bagge et al. (2020) apply Viscoelastic Lithosphere and Mantle model (VILMA) (Klemann et al., 2008; Martinec et al., 2018) where field equations are solved according to the spectral finite-element model of Martinec (2000). Earth's density structure and elastic parameters are modified from seismically constrained Preliminary reference Earth model (PREM) (Dziewonski and Anderson, 1981). The sea-level equation with included rotational feedback, deformational and gravitational effects is following the studies of Hagedoorn et al. (2007); Martinec and Hagedoorn (2005). Spherical harmonics have a spectral resolution of 170 degrees which is corresponding to a wavelength of $\sim$ 120 km. The distance of nodes in the radial finite-element is 5 km for the first 420 km of depth, from 420 up to 670 km is 10 km and for the depth of 670 km to 6371 km the distance of nodes is 40-60 km. Glaciation histories ICE6G_C and ICE5G were considered, both are covering the period from 123 ka BP till present day.

5.1.1 Parameterisation of 3D mantle-viscosity

We follow the set-up of Bagge et al. (2020) where Earth structure parameterisation is achieved from the tomography model SL2013SV for depths up to 200 km (Schaeffer and Lebedev, 2013), below that, the 3D structure from Grand (2002) is applied. The reason for the combination of these two models is a decrease in performance of the SL2013SV model with depth (Steinberger, 2016). Seismic velocity anomalies are converted to temperature anomalies below the lithosphere by following the Model M2 from Steinberger and Calderwood (2006) defined by equations:

$$-\left(dv_s/dT\right)/v_s \sim 10 - 15 \times 10^{-5} K^{-1} \,, \tag{5.1}$$

eq. (5.1) is presenting a conversion factor, where v_s is seismic velocity and (5.2) is the Arrhenius law for viscosity, μ (Steinberger and Calderwood, 2006):

$$\mu \sim exp(rH/(RT)) \; . \tag{5.2}$$

Here, H is the activation enthalpy, $R = 8.3144$ J/K/mol is the universal gas constant, r is a reduction factor adjustable for each model and T is the temperature. The reduction factor is introduced because non-Newtonian flow can be closely reproduced by Newtonian flow with reduced activation enthalpy (Christensen, 1983). Here, activation enthalpy is adopted from Steinberger and Calderwood (2006); in the upper mantle, it is $\sim 500 - 700$ kJ/mol. A more detailed description of the conversion of parameters can be found in Steinberger and Calderwood (2006) and Steinberger (2016). For all viscosity distributions, the threshold value is set to be 10^{19} Pa s to reduce computing time. Lateral variations are considered down to a depth of 870 km. Below, the viscosity value is calculated as the lateral mean at the specific depth.

Fig. 5.1 presents lithospheric thickness variation, as well as viscosity changes at different

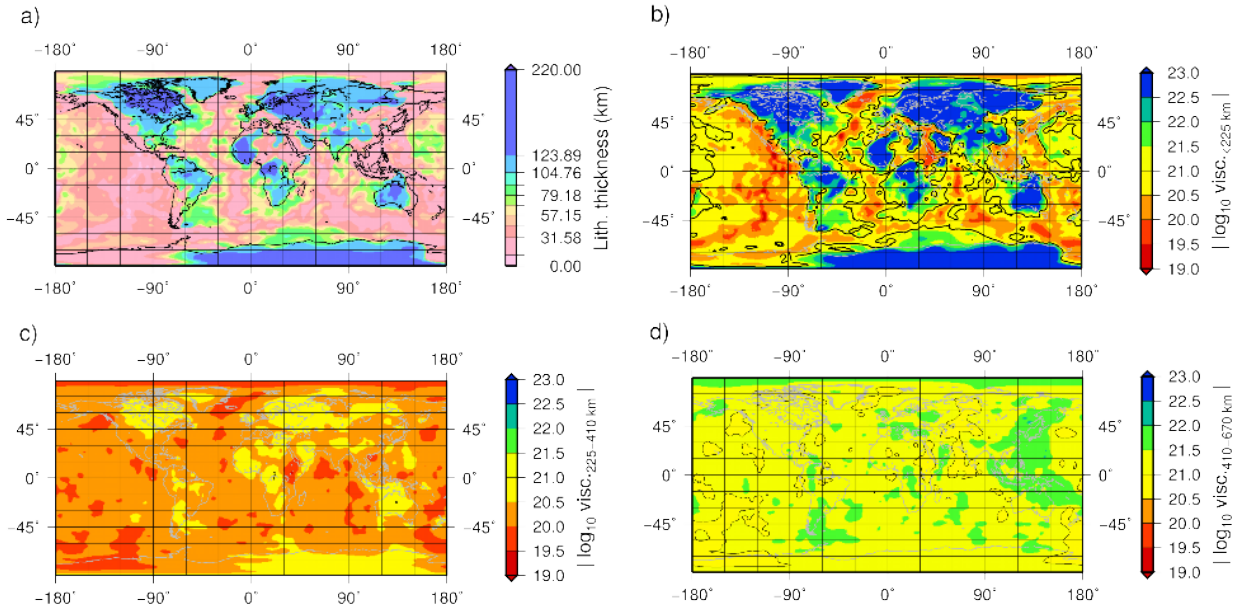

FIGURE 5.1: Reference viscosity structure $v\_0.4$. (a) Lithospheric thickness (defined as the region with viscosities higher than $10^{23.5}$ Pa s). Average of viscosity for (b) asthenosphere (between base of lithosphere and 225 km depth), (c) upper mantle (225 km to 410 km), (d) transition zone (410 km to 670 km) Figure from Bagge et al. (2020).

depth ranges of the reference model $v\_0.4$, which is adapted from Steinberger (2016). Here, depths are defined as follows: lithosphere spreads down to a depth where viscosity is $>10^{23.5}$ Pa s, after that the Earth structure is transferring to less solid-state, and asthenosphere extends from lithosphere to 225 km of depth, below that to 410 km we define an upper mantle,

from 670 km down to 1000 km is considered to be a lower mantle, and between upper and lower mantle is a transition zone (Bagge et al., 2020).
Lithospheric thickness varies between 20 and 220 km. The average viscosity in the asthenosphere varies between 10^{19} and 10^{23} Pa s, especially in regions with cratonic lithosphere discontinuities like Fennoscandia and Laurentia (Figure 5.1 b). The asthenosphere extends from the upper threshold down to 225 km and, accordingly, its log-mean value shown in Fig. 5.1 (b) is not representing the minimum viscosities reached in this layer. Upper mantle viscosity varies between 10^{20} and 10^{21} Pa s and viscosity in the transition zone (400 to 670 km) is between 10^{21} and 10^{22} Pa s.

5.1.2 3D models

The mantle viscosity structure in studies can vary depending on the methods used to infer it. The derivation of a 3D viscosity structure can widely differ depending on tomography models, transformations of seismic velocities to temperature and temperature to viscosity. We investigate ten models over the region of SW Fennoscandia and Ångermanland to come to the conclusion how different parameters in the Earth structure correspond to observed RSL. In Fig. 5.2 we can see the mean radial profile of all ten models considered in this study and, in Figs. 5.4 and 5.5, we see viscosity profile cross-sections of each model for the region of interest that are presented in Fig. 5.3. Bagge et al. (2020) classified models into three different classes based on the conversion of velocity to viscosity structure in order to investigate if there is a similar behavior within classes. In Table 5.1 we present models where Class number states in which group they are classified, r is the value of reduction factor r in eq. (5.2), TF is the temperature factor that multiplies the transformation from seismic velocity to temperature variations. RVP is the name of the radial viscosity profile, where $s16$ is from Steinberger (2016) and sc06 and sc06b from Steinberger and Calderwood (2006). Lithosphere thickness is T_{lith}, and η_a, η_{um} and η_{tz} are averaged viscosities of asthenosphere, upper mantle and transition zone respectively. In the first column, Name, we introduced simplified abbreviations for each model, and these we will use in the following text and figures.
Class-I: Each model has a different reduction factor r, meaning that they do not have the same conversion from temperature to viscosity. Factor r goes from 0.2857 up to 1.0 to imitate a dislocation creep (non-Newtonian viscosity). The strain-rate dependency of viscosity changes with the value of r, the higher the value, the stronger the dependency (Christensen, 1983; Steinberger and Calderwood, 2006). As visible from Fig. 5.4, the main difference among members of Class-I is in lithospheric thickness, and asthenospheric viscosity.
Class-II: In this class, there are two models with the same reduction factor as the reference model ($r = 0.4$). Below the depth of 250 km, the adiabatic temperature profile of mantle is multiplied by factors 4/3 and 5/3 that serve as damping factors of tomography models.

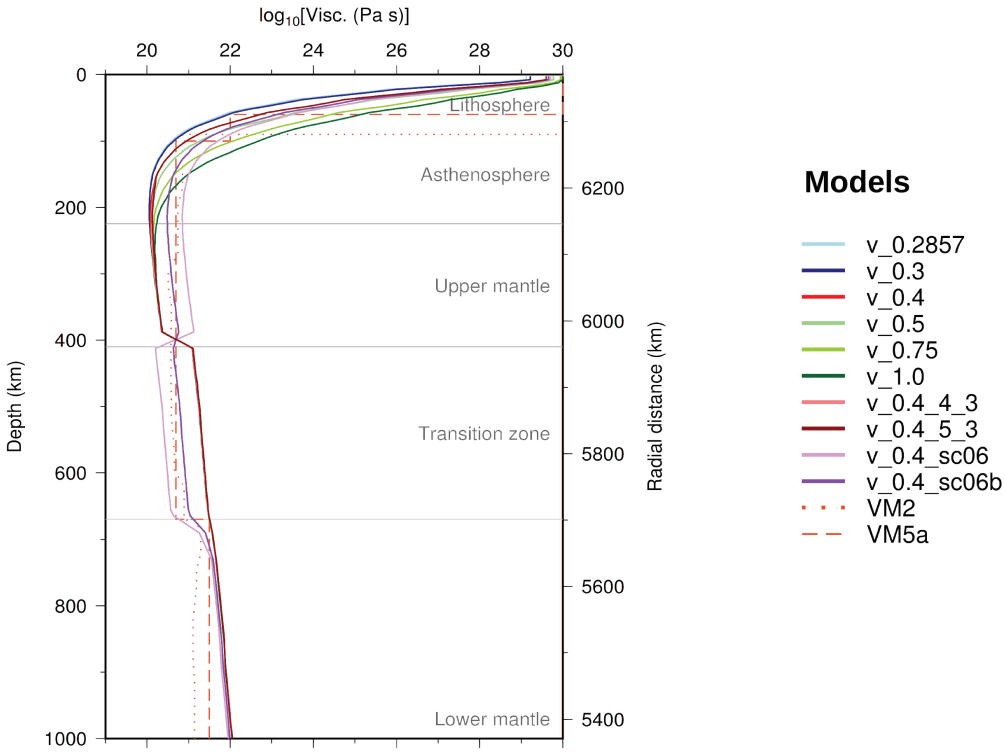

FIGURE 5.2: Global mean viscosity structures from ten 3D models and two 1D models from Peltier, VM2 and VM5a (Peltier, 2004a; Peltier et al., 2015). Figure provided by Meike Bagge.

TABLE 5.1: List of models with considered 3D Earth structures. Model m_3 is a reference model. The dependence between temperature and viscosity is defined by the Arrhenius law and the values (0.2875 to 1.0) of the model name describe the reducing factor for the activation energy.

Name	Model	Class	r	TF	RVP	$T_{lith}(km)$	η_a	η_{um}	η_{tz}
							$[log_{10}$ Pa s$]$		
m_1	v_0.2875	I	0.2857	1	s16	46.51	21.05	20.25	21.28
m_2	v_0.3	I	0.3	1	s16	48.07	21.06	20.25	21.28
m_3	v_0.4	I	0.4	1	s16	57.62	21.17	20.26	21.28
m_4	v_0.4_4:3	II	0.4	4/3	s16	57.62	21.19	20.27	21.29
m_5	v_0.4_5:3	II	0.4	5/3	s16	57.63	21.20	20.28	21.30
m_6	v_0.4_sc06	III	0.4	1	sc06	65.40	21.89	20.93	20.40
m_7	v_0.4_sc06b	III	0.4	1	sc06b	61.49	21.55	20.61	20.82
m_8	v_0.5	I	0.5	1	s16	65.29	21.26	20.26	21.29
m_9	v_0.75	I	0.75	1	s16	79.52	21.50	20.28	21.29
m_10	v_1.0	I	1.0	1	s16	90.12	21.88	20.30	21.30

Class-II models do not have significant deviations from the reference model in the viscosity profile, apart from the slightly thicker lithosphere (Fig. 5.5).

Class-III: Two models from this class also have the same reduction factor as a reference

model and their viscosity structure corresponds to models from Steinberger and Calderwood (2006). Model v_0.4_sc06 correlates to the Model M2 and shows the lowest viscosity in the transition zone from 410 to 660 km, with viscosity jumps before and after this depth range (Fig. 5.2). Model v_0.4_sc06b, with the viscosity structure based on the model M2b, has the lowest viscosity in the upper mantle, with an increase after the transition zone. Models from this class mainly differ in the asthenosphere, upper mantle and transition zone from other models, while lower mantle has similar behaviour for all of them (Fig.5.2).
In Fig. 5.3 we show the viscosity changes along the profile A-B, passing SW Fennoscandia and ending in Ångermanland. Light blue dashed lines present Trans-Europian Suture Zone, together with its branches. We use this figure to visualise cross-sections along the A-B profile

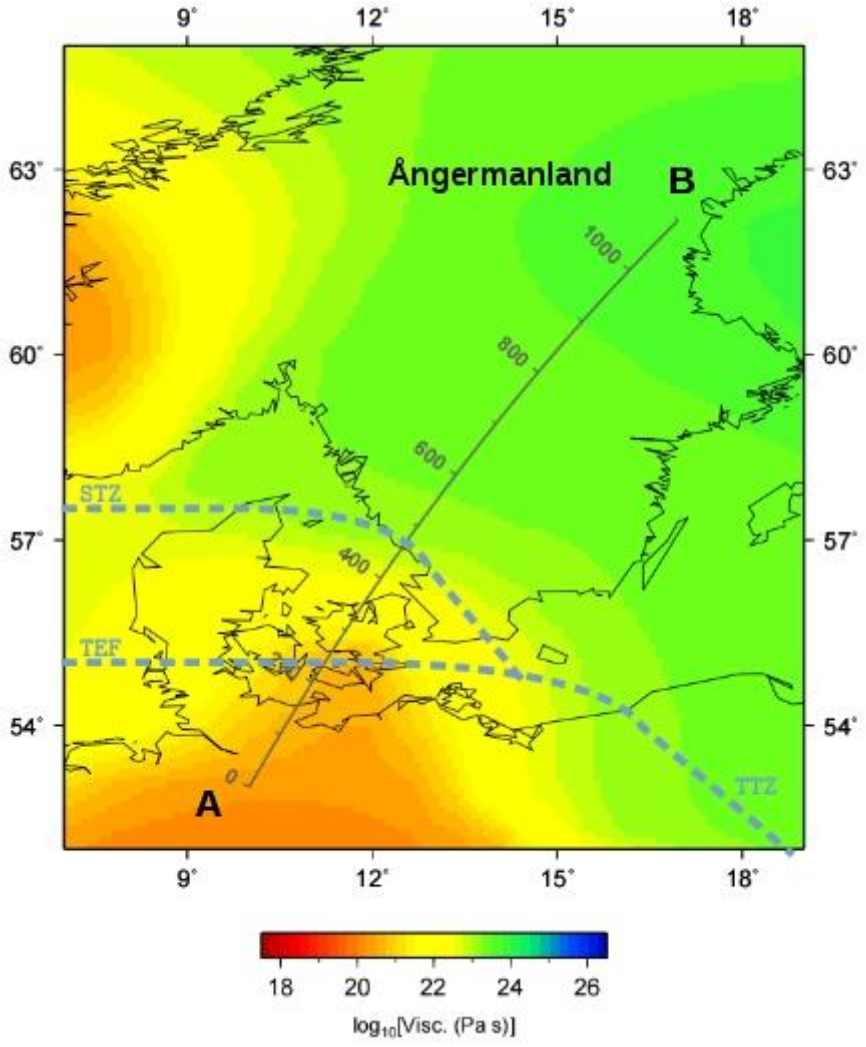

FIGURE 5.3: Viscosity at 100 km depth of the model m_1 at the region of interest. Trans Europian Suture Zone (TSZ) with its two branches: the Sorgenfrei-Tornquist Zone (STZ) and Teisseyre-Tornquist Zone (TTZ) are marked with the light blue dashed line.

of each model, and their viscosity profiles are further presented in Figs. 5.4 and 5.5. Changes in the viscosity along the profile crossing we discuss in the following section.

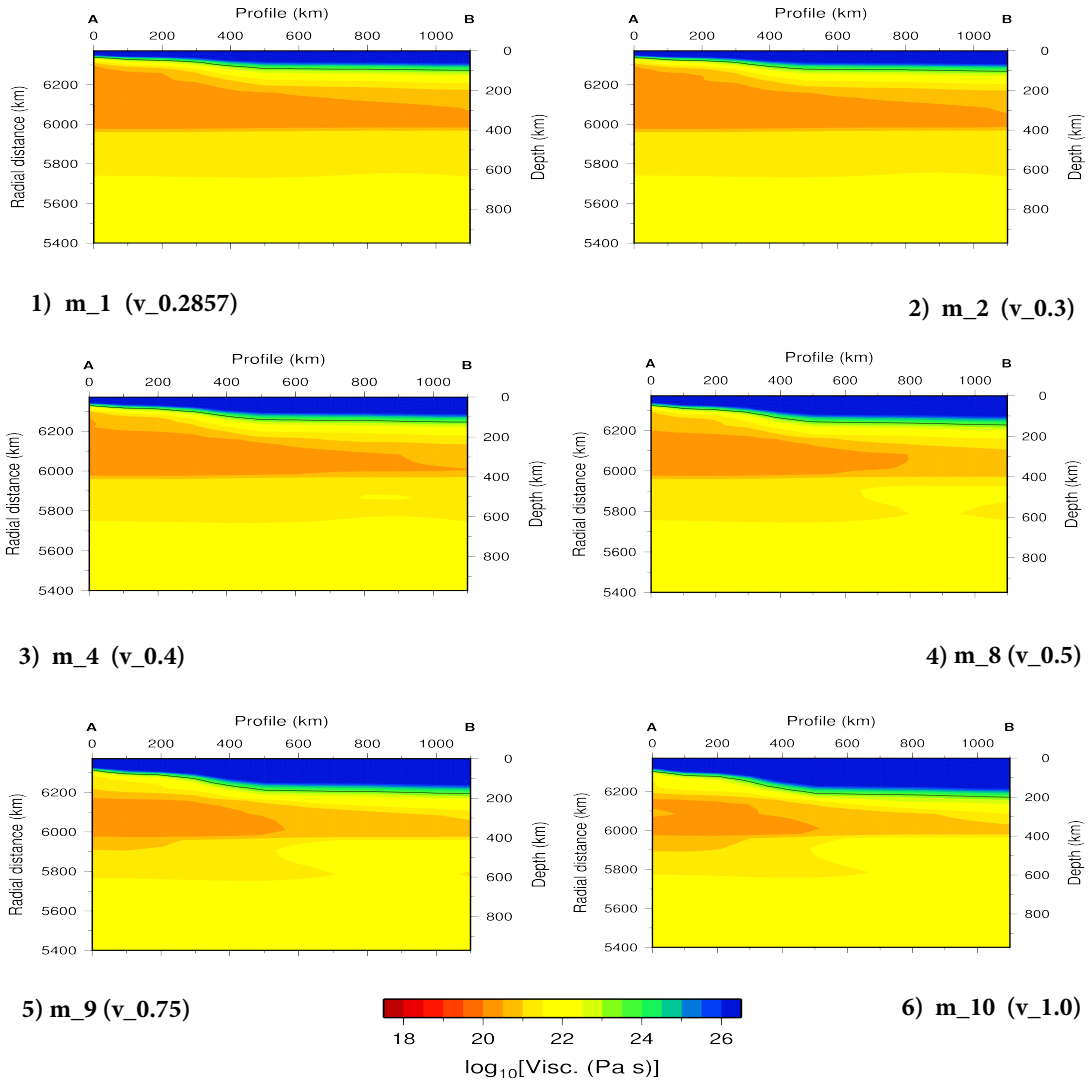

FIGURE 5.4: Viscosity cross-sections of 3D models of Class-I.

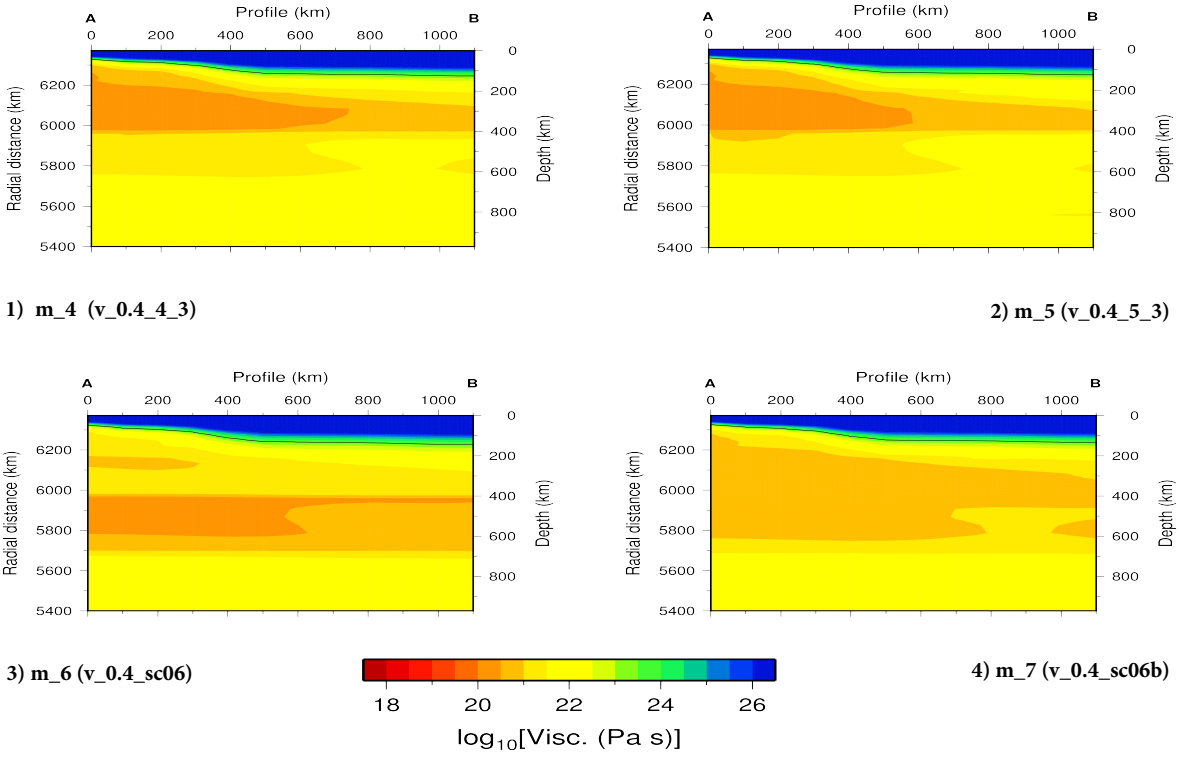

FIGURE 5.5: Viscosity cross-sections of 3D models of Class-II and Class-III. Models 1) and 2) belong to Class-II and models 3) and 4) to Class-III.

5.2 Results

We apply VAM presented in Chapter 2 to determine the best fitting 3D model among ten models described in the previous section and to analyse the impact of 3D variability. First, we apply models with ICE6G_C glaciation history; then we compare the results with the 1D model from Chapter 3 with the same glaciation history. And finally, we compare 3D models with two different glaciation histories (ICE5G vs ICE6G_C).

5.2.1 3D models with ICE6G_C glaciation history

We get the same best-fitting model for the two regions belonging to Germany, N and NE Germany (Figs. 5.6 and 5.7). The model with the name m_4 in Table 5.1, with reduction factor 0.4 and 4/3 damping factor, predicts former RSL that resembles most to observation values in these two regions. Model m_1 fits to the Belt Sea region better than other models (Fig. 5.8), and model m_6 proved to be suitable for Ångermanland region (Fig. 5.9). From the spread of all ten models in Figs. 5.6–5.8 we can see that all models are overestimating observation values in the region of SW Fennoscandia. Models with the higher reduction factor (r>0.5) and models from the Class-II are overestimating former RSL for $\sim$ 10 m around 8 ka BP in NE and N Germany. This difference is reducing towards present day. Samples that appear to be outliers in Fig. 5.7 are all limiting points that are indicating the lowest RSL. The uncertainty of these SLIs is explained in Chapter 4, Section 4.5. In the Belt Sea region, the model with the highest likelihood is overestimating RSL for $\sim$ 10 m at 8 ka BP. At the same period, Class-II models are exceeding RSL for $\sim$ 20 m. Close to the centre of the former ice sheet, in Ångermanland, all models are underestimating RSL from 8 ka BP until 7 ka BP (Fig. 5.9). After this period, models m_1, m_2 and Class-III models are slightly overestimating the RSL curve. Highest misfit is noticeable with models m_9 and m_10, while the best fitting model, m_6, shows misfit only around 8 ka BP for $\sim$ 20 m.
After application of equations 2.20 and 2.21 on respective PDFs of all four regions, we calculate Bayes factors K_i and determine three models with the highest likelihood for the region of SW Fennoscandia to be models m_4, m_3 and m_1. In Fig. 5.12 a) Bayes factors for each model are presented. Model with the Bayes factor 0 is depicting the 3D model with ICE6G_C glaciation history that has the highest likelihood in SW Fennoscandia.

From Figs. 5.4 and 5.5 it is visible that the viscosity cross-section along the A-B profile varies between models m_1 and m_4, which are best-fitting models for SW Fennoscandia. These two models have slightly different lithosphere thickness along the whole A-B profile. Model m_1 has around 50 km thick lithosphere in N and NE Germany, with an increase to 70-80 km in the Belt Sea region, which is located between 200 and 400 km of the profile cross-section (Figs. 5.4 and 5.5). The thickest lithosphere is at the point "B", around 100 km

of depth, while m_4 has ∼ 20 km thicker lithosphere with incremental change lengthwise the profile. In the Belt Sea region, at ∼ 200 km on the profile, the preferable model m_1 shows a steeper change in the asthenosphere and upper-mantle viscosity, from ∼ 10^{21} to lower viscosity.

Furthermore, the Belt Sea region is located between two branches STZ and TTZ; therefore, there appears a likely change in upper-mantle viscosity towards northern Germany, which is resembled by model m_1. The viscosity of the transition zone and lower mantle viscosity is constant down the A-B profile in model m_1. In contrast, model m_4 shows a deviation in the transition zone closer to the centre of the former ice sheet. Northern Germany yields a more viscose asthenosphere than m_1 provides, but is less viscous than m_6, the best-fitting model for Ångermanland. The model m_6 has a thicker lithosphere at the point "B" of the profile, and higher viscosity in the asthenosphere and upper-mantle. However, this model has a lower viscosity in the transition zone than other two models, m_1 and m_4.

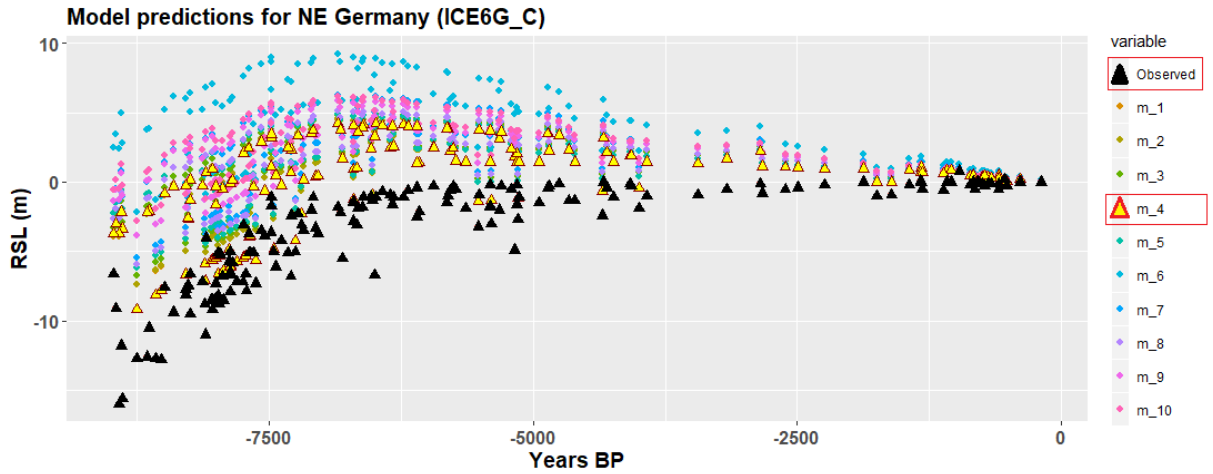

FIGURE 5.6: Ten models with 3D viscosity and ICE6G_C glaciation history in the region of NE Germany. Black triangles present observation values and yellow present the best-fitting model.

In Fig. 5.10 we present best-fitting models for each region together with Peltier's 1D models; VM5a and VM2 (Peltier et al., 2015; Peltier, 2004b). Models m_1 and m_4 are shown with green and blue lines respectively and are predicting quite similar RSL in the Belt Sea region. In this region, Peltier's 1D models are predicting RSL lower for around 3 m than models m_1 and m_4. In N and NE Germany, the best-fitting model is predicting lower RSL from the rest of the models, apart from VM2 in NE Germany in the period until 8 ka BP. The best fitting model in Ångermanland region, m_6, is overestimating RSL in the rest of the regions, while in Ångermanland itself is underestimating RSL until 7 ka BP.

After analysing the results and properties of all ten models, we conclude that the model with the highest likelihood for the whole region m_4, is suitable GIA model for the region

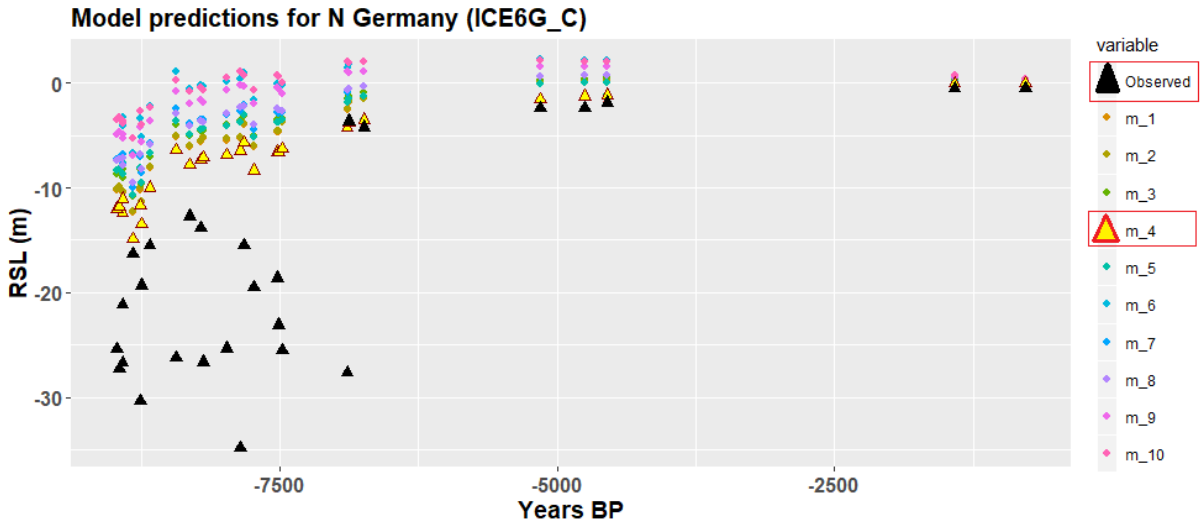

FIGURE 5.7: Ten models with 3D viscosity and ICE6G_C glaciation history in the region of N Germany. Black triangles present observation values and yellow present the best-fitting model.

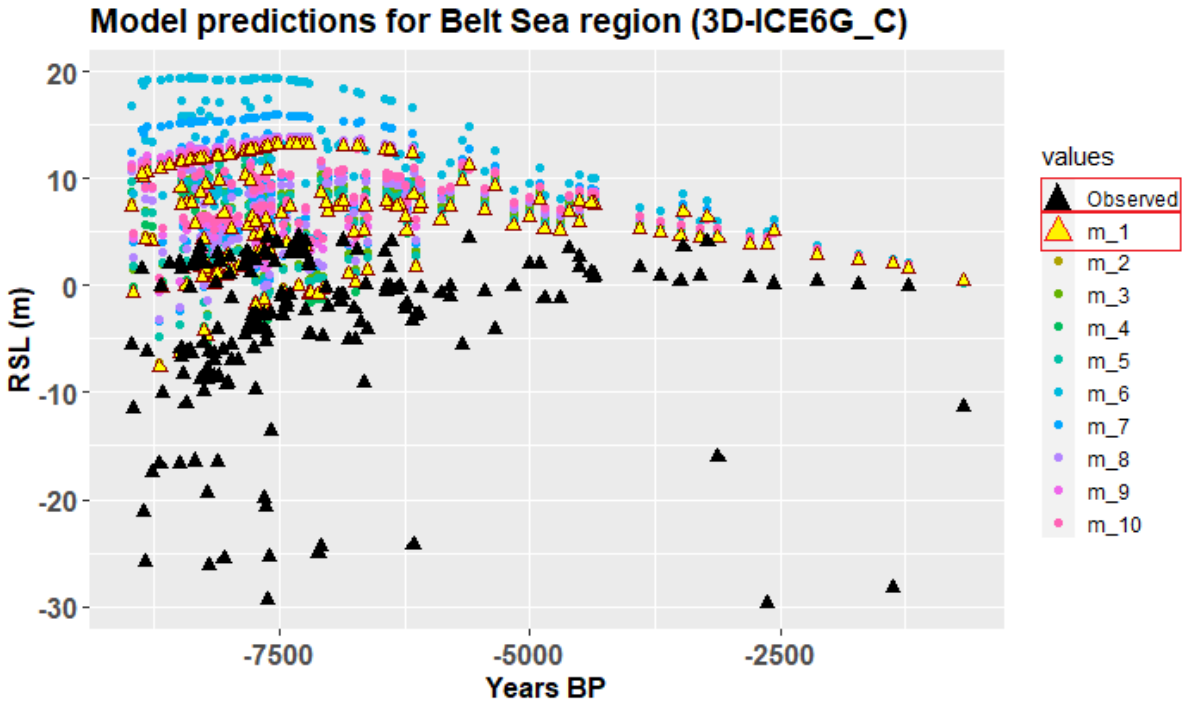

FIGURE 5.8: Ten models with 3D viscosity and ICE6G_C glaciation history in the Belt Sea region. Black triangles present observation values and yellow present the best-fitting model.

of SW Fennoscandia. However, further modifications could improve the performance of the model; for e.g. steeper change in upper-mantle viscosity in Belt Sea region, as well as the adjustment of upper-mantle and, transition zone viscosity in the central region of former Fennoscandian ice sheet to be represented as in model m_6.

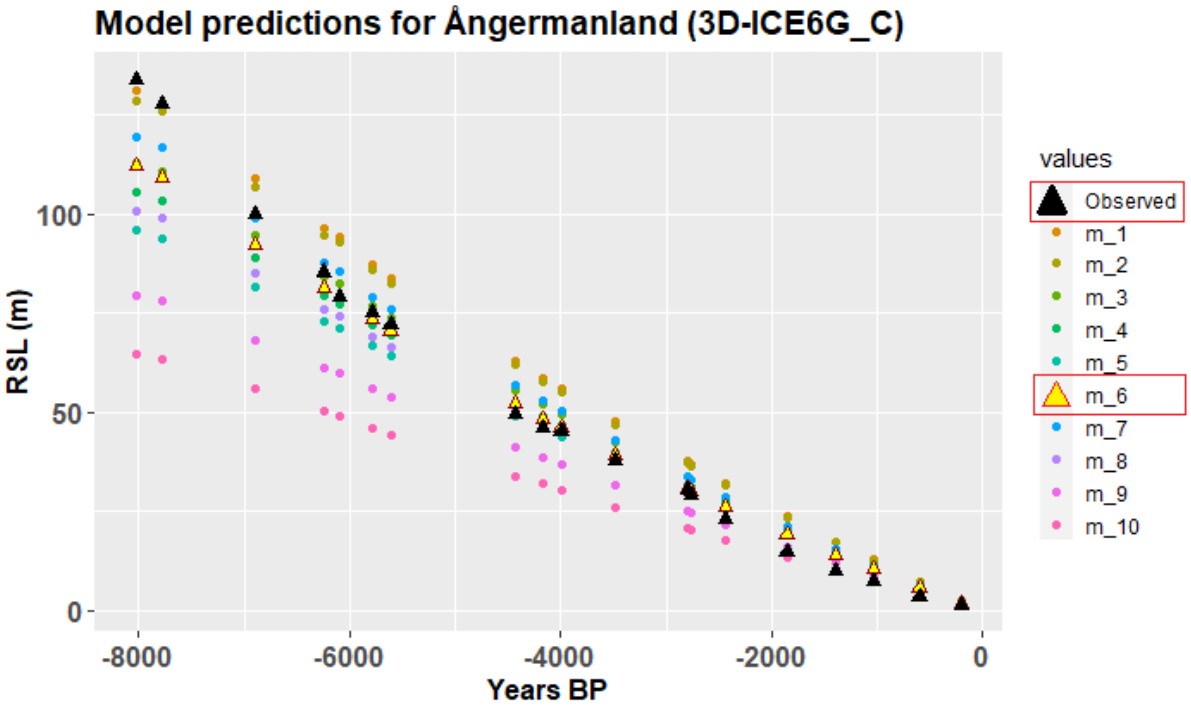

FIGURE 5.9: Ten models with 3D viscosity and ICE6G_C glaciation history in Ångermanland. Black triangles present observation values and yellow present the best-fitting model.

5.2.2 3D vs 1D models (ICE6G_C)

Here we compare the model ensemble with radial viscosity profile analysed in Chapter 3 with the analysis of 3D models from this chapter. The viscosity profile in 1D model members that showed the highest likelihood for regions of interest, coincides with the viscosity of 3D models that are best-fitting for said regions. Lithosphere thickness appears to be thinner in the region of N and NE Germany with an incremental change towards Ångermanland, where it reaches 100 km of thickness. Upper-mantle viscosity is one order of magnitude lower than in the central region, and lower mantle viscosity has the same order of magnitude for the whole region. The Belt Sea region appears to be an outlier with one order of magnitude higher viscosity in the lower mantle in the 1D model (5×10^{22} Pa s) than in the best-fitting 3D model ($\sim 10^{21}$). Impact from lateral heterogeneity in the Belt Sea regions was expected due to its tectonic setting.

In all three regions of SW Fennoscandia predictions from the best-fitting 1D model ensemble members are underestimating RSL in comparison to SLI values (Figs. 4.5 – 4.7), while best-fitting 3D models for the same regions are overestimating RSL for $\sim$ 10 m (Figs. 5.6–5.8). Reason for this is that these regions correlate with areas of low viscosity and thin lithosphere in 3D models that fit the best to these regions, m_1 to the Belt Sea and m_4 to N and NE Germany, resulting in a faster rebound of the material and deformation (Meike Bagge, 2020,

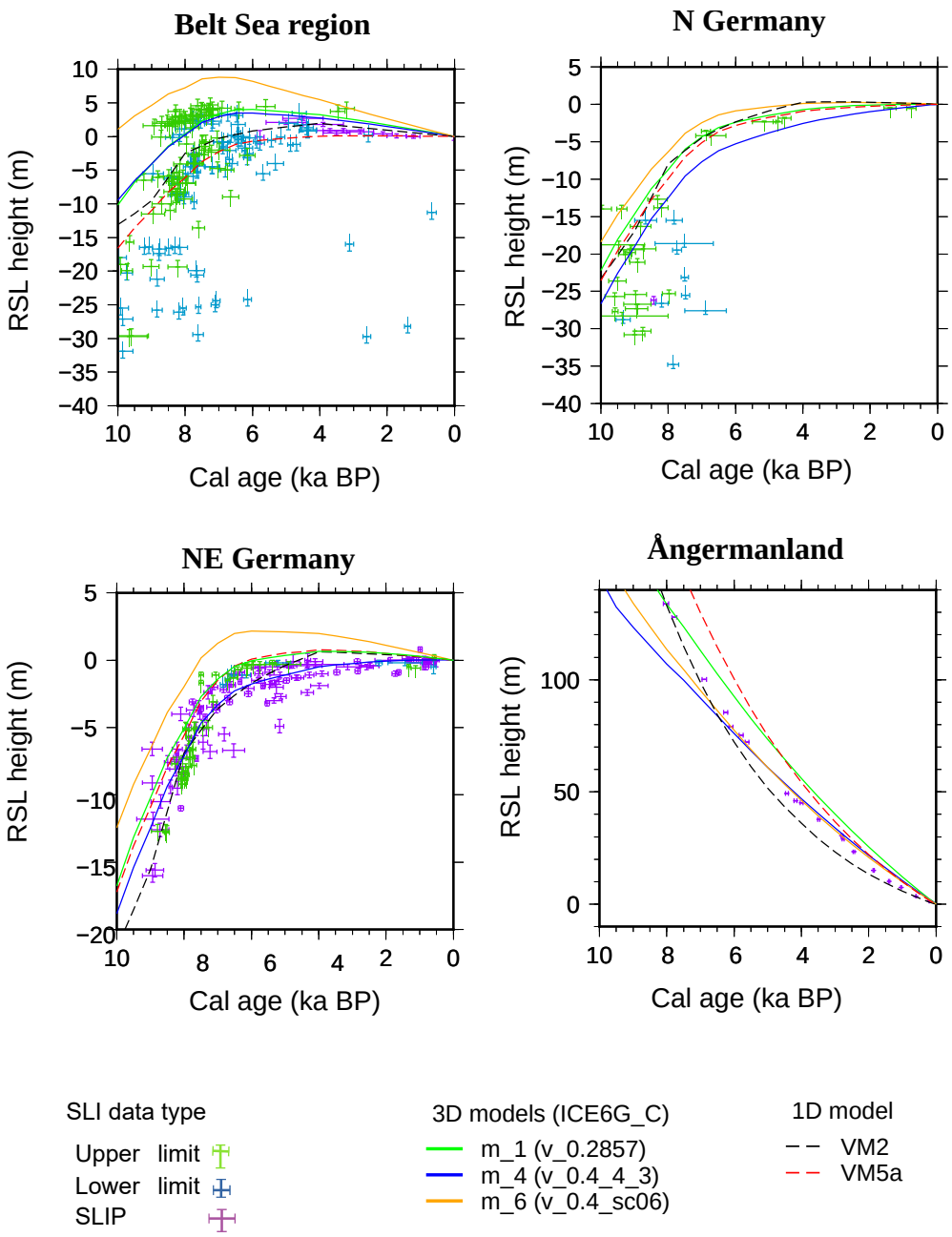

FIGURE 5.10: RSL predictions from three 3D models (ICE6G_C) and two 1D model. Black dashed line is VM2 and red dashed line presents VM5a (Peltier, 2004b; Peltier et al., 2015). The best fitting model for N and NE Germany is presented with the blue line. Green line is for the Belt Sea region, and orange line shows model for Ångermanland.

pers. comm.). In Ångermanland 3D model with the highest likelihood m_6 underestimates RSL until 4.5 ka BP, whereas 1D model member overestimates RSL from ca. 7 ka BP till

ca. 3 ka BP. The region near the centre of the former ice sheet has a high viscosity and thick lithosphere in the 3D model (Fig. 5.5 3)). However, a 1D model with the high viscous material and thinner lithosphere is resulting in the faster rebound than the 3D model. Thus, leading to the overestimation of the short-term deformation in the 1D model (Meike Bagge, 2020, pers. comm.).

If we observe application of one 1D ensemble member in the whole region, in Fig. 4.10 we see that all four 1D ensemble members presented in the plot show large deviations in RSL predictions between them. Differences are around 5 m for near field region (SW Fennoscandia) and 20-30 m in Ångermanland. The best fitting 1D model ensemble member for Ångermanland (m_100_121_121) is underestimating RSL in other three regions (orange line in Fig. 4.10) showing that one 1D model is not suitable for the whole region. Locally optimised 1D model appears sufficient for the modeling of small regions. However, the influence of lateral variations in viscosity on the GIA reconstructions is too significant to be ignored in the global GIA models and more extensive areas with complex tectonic structure.

5.2.3 3D models with ICE6G_C vs models with ICE5G glaciation history

Peltier et al. (2015) developed a deglaciation model called ICE6G_C which he states that it is a refined version of ICE5G (Peltier, 2004b). The difference between the new model and previous ICE5G is mainly in the data that was used to measure the vertical motion of the crust and more rigorously constrain ice sheets. In the case of the ICE6G_C model, the authors used GPS data to constrain ice thickness and the timing of ice loss in Antarctica (which depicts suffix C in the name of the model) (Peltier et al., 2015). As a result, ICE6G_C comprises different ice thickness in 62 locations in Antarctica and computes less ice loss in the Holocene in comparison to ICE5G, which means that the deglaciation history is well constrained for Antarctica in the ICE6G_C model. The previous model, ICE5G, was tuned to fit Barbados coral data, where it shows better performance than ICE6G_C (Peltier et al., 2015). GRACE and GPS (BIFROST) observations were used to check both models in the region of Northwestern Euroasia, and Peltier et al. (2015) states that ICE6G_C (VM5a) is providing a better fit to vertical motion than its successor ICE5G (VM2). However, Peltier compared model results with 12 locations of SLIs in Fennoscandia and found that the fit is weaker than with GPS and GRACE data and argued that is due to the complexity of RSL in this region governed by lake stages (Peltier et al., 2015).

Here we compare both deglaciation histories and keep viscosity structure the same to determine if the centre and near field regions are sensitive to these changes. Model VM5a is a model with radial viscosity profile with ICE6G_C deglaciation, that is basically a multilayer fit to its predecessor VM2 with deglaciation history ICE5G.

We consider ten 3D models that are based on one geodynamical model. Models are classified in three classes based on variations of the conversion from seismic velocities to the viscosity (Bagge et al., 2020). Differences between the viscosity structure of classes are producing variability in predicted RSL. Highest variability in RSL is shown in the region closest to the centre of the Fennoscandian ice sheet Ångermanland, $\sim$ 100 m (Figs. 5.9 and 5.15). While in the marginal area, SW Fennoscandia, variability is lower $\sim$ 10 m (Figs. 5.6 – 5.8, 5.11, 5.13 and 5.14). According to Bagge et al. (2020), the largest variability is expected in the regions covered by dominant ice sheets. In the region of SW Fennoscandia highest RSL is predicted by Class-III models and Class-I models with the highest reduction factor, $r = 0.75$ and $r = 1$. Faster rebound, and thus higher RSL is caused by the lower viscosity in the transition zone in Class-III models, and due to the fact that Class-I models with larger reduction factors produce a higher lateral variability (Meike Bagge, 2019, pers. comm.). In Ångermanland, Class-I models with the lowest reduction factors, m_1 and m_2 predict the highest RSL. These models have thinner lithosphere than other models in the central region, which causes faster rebound. Whereas in the near field region, same models are predicting lower RSL than other models.

We now analyse performance of ten 3D models with ICE5G glaciation history. After application of VAM and calculation of Bayes factors, we get that the model m_5 shows the best capability in the Belt Sea region, while now m_1 has the best performance in N and NE Germany, and in Ångermanland, Class-III model m_6 has the best performance. The Belt Sea region shows the requirement for higher viscosity in first 350 km of depth with ICE5G than with ICE6G_C deglaciation. In N and NE Germany, the glaciation history compensates the difference in the asthenosphere viscosity between m_1 and m_4. Alterations in the new glaciation history (ICE6G_C) did not affect the performance of m_6 model in Ångermanland which shows the best fit with both glaciation histories.
We present graphically the misfit between all models in each region (Figs. 5.11 – 5.15). In Figs. 5.11, 5.13 and 5.14, we can see that the models with higher reduction factors (m_9, m_10) and Class-III models (m_6, m_7) have the highest misfit in SW Fennoscandia. In Ångermanland the weakest fit is also presented by models with the highest reduction factors, but Class-III models are showing the best fit (Fig. 5.15). We present best-fitting models with ICE5G deglaciation histories and both 1D models of Peltier; VM2 and VM5a in Fig. 5.16. Here we see that, when we compare models with both glaciation histories, ICE6G_C is predicting slightly higher RSL in SW Fennoscandia, while in Ångermanland, most of the models are predicting lower RSL. Also, ICE6G_C is presenting a smoother sea-level rise in SW Fennoscandia around 8 ka BP, while with ICE5G we see a steeper transition. The difference in best-fitting models in SW Fennoscandia leads us to the conclusion that dependency on ice history increases away from glaciation centre. The Belt Sea region, or the region of

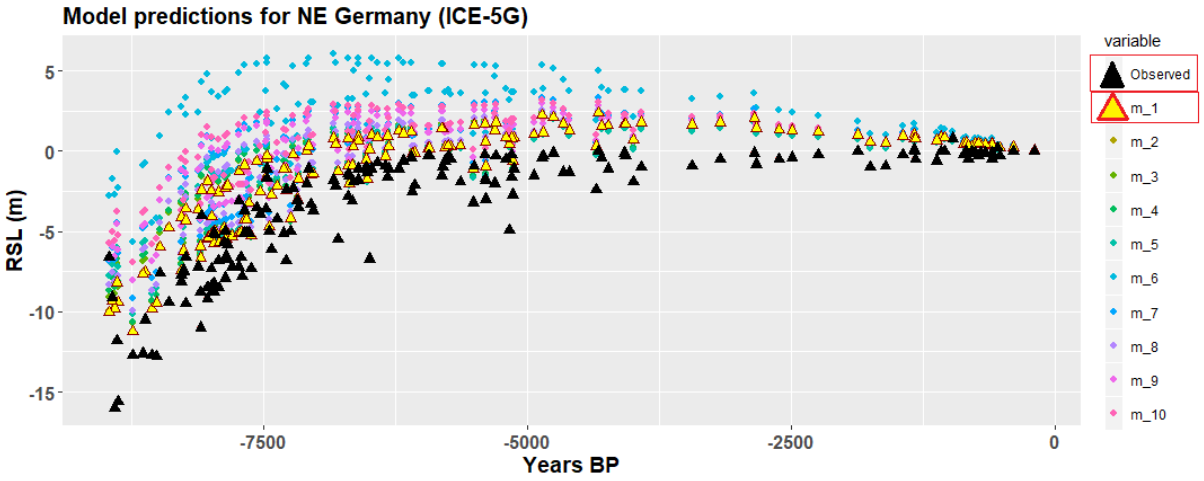

FIGURE 5.11: Ten models with 3D viscosity and ICE5G glaciation history in the region of NE Germany. Black triangles present observation values and yellow present the best-fitting model.

the tectonic boundary, proves to be sensitive to the viscosity structure and to depend on ice sheet history.

Finally, we apply equations 2.20 and 2.21 on all four models to get the highest likelihood of the model for the whole region. Results show that same four models are models with the highest likelihood as with the ICE6G_C glaciation history. Logarithmic Bayes factors of best models for the whole area are presented in Fig. 5.12. Models are ordered by the fit, and the model with K=0 has the highest likelihood. Misfits between 3D models with ICE5G

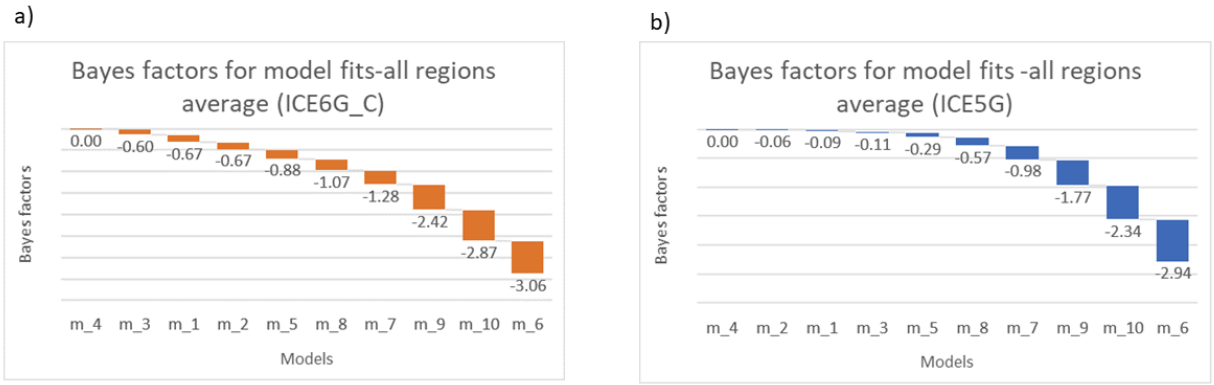

FIGURE 5.12: Logarithmic Bayes factors of model fits with both glaciation histories for the whole area. Vertical extent of each fit presents it's deviation from the 0 fit in comparison to all fits.

are slightly smaller (Fig. 5.12 b)) than misfits between models with ICE6G_C glaciation history (Fig. 5.12 a)), which indicates more considerable variability of RSL predicted with latter ones.

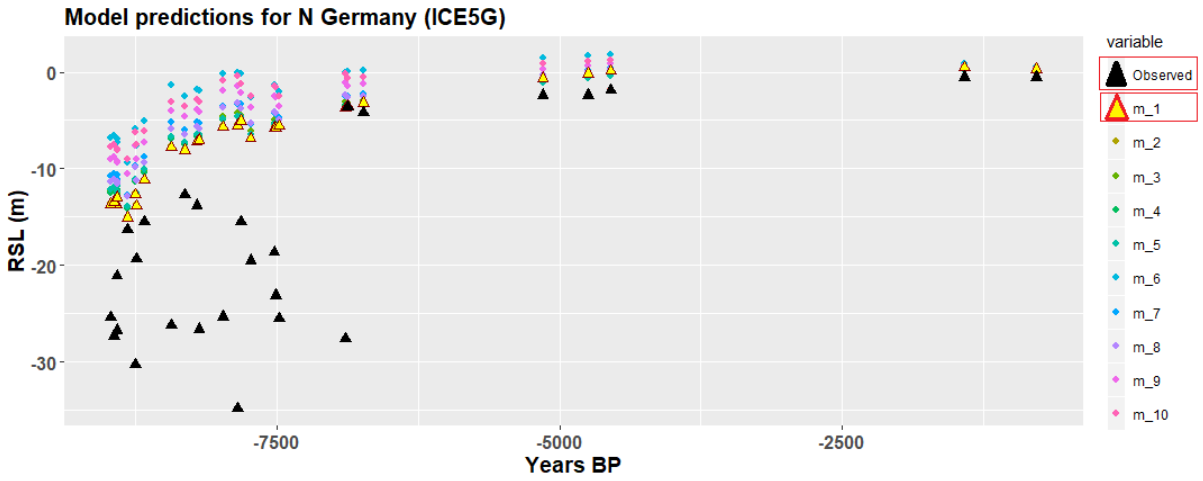

FIGURE 5.13: Ten models with 3D viscosity and ICE5G glaciation history in the region of N Germany. Black triangles present observation values and yellow present the best-fitting model.

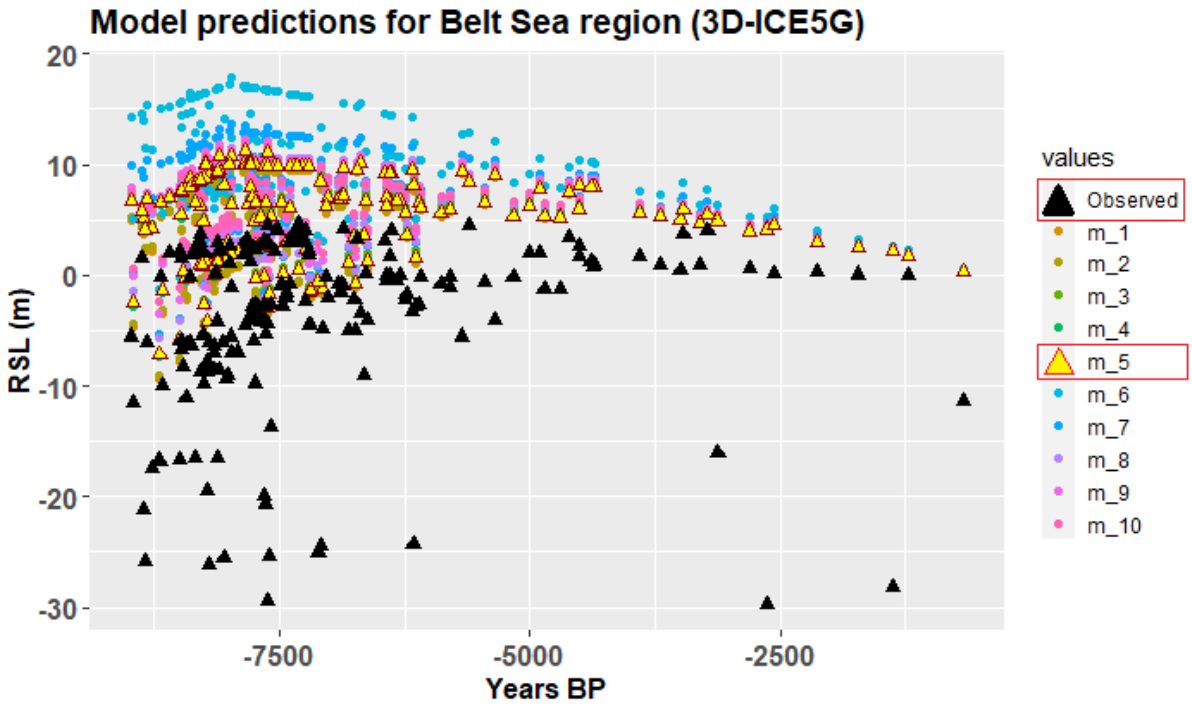

FIGURE 5.14: Ten models with 3D viscosity and ICE5G glaciation history in the Belt Sea region. Black triangles present observation values and yellow present the best-fitting model.

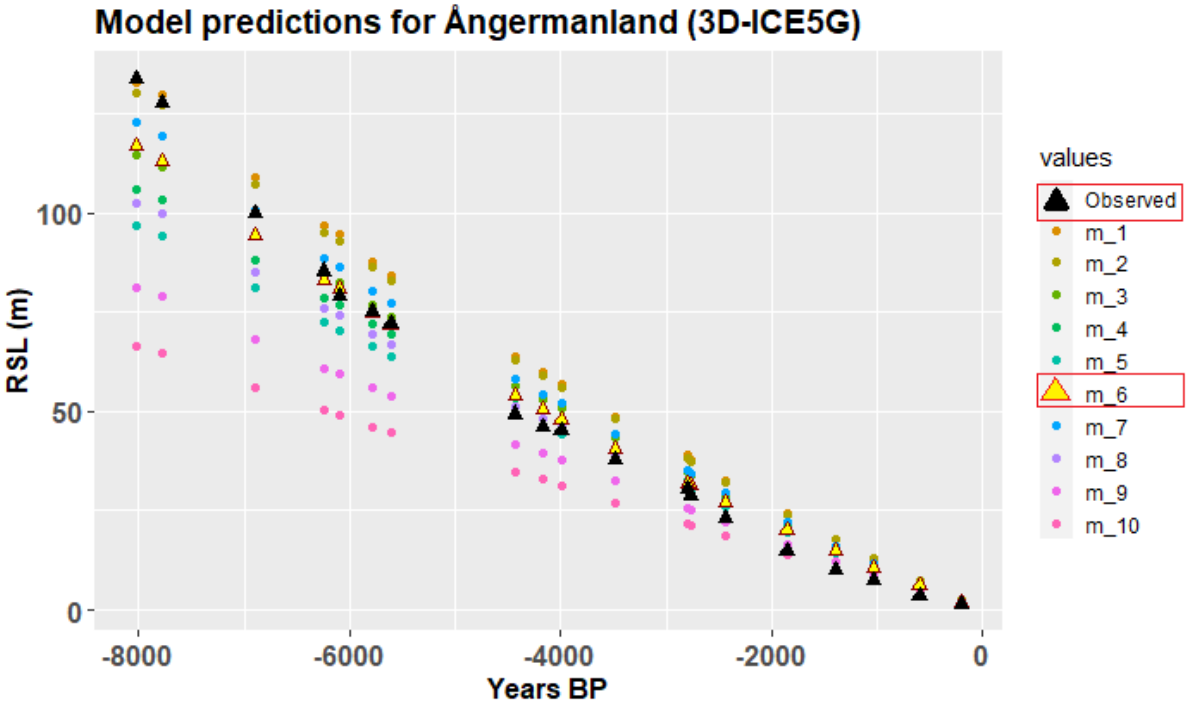

FIGURE 5.15: Ten models with 3D viscosity and ICE5G glaciation history in Ångermanland. Black triangles present observation values and yellow present the best-fitting model.

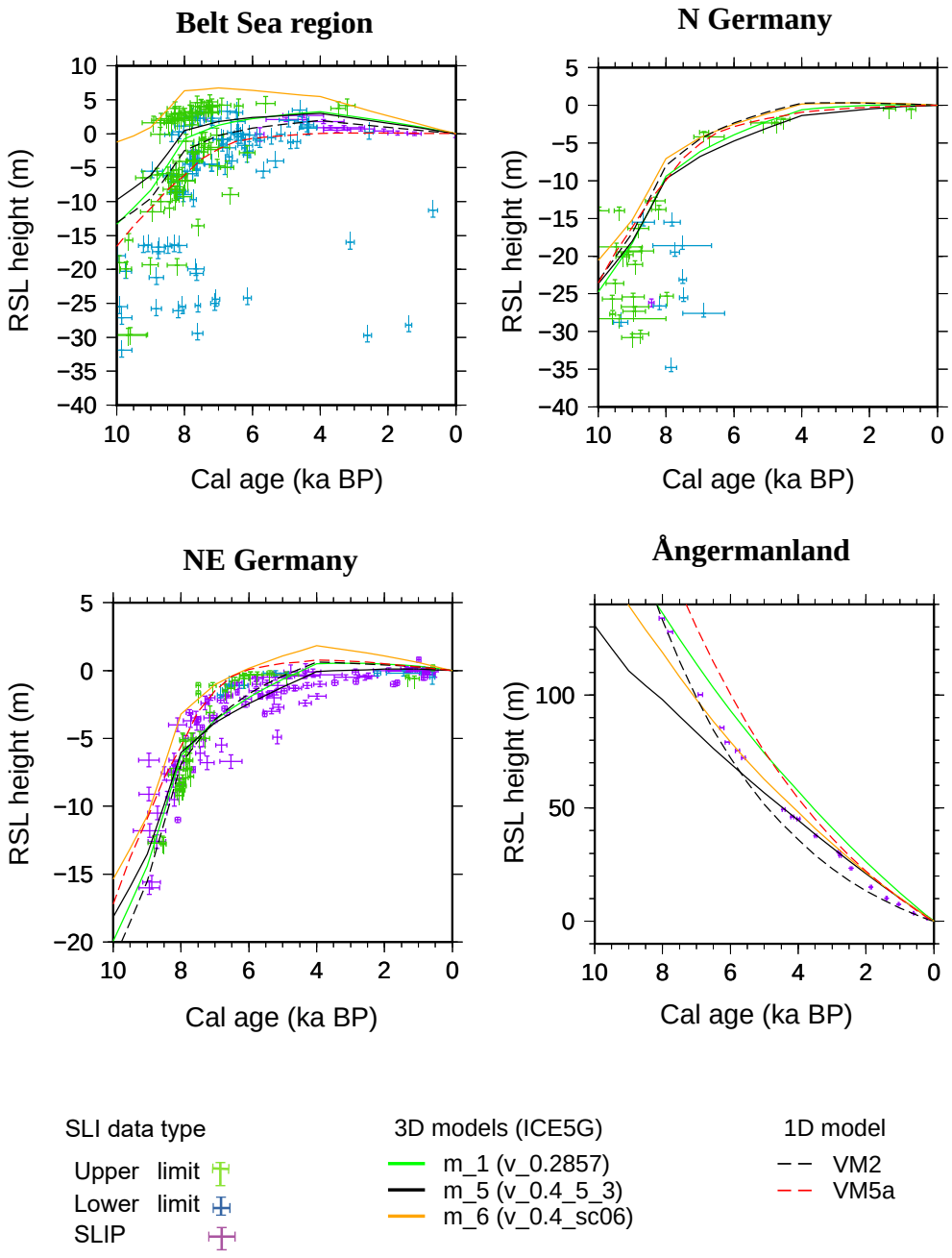

FIGURE 5.16: RSL predictions from three 3D models (ICE5G) and 1D models VM2 (black dashed line) and VM5a (red dashed line) from Peltier (2004b); Peltier et al. (2015). Best fitting model for N and NE Germany is presented with a blue line, black line for Belt Sea region and orange for Ångermanland.

5.3 Summary

Glacial isostatic adjustment models with lateral viscosity variations (3D) are fitted to the region of SW Fennoscandia and compared to models with radial viscosity variations (1D). Region of SW Fennoscandia is attractive for several reasons. It has a dynamical geomorphological evolution, and it has undergone through several lake and sea stages (Björck, 1995). Sea-level rise in this region was triggered due to final melting of the Laurentide ice sheet, and there is an ongoing adjustment process from the deglaciation of the Fennoscandian ice sheet and transition from Phanerozoic to Precambrian orogen (Kaufmann et al., 2000).
Relative sea-level predictions from 3D models and 1D models were validated against sea-level indicators by applying Validation Method (VAM). 1D GIA model ensemble contains 140 members that vary in lithosphere thickness, upper- and lower-mantle viscosity. Ten 3D models were derived from seismic tomography models with three different conversions. Results are summarized in the Table 5.2. Additionally, we compare lateral models with different ice histories. Special investigation is put on the region of plate boundaries, called the Trans Europian Suture Zone. Results from our study show that there is a lateral variation in this region in viscosity and that 3D models should be applied rather than models with radial varying viscosity. This conclusion is in accordance with the study of Whitehouse et al. (2006). It is argued in several studies that lithosphere thickness is around 200 km at

Table 5.2: List of best fitting models for each region.

Region	3D (ICE5G)	3D (ICE6G_C)	1D model (ICE6G_C)		
			Lithosphere thickness [km]	Upper-mantle [Pa s]	Lower-mantle [Pa s]
Belt Sea	v_0.4_5:3	v_0.2875	100	10^{21}	5×10^{22}
North Germany	v_0.2875	v_0.4_4:3	80	0.8×10^{21}	5×10^{22}
North East Germany	v_0.2875	v_0.4_4:3	80	0.5×10^{21}	2×10^{21}
Ångermanland	v_0.4_sc06	v_0.4_sc06	100	10^{21}	10^{21}

the center of Fennoscandia and that it is gradually decreasing outwards to 80 km in North Germany (Steffen and Wu, 2011; Kaufmann and Wu, 2002; Martinec and Wolf, 2005). In this study we came to the same conclusion with 3D models, while in 1D models we set a limit to the lithosphere thickness to be 120 km, however, we get thickness of 100 km to correspond to Ångermanland. Based on the overview of GIA studies in Fennoscandia from Steffen and Wu (2011), upper-mantle viscosity is between 10^{20} and 10^{21} Pa s, and viscosity is increasing while reaching lower viscosity by one order of magnitude, which coincides with the results from this study. Our results show that in the marginal areas, upper-mantle viscosity ($\sim 200 - 400$ km) yields lower values than in the area near centre of former glaciation, while

in the transition zone ($\sim 400 - 670$ km) is the opposite situation, marginal areas require higher values than in the area closer to the glaciation centre for one order of magnitude. The analysis in SW Fennoscandia and Ångermanland show that the consideration of lateral variations in viscosity structure is necessary to reconstruct the RSL. However, the 3D Earth can be approximated by a locally adapted 1D viscosity structure to reconstruct the regional RSL. From ten different 3D models applied to the selected region, we get different models to fit specific areas with ICE6G_C and ICE5G glaciation history. Finally, we conclude that the model that resulted with the highest likelihood for the whole region with both considered glaciation histories, can be adjusted to better fit requirements of the complex region.

6

Discussion and outlook

6.1 Discussion

This thesis introduces a new statistical method for rigorous interpretation of sea-level data for the purpose of validating GIA models. Chapters 2 and 3 present a new statistical method and provide a quantitative evaluation measure for each GIA model concerning different geological proxy records (RQ1). We applied a GIA reconstruction in the region of SW Fennoscandia in Chapters 4 and 5 to investigate if the radial viscosity structure is sufficient to reconstruct Holocene sea-level change, or if it is necessary to consider lateral viscosity structure (RQ2 and RQ3).

RQ1: How can different types of sea-level indicators be rigorously applied to constrain GIA model-based reconstructions?

This thesis proposes a novel statistical method (VAM) that considers comprehensive information from sea-level indicators (SLIs). The standard approach for validation of GIA models with geological data is application of the basic goodness of fit (e.g., Tushingham and Peltier, 1991; Steffen and Kaufmann, 2005; Whitehouse et al., 2012; Melini and Spada, 2019). Few studies went beyond this basic method and applied statistical reconstructions of the SLI's indicative meaning (e.g., Kopp et al., 2009; Khan et al., 2015; Vacchi et al., 2018). However, previous methods either do not distinguish between different SLI types or disregard those of

lower quality. Heterogeneous compilations of indicators demand a more sophisticated strategy: VAM, therefore, defines joint probabilities considering individual PDFs designed for specific indicative meanings, like marine or terrestrial limiting points and indicators found in the living position. VAM is comprised of well-known statistical tools that were used for the first time in the reconstruction of sea level (e.g. the two parameter gamma distribution) and of a combination of published methods (e.g., Hibbert et al., 2016; Caron et al., 2018). In this study, we re-investigate information regarding levelling and dating of each SLI and relate it to a specific probability distribution based on its properties. This augments the interpretation of the temporal and spatial resolution of each SLI to reconstruct past sea level statistically. Even though sampling and dating techniques are improving, there are still several aspects that are inducing uncertainties in the elevation and age estimates of sea-level points such as noise in the records and climate change (Shennan et al., 2015). In this context, the here developed approach is a significant advancement, as it allows for quantitative analysis and expression of these uncertainties.

Kopp et al. (2009) developed a method to construct the posterior distribution of sea level that is based on the multivariate Gaussian prior spatial and temporal distributions. In contrast, in this study, we do not use generalised distributions as priors. Khan et al. (2015) applied empirical hierarchical modelling with Gaussian process priors to show Holocene RSL variability. However, Khan et al. (2015) only considers SLIPs and exclude limiting points. Furthermore, temporal and spatial variabilities are represented by normal distributions (based on the study of Kopp et al. (2009)), while in our study, we use non-normal distributions that are more suitable to represent frequency distributions of geophysical variables such as waves and tides. Vacchi et al. (2018) used a similar approach to Kopp et al. (2009) and Khan et al. (2015), but also restricted it to SLIPs. We base our interpretation of indicators found in living position on the study of Hibbert et al. (2016). However, while Hibbert et al. (2016) based their sea-level reconstruction only on the habitat of corals, we expanded the approach to other types of indicators such as shells.

We adapted VAM to types of indicators found in two areas; Hudson Bay and Fennoscandia. This means that we also have to consider environmental characteristics of these specific areas in the definition of the respective distributions. As a result, VAM was able to provide a measure of fit for each GIA model in both regions of interest.

Uncertainties in the choice of a proper calibration curve can cause errors in calibrated ages of $\sim$ 400 yrs, and we, thus, excluded sites where identification of the calibration curve was not possible. Two regions where this is the case were presented: Arkona Basin and North Jylland with Kattegat, where lake stages affected the salinity of the area, producing uncertainties in the radiocarbon dating (Section 4.3.2 and Appendix D).

The here developed method is thus more rigorous than previous analyses in that it allows consideration of all types of SLIs, accounts for measurement uncertainties and produces

quantitative value for the fit of GIA models.

RQ2: To which degree does a radial viscosity structure fit to SLI based reconstructions of the former sea level in SW Fennoscandia?

In GIA modelling, the most common approach is to assume that Earth's viscosity profile has only radial variability (Whitehouse, 2018). However, an increasing number of studies have included more realistic 3D variations in mantle viscosity (e.g., Martinec, 2000; Kaufmann and Wu, 2002; Latychev et al., 2005; Klemann et al., 2008; van der Wal et al., 2015). Still, it remains a question if it is necessary to include such complexity in GIA models (Whitehouse, 2018).
We applied a model with a radial viscosity and 140 combinations of Earth structure parameters (Table A.1) to the region of SW Fennoscandia and Ångermanland - an area near the centre of the former ice sheet, to investigate the performance of the 1D GIA model. Ensemble members were validated against set of geological records from this region by applying VAM. The Belt Sea region lies between two branches of the Trans-European Suture zone; hence we expected variability in lithosphere thickness in this region. We identified different radial profiles to better fit the most southern part, N and NE Germany, and the Belt Sea region. Our results suggest that a lateral variation in a GIA model should be included in the area of SW Fennoscandia. However, the locally adapted 1D model is sufficient for smaller regions. Areas closer to the centre of the ice sheet require thicker lithosphere and less viscous lower-mantle than marginal areas. We got an averaged result for the whole area (SW Fennoscandia and Ångermanland) from the results of four selected regions with a lithospheric thickness of 80 km, an upper-mantle viscosity 5×10^{20} Pa s and a lower-mantle viscosity of 2×10^{21} Pa s. Similar viscosity values have been observed by Lambeck et al. (1998); Klemann and Wolf (2005); Martinec and Wolf (2005) and Lidberg et al. (2010). However, other studies found that the average lithosphere thickness in Fennoscandia is larger than 80 km (Davis et al., 1999; Kaufmann and Lambeck, 2002; Steffen and Kaufmann, 2005; Steffen et al., 2010).
Our results lead to the conclusion that 1D GIA models have a higher degree of fit when applied to each analysed region individually and the inferred viscosity structure differs between the respective regions. The inferred higher variability in the lower-mantle viscosity is consistent with Steffen and Wu (2011), who claim that the lower-mantle viscosity is poorly resolved probably due to the effect of lateral heterogeneity.
Application of VAM enabled us to determine which radial viscosity structure from 140 ensemble members has the highest likelihood in the region of SW Fennoscandia, and to identify the sensitivity of the tectonic structure to the viscosity profile.

RQ3: Is the GIA reconstruction for SW Fennoscandia compatible with geodynamic and tectonic constraints of the Earth structure?

SW Fennoscandia lies directly on the major lithospheric boundary and the longest lineament in Europe, the Trans-European Suture Zone (TESZ). Seismic studies suggest a gradient in the lithosphere structure beneath the TESZ (e.g., Guterch et al., 1999), which makes inferring viscosity structure for this region challenging. This motivated us to select the region of SW Fennoscandia as a region of interest to investigate the performance of GIA models regarding tectonic constraints of the Earth. Furthermore, the majority of previous studies deal with the tectonic structure of a whole region that was once covered with Fennoscandian ice sheet (Lambeck et al., 1998; Kaufmann et al., 2000; Whitehouse et al., 2006, e.g.), whereas we focused here specifically to the TESZ.

As mentioned previously, the Belt Sea region is located between two linear branches of the TESZ: The Sorgenfrei-Tornquist Zone (STZ) and the Teisseyre-Tornquist Zone (TTZ). Two other regions, N and NE Germany, are located south of the TESZ (Figs. 4.2 and 5.3). In the analysis with the 1D model, we confirmed that there is a difference in preferable viscosity profile between these regions (Table 5.2). We further analysed ten models with lateral variations in Earth rheology and two different ice histories. After applying VAM to determine misfit between models and sea-level data, results showed that between the branches of the TESZ, there is a variation in lithosphere thickness and in the asthenospheric viscosity in comparison to other parts of SW Fennoscandia. These results are consistent with several studies starting with Sabadini et al. (1986) who showed that lateral variation is more significant at the margins of ice sheet than in the centre of it. Kaufmann et al. (1997) and Wu et al. (1998a) showed that the output of GIA models is sensitive to lateral variations in the asthenosphere. Wu et al. (1998a) also found that lateral heterogeneity in the lower mantle should be incorporated in GIA models. However, 3D models analysed in this study are limited by the absence of lateral variation below 870 km in lower-mantle viscosity, and thus, cannot confirm the influence of the lateral heterogeneity below this depth on the predicted RSL. GIA models applied in this study are also restricted to fixed glaciation histories ICE5G and ICE6G_C (Peltier, 2004b; Peltier et al., 2015) that are derived from a specific viscosity structure. Keeping deglaciation fixed while changing viscosity can produce misfits, which can explain overestimation of predicted RSL by our 3D models (Whitehouse et al., 2012). But the fixed glaciation does not change the fact that the region of SW Fennoscandia is sensitive to the viscosity structure and from our results, although limited by the small number of 3D models, we hypothesize that GIA reconstructions should consider the tectonic constraints in dynamic regions like SW Fennoscandia and that a 3D approximation of the Earth structure should not be neglected.

6.2 Outlook and future research

This thesis presents a statistical method for validation of GIA models that goes beyond current standard procedure. It has the advantage that it considers a variety of sea-level data regarding their quality, and it provides a rigorous process on how to treat uncertainties in age and elevation. Future work on the development of the method should include expansion of tailored probability density functions on different types of RSL data. Furthermore, application of the method would be significantly enhanced with the automatic classification of the data based on PDFs, which would lead to a more automated process. Specifically, the analysis of GIA models in the region of SW Fennoscandia can also benefit from extending the statistical method to include other data such as the extensive GPS network in this region, BIFROST (Johansson et al., 2002) and gravimetry measurements from the GRACE and GRACE-FO satellites, because these data sets can provide additional constraints for the determination of deep mantle viscosity (Wahr and Davis, 2013).

Future work regarding GIA reconstruction in SW Fennoscandia should include lateral variability of the viscosity structure. 3D models need be modified in order to find a single 3D distribution able to fit data from SW Fennoscandia and the central region at the same time. To this end, the parameter space will need to be extended to include lateral variability in the lower-mantle viscosity, and the tectonic boundary (the Belt Sea region) requires steeper changes in the asthenosphere and upper-mantle viscosity.

In this study we did not consider variations in the glaciation history: testing several ice-history models while changing the viscosity structure in the GIA model (e.g., Gowan et al., 2016; Vestøl et al., 2019) would improve constraint on rheological properties of Earth's mantle in the model. There are several regional ice models with Fennoscandian ice-sheet history such as Naslünd (SKB, 2006) and FBKS8 (Lambeck et al., 1998). These models were constrained with the data from this region, meaning that they are more consistent with the glaciological data for the local ice retreat than global models, and their application could be beneficial for the future investigation of GIA in this region.

A

List of ensemble members of 1D model

Table with detailed list of all 140 ensemble members of 1D model used in Chapters 3 and 4. First column in this table presents names of members that are used in figs. 4.5, 4.6, 4.7 and 4.8. Other three columns are depicting values for lithosphere thickness, upper-mantle and lower-mantle viscosity.

Table A.1: Ensemble members of 1D model

Model	Upper-mantle [Pa s]	Lower-mantle [Pa s]
Lithosphere thickness= 60 km		
m_1	10^{20}	10^{21}
m_2	10^{20}	10^{22}
m_3	10^{20}	2×10^{21}
m_4	10^{20}	2×10^{22}
m_5	10^{20}	5×10^{21}
m_6	10^{20}	5×10^{22}
m_7	10^{20}	8×10^{21}
m_8	10^{21}	10^{21}
m_9	10^{21}	10^{22}
m_10	10^{21}	2×10^{21}
m_11	10^{21}	2×10^{22}

Model	Upper-mantle [Pa s]	Lower-mantle [Pa s]
m_12	10^{21}	5×10^{21}
m_13	10^{21}	5×10^{22}
m_14	10^{21}	8×10^{21}
m_15	2×10^{20}	10^{21}
m_16	2×10^{20}	10^{22}
m_17	2×10^{20}	2×10^{21}
m_18	2×10^{20}	2×10^{22}
m_19	2×10^{20}	5×10^{21}
m_20	2×10^{20}	5×10^{22}
m_21	2×10^{20}	8×10^{21}
m_22	5×10^{20}	10^{21}
m_23	5×10^{20}	10^{22}
m_24	5×10^{20}	2×10^{21}
m_25	5×10^{20}	2×10^{22}
m_26	5×10^{20}	5×10^{21}
m_27	5×10^{20}	5×10^{22}
m_28	5×10^{20}	8×10^{21}
m_29	8×10^{20}	10^{21}
m_30	8×10^{20}	10^{22}
m_31	8×10^{20}	2×10^{21}
m_32	8×10^{20}	2×10^{22}
m_33	8×10^{20}	5×10^{21}
m_34	8×10^{20}	5×10^{22}
m_35	8×10^{20}	8×10^{21}
Lithosphere thickness= 80 km		
m_36	10^{20}	10^{21}
m_37	10^{20}	10^{22}
m_38	10^{20}	2×10^{21}
m_39	10^{20}	2×10^{22}
m_40	10^{20}	5×10^{21}
m_41	10^{20}	5×10^{22}
m_42	10^{20}	8×10^{21}
m_43	10^{21}	10^{21}
m_44	10^{21}	10^{22}
m_45	10^{21}	2×10^{21}
m_46	10^{21}	2×10^{22}
m_47	10^{21}	5×10^{21}

Model	Upper-mantle [Pa s]	Lower-mantle [Pa s]
m_48	10^{21}	5×10^{22}
m_49	10^{21}	8×10^{21}
m_50	2×10^{20}	10^{21}
m_51	2×10^{20}	10^{22}
m_52	2×10^{20}	2×10^{21}
m_53	2×10^{20}	2×10^{22}
m_54	2×10^{20}	5×10^{21}
m_55	2×10^{20}	5×10^{22}
m_56	2×10^{20}	8×10^{21}
m_57	5×10^{20}	10^{21}
m_58	5×10^{20}	10^{22}
m_59	5×10^{20}	2×10^{21}
m_60	5×10^{20}	2×10^{22}
m_61	5×10^{20}	5×10^{21}
m_62	5×10^{20}	5×10^{22}
m_63	5×10^{20}	8×10^{21}
m_64	8×10^{20}	10^{21}
m_65	8×10^{20}	10^{22}
m_66	8×10^{20}	2×10^{21}
m_67	8×10^{20}	2×10^{22}
m_68	8×10^{20}	5×10^{21}
m_69	8×10^{20}	5×10^{22}
m_70	8×10^{20}	8×10^{21}
Lithosphere thickness= 100 km		
m_71	10^{20}	10^{21}
m_72	10^{20}	10^{22}
m_73	10^{20}	2×10^{21}
m_74	10^{20}	2×10^{22}
m_75	10^{20}	5×10^{21}
m_76	10^{20}	5×10^{22}
m_77	10^{20}	8×10^{21}
m_78	10^{21}	10^{21}
m_79	10^{21}	10^{22}
m_80	10^{21}	2×10^{21}
m_81	10^{21}	2×10^{22}
m_82	10^{21}	5×10^{21}
m_83	10^{21}	5×10^{22}

Model	Upper-mantle [Pa s]	Lower-mantle [Pa s]
m_84	10^{21}	8×10^{21}
m_85	2×10^{20}	10^{21}
m_86	2×10^{20}	10^{22}
m_87	2×10^{20}	2×10^{21}
m_88	2×10^{20}	2×10^{22}
m_89	2×10^{20}	5×10^{21}
m_90	2×10^{20}	5×10^{22}
m_91	2×10^{20}	8×10^{21}
m_92	5×10^{20}	10^{21}
m_93	5×10^{20}	10^{22}
m_94	5×10^{20}	2×10^{21}
m_95	5×10^{20}	2×10^{22}
m_96	5×10^{20}	5×10^{21}
m_97	5×10^{20}	5×10^{22}
m_98	5×10^{20}	8×10^{21}
m_99	8×10^{20}	10^{21}
m_100	8×10^{20}	10^{22}
m_101	8×10^{20}	2×10^{21}
m_102	8×10^{20}	2×10^{22}
m_103	8×10^{20}	5×10^{21}
m_104	8×10^{20}	5×10^{22}
m_105	8×10^{20}	8×10^{21}
LITHOSPHERE THICKNESS= 120 KM		
m_106	10^{20}	10^{21}
m_107	10^{20}	10^{22}
m_108	10^{20}	2×10^{21}
m_109	10^{20}	2×10^{22}
m_110	10^{20}	5×10^{21}
m_111	10^{20}	5×10^{22}
m_112	10^{20}	8×10^{21}
m_113	10^{21}	10^{21}
m_114	10^{21}	10^{22}
m_115	10^{21}	2×10^{21}
m_116	10^{21}	2×10^{22}
m_117	10^{21}	5×10^{21}
m_118	10^{21}	5×10^{22}
m_119	10^{21}	8×10^{21}

Model	Upper-mantle [Pa s]	Lower-mantle [Pa s]
m_120	2×10^{20}	10^{21}
m_121	2×10^{20}	10^{22}
m_122	2×10^{20}	2×10^{21}
m_123	2×10^{20}	2×10^{22}
m_124	2×10^{20}	5×10^{21}
m_125	2×10^{20}	5×10^{22}
m_126	2×10^{20}	8×10^{21}
m_127	5×10^{20}	10^{21}
m_128	5×10^{20}	10^{22}
m_129	5×10^{20}	2×10^{21}
m_130	5×10^{20}	2×10^{22}
m_131	5×10^{20}	5×10^{21}
m_132	5×10^{20}	5×10^{22}
m_133	5×10^{20}	8×10^{21}
m_134	8×10^{20}	10^{21}
m_135	8×10^{20}	10^{22}
m_136	8×10^{20}	2×10^{21}
m_137	8×10^{20}	2×10^{22}
m_138	8×10^{20}	5×10^{21}
m_139	8×10^{20}	5×10^{22}
m_140	8×10^{20}	8×10^{21}

B

Data used in Chapter 3

The list of indicators is provided in the NRCAN database of sea-level indicators compiled by Art Dyke. Its content is stored in a relational database system at GFZ Potsdam. The ^{14}C ages were re-calibrated using OxCal, where for most datings a correction for δ^{13}C and reservoir effect was applied. In addition to the range and median given here, also the probability distribution of each individual dating was extracted. The tables present only the information relevant for the current study, whereas in the database 23 attributes are given for each indicator. IDs marked with a dagger (in Table 1) are excluded due to deposit feeding. IDs marked with an asterisk (in Tables 2 and 3) note samples interpreted as *in situ* in the original publication. Samples, for which no reference is given, could not be retrieved from literature provided in the database and, so, have to be interpreted as unpublished.

Table B.1: List of considered shells of species Macoma balthica, Ids with a dagger are excluded due to deposit feeding:

Id	Location [°E/°N]	Lab-code	^{14}C age [a BP]	Elev. [m]	cal. age [a BP] min.	cal. age [a BP] med.	cal. age [a BP] max.	Reference
Curve: Eastmain - Fort Rupert, QC								
5079†	−79.25/51.5667	GSC-3121	1660 ± 200	0.3	1182	1592	2054	
5080†	−78.5167/52.2	GSC-3415	70 ± 100	-0.5	0	133	288	
Curve: Nottaway & Harricana Rivers, QC								
5097†	−79.283/50.767	GSC-1492	4770 ± 140	60	5053	5490	5886	Skinner (1973)

Id	Location [°E/°N]	Lab-code	^{14}C age [a BP]	Elev. [m]	cal. age [a BP] min.	med.	max.	Reference
		Curve: Mattagami, ON						
5110†	−80.575/50.558	GSC-1396	4830 ± 130	51	5308	5556	5894	
		Curve: Churchill, MB						
5154	−94.143/59.7517	GSC-4507	2380 ± 100	7	2158	2460	2737	Dredge and Nixon (1992)

TABLE B.2: List of considered shells of species Portlandia arctica, Ids with asterisk denote samples interpreted as *in situ* in the original publication:

Id	Location [°E/°N]	Lab-code	^{14}C age [a BP]	Elev. [m]	cal. age [a BP] min.	med.	max.	Reference
	CURVE: DECEPTION BAY, QC							
4720	−74.275/62.12	AA-14686	8315 ± 65	52	9126	9326	9474	Bruneau and Gray (1997)
4721	−74.275/62.12	AA-17260	8385 ± 80	52	9140	9390	9533	Bruneau and Gray (1997)
4722	−74.275/62.12	AA-17261	8645 ± 80	52	9495	9632	9888	Bruneau and Gray (1997)
4723	−74.275/62.12	AA-17262	9485 ± 170	52	10297	10794	11210	Bruneau and Gray (1997)
4724	−74.275/62.12	AA-17263	11010 ± 130	58	12700	12892	13099	Bruneau and Gray (1997)
4725	−74.0117/62.308	AA-7561	8815 ± 80	107	9609	9874	10170	Gray et al. (1993); Bruneau and Gray (1997)
4726	−74.275/62.12	AA-7562	10725 ± 100	52	12424	12654	12798	Gray et al. (1993); Bruneau and Gray (1997)
4727	−74.275/62.12	AA-8393	8925 ± 100	58	9694	10014	10244	Bruneau and Gray (1997)
4728	−74.275/62.12	AA-8394	8475 ± 110	58	9138	9467	9694	Bruneau and Gray (1997)
4729	−74.275/62.12	AA-8395	8595 ± 120	58	9308	9612	10124	Bruneau and Gray (1997)
4730*	−74.267/62.117	Beta-11121	9400 ± 220	52	10170	10680	11254	Bruneau and Gray (1997); Gray and Lauriol (1985)
4738*	−74.267/62.117	Beta-13861	9610 ± 140	58	10562	10938	11261	Gray and Lauriol (1985); Bruneau and Gray (1997)
4756*	−74.2/62.2167	Beta-19853	9290 ± 180	114	10158	10519	11159	Gray and Lauriol (1985); Bruneau and Gray (1997)
4760*	−74.267/62.117	Beta-29085	9535 ± 90	58	10588	10880	11164	Bruneau and Gray (1997)
4764*	−74.267/62.117	GSC-4335	8510 ± 230	58	9008	9524	10182	Bruneau and Gray (1997)

Id	Location [°E/°N]	Lab-code	^{14}C age [a BP]	Elev. [m]	cal. age [a BP] min.	med.	max.	Reference
4783*	−74.05/62.3167	TO-1274	8800 ± 70	107	9600	9844	10156	Bruneau and Gray (1991, 1997)
4784	−73.8/62.4167	TO-1275	8690 ± 70	100	9535	9664	9900	Bruneau and Gray (1991, 1997)
4785*	−74.2667/62.1167	TO-1397	9000 ± 60	58	9916	10172	10250	Bruneau and Gray (1991, 1997)
	Curve: Douglas Harbour, QC							
4848	−73.05/62.15	TO-1738	8060 ± 70	91	8648	8944	9234	Gray et al. (1993)

TABLE B.3: List of considered shells of species Mytilus edulis, Ids with asterisk denote samples interpreted as *in situ*:

Id	Location [°E/°N]	Lab-code	^{14}C age [a BP]	Elev. [m]	cal. age [a BP] min.	med.	max.	Reference
	CURVE: UNGAVA BAY W, QC							
4574	−70.0833/59.25	Gx-4738	6755 ± 180	87	7320	7628	7953	
4589*	−70.0833/59.25	Gx-5308	6920 ± 205	85	7434	7775	8162	Gray et al. (1980)
	CURVE: DECEPTION BAY, QC							
4758	−74.5/62.1	Beta-19855	3710 ± 100	1.7	3830	4063	4408	
4763	−74.2667/62.1333	GSC-4319	6800 ± 80	60	7508	7647	7824	
	CURVE: UNGAVA PENINSULA NW, QC							
4818	−77.25/61.5961	GSC-5312	6110 ± 80	73	6758	6994	7238	
4819	−78.0903/62.5772	GSC-5322	2770 ± 50	22	2762	2867	2978	
4820	−77.8381/61.7294	GSC-5344	3740 ± 80	36	3888	4102	4404	
4822	−78.1156/62.1817	GSC-5399	3580 ± 70	32	3694	3882	4084	
	CURVE: OTTAWA ISLANDS, NU							
4864	−79.8233/59.2833	GSC-1024	6450 ± 140	33	7018	7357	7592	Andrews and Falconer (1969)
	CURVE: C SMITH-POVUNGNITUK, QC							
4896	−77.2667/60.2167	Gif-1818	3400 ± 80	35	3454	3654	3846	
4898	−77.325/60.0583	GSC-1588	3380 ± 130	35	3358	3638	3976	
	CURVE: INUKJUAK, QC							
4926	−78.5/58.25	UQ-955	4800 ± 100	3	5312	5520	5734	
	CURVE: LAC GUILLAUME-DELISLE, QC							
4930	−76.5/56.2667	GSC-1261	6430 ± 150	172	6996	7337	7590	Walcott (1972a); Hillaire-Marcel (1976)
4931	−76.5/56.2833	GSC-1287	6000 ± 160	137	6492	6860	7251	Walcott (1972a); Hillaire-Marcel (1976)
4933	−76.4833/56.2833	GSC-1328	6390 ± 180	77	6883	7289	7614	Walcott (1972a); Hillaire-Marcel (1976)
4934	−76.5/56.45	GSC-1364	6230 ± 220	154	6644	7106	7566	Walcott (1972a)

Id	Location [°E/°N]	Lab-code	^{14}C age [a BP]	Elev. [m]	cal. age [a BP] min.	med.	max.	Reference
	Curve: Poste-de-la-Baleine, QC							
4972	−77.3167/55.58	GSC-2070	3360 ± 60	58	3450	3600	3819	Hillaire-Marcel (1976); Walcott and Craig (1975)
4973	−77.3083/55.575	GSC-2074	1790 ± 60	22	1565	1714	1864	Hillaire-Marcel (1976); Walcott and Craig (1975)
4974	−77.3017/55.5783	GSC-2129	2030 ± 60	29	1867	1991	2146	Walcott and Craig (1975)
4975	−77.3033/55.58	GSC-2348	2760 ± 80	44	2746	2872	3068	Walcott and Craig (1975)
4984	−77.3333/55.6667	Qu-1064	890 ± 100	13.31	662	816	980	Allard and Tremblay (1983)
4988	−77.6333/55.3667	Qu-1068	490 ± 80	8.89	318	522	655	Allard and Tremblay (1983)
4989	−77.6333/55.3667	Qu-1081	580 ± 70	13.21	512	593	666	Allard and Tremblay (1983)
4995	−77.4833/55.4833	Qu-1087	1680 ± 390	21.43	832	1661	2698	Allard and Tremblay (1983)
5005	−77.6333/55.3667	Qu-1097	2470 ± 100	31.71	2340	2549	2754	Allard and Tremblay (1983)
5006	−77.6333/55.3667	Qu-1098	2230 ± 100	29.94	1950	2226	2674	Allard and Tremblay (1983)
5007	−77.6333/55.3667	Qu-1099	2430 ± 100	28.91	2214	2516	2750	Allard and Tremblay (1983)
5008	−77.6333/55.3667	Qu-1100	2026 ± 100	27.26	1737	1996	2306	Allard and Tremblay (1983)
5009	−77.6333/55.3667	Qu-1101	2260 ± 100	26.57	1994	2256	2694	Allard and Tremblay (1983)
5010	−77.6333/55.3667	Qu-1102	2020 ± 100	23.69	1730	1988	2304	Allard and Tremblay (1983)
5011	−77.6333/55.3667	Qu-1103	2050 ± 100	21.94	1818	2026	2310	Allard and Tremblay (1983)
5012	−77.6333/55.3667	Qu-1104	1760 ± 90	20.38	1419	1680	1890	Allard and Tremblay (1983)
5013	−77.6333/55.3667	Qu-1105	1680 ± 90	18.8	1396	1590	1816	Allard and Tremblay (1983)

Id	Location [°E/°N]	Lab-code	^{14}C age [a BP]	Elev. [m]	cal. age [a BP] min.	med.	max.	Reference
5014	−77.6333/55.3667	Qu-1106	1490 ± 90	17.26	1264	1398	1594	Allard and Tremblay (1983)
5029	−77.25/55.75	Qu-1288	2860 ± 100	34.25	2764	2998	3316	Allard and Tremblay (1983)
5031	−77.25/55.75	Qu-1290	3480 ± 100	52.3	3480	3756	4066	Allard and Tremblay (1983)
5036	−77.25/55.75	Qu-1295	2410 ± 90	31.5	2213	2494	2742	Allard and Tremblay (1983)
5037	−77.25/55.75	Qu-1296	2510 ± 80	32	2364	2576	2748	Allard and Tremblay (1983)
5039	−77.25/55.75	Qu-1298	670 ± 80	4.4	524	628	735	Allard and Tremblay (1983)
	Curve: Fort George, QC							
5050	−77.6719/53.5511	GSC-1959	6500 ± 90	178	7264	7408	7566	Vincent (1977)
	Curve: Mattagami, ON							
5115	−82.35/50.1917	GSC-1499	6620 ± 240	100	7004	7504	7956	Skinner (1973)
	Curve: C Henrietta Maria, ON							
5127	−82.6/54.8333	I-3909	2310 ± 200	40.6	1872	2353	2792	Webber et al. (1970)
5130	−82.3/54.8667	I-3983	1430 ± 190	22.6	954	1352	1804	Webber et al. (1970)
	Curve: Severn River, ON							
5139	−86.85/55.4167	GSC-1561	5940 ± 140	88	6466	6782	7160	
5140	−86.9433/55.65	GSC-1567	3270 ± 190	40	2998	3510	3984	
	Curve: Churchill, MB							
5150	−94.0806/58.7417	GSC-261	3040 ± 130	23	2876	3219	3555	Dredge and Nixon (1992)
5153	−94.9667/58.8917	GSC-3851	4000 ± 90	30	4183	4482	4820	Dredge and Nixon (1992)
5155	−93.8408/58.7458	GSC-682	1240 ± 130	10.5	920	1152	1398	Craig (1969); Dredge and Nixon (1992)
5156	−93.8431/58.7028	GSC-683	2320 ± 130	27	2055	2366	2735	Craig (1969); Dredge and Nixon (1992)

Id	Location [°E/°N]	Lab-code	^{14}C age [a BP]	Elev. [m]	cal. age [a BP] min.	med.	max.	Reference
5157	−93.95/58.7597	GSC-684	1020 ± 140	6.5	688	944	1254	Craig (1969); Dredge and Nixon (1992)
5158	−93.8111/58.6189	GSC-685	3180 ± 140	38.5	3002	3396	3810	Dredge and Nixon (1992)
5159	−93.9806/58.7569	GSC-723	2120 ± 130	22	1740	2108	2420	Craig (1969); Dredge and Nixon (1992)
5163	−94.275/59.75	Gx-1065	3190 ± 80	38	3212	3414	3592	Dredge and Nixon (1992)
	Curve: Nelson River, MB							
5186	−92.75/56.25	GSC-1955	6610 ± 110	75	7310	7502	7674	Lowdon et al. (1977); Dredge and Nixon (1992); Klassen (1986)

TABLE B.4: List of considered shells of species Hiatella arctica:

Id	Location [°E/°N]	Lab-code	^{14}C age [a BP]	Elev. [m]	cal. age [a BP] min.	med.	max.	Reference
	CURVE: UNGAVA BAY W, QC							
4570	−69.9833/58.65	DIC-1516	4770 ± 60	23	5324	5504	5602	
	CURVE: AKPATOK ISLAND, NU							
4603	−67.85/60.5	Beta-34755	7240 ± 100	0	7866	8070	8312	
4604	−67.85/60.5	Beta-34754	6860 ± 100	32	7565	7709	7931	
4605	−67.85/60.5	Beta-34753	6790 ± 90	3	7490	7642	7826	
4606	−67.85/60.5	Beta-34756	6470 ± 110	48	7174	7378	7570	
	DIANA ISLAND, QC/NU							
4642	−69.925/61.0333	I-9246	7220 ± 115	52	7834	8050	8320	Gray et al. (1993, 1980); Gray and Lauriol (1985)
	CURVE: GEORGE RIVER, QC							
4698	−65.975/58.7	UL-263	6020 ± 230	24	6404	6885	7416	Allard et al. (1989)
	CURVE: DECEPTION BAY, QC							
4737	−74.2667/62.1167	Beta-13860	6980 ± 110	97	7616	7812	7999	Lauriol and Gray (1987)
4739	−74.2667/62.1167	Beta-19004	5910 ± 120	11	6439	6741	7152	
4774	−73.7/62.4333	I-2444	6580 ± 125	45	7264	7477	7670	
4776	−74.75/62.15	N-283	6980 ± 150	84	7570	7816	8155	Matthews (1967)
	CURVE: CAPE WEGGS, QC							
4789	−72.9/62.8333	I-2444	6580 ± 125	44	7264	7477	7670	
	CURVE: SUGLUK, QC							
4791	−75.6333/62.2167	Beta-11127	6990 ± 130	95	7580	7822	8044	
4801	−77.75/62.45	Gx-12035	6920 ± 100	28	7591	7762	7939	
4803	−76.3833/62.3667	Gx-12037	7275 ± 190	85	7706	8103	8424	
4806	−75.7/62.2333	I-729	7650 ± 250	111	7968	8500	9120	Matthews (1966)

Id	Location [°E/°N]	Lab-code	^{14}C age [a BP]	Elev. [m]	cal. age [a BP] min.	med.	max.	Reference
4807	−76.05/62.7667	L-702A	7050 ± 150	111	7614	7876	8170	Matthews (1967); Lauriol and Gray (1987)
	Curve: Ungava Peninsula NW, QC							
4817	−77.8792/62.1403	GSC-5310	7400 ± 110	98	8008	8220	8401	
4821	−77.0739/61.8706	GSC-5353	6790 ± 80	67	7500	7639	7818	
	Curve: Charles Island, NU							
4828	−74.1833/62.6333	GSC-4756	7030 ± 100	60	7666	7854	8024	
	Curve: Douglas Harbour, QC							
4841	−73.1833/62.0667	GSC-5165	5520 ± 100	13	6010	6320	6532	
4842	−72.9833/62.1667	GSC-5178	4500 ± 100	11	4859	5144	5449	
	Curve: Southampton I, NU							
4889	−83.1833/64.1833	S-12	3670 ± 270	32	3397	4040	4820	
	Curve: C Smith-Povungnituk, QC							
4899	−78.4639/60.75	GSC-4332	6850 ± 110	86	7512	7702	7932	Lauriol and Gray (1987); Gray et al. (1993)
4905	−76.7667/60.05	UQ-830	3100 ± 80	30	3073	3298	3478	
4910	−78.4167/60.75	UQ-956	8700 ± 140	30	9490	9754	10166	Gray and Lauriol (1985)
4911	−78.4167/60.75	UQ-957	6000 ± 100	35	6639	6850	7158	
	Curve: Inukjuak, QC							
4924	−78.5/58.25	UQ-1757	2000 ± 150	25	1618	1969	2332	
4925	−78.5/58.25	UQ-813	4270 ± 100	73	4524	4834	5272	
	Curve: Lac Guillaume-Delisle, QC							
4929	−76.5/56.2667	GSC-1238	6720 ± 150	175	7324	7592	7922	Walcott (1972a); Hillaire-Marcel (1976)
4932	−76.4333/56.35	GSC-1326	4070 ± 140	24	4150	4577	4954	Walcott (1972a); Hillaire-Marcel (1976)
4935	−76.4167/56.45	GSC-1725	6000 ± 210	153	6400	6862	7408	Walcott (1972a)
4938	−76.7/55.95	GSC-595	6420 ± 240	54	6750	7303	7746	Hillaire-Marcel (1976)

Id	Location [°E/°N]	Lab-code	^{14}C age [a BP]	Elev. [m]	cal. age [a BP] min.	med.	max.	Reference
	Curve: Fort George, QC							
5051	−77.5/53.5833	GSC-2239	7290 ± 90	175	7957	8108	8317	Hardy (1977)
5053	−77.7167/53.6167	GSC-2244	6810 ± 80	168	7513	7655	7830	Hardy (1976)
5058	−77.9667/53.7167	QU-119	5560 ± 130	123	6012	6361	6656	Hardy (1977)
5059	−78.7528/53.7403	QU-121	4110 ± 120	37	4249	4630	4948	Hardy (1977)
5061	−77.5667/53.35	QU-124	7750 ± 180	162.1	8189	8592	9022	Hardy (1977)
5066	−77.8667/53.7	QU-245	7110 ± 180	166	7619	7939	8311	Hardy (1977)
5067	−77.6667/53.5778	QU-246	7220 ± 330	171	7434	8070	8774	
5068	−77.8667/53.7333	QU-247	6910 ± 350	183	7029	7784	8514	Hardy (1977)
5070	−77.5/53.4667	QU-249	6660 ± 190	164	7178	7542	7931	Hardy (1977)
5072	−78.3333/53.6667	QU-256	5080 ± 180	99	5472	5838	6276	Hardy (1977)
	Curve: Eastmain - Fort Rupert, QC							
5077	−77.4306/51.47	GSC-2135	7360 ± 100	205	7998	8178	8374	Vincent (1977)
5086	−77.1333/52.2167	QU-252	7030 ± 210	222	7511	7869	8311	Hardy (1977)
5088	−77.0833/52.3083	QU-254	7140 ± 210	218	7610	7973	8372	Hardy (1977)
5089	−77.9167/52.4167	QU-258	7440 ± 210	200	7826	8254	8724	Hardy (1977)
	Curve: Mattagami, ON							
5107	−81.65/50.275	GSC-1241	7160 ± 160	135	7686	7988	8318	Skinner (1973)
5108	−82.8958/50.3	GSC-1309	7630 ± 170	112	8054	8449	8976	Skinner (1973)
5113	−82.8536/50.2167	GSC-1436	7280 ± 150	102	7830	8108	8392	Skinner (1973)
5114	−82.375/50.3	GSC-1489	6890 ± 220	86	7334	7752	8182	Skinner (1973)
5117	−84.3/50.2167	GSC-897	7760 ± 160	105	8214	8594	9012	Craig (1969); Skinner (1973)
5118	−84.2333/50.2167	GSC-915	7540 ± 140	99	8032	8343	8597	Craig (1969); Skinner (1973)
	Curve: Severn River, ON							
5138	−88.2667/54.4833	GSC-877	7400 ± 140	137	7952	8216	8450	Craig (1969)
	Curve:Churchill, MB							
5149	−95.3833/59.3	GSC-2579	6790 ± 100	85	7472	7644	7841	Dredge and Nixon (1992)
5151	−95.8333/58.55	GSC-3070	7770 ± 140	106	8356	8595	8996	Dredge and Nixon (1992)

Id	Location [°E/°N]	Lab-code	^{14}C age [a BP]	Elev. [m]	cal. age [a BP] min.	med.	max.	Reference
	Curve: Nelson River, MB							
5170	−94/56.5417	BGS-711	6280 ± 180	67	6750	7171	7557	Nielsen et al. (1986); Nielsen and Dredge (1982); Dredge and Nixon (1992)
5171	−94.2/56.43	BGS-712	6990 ± 130	82	7580	7822	8044	Nielsen et al. (1986); Nielsen and Dredge (1982); Dredge and Nixon (1992)
5172	−94.2167/56.42	BGS-713	6750 ± 150	90	7334	7619	7934	Nielsen et al. (1986); Nielsen and Dredge (1982); Dredge and Nixon (1992)
5173	−94.0833/56.5333	BGS-714	6900 ± 150	72	7492	7752	8008	Nielsen et al. (1986); Nielsen and Dredge (1982); Dredge and Nixon (1992)
5174	−94/56.5417	BGS-791	6760 ± 100	67	7436	7619	7816	Nielsen et al. (1986); Nielsen and Dredge (1982); Dredge and Nixon (1992)
5176	−94.0833/56.5333	BGS-798	6900 ± 100	76	7584	7746	7933	Nielsen et al. (1986); Nielsen and Dredge (1982); Dredge and Nixon (1992)
5178	−94.2167/56.4167	BGS-813	8200 ± 300	90	8414	9132	9888	Nielsen et al. (1986); Dredge and Nixon (1992)
5179	−94.2167/56.4167	BGS-814	7300 ± 200	80	7714	8125	8510	Nielsen et al. (1986); Dredge and Nixon (1992)

Id	Location [°E/°N]	Lab-code	^{14}C age [a BP]	Elev. [m]	cal. age [a BP] min.	med.	max.	Reference
5180	−94.175/56.435	BGS-815	7050 ± 150	90	7614	7876	8170	Nielsen et al. (1986); Dredge and Nixon (1992)
5187	−94.08/56.52	GSC-2294	7030 ± 170	90	7570	7862	8189	Teller (1980); Dredge and Nixon (1992); Klassen (1986)
5189	−94.0167/56.53	GSC-3326	7180 ± 70	72	7864	8001	8169	Nielsen and Dredge (1982); Dredge and Nixon (1992)
5190	−94.12/56.53	GSC-3367	6750 ± 80	67	7464	7608	7748	Nielsen and Dredge (1982); Dredge and Nixon (1992)
5194	−93.6083/56.75	GSC-3904	7250 ± 80	15	7932	8076	8294	Dredge and Nixon (1992)
5196	−92.6333/57.0267	GSC-3921	7020 ± 100	16	7665	7846	8018	Dredge and Nixon (1992)
5200	−93.7778/56.6917	GSC-4725	6810 ± 80	62	7513	7655	7830	
5201	−93.7778/56.6903	GSC-4746	7290 ± 80	45	7960	8104	8310	
5202	−93.8083/56.6903	GSC-4833	6710 ± 110	64	7422	7578	7788	
5204	−93.2833/56.0389	GSC-878	7570 ± 140	114	8037	8376	8640	Dredge and Nixon (1992)
	Curve: Baker Lake, NU							
5216	−94.8/62.8167	GSC-1016	6570 ± 140	122	7177	7467	7688	
5217	−96.9667/64.05	GSC-1083	5970 ± 140	96	6479	6821	7171	
5219	−96.9833/64.05	GSC-1164	5910 ± 140	101	6412	6744	7155	
5220	−94.0708/63.5575	GSC-2042	6520 ± 70	120	7305	7433	7566	
5223	−96.05/64.5167	GSC-299	5480 ± 150	90	5930	6266	6618	
5224	−95.6667/63.7667	GSC-439	5900 ± 130	76	6408	6730	7154	
5225	−96.05/64.3167	GSC-725	5220 ± 140	6	5663	5998	6286	
	Curve: Eskimo Point, NU							
5245	−96.4653/61.9333	GSC-5234	6770 ± 120	110	7430	7631	7850	

C

Data used in Chapters 4 and 5

List of indicators provided by different authors is stored in a relational database system at GFZ Potsdam. Data from the Baltic Sea is from Rosentau et al. (2020). The ^{14}C ages were recalibrated using OxCal, where for most dating, a correction for δ^{13}C and reservoir effect was applied. In addition to the range and median given here, also the probability distribution of each dating was extracted. The tables present only the information relevant for the current study, whereas, in the database, 23 attributes are given for each indicator. Type columns indicate the type of data, -1 for lower or marine limit, 0 for a range or SLIP and $+1$ for an upper or terrestrial limit. Samples, for which no reference is given, could not be retrieved from literature provided in the database and, so, have to be interpreted as unpublished.

Table C.1: List of considered sea-level indicators in the Denmark region:

Id	Location	^{14}C age	Elev.	cal. age [a BP]			type	Reference
	[°E/°N]	[a BP]	[m]	min.	med.	max.		
	Curve: Belt Sea region							
503	10.4167/56.25	7620 ± 110	-6.2	8186	8427	8626.5	-1	(Fischer, 2005)
511	10.9622/55.415	7330 ± 75	-26.1	8019	8197.5	8346.5	-1	(Bennike et al., 2004)
523	12.741/55.78	7910 ± 70	-21.2	8618.5	8858	9039	-1	(Bennike et al., 2012)
529	10.4167/56.25	7690 ± 45	-6.7	8401.5	8477.5	8560.5	1	(Fischer, 2005)
530	10.4167/56.25	7560 ± 35	-6.4	8331.5	8379	8416.5	1	(Fischer, 2005)

Id	Location [°E/°N]	^{14}C age [a BP]	Elev. [m]	cal. age [a BP] min.	med.	max.	type	Reference
531	10.4167/56.25	7550 ± 40	-6.4	8219	8371.5	8421	1	(Fischer, 2005)
537	11.2/55.3914	7245 ± 65	-6	7955	8069.5	8180.5	1	(Christensen et al., 1997)
543	9.8233/55.3917	6820 ± 55	-2.7	7575.5	7654	7782	1	(Andersen, 2013)
544	9.8278/55.3917	6905 ± 55	-2.7	7621	7739.5	7914.5	1	(Andersen, 2013)
546	10.3183/54.995	7400 ± 150	-19.4	7940	8215	8512.5	1	(Krog, 1979)
571	11.2485/55.3929	7190 ± 100	-9	7794	8016.5	8274.5	-1	(Petersen, 1978)
609	11.0849/55.2067	7340 ± 110	-8.5	7969	8158	8367.5	-1	(Christensen et al., 1997)
612	9.8278/55.3917	6550 ± 80	-2.7	7310	7460	7581	1	(Andersen, 2013)
613	11.0043/55.3314	7090 ± 110	-6.9	7690	7908.5	8158.5	1	(Christensen et al., 1997)
614	10.4167/56.25	7390 ± 160	-6.1	7932	8206	8536	-1	(Fischer, 2005)
616	11.0043/55.3314	7160 ± 130	-7	7695	7987	8295	1	(Christensen et al., 1997)
617	11.0043/55.3314	7340 ± 110	-7	7969	8158	8367.5	1	(Christensen et al., 1997)
620	10.5528/56.3069	3860 ± 85	0.8	4113	4364.5	4612	-1	(Petersen and Rasmussen, 1995)
622	10.5528/56.3069	3850 ± 85	1	4094.5	4350.5	4586.5	-1	(Petersen and Rasmussen, 1995)
623	10.5528/56.3069	4600 ± 90	-4	5077	5351.5	5565.5	-1	(Petersen and Rasmussen, 1995)
624	10.5528/56.3069	4910 ± 90	-5.5	5489.5	5681	5884.5	-1	(Petersen and Rasmussen, 1995)
625	10.5528/56.3069	7240 ± 110	-8.5	7900	8102.5	8341.5	-1	(Petersen and Rasmussen, 1995)
627	10.5528/56.3069	7370 ± 110	-8.7	7990	8231	8440.5	-1	(Petersen and Rasmussen, 1995)
628	10.5528/56.3069	7380 ± 110	-8.7	7996	8240.5	8453	-1	(Petersen and Rasmussen, 1995)
629	10.6272/55.8895	6030 ± 100	-0.8	6664.5	6888	7162.5	-1	(Rasmussen, 1995)
630	10.6272/55.8895	7150 ± 110	-1.1	7730.5	7975	8187	1	(Rasmussen, 1995)
631	10.6272/55.8895	5480 ± 95	0	6083	6299.5	6526	-1	(Rasmussen, 1995)
632	10.6272/55.8895	5580 ± 70	0	6259	6394	6568	-1	(Rasmussen, 1995)
633	10.6272/55.8895	6030 ± 100	-0.8	6673	6918.5	7159	-1	(Rasmussen, 1995)
634	9.8278/55.3917	5370 ± 100	-2.8	5922.5	6143	6385.5	1	(Andersen, 2013)
635	9.8278/55.3917	6380 ± 100	4.7	7023	7306.5	7481.5	1	(Andersen, 2013)
639	10.5528/56.3069	3960 ± 65	1.7	4325.5	4504.5	4767.5	-1	(Petersen, 1993)
640	10.5528/56.3069	3880 ± 65	1.3	4189.5	4394	4582.5	-1	(Petersen, 1993)
641	10.5528/56.3069	6750 ± 100	-4.4	7441.5	7625	7824.5	-1	(Petersen, 1993)
642	10.5528/56.3069	6990 ± 100	-4.5	7639.5	7848	8049.5	-1	(Petersen, 1993)
643	10.5528/56.3069	7990 ± 100	-5.5	8649.5	8975	9259.5	-1	(Petersen, 1993)

Id	Location [°E/°N]	^{14}C age [a BP]	Elev. [m]	cal. age [a BP] min.	med.	max.	type	Reference
655	10.0528/56.3069	4030 ± 85	3.5	4396.5	4604	4818	-1	(Petersen and Rasmussen, 1995)
661	11.1691/55.4575	8070 ± 115	-11.5	8605.5	8966.5	9296	1	(Christensen et al., 1997)
662	11.114/55.351	5920 ± 100	-2.1	6491.5	6751	7000	-1	(Christensen et al., 1997)
663	11.114/55.351	5450 ± 100	-1.7	5991.5	6233.5	6435.5	-1	(Christensen et al., 1997)
664	11.114/55.351	6530 ± 100	-2	7262.5	7438.5	7586	1	(Christensen et al., 1997)
665	11.114/55.351	5840 ± 100	-9	6412.5	6650	6889	1	(Christensen et al., 1997)
691	10.9955/55.3427	6710 ± 110	-13.6	7421.5	7578	7788	1	(Christensen et al., 1997)
693	10.9403/55.3231	7200 ± 120	-9.3	7791	8029	8311	1	(Christensen et al., 1997)
694	11.114/55.351	6520 ± 85	-1.5	7276.5	7431	7568	1	(Christensen et al., 1997)
695	11.114/55.351	7300 ± 110	-4.1	7938.5	8120.5	8349	1	(Christensen et al., 1997)
696	10.9823/55.3313	7330 ± 115	-6.3	7958.5	8148.5	8371	1	(Christensen et al., 1997)
697	10.4333/54.8967	5910 ± 75	-5	6549	6736	6936	1	(Skaarup and Grøn, 2004)
699	12.0967/55.7217	7490 ± 110	3.7	8041.5	8293.5	8514	1	(Rasmussen, 1992)
700	12.0967/55.7217	6960 ± 110	1.3	7596	7796	7976	1	(Rasmussen, 1992)
701	9.8278/55.3917	5940 ± 70	-5	6636	6806	6984	-1	(Petersen and Rasmussen, 1995)
702	9.8278/55.3917	5780 ± 70	-4	6438.5	6615.5	6784.5	-1	(Petersen and Rasmussen, 1995)
709	10.7125/56.1622	4260 ± 90	2	4648.5	4902	5206.5	-1	(Petersen and Rasmussen, 1995)
715	11.1695/55.4025	7410 ± 115	-7.8	8002.5	8228	8412.5	1	(Christensen et al., 1997)
716	11.1805/55.397	7490 ± 115	-8.7	8039.5	8293	8517	1	(Christensen et al., 1997)
719	11.0724/55.4127	7830 ± 120	-10	8419	8667.5	8989	1	(Christensen et al., 1997)
723	12.5833/55.6667	7680 ± 115	-5.9	8199.5	8487	8773.5	1	(Fischer, 1993)
724	10.4333/54.8967	6170 ± 85	-4.75	6804.5	7066.5	7264.5	1	(Skaarup and Grøn, 2004)
727	10.2333/56	6130 ± 135	-2	6677	7014	7310	1	(Rahbek and Rasmussen, 1994)
736	10.7471/55.4707	7630 ± 75	-11	8323.5	8435.5	8589.5	1	(Christensen et al., 1997)
738	11.0924/55.4103	7410 ± 80	-8.2	8044.5	8238.5	8376.5	1	(Christensen et al., 1997)
739	11.1603/55.4426	7650 ± 90	-8.2	8218.5	8456	8628	1	(Christensen et al., 1997)
740	11.275/55.194	6310 ± 80	-2.3	7016.5	7235.5	7419.5	1	(Christensen et al., 1997)
741	11.114/55.351	6900 ± 115	-4	7570	7747.5	7955.5	1	(Christensen et al., 1997)
742	11.114/55.351	6810 ± 100	-4	7488	7661	7915	1	(Christensen et al., 1997)
743	11.114/55.351	6860 ± 110	-4	7516	7711.5	7934	1	(Christensen et al., 1997)
744	11.114/55.351	6830 ± 110	-4	7501.5	7682	7928	1	(Christensen et al., 1997)
755	10.4333/54.8967	6290 ± 75	-4.5	7006	7212.5	7415	-1	(Skaarup and Grøn, 2004)
756	10.4333/54.8967	6270 ± 80	-4.5	6975	7189	7414	-1	(Skaarup and Grøn, 2004)

Id	Location [°E/°N]	^{14}C age [a BP]	Elev. [m]	cal. age [a BP] min.	med.	max.	type	Reference
776	10.45/56.1	1440 ± 30	-28.2	1298	1377	1479	-1	(Jensen and Bennike, 2009)
777	10.45/56.1	2460 ± 35	-29.7	2493	2635	2724	-1	(Jensen and Bennike, 2009)
778	10.35/56.1167	7470 ± 50	-16.4	8197.5	8335	8425	-1	(Jensen and Bennike, 2009)
779	10.35/56.1167	7840 ± 50	-17.4	8599.5	8767	8948	-1	(Jensen and Bennike, 2009)
780	10.35/56.1167	2890 ± 35	-16	2994.5	3123	3235.5	-1	(Jensen and Bennike, 2009)
784	9.8358/55.223	7880 ± 50	-16.7	8558	8694	8975.5	-1	(Bennike and Jensen, 2011)
787	9.8358/55.223	7700 ± 70	-16.6	8383.5	8489.5	8599.5	-1	(Bennike and Jensen, 2011)
788	9.8112/55.3847	6880 ± 40	-9.7	7648	7739	7840	-1	(Bennike and Jensen, 2011)
789	9.8112/55.3847	7420 ± 50	-9.8	8162	8256	8370	1	(Bennike and Jensen, 2011)
790	10.6278/55.9317	4685 ± 30	-0.56	5324.5	5448	5546.5	-1	(Sander et al., 2015)
791	10.6278/55.9317	6010 ± 35	-1.54	6778	6888	6991	-1	(Sander et al., 2015)
793	10.6278/55.9317	5615 ± 35	-0.44	6319	6426.5	6528	-1	(Sander et al., 2015)
794	10.6278/55.9317	5985 ± 50	-0.85	6720.5	6856.5	6994.5	-1	(Sander et al., 2015)
795	10.6/55.8917	5515 ± 35	-0.43	6257.5	6328	6409	-1	(Sander et al., 2015)
796	10.6/55.8917	6870 ± 40	-2.76	7639	7729	7831.5	-1	(Sander et al., 2015)
797	10.6/55.8917	5300 ± 40	-2.56	5981.5	6110.5	6217.5	-1	(Sander et al., 2015)
798	10.5592/55.7736	4095 ± 30	-1.17	4578.5	4699.5	4801.5	-1	(Sander et al., 2015)
799	10.5592/55.7736	6820 ± 40	-4.1	7590	7679.5	7779.5	-1	(Sander et al., 2015)
800	10.5592/55.7736	4460 ± 35	-0.09	5036	5167.5	5279.5	-1	(Sander et al., 2015)
801	10.5592/55.7736	4240 ± 35	-1.21	4794	4858	4961	-1	(Sander et al., 2015)
802	10.5592/55.7736	5105 ± 35	-0.74	5769	5889.5	5976	-1	(Sander et al., 2015)
803	10.8573/54.6465	6740 ± 80	-29.4	7464	7613	7779	-1	(Bennike and Jensen, 1998)
804	10.5592/55.7736	5425 ± 35	-2.09	6168	6243	6315	-1	(Sander et al., 2015)
805	10.6/55.8917	6950 ± 50	-3.82	7691	7813	7924	-1	(Sander et al., 2015)
806	10.6/55.8917	6770 ± 50	-5.2	7546	7634	7752.5	-1	(Sander et al., 2015)
807	10.6278/55.9317	6910 ± 50	-2.74	7661	7770.5	7897.5	-1	(Sander et al., 2015)
808	10.6/55.8917	7440 ± 35	-5.35	8184	8263	8344	1	(Sander et al., 2015)
809	10.6/55.8917	5825 ± 35	0.15	6530.5	6637.5	6734	-1	(Sander et al., 2015)
810	10.6/55.8917	6595 ± 35	-0.76	7431	7488.5	7564.5	1	(Sander et al., 2015)

Id	Location [°E/°N]	^{14}C age [a BP]	Elev. [m]	cal. age [a BP] min.	cal. age [a BP] med.	cal. age [a BP] max.	type	Reference
811	10.6/55.8917	6910 ± 40	-3.37	7669.5	7738	7834	0	(Sander et al., 2015)
812	10.6/55.8917	6595 ± 35	-0.97	7431	7488.5	7564.5	1	(Sander et al., 2015)
813	10.5592/55.7736	6715 ± 35	-2.59	7509.5	7583	7659	-1	(Sander et al., 2015)
814	11.066/54.5693	6770 ± 130	-19.9	7425	7648.5	7904.5	-1	(Bennike and Jensen, 1998)
815	10.45/56.1	6165 ± 35	-24.4	6968.5	7084	7184	-1	(Jensen and Bennike, 2009)
816	10.45/56.1	7200 ± 40	-25.5	7963	8057	8154.5	-1	(Jensen and Bennike, 2009)
817	10.4333/56.1167	5340 ± 35	-24.2	6032.5	6164.5	6261.5	-1	(Jensen and Bennike, 2009)
818	10.4333/56.1167	7890 ± 40	-25.8	8686	8846.5	8980.5	-1	(Jensen and Bennike, 2009)
819	9.7795/55.213	6190 ± 40	-25	6991.5	7112	7224.5	-1	(Bennike and Jensen, 2011)
820	9.7617/55.2095	6740 ± 40	-25.3	7529	7609	7690.5	-1	(Bennike and Jensen, 2011)
825	11.0695/54.5727	6760 ± 100	-20.6	7451	7634.5	7835.5	-1	(Bennike and Jensen, 1998)
826	10.7672/55.4807	7460 ± 70	-8.7	8160.5	8276.5	8407.5	1	(Christensen et al., 1997)
827	10.7672/55.4807	7450 ± 70	-8.7	8065	8269.5	8401.5	1	(Christensen et al., 1997)
831	11.0148/55.35	7300 ± 120	-16.5	7932	8122	8373.5	-1	(Christensen et al., 1997)
837	11.1772/54.539	720 ± 65	-11.3	544.5	677.5	804	-1	(Bennike and Jensen, 1998)
839	11.2333/55.6847	5040 ± 65	-1	5645.5	5791	5916.5	0	(Hede, 2003)
840	11.2333/55.6847	5040 ± 60	-0.1	5654.5	5793	5910.5	0	(Hede, 2003)
841	11.2333/55.6847	5300 ± 65	-0.2	5929	6084.5	6269	-1	(Hede, 2003)
842	11.2333/55.6847	6140 ± 60	-0.2	6858.5	7040	7236	1	(Hede, 2003)
843	11.2333/55.6847	6495 ± 60	-0.8	7275.5	7400	7507.5	1	(Hede, 2003)
844	11.2333/55.6847	5650 ± 70	0	6300	6436	6627.5	-1	(Hede, 2003)
845	12.0531/55.9876	2402 ± 27	0.2	2435	2559.5	2680.5	-1	(Bennike et al., 2017)
846	12.0531/55.9876	5342 ± 30	-3.2	6058.5	6169	6260	-1	(Bennike et al., 2017)
847	12.0531/55.9876	5842 ± 37	-3.4	6585	6689.5	6795	-1	(Bennike et al., 2017)
849	12.0531/55.9876	7130 ± 30	-5.5	7917	7981	8078	-1	(Bennike et al., 2017)
850	12.0531/55.9876	7543 ± 34	-6	8330	8397.5	8495	-1	(Bennike et al., 2017)
851	12.0531/55.9876	7950 ± 40	-6.1	8645.5	8821	8982.5	1	(Bennike et al., 2017)
857	12.55/55.8528	7026 ± 80	1.95	7686	7854	7980.5	1	(Christensen, 1982)
858	12.55/55.8528	6749 ± 120	4.55	7426.5	7612.5	7839.5	1	(Christensen, 1982)
860	12.55/55.8528	6656 ± 120	4	7316	7534.5	7737	1	(Christensen, 1982)

Id	Location	^{14}C age	Elev.	cal. age [a BP]			type	Reference
	[°E/°N]	[a BP]	[m]	min.	med.	max.		
861	12.55/55.8528	6440 ± 120	3.95	7029	7352.5	7577.5	1	(Christensen, 1982)
862	12.55/55.8528	7002 ± 100	3.2	7659	7830.5	8009	1	(Christensen, 1982)
863	12.55/55.8528	7006 ± 95	3.23	7668.5	7834	7999.5	1	(Christensen, 1982)
864	12.55/55.8528	6971 ± 100	3.02	7619.5	7804.5	7969.5	1	(Christensen, 1982)
865	12.55/55.8528	6933 ± 105	2.56	7594	7773.5	7951.5	1	(Christensen, 1982)
866	12.55/55.8528	6436 ± 95	3.6	7169	7353.5	7553.5	1	(Christensen, 1982)
867	12.55/55.8528	6325 ± 110	4.1	6959.5	7244	7436	1	(Christensen, 1982)
868	12.55/55.8528	6012 ± 105	4.23	6635.5	6866.5	7165	1	(Christensen, 1982)
869	12.55/55.8528	5905 ± 95	3.3	6490.5	6731.5	6967	-1	(Christensen, 1982)
871	12.55/55.8528	5656 ± 95	3.14	6289	6451	6657	-1	(Christensen, 1982)
872	12.55/55.8528	5596 ± 65	4.1	6279.5	6378	6528	1	(Christensen, 1982)
873	12.55/55.8528	7691 ± 110	2.2	8209.5	8495	8851.5	1	(Christensen, 1982)
874	12.55/55.8528	7575 ± 115	1.85	8163.5	8380	8601.5	1	(Christensen, 1982)
875	12.55/55.8528	7432 ± 105	2.05	8024	8248	8409.5	1	(Christensen, 1982)
876	12.55/55.8528	7267 ± 125	2.4	7859.5	8095.5	8360	1	(Christensen, 1982)
877	12.55/55.8528	7269 ± 105	2.19	7878	8095	8334.5	1	(Christensen, 1982)
878	12.55/55.8528	7176 ± 100	2.7	7787.5	8002	8197.5	1	(Christensen, 1982)
879	12.55/55.8528	6751 ± 100	2.9	7437	7611	7789	1	(Christensen, 1982)
880	12.55/55.8528	6492 ± 100	3.06	7181.5	7397.5	7578.5	1	(Christensen, 1982)
882	12.55/55.8528	6449 ± 90	3.1	7175	7362.5	7558	1	(Christensen, 1982)
883	12.55/55.8528	6323 ± 95	3.05	7005	7247.5	7427	1	(Christensen, 1982)
884	12.55/55.8528	6351 ± 90	3.26	7019	7281	7433.5	1	(Christensen, 1982)
885	12.55/55.8528	6492 ± 100	3.06	7181.5	7397.5	7578.5	0	(Christensen, 1982)
886	12.55/55.8528	7325 ± 105	0.26	7962.5	8141.5	8353.5	-1	(Christensen, 1982)
887	12.55/55.8528	7179 ± 110	1.13	7758.5	8006	8290.5	-1	(Christensen, 1982)
888	12.55/55.8528	7850 ± 110	-0.07	8440.5	8691.5	8992	1	(Christensen, 1982)
889	12.55/55.8528	7794 ± 110	2	8402.5	8605.5	8977.5	1	(Christensen, 1982)
890	12.55/55.8528	7674 ± 105	1.54	8208.5	8479	8719.5	1	(Christensen, 2014)
891	12.55/55.8528	7676 ± 80	1.62	8348	8475.5	8604.5	1	(Christensen, 1982)
893	12.55/55.8528	7584 ± 105	-0.15	8186	8390	8583.5	-1	(Christensen, 1982)
894	12.55/55.8528	6888 ± 100	2.37	7579	7735	7931	-1	(Christensen, 1982)
895	12.55/55.8528	6678 ± 75	2.25	7436	7546.5	7660.5	-1	(Christensen, 2014)
896	12.55/55.8528	6295 ± 115	2.25	6933.5	7206.5	7432	-1	(Christensen, 2014)
897	12.55/55.8528	6295 ± 95	1.82	6988.5	7212.5	7422	-1	(Christensen, 1982)
898	12.55/55.8528	5610 ± 90	1.77	6220	6402	6634	-1	(Christensen, 1982)
899	12.55/55.8528	6951 ± 100	2.55	7613	7787.5	7959	-1	(Christensen, 1982)
900	12.55/55.8528	6797 ± 100	3.15	7474	7649.5	7848	-1	(Christensen, 1982)
901	12.55/55.8528	4870 ± 85	4.47	5327.5	5612	5883.5	1	(Christensen, 2014)
902	12.55/55.8528	8011 ± 110	1.6	8589.5	8870	9245	1	(Christensen, 2014)

Id	Location [°E/°N]	^{14}C age [a BP]	Elev. [m]	cal. age [a BP] min.	cal. age [a BP] med.	cal. age [a BP] max.	type	Reference
904	12.55/55.8528	7498 ± 105	2	8048.5	8301.5	8517.5	1	(Christensen, 2014)
905	12.55/55.8528	6756 ± 100	2.9	7437	7615.5	7792	-1	(Christensen, 2014)
906	12.55/55.8528	6637 ± 90	4.05	7334.5	7520.5	7674	1	(Christensen, 2014)
907	12.55/55.8528	3040 ± 95	4.12	2970	3226	3446	1	(Christensen, 2014)
908	12.55/55.8528	7514 ± 105	2.85	8054.5	8317.5	8542	1	(Christensen, 2014)
909	12.55/55.8528	7474 ± 65	3	8176.5	8288.5	8395	1	(Christensen, 2014)
910	12.55/55.8528	7320 ± 60	3	8004.5	8119.5	8307.5	1	(Christensen, 2014)
911	12.55/55.8528	6403 ± 105	3.9	7027.5	7325.5	7557.5	1	(Christensen, 2014)
912	12.55/55.8528	3236 ± 80	3.72	3252.5	3466.5	3681	1	(Christensen, 2014)
962	10.7605/55.694	6890 ± 80	-5.9	7600	7753.5	7919.5	-1	(Bennike et al., 2004)
	Curve: Arkona Basin							
504	12.9115/54.6483	5865 ± 65	-19.2	6550.5	6718	6887.5	-1	(Bennike and Jensen, 1998)
515	12.5007/54.5778	510 ± 45	-15.9	455	518.5	614.5	-1	(Bennike and Jensen, 1998)
526	12.5007/54.5778	1070 ± 120	-16	776	1025.5	1266.5	-1	(Bennike and Jensen, 1998)
548	12.169/54.331	760 ± 90	-17.3	556.5	719.5	896	-1	(Bennike and Jensen, 1998)
581	11.981/54.4233	7650 ± 150	-23.7	8169.5	8467	8975	NA	(Bennike and Jensen, 1998)
687	12.4492/55.0728	7900 ± 135	-13.4	8416	8758.5	9088	1	(Jensen and Stecher, 1992)
689	12.4197/55.0822	8010 ± 105	-14.6	8590	8867.5	9239.5	1	(Jensen and Stecher, 1992)
731	12.1077/54.3743	7800 ± 125	-20.6	8400	8625.5	8986.5	1	(Bennike and Jensen, 1998)
750	12.9547/54.6518	5720 ± 110	-19.7	6297	6552	6798	-1	(Bennike and Jensen, 1998)
759	11.9842/54.3253	1310 ± 70	-19.7	1101	1263	1406.5	-1	(Bennike and Jensen, 1998)
770	11.8782/54.3547	6560 ± 90	-19.6	7290	7462	7615	-1	(Jensen et al., 1997)
781	11.5377/54.39	6210 ± 100	-28.3	6884	7123	7343.5	-1	(Jensen et al., 1997)
792	11.5377/54.39	6820 ± 90	-29.5	7520.5	7689.5	7884.5	-1	(Jensen et al., 1997)
832	14.5295/54.804	8050 ± 100	-23.8	8630	8920.5	9254.5	-1	(Nielsen et al., 2004)
834	14.5543/54.7922	4785 ± 90	-23.1	5314.5	5540.5	5727	-1	(Nielsen et al., 2004)
835	14.4998/54.8055	1580 ± 75	-22.4	1350.5	1539	1722	-1	(Nielsen et al., 2004)

Id	Location [°E/°N]	^{14}C age [a BP]	Elev. [m]	cal. age [a BP] min.	med.	max.	type	Reference
848	11.995/54.4927	5990 ± 90	-17.3	6658.5	6868	7117	-1	(Bennike and Jensen, 1998)
859	11.8935/54.4928	1900 ± 75	-14.9	1724.5	1915.5	2109	-1	(Bennike and Jensen, 1998)
870	11.9033/54.5077	2200 ± 70	-12.3	2089	2273	2478	-1	(Bennike and Jensen, 1998)
881	12.0638/54.477	4940 ± 90	-16.1	5539.5	5711	5910	-1	(Bennike and Jensen, 1998)
892	12.1077/54.3743	7820 ± 80	-20.6	8424.5	8621	8975	1	(Bennike and Jensen, 1998)
913	12.973/54.8853	2410 ± 80	-36.6	2344	2550.5	2724.5	-1	(Bennike and Jensen, 1998)
914	11.981/54.4233	7730 ± 110	-22.3	8342	8529.5	8972	-1	(Bennike and Jensen, 1998)
926	12.9632/54.7287	6250 ± 80	-28.3	6972	7174.5	7352	-1	(Bennike and Jensen, 1998)
929	12.345/54.8038	6540 ± 70	-25	7310	7447	7567.5	-1	(Bennike and Jensen, 1998)
930	12.345/54.8038	7520 ± 65	-25	8189.5	8333	8417.5	-1	(Bennike and Jensen, 1998)
931	12.5232/54.8207	6690 ± 90	-26.3	7414.5	7569	7741	-1	(Bennike and Jensen, 1998)
935	12.1077/54.3743	7940 ± 75	-20.6	8601	8797.5	8996	-1	(Bennike and Jensen, 1998)
950	13.6665/54.9322	6075 ± 50	-51	6843	6974	7135	-1	(Bennike and Jensen, 1998)
	Curve: Kattegat							
550	11.0052/57.2616	2920 ± 85	4.1	2928.5	3161	3372.5	0	(Hansen, 1977)
680	11/57.2333	7350 ± 110	8	7974	8212.5	8413.5	-1	(Petersen and Rasmussen, 1995)
953	11.6088/56.3857	7940 ± 80	-22.8	8627	8896.5	9121.5	-1	(Bennike et al., 2000)
	Curve: Northern Jylland							
547	10.4917/57.4883	3990 ± 130	4	4095	4466	4832	-1	(Krog and Tauber, 1974)
549	10.4917/57.4883	4290 ± 130	4	4525	4871.5	5289.5	-1	(Krog and Tauber, 1974)
553	10.5133/57.4617	3980 ± 140	4	4083.5	4449	4838	-1	(Krog and Tauber, 1974)
554	10.5417/57.445	5240 ± 120	1.3	5745	6025	6282	-1	(Krog and Tauber, 1974)
555	10.5417/57.445	5180 ± 150	0.3	5644.5	5949.5	6279.5	-1	(Krog and Tauber, 1974)
556	10.5133/57.4633	2440 ± 100	4	2318	2525.5	2750.5	-1	(Krog and Tauber, 1974)

Id	Location [°E/°N]	^{14}C age [a BP]	Elev. [m]	cal. age [a BP] min.	cal. age [a BP] med.	cal. age [a BP] max.	type	Reference
572	8.8333/56.9333	6650 ± 100	0.5	7330.5	7529.5	7686	-1	(Petersen, 1976)
573	9.2167/57.0833	1910 ± 100	0	1612	1851	2113	-1	(Petersen, 1976)
574	8.8333/56.9333	7040 ± 110	0.5	7659.5	7863	8150.5	1	(Petersen, 1976)
575	8.8333/56.9333	6260 ± 105	1.4	6942.5	7179.5	7401.5	-1	(Petersen, 1976)
576	8.8333/56.9333	7460 ± 120	0	8013	8266.5	8509.5	1	(Petersen, 1976)
577	9.0833/56.8833	6420 ± 105	0.7	7148.5	7337	7537.5	-1	(Petersen, 1976)
578	9.0833/56.8833	5910 ± 105	1.5	6503.5	6774.5	7044	-1	(Petersen, 1976)
579	9.2333/57.0333	3990 ± 65	4	4393	4547.5	4775.5	-1	(Petersen, 1976)
580	9.2333/57.0667	6980 ± 110	3.5	7610	7839	8060.5	-1	(Petersen, 1976)
582	9.2833/56.9833	4990 ± 95	6	5572.5	5761.5	5961	-1	(Petersen, 1976)
583	9.25/57.0167	5790 ± 105	3	6389.5	6630	6887	-1	(Petersen and Rasmussen, 1995)
587	9.0727/57.1019	3250 ± 70	0.9	3344.5	3480.5	3676.5	1	(Petersen and Rasmussen, 1995)
588	9.0727/57.1019	4050 ± 65	-1.5	4444.5	4631.5	4803.5	-1	(Petersen and Rasmussen, 1995)
589	9.0727/57.1019	7580 ± 120	-24.5	8174	8453	8764	-1	(Petersen and Rasmussen, 1995)
590	9.0727/57.1019	4210 ± 85	-4.5	4555.5	4828.5	5065	-1	(Petersen and Rasmussen, 1995)
591	9.0727/57.1019	5460 ± 95	-13.5	6033	6277.5	6486	-1	(Petersen and Rasmussen, 1995)
593	9.0727/57.1019	6550 ± 110	-20.5	7253	7452.5	7642.5	-1	(Petersen and Rasmussen, 1995)
594	9.0727/57.1019	6810 ± 110	-23	7489	7683	7909	-1	(Petersen and Rasmussen, 1995)
596	9.0583/56.5033	5320 ± 70	-4	5955	6126.5	6274.5	-1	(Petersen and Rasmussen, 1995)
597	9.0583/56.5033	3420 ± 80	-2	3555	3769	3984.5	-1	(Petersen and Rasmussen, 1995)
598	9.2167/56.5986	2750 ± 80	0.5	2752.5	2942	3149.5	-1	(Petersen and Rasmussen, 1995)
599	9.0727/57.1019	3130 ± 70	1.2	3238	3419	3589.5	-1	(Petersen and Rasmussen, 1995)
600	9.0727/57.1019	7660 ± 115	-24.5	8309.5	8540.5	8898.5	-1	(Petersen and Rasmussen, 1995)
601	9.0727/57.1019	7860 ± 115	-24.5	8485.5	8793.5	9105	-1	(Petersen and Rasmussen, 1995)

Id	Location [°E/°N]	^{14}C age [a BP]	Elev. [m]	cal. age [a BP] min.	med.	max.	type	Reference
602	9.0727/57.1019	7380 ± 110	-24.5	7996	8240.5	8453	-1	(Petersen and Rasmussen, 1995)
604	9.2167/56.5986	3650 ± 85	1.5	3845.5	4080	4338	-1	(Petersen and Rasmussen, 1995)
605	9.2167/56.5986	7260 ± 110	-8	7919.5	8122	8349.5	-1	(Petersen and Rasmussen, 1995)
606	9.1875/56.5089	7150 ± 110	-5	7790	8015	8267.5	-1	(Petersen and Rasmussen, 1995)
607	9.3028/56.4822	6190 ± 105	1	6845	7099.5	7330.5	-1	(Petersen and Rasmussen, 1995)
608	9.4705/56.5139	5820 ± 100	1	6425	6665.5	6910.5	-1	(Petersen and Rasmussen, 1995)
610	9.2542/56.5	6550 ± 105	-1.5	7259	7452.5	7631.5	-1	(Petersen and Rasmussen, 1995)
611	9.2542/56.5	5400 ± 95	-0.5	5978	6211.5	6408.5	-1	(Petersen and Rasmussen, 1995)
618	9.1903/56.7889	3690 ± 80	0.5	3912	4136.5	4378	-1	(Petersen, 1986)
619	9.1903/56.7889	5280 ± 90	1.5	5899	6083	6269.5	-1	(Petersen, 1986)
621	9.2542/56.5	7630 ± 110	-1.8	8279	8503.5	8846	-1	(Petersen and Rasmussen, 1995)
636	8.2424/56.7243	410 ± 65	-4	300	438	530.5	-1	(Petersen and Rasmussen, 1995)
638	8.2287/56.7425	3650 ± 85	-6	3845.5	4080	4338	-1	(Petersen and Rasmussen, 1995)
644	9.1903/56.7889	5840 ± 95	1	6458	6689.5	6924.5	-1	(Petersen and Rasmussen, 1995)
645	8.2424/56.7243	2110 ± 70	-9	1989.5	2175	2328.5	-1	(Petersen and Rasmussen, 1995)
646	8.2287/56.7425	7290 ± 110	-24	7940	8152	8365.5	-1	(Petersen and Rasmussen, 1995)
647	9.1903/56.7889	6000 ± 100	1	6653	6881.5	7142	-1	(Petersen, 1986)
649	9.1903/56.7889	5840 ± 95	1	6458	6689.5	6924.5	-1	(Petersen, 1986)
650	9.1903/56.7889	5790 ± 95	1	6404.5	6629	6859.5	-1	(Petersen, 1986)
651	8.2167/56.6667	6800 ± 105	-9.5	7484.5	7673	7890	-1	(Petersen and Rasmussen, 1995)
652	8.2167/56.6667	6500 ± 100	-8.5	7228.5	7408	7583.5	-1	(Petersen and Rasmussen, 1995)
653	8.2167/56.6667	6320 ± 100	-7.5	7005	7245.5	7428	-1	(Petersen and Rasmussen, 1995)

Id	Location [°E/°N]	^{14}C age [a BP]	Elev. [m]	cal. age [a BP] min.	med.	max.	type	Reference
654	10.0944/57.0417	5370 ± 95	-34	5954.5	6178	6379.5	-1	(Petersen and Rasmussen, 1995)
656	8.1222/56.3561	3100 ± 75	6.5	3190.5	3383.5	3568.5	-1	(Petersen and Rasmussen, 1995)
657	8.1222/56.3561	6740 ± 130	12	7405.5	7621	7889	-1	(Petersen and Rasmussen, 1995)
658	8.8472/57.0305	7020 ± 110	-15.5	7659	7877.5	8118.5	-1	(Petersen and Rasmussen, 1995)
660	8.8472/57.0305	6640 ± 105	-4	7333	7527.5	7724	-1	(Petersen and Rasmussen, 1995)
666	10.5/57.4583	2710 ± 75	0	2734.5	2893	3091	-1	(Petersen, 1991)
667	10.5/57.4583	2720 ± 75	0	2739	2904.5	3103.5	-1	(Petersen, 1991)
668	10.5/57.5	5170 ± 70	2.4	5792.5	5965.5	6166	-1	(Petersen, 1991)
669	10.5/57.5	4240 ± 85	2	4608.5	4873	5172	-1	(Petersen, 1991)
671	10.5/57.5	3180 ± 80	3.7	3274.5	3476.5	3685.5	-1	(Petersen, 1991)
672	10.5/57.5	2640 ± 75	4.2	2683.5	2819.5	3012	-1	(Petersen, 1991)
674	9.2347/56.878	4200 ± 85	2.7	4547.5	4814	5044	-1	(Petersen and Rasmussen, 1995)
675	9.2347/56.878	4520 ± 85	1.6	4974	5235.5	5458	-1	(Petersen and Rasmussen, 1995)
676	9.2347/56.878	4460 ± 85	2.5	4894.5	5151	5394.5	-1	(Petersen and Rasmussen, 1995)
677	9.2347/56.878	4360 ± 85	1.9	4829.5	5028.5	5263.5	-1	(Petersen and Rasmussen, 1995)
678	9.2347/56.878	4330 ± 90	2	4801.5	4991.5	5262	-1	(Petersen and Rasmussen, 1995)
679	10.1583/57.4542	7210 ± 110	8	7859	8074.5	8313	-1	(Petersen and Rasmussen, 1995)
682	10.825/56.4972	6520 ± 105	6	7236	7426	7609	-1	(Petersen and Rasmussen, 1995)
683	10.7114/56.5289	5890 ± 95	3	6506	6750	6985	-1	(Petersen and Rasmussen, 1995)
684	10.6528/56.5167	5560 ± 95	4	6194.5	6380	6604.5	-1	(Petersen and Rasmussen, 1995)
685	10.3/57.6333	6850 ± 100	8	7546.5	7719	7924	-1	(Petersen, 1991)
686	10.4333/57.6833	3850 ± 65	8	4013.5	4267	4431	-1	(Petersen, 1991)
853	10.4333/57.475	6440 ± 80	12.2	7177	7357	7500.5	0	(Christensen and Nielsen, 2008)

Id	Location [°E/°N]	^{14}C age [a BP]	Elev. [m]	cal. age [a BP] min.	med.	max.	type	Reference
854	10.4333/57.475	6060 ± 80	12.4	6738.5	6923	7160.5	0	(Christensen and Nielsen, 2008)
855	10.4333/57.475	6210 ± 65	12.4	6950.5	7105	7261	0	(Christensen and Nielsen, 2008)
856	10.4333/57.475	6080 ± 100	12.8	6718.5	6953.5	7240.5	0	(Christensen and Nielsen, 2008)
698	10.3667/57.6444	7010 ± 105	3	7655.5	7867.5	8098	-1	(Petersen and Rasmussen, 1995)
705	10.825/56.4972	5970 ± 70	4	6656.5	6841	7023.5	-1	(Petersen and Rasmussen, 1995)
706	9.97/57.2583	6370 ± 105	1	7063.5	7293.5	7494	-1	(Petersen and Rasmussen, 1995)
707	9.97/57.2583	6050 ± 100	1	6699	6943.5	7184.5	-1	(Petersen and Rasmussen, 1995)
708	9.97/57.2583	6000 ± 100	1	6653	6881.5	7142	-1	(Petersen and Rasmussen, 1995)
710	10.4375/57.5422	500 ± 50	0.5	440.5	512	615	-1	(Petersen and Rasmussen, 1995)
711	10.4375/57.5422	420 ± 50	0.5	326	452.5	524.5	-1	(Petersen and Rasmussen, 1995)
712	10.4375/57.5422	320 ± 50	0.5	273.5	364.5	462.5	-1	(Petersen and Rasmussen, 1995)

TABLE C.2: List of considered sea-level indicators in the region of N Germany:

Id	Location [°E/°N]	^{14}C age [a BP]	Elev. [m]	cal. age [a BP] min.	med.	max.	type	Reference
	CURVE: KIELER BUCHT							
1145	10.67/54.4367	8070 ± 80	-21.1	8695	8917	9139	1	(Winn et al., 1986)
1146	10.69/54.52	8100 ± 100	-25.4	8645	8970	9295	1	(Winn et al., 1986)
1147	10.6783/54.5283	8065 ± 110	-27.3	8605	8942	9279	1	(Winn et al., 1986)
1150	10.0283/54.79	7060 ± 90	-34.8	7685	7852	8019	-1	(Winn et al., 1986)
1153	10.0483/54.5333	6720 ± 450	-18.6	6660	7525	8390	-1	(Winn et al., 1986)
1154	10.0483/54.5333	7870 ± 165	-19.3	8365	8747	9129	1	(Winn et al., 1986)
1155	10.33/54.67	7170 ± 100	-25.3	7785	7980	8175	1	(Winn et al., 1986)
1159	10.1667/54.68	7880 ± 105	-30.3	8510	8755	9000	1	(Winn et al., 1986)
1160	10.0717/54.4967	6600 ± 90	-23.1	7405	7510	7615	-1	(Winn et al., 1986)
1167	10.155/54.36	7960 ± 120	-16.3	8510	8820	9130	1	(Winn et al., 1986)
1169	10.17/54.3783	6910 ± 85	-19.5	7600	7735	7870	-1	(Winn et al., 1986)
1175	10.09/54.5567	6040 ± 310	-27.6	6280	6892	7504	-1	(Winn et al., 1986)
1177	10.65/54.32	5870 ± 200	-4.2	6290	6737	7184	1	(Ernst, 1974)
1178	10.65/54.32	6050 ± 90	-3.6	6745	6877	7009	1	(Ernst, 1974)
1179	10.65/54.32	4260 ± 45	-2.35	4620	4750	4880	1	(Ernst, 1974)
1180	10.65/54.32	4470 ± 170	-2.35	4805	5150	5495	1	(Ernst, 1974)
1181	10.65/54.32	1490 ± 100	-0.51	1235	1417	1599	1	(Ernst, 1974)
1182	10.65/54.32	4040 ± 80	-1.85	4350	4545	4740	1	(Ernst, 1974)
1183	10.65/54.32	800 ± 90	-0.52	640	780	920	1	(Ernst, 1974)
	CURVE: FEHMARN							
1144	10.93/54.4233	7550 ± 140	-12.7	8025	8315	8605	1	(Winn et al., 1986)
1162	10.9783/54.4033	7440 ± 125	-13.8	8000	8212	8424	1	(Winn et al., 1986)
1165	10.92/54.4017	7010 ± 160	-15.5	7575	7820	8065	-1	(Winn et al., 1986)
1166	10.92/54.4017	7770 ± 140	-15.5	8345	8672	8999	-1	(Winn et al., 1986)
1171	11.2733/54.2517	7390 ± 115	-26.6	8000	8192	8384	-1	(Winn et al., 1986)
1172	11.2733/54.2517	8030 ± 175	-26.7	8510	8917	9324	1	(Winn et al., 1986)
1190	10.87/54.07	6590 ± 41	-25.5	7360	7480	7600	-1	(Harders et al., 2005)
1192	11.107/54.58	7680 ± 40	-26.2	8351	8433	8515	0	(Feldens and Schwarzer, 2012)

TABLE C.3: List of considered sea-level indicators in the region of NE Germany:

Id	Location [°E/°N]	^{14}C age [a BP]	Elev. [m]	cal. age [a BP] min.	med.	max.	type	Reference
	CURVE: USEDOM RÜGEN							
222	13.7137/54.3131	7810 ± 110	-10.5	8412.5	8629	8978.5	0	(Hoffmann et al., 2009)
304	13.6962/54.3102	7840 ± 70	-12.6	8452.5	8646	8976	0	(Hoffmann et al., 2009)
315	13.7082/54.3077	8025 ± 85	-15.6	8608	8880	9128	0	(Hoffmann et al., 2009)
326	13.7129/54.2881	8050 ± 85	-16	8636.5	8917	9242	0	(Hoffmann et al., 2009)
337	14.0609/53.9944	4490 ± 25	-4.9	5042.5	5173	5289	0	(Hoffmann et al., 2009)
348	13.6971/54.3072	6355 ± 25	-2.4	7180	7285.5	7413	0	(Hoffmann et al., 2009)
359	13.8602/54.0008	6810 ± 35	-5.1	7586	7643	7690	0	(Hoffmann et al., 2009)
370	13.7151/54.314	8070 ± 90	-6.6	8648	8968.5	9254	0	(Hoffmann et al., 2009)
381	14.0496/53.9932	975 ± 50	-0.2	766.5	867	972.5	0	(Hoffmann et al., 2009)
223	13.7237/54.3343	4600 ± 55	-2	5052	5316	5469	0	(Hoffmann et al., 2009)
234	13.7171/54.3163	5690 ± 150	-6.7	6199.5	6500	6856.5	0	(Hoffmann et al., 2009)
245	13.8737/54.06	5965 ± 70	-5.5	6644.5	6802	6979.5	0	(Hoffmann et al., 2009)
256	14.0496/53.9932	6360 ± 90	-6.8	7021	7290.5	7438	0	(Hoffmann et al., 2009)
267	13.7175/54.3293	6390 ± 25	-5.1	7265	7316.5	7416.5	0	(Hoffmann et al., 2009)
278	14.1036/53.9975	6520 ± 70	-6.1	7305	7433	7566	0	(Hoffmann et al., 2009)
289	14.0496/53.9932	7180 ± 65	-8.4	7869.5	7999.5	8164.5	0	(Hoffmann et al., 2009)
300	13.7041/54.3057	7320 ± 70	-7.2	8000.5	8124.5	8315.5	0	(Hoffmann et al., 2009)
302	14.0619/53.9766	7430 ± 65	-7.5	8054.5	8258.5	8386	0	(Hoffmann et al., 2009)
303	14.1026/53.9854	7440 ± 65	-7.4	8064	8264	8389.5	0	(Hoffmann et al., 2009)
	CURVE: RÜGEN HIDDENSEE							
305	13.2927/54.5488	5393 ± 29	-1.1	6027.5	6221.5	6284.5	-1	(Lampe et al., 2010)
306	13.2927/54.5488	5704 ± 30	-1.1	6406.5	6482.5	6600	-1	(Lampe et al., 2010)
307	13.2927/54.5488	5802 ± 30	-1.1	6503	6604	6670	-1	(Lampe et al., 2010)
308	13.2927/54.5488	5879 ± 35	-1.4	6635.5	6700.5	6785	-1	(Lampe et al., 2010)
309	13.3373/54.5802	6005 ± 26	-1.8	6755.5	6843	6929.5	-1	(Lampe et al., 2010)
310	13.4882/54.4811	5030 ± 35	-1	5661.5	5804.5	5894.5	0	(Lampe et al., 2010)
311	13.4882/54.4811	5980 ± 35	-2.2	6729	6818	6923	0	(Lampe et al., 2010)
312	13.4873/54.4809	1065 ± 30	0.8	927	967.5	1053.5	0	(Lampe et al., 2010)
313	13.4873/54.4809	4580 ± 30	-0.3	5065	5301.5	5446.5	0	(Lampe et al., 2010)
314	13.4873/54.4809	4770 ± 50	-0.9	5325.5	5509.5	5599	0	(Lampe et al., 2010)
316	13.4873/54.4809	5080 ± 90	-1.5	5609.5	5815.5	5993.5	0	(Lampe et al., 2010)
317	13.4873/54.4809	5530 ± 35	-1.6	6283	6328.5	6398.5	0	(Lampe et al., 2010)
318	13.4873/54.4809	5810 ± 55	-1.8	6482	6609.5	6741.5	0	(Lampe et al., 2010)
319	13.4873/54.4809	6205 ± 35	-2	7001.5	7093	7241.5	0	(Lampe et al., 2010)
320	13.4873/54.4809	6300 ± 30	-2.3	7164	7221.5	7275	0	(Lampe et al., 2010)

Id	Location [°E/°N]	^{14}C age [a BP]	Elev. [m]	cal. age [a BP] min.	cal. age [a BP] med.	cal. age [a BP] max.	type	Reference
321	13.4873/54.4809	6905 ± 45	-3.1	7658.5	7735.5	7843	0	(Lampe et al., 2010)
322	13.5651/54.4703	3890 ± 30	0	4239.5	4332	4416.5	0	(Lampe et al., 2010)
323	13.5651/54.4703	4240 ± 70	-0.1	4568	4753	4969	0	(Lampe et al., 2010)
324	13.2106/54.5498	1440 ± 25	0	1298	1330	1374.5	0	(Lampe et al., 2010)
325	13.2106/54.5498	1155 ± 100	0	914.5	1083.5	1290	0	(Lampe et al., 2010)
327	13.2106/54.5498	1120 ± 100	0	799.5	1048.5	1276.5	0	(Lampe et al., 2010)
328	13.2106/54.5498	2755 ± 45	-0.1	2765	2848	2950.5	0	(Lampe et al., 2010)
329	13.2106/54.5498	4290 ± 50	-0.4	4654	4859.5	5033	0	(Lampe et al., 2010)
330	13.2106/54.5498	4300 ± 40	-0.4	4824.5	4862.5	4971.5	0	(Lampe et al., 2010)
331	13.2927/54.5488	6181 ± 35	-1.1	6959.5	7079	7173.5	1	(Lampe et al., 2010)
332	13.2927/54.5488	6574 ± 35	-1.1	7425.5	7472	7561.5	1	(Lampe et al., 2010)
333	13.3373/54.5802	6577 ± 32	-1.7	7427	7472.5	7560	1	(Lampe et al., 2010)
334	13.6066/54.3999	5844 ± 70	-1.9	6479	6654	6844.5	0	(Lampe et al., 2010)
335	13.6066/54.3999	7698 ± 46	-7.6	8406.5	8483.5	8579.5	0	(Lampe et al., 2010)
336	13.6055/54.4022	8060 ± 80	-9.1	8644.5	8941.5	9243	0	(Lampe et al., 2010)
338	13.283/54.5516	6840 ± 100	-3.7	7512.5	7689	7926	0	(Lampe et al., 2010)
339	13.283/54.5516	6700 ± 90	-3.5	7426.5	7567.5	7695.5	0	(Lampe et al., 2010)
340	13.1038/54.5792	8010 ± 195	-11.8	8449.5	8894.5	9405.5	0	(Lampe et al., 2010)
341	13.1212/54.5292	7400 ± 55	-6.6	8049	8240	8360.5	0	(Lampe et al., 2010)
342	13.145/54.5744	595 ± 65	-0.5	520	597	667	0	(Lampe et al., 2010)
343	13.0725/54.5009	7475 ± 90	-8.1	8049	8283.5	8427.5	0	(Lampe et al., 2010)
344	13.1254/54.5334	7260 ± 135	-4	7841	8090.5	8365.5	0	(Lampe et al., 2010)
345	13.5259/54.4814	4632 ± 38	-0.2	5296.5	5403.5	5468	1	(Lampe et al., 2010)
346	13.5259/54.4814	5324 ± 39	-0.4	5991.5	6100	6262.5	1	(Lampe et al., 2010)
347	13.5259/54.4814	5368 ± 38	-0.6	6005.5	6177	6278.5	1	(Lampe et al., 2010)
349	13.5259/54.4814	5645 ± 39	-0.7	6315.5	6425.5	6497	1	(Lampe et al., 2010)
378	13.1058/54.5376	7600 ± 35	-9.4	8355	8399.5	8449.5	0	(Naumann and Lampe, 2014)
	Curve: Fischland Zingst							
350	12.3618/54.2672	6255 ± 74	-3.5	6952.5	7173	7323	0	(Lampe et al., 2010)
351	12.3618/54.2672	6150 ± 40	-3.3	6941	7058.5	7164.5	0	(Lampe et al., 2010)
352	12.3618/54.2672	5881 ± 36	-2.8	6634.5	6702	6789	0	(Lampe et al., 2010)
353	12.3618/54.2672	5285 ± 65	-2.1	5921.5	6073	6263	0	(Lampe et al., 2010)
354	12.3618/54.2672	4657 ± 56	-1.8	5292	5403	5581.5	0	(Lampe et al., 2010)
355	12.3618/54.2672	3611 ± 54	-1	3728	3923	4086.5	0	(Lampe et al., 2010)
356	12.36/54.2666	780 ± 25	-0.1	673	700.5	732	0	(Lampe et al., 2010)
357	12.36/54.2666	2175 ± 25	-0.2	2116	2243	2307.5	0	(Lampe et al., 2010)
358	12.36/54.2666	2745 ± 30	-0.8	2767	2829.5	2922	0	(Lampe et al., 2010)

Id	Location [°E/°N]	^{14}C age [a BP]	Elev. [m]	cal. age [a BP] min.	med.	max.	type	Reference
360	12.36/54.2666	3225 ± 30	-0.9	3377	3438	3555.5	0	(Lampe et al., 2010)
361	12.36/54.2666	3835 ± 30	-1.1	4148.5	4237	4405	0	(Lampe et al., 2010)
362	12.36/54.2666	4095 ± 30	-1.3	4449	4602.5	4809.5	0	(Lampe et al., 2010)
363	12.36/54.2666	4390 ± 30	-1.5	4866.5	4943	5040	0	(Lampe et al., 2010)
364	12.36/54.2666	4655 ± 30	-1.7	5313	5402.5	5466	0	(Lampe et al., 2010)
365	12.36/54.2666	4920 ± 30	-1.9	5595	5637	5714.5	0	(Lampe et al., 2010)
366	12.36/54.2666	4550 ± 25	-1.6	5056	5155.5	5316.5	0	(Lampe et al., 2010)
367	12.36/54.2666	4920 ± 30	-1.9	5595	5637	5714.5	0	(Lampe et al., 2010)
368	12.36/54.2666	5325 ± 30	-2.5	5996	6098	6200	0	(Lampe et al., 2010)
369	12.36/54.2666	5845 ± 30	-3.1	6563	6664	6739	0	(Lampe et al., 2010)
371	12.36/54.2666	6135 ± 35	-3.7	6937.5	7035.5	7160	0	(Lampe et al., 2010)
372	12.36/54.2666	6475 ± 30	-4.2	7319	7377	7434	0	(Lampe et al., 2010)
373	12.3722/54.2677	6670 ± 35	-3.9	7475.5	7537	7594.5	0	(Lampe et al., 2010)
374	12.6848/54.4565	7395 ± 40	-9.5	8063.5	8241	8340.5	0	(Lampe et al., 2010)
375	12.8068/54.3867	7100 ± 35	-6.8	7849.5	7935.5	7997	0	(Lampe et al., 2010)
376	12.764/54.4173	7020 ± 30	-5	7791	7865.5	7934.5	0	(Naumann and Lampe, 2014)
377	12.7405/54.4402	7005 ± 40	-5.8	7739	7845	7936.5	0	(Naumann and Lampe, 2014)
379	12.7844/54.3756	6585 ± 30	-3.6	7429.5	7478.5	7561.5	0	(Naumann and Lampe, 2014)
380	12.7844/54.3756	4125 ± 30	-1.3	4529	4664	4815.5	0	(Naumann and Lampe, 2014)
382	12.3603/54.2672	4490 ± 100	-1.1	4857	5134	5446.5	0	(Lampe et al., 2010)
383	12.3603/54.2672	595 ± 65	-0.1	520	597	667	0	(Lampe et al., 2010)
384	12.3603/54.2672	820 ± 80	-0.1	659	754.5	919	0	(Lampe et al., 2010)
385	12.3603/54.2672	710 ± 80	-0.1	540	662	786	0	(Lampe et al., 2010)
386	12.3603/54.2672	2555 ± 70	-0.5	2378.5	2614	2779	0	(Lampe et al., 2010)
387	12.3603/54.2672	2410 ± 90	-0.4	2213	2493.5	2742.5	0	(Lampe et al., 2010)
388	12.3603/54.2672	355 ± 85	0	1950	397	539.5	0	(Lampe et al., 2010)
389	13.0744/54.5572	7220 ± 50	-9.2	7959	8034.5	8161	1	(Naumann and Lampe, 2014)
390	12.8716/54.4245	7195 ± 40	-7.3	7939.5	8001	8155	1	(Naumann and Lampe, 2014)
	Curve: Salt meadows							
391	12.3603/54.2672	355 ± 85	0	1950	397	539.5	0	(Lampe and Janke, 2004)
227	12.6864/54.3682	780 ± 105	-0.3	554.5	728.5	922.5	0	(Lampe and Janke, 2004)
228	13.6843/54.1653	920 ± 55	0	728.5	838.5	932	0	(Lampe and Janke, 2004)

Id	Location [°E/°N]	^{14}C age [a BP]	Elev. [m]	cal. age [a BP] min.	med.	max.	type	Reference
229	13.3932/54.1428	1420 ± 80	0.1	1182	1335	1522	0	(Lampe and Janke, 2004)
230	12.6864/54.3682	1505 ± 240	-0.2	934	1439.5	1947.5	0	(Lampe and Janke, 2004)
231	13.3932/54.1428	1919 ± 184	0	1418.5	1873	2331	0	(Lampe and Janke, 2004)
232	12.3603/54.2672	2410 ± 90	-0.4	2213	2493.5	2742.5	0	(Lampe and Janke, 2004)
235	12.6864/54.3682	3000 ± 135	-0.5	2804.5	3170.5	3478.5	0	(Lampe and Janke, 2004)
236	13.3932/54.1428	3730 ± 70	-0.1	3879.5	4084.5	4347	0	(Lampe and Janke, 2004)
237	13.3932/54.1428	3690 ± 310	-0.3	3251	4074	4950	0	(Lampe and Janke, 2004)
238	13.6843/54.1653	3880 ± 145	-0.4	3901	4302	4809.5	0	(Lampe and Janke, 2004)
240	13.3932/54.1428	4500 ± 140	-0.2	4837.5	5148.5	5577	0	(Lampe and Janke, 2004)
241	13.6843/54.1653	4555 ± 130	-0.5	4868.5	5206.5	5579	0	(Lampe and Janke, 2004)
242	12.4658/54.2494	4990 ± 75	-0.5	5601.5	5733	5898	0	(Lampe and Janke, 2004)
243	13.3892/54.1571	5035 ± 105	-0.6	5588.5	5783	5989.5	0	(Lampe and Janke, 2004)
244	13.6843/54.1653	5550 ± 75	-0.9	6208	6349.5	6490.5	0	(Lampe and Janke, 2004)
246	12.7845/54.3813	5520 ± 100	-1.1	6010.5	6319.5	6532	0	(Lampe and Janke, 2004)
247	13.6843/54.1653	5734 ± 70	-1	6350	6533	6716	0	(Lampe and Janke, 2004)
248	13.3902/54.1731	1190 ± 45	-0.6	982	1117.5	1256	1	(Lampe and Janke, 2004)
249	13.3932/54.1428	1410 ± 40	-0.5	1279	1319	1380.5	1	(Lampe and Janke, 2004)
250	13.6843/54.1653	4280 ± 85	-0.3	4533.5	4850	5259.5	1	(Lampe and Janke, 2004)
251	13.6843/54.1653	5000 ± 160	-0.3	5329	5755.5	6177.5	1	(Lampe and Janke, 2004)
252	13.6843/54.1653	5175 ± 160	-0.3	5610.5	5944	6280.5	1	(Lampe and Janke, 2004)
253	13.6843/54.1653	5175 ± 72	-0.3	5745	5935.5	6178	1	(Lampe and Janke, 2004)
	Curve: Poel							
254	11.6347/54.143	7919 ± 37	-12.7	8605.5	8742.5	8976.5	1	(Lampe et al., 2010)
255	11.6347/54.143	7788 ± 38	-12.7	8454.5	8565.5	8634.5	1	(Lampe et al., 2010)
257	11.6347/54.143	7741 ± 38	-12.8	8434	8515	8590	1	(Lampe et al., 2010)
258	11.6539/54.1552	7464 ± 46	-7.7	8189	8282	8372.5	1	(Lampe et al., 2010)
259	11.6612/54.1489	7290 ± 32	-8.8	8023	8100.5	8171.5	1	(Lampe et al., 2010)
260	11.6508/54.144	7229 ± 38	-8.5	7969	8038.5	8159	1	(Lampe et al., 2010)
261	11.6508/54.144	7224 ± 32	-8.5	7966.5	8026.5	8157.5	1	(Lampe et al., 2010)
262	11.6612/54.1489	7197 ± 33	-8.8	7947	7999.5	8152	1	(Lampe et al., 2010)
263	11.6638/54.1469	7158 ± 40	-5.1	7874.5	7977.5	8038.5	1	(Lampe et al., 2010)
264	11.6612/54.1489	7150 ± 31	-8.8	7933.5	7972	8018	1	(Lampe et al., 2010)
265	11.6612/54.1489	7146 ± 33	-8.8	7879	7969.5	8019.5	1	(Lampe et al., 2010)
266	11.6638/54.1469	7133 ± 50	-5.2	7847.5	7959	8029.5	1	(Lampe et al., 2010)
268	11.6638/54.1469	7032 ± 35	-5.7	7791	7875.5	7943	1	(Lampe et al., 2010)
269	11.6638/54.1469	6856 ± 33	-5.1	7614	7682.5	7781	1	(Lampe et al., 2010)
270	11.6638/54.1469	6842 ± 27	-5.1	7611.5	7670	7724	1	(Lampe et al., 2010)
271	11.671/54.1485	6243 ± 34	-3.1	7021.5	7187	7257.5	1	(Lampe et al., 2010)

Id	Location [°E/°N]	^{14}C age [a BP]	Elev. [m]	cal. age [a BP] min.	med.	max.	type	Reference
272	11.6711/54.1483	5870 ± 28	-1.5	6635.5	6693.5	6771.5	1	(Lampe et al., 2010)
273	11.6712/54.1484	5725 ± 36	-1.3	6434.5	6517.5	6634.5	1	(Lampe et al., 2010)
274	11.3677/53.9933	6532 ± 44	-5	7328	7448.5	7559.5	1	(Lampe et al., 2010)
275	11.3678/53.9932	6319 ± 43	-5	7161	7248.5	7411	1	(Lampe et al., 2010)
276	11.4524/54.0543	6882 ± 33	-7.8	7627	7710	7794	1	(Lampe et al., 2010)
277	11.4707/54.0511	7154 ± 41	-8.2	7870.5	7974.5	8039.5	1	(Lampe et al., 2010)
279	11.4707/54.0511	7090 ± 32	-8.5	7849	7926.5	7971.5	1	(Lampe et al., 2010)
280	11.4727/54.0527	7022 ± 44	-6.5	7751.5	7862	7949.5	1	(Lampe et al., 2010)
281	11.4727/54.0527	7014 ± 36	-6.7	7757.5	7857	7938	1	(Lampe et al., 2010)
282	11.4719/54.0517	6969 ± 33	-7.2	7701	7800.5	7922.5	1	(Lampe et al., 2010)
283	11.4719/54.0519	6916 ± 35	-7.2	7675.5	7741	7828.5	1	(Lampe et al., 2010)
284	11.4729/54.0527	6888 ± 35	-6.6	7658.5	7716.5	7820	1	(Lampe et al., 2010)
285	11.464/54.053	7022 ± 33	-7.9	7787	7866.5	7939	1	(Lampe et al., 2010)
286	11.3883/53.9728	885 ± 25	0	731.5	790	905	0	(Lampe et al., 2010)
287	11.3947/53.9652	6775 ± 35	-7.3	7578.5	7625	7672	0	(Lampe et al., 2010)
288	11.4856/53.9478	4791 ± 33	-3.2	5468.5	5516	5595	0	(Lampe et al., 2010)
290	11.4856/53.9478	4624 ± 45	-3	5084	5394.5	5571	0	(Lampe et al., 2010)
291	11.4856/53.9478	4466 ± 37	-2.7	4970	5142.5	5289.5	0	(Lampe et al., 2010)
292	11.4856/53.9478	3918 ± 57	-2.4	4157	4347	4518	0	(Lampe et al., 2010)
293	11.4856/53.9478	3664 ± 80	-1.9	3728.5	3997	4237.5	0	(Lampe et al., 2010)
294	11.4856/53.9478	1810 ± 31	-1	1625	1748.5	1823	0	(Lampe et al., 2010)
295	11.4856/53.9478	1707 ± 26	-0.9	1551.5	1607	1696	0	(Lampe et al., 2010)
296	11.4856/53.9478	895 ± 33	-0.5	734.5	820	910.5	0	(Lampe et al., 2010)
297	11.4856/53.9478	535 ± 23	0.2	515	539	626.5	0	(Lampe et al., 2010)
298	11.4856/53.9478	490 ± 23	-0.3	504.5	521	539.5	0	(Lampe et al., 2010)
299	11.4856/53.9478	226 ± 33	0	1950	196	420	0	(Lampe et al., 2010)
301	11.5136/54.0387	7285 ± 35	-11	8018.5	8098.5	8172	0	(Lampe et al., 2010)

TABLE C.4: List of considered sea level indicators in the region of Ångermanland:

Id	Location [°E/°N]	^{14}C age [a BP]	Elev. [m]	cal. age [a BP] min.	med.	max.	Reference
	CURVE: ÅNGERMANLAND						
64	17.7822/63.0439	1039 ± 10	7.5	1049	1039	1029	(Cato, 1992, 1987)
65	17.8128/63.0228	600 ± 6	3.5	606	600	594	(Cato, 1992, 1987)
66	17.8031/63.0056	204 ± 2	1.5	206	204	202	(Cato, 1992, 1987)
67	17.4167/63.0333	7775 ± 77	127.8	7698	7775	7852	(Cato, 1992; Wallin, 1996)
68	17.9/62.9667	2761 ± 27	29	2734	2761	2788	(Cato, 1992; Wallin, 1996)
174	16.8913/63.4395	8022 ± 80	133.9	7942	8022	8102	(Cato, 1998, 1992; Lidén, 1938)
175	17.0761/63.3369	6890 ± 68	100.1	6822	6890	6958	(Cato, 1998, 1992; Lidén, 1938)
176	17.2065/63.2735	6246 ± 62	85.4	6184	6246	6308	(Cato, 1998, 1992; Lidén, 1938)
177	17.1956/63.2539	5791 ± 57	75.2	5734	5791	5848	(Cato, 1998, 1992; Lidén, 1938)
178	17.1956/63.2344	5613 ± 56	72.2	5557	5613	5669	(Cato, 1998, 1992; Lidén, 1938)
179	17.2934/63.1758	4432 ± 44	49.4	4388	4432	4476	(Cato, 1998, 1992; Lidén, 1938)
180	17.3695/63.1563	4172 ± 41	46.1	4131	4172	4213	(Cato, 1998, 1992; Lidén, 1938)
181	17.4021/63.1612	3996 ± 39	45.2	3957	3996	4035	(Cato, 1998, 1992; Lidén, 1938)
182	17.4674/63.1758	3486 ± 34	37.7	3452	3486	3520	(Cato, 1998, 1992; Lidén, 1938)
183	17.6087/63.1758	2443 ± 24	23.3	2419	2443	2467	(Cato, 1998, 1992; Lidén, 1938)
184	17.7499/63.1221	1857 ± 18	15	1839	1857	1875	(Cato, 1998, 1992; Lidén, 1938)
185	17.7636/63.0769	1395 ± 13	10.2	1408	1395	1382	(Cato, 1998, 1992; Lidén, 1938)
186	17.7/62.8333	6098 ± 60	79	6038	6098	6158	(Cato, 1992; Segerström et al., 1984)
187	18.3/62.95	2799 ± 27	30.4	2772	2799	2826	(Cato, 1992; Segerström et al., 1984)

D

Data excluded from the study

We present results from regions Kattegat, northern Jutland (Jylland) and Arkona Basin that were excluded from this study due to uncertainties in RSL caused by their location. First two figures present variability of 1D model ensemble (Figs. D.1, D.2). Last four figures are showing overestimation of ten 3D models used in this study (Figs. D.3 – D.6).

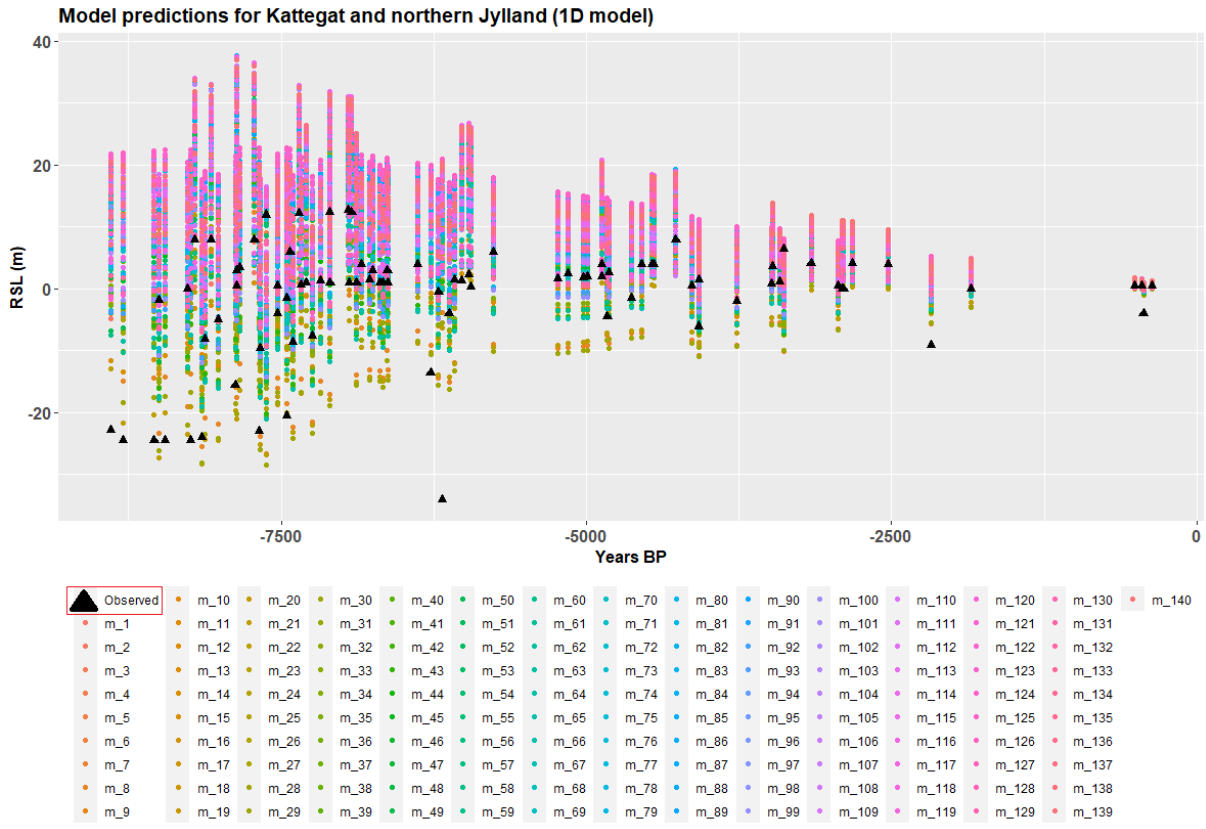

FIGURE D.1: Variability of model ensemble prediction for the region of northern Jutland and the Kattegat. Black triangles are presenting SLIs.

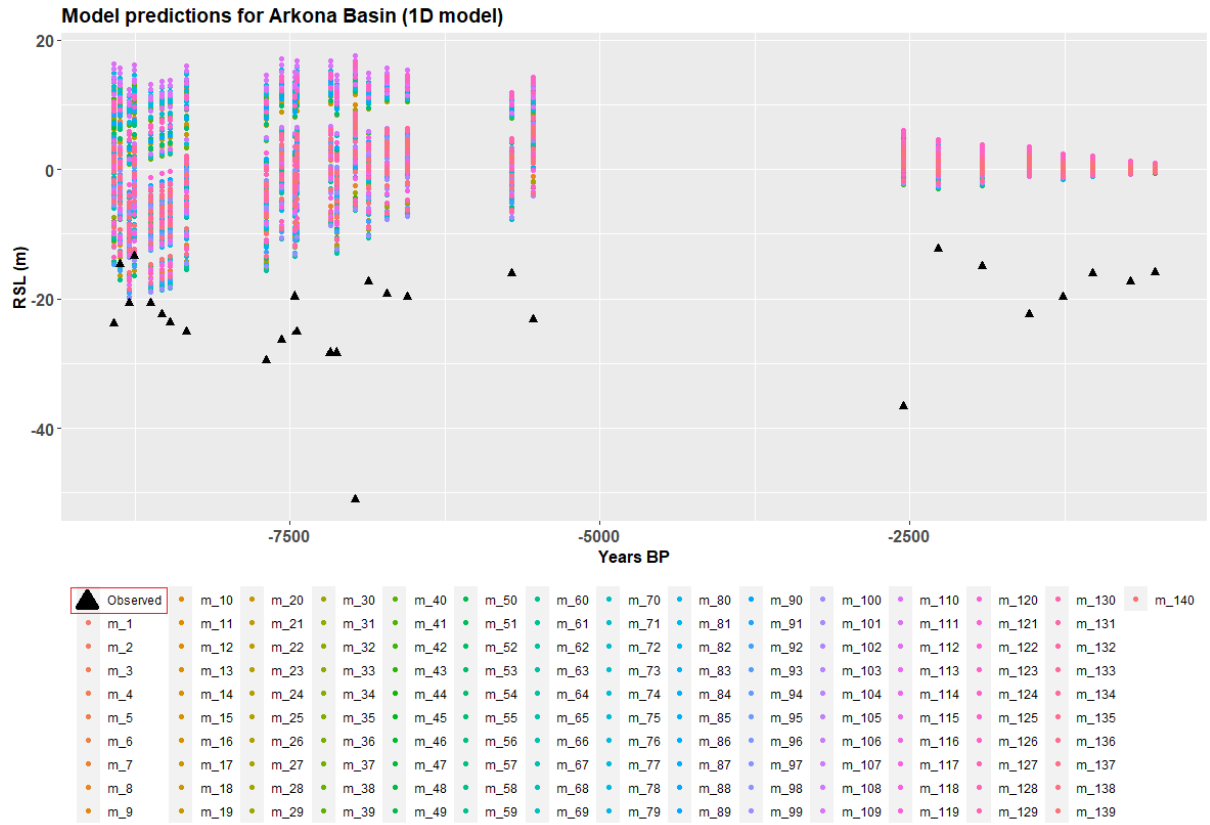

FIGURE D.2: Variability of model ensemble prediction for the Arkona Basin. Black triangles are presenting SLIs.

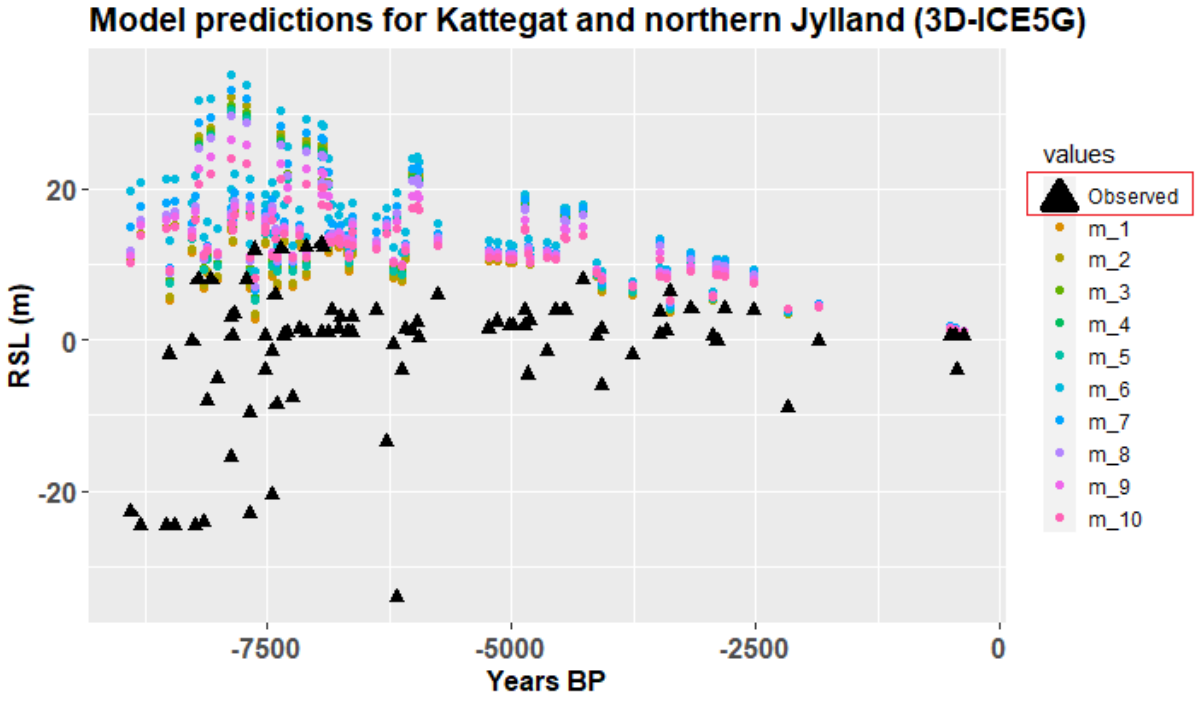

FIGURE D.3: Ten 3D models (ICE5G) in the northern Jutland and the Kattegat.

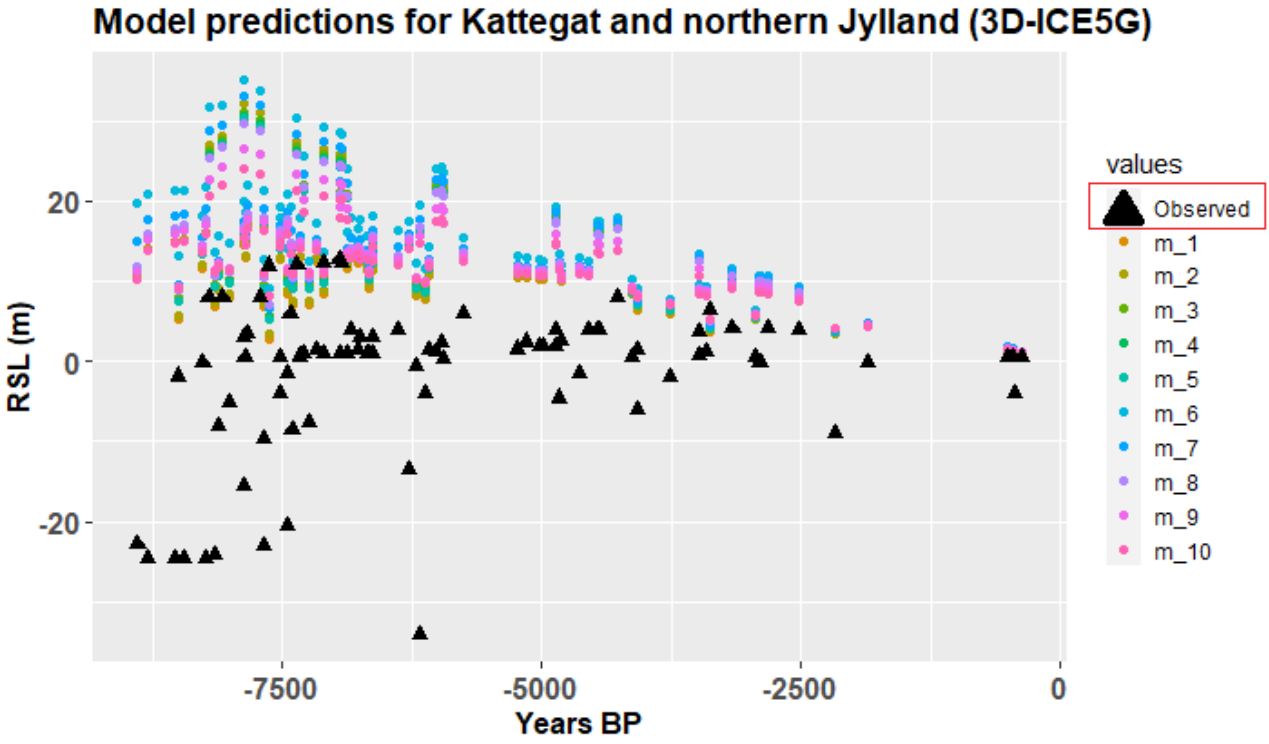

FIGURE D.4: Ten 3D models (ICE6G_C) in the northern Jutland and the Kattegat.

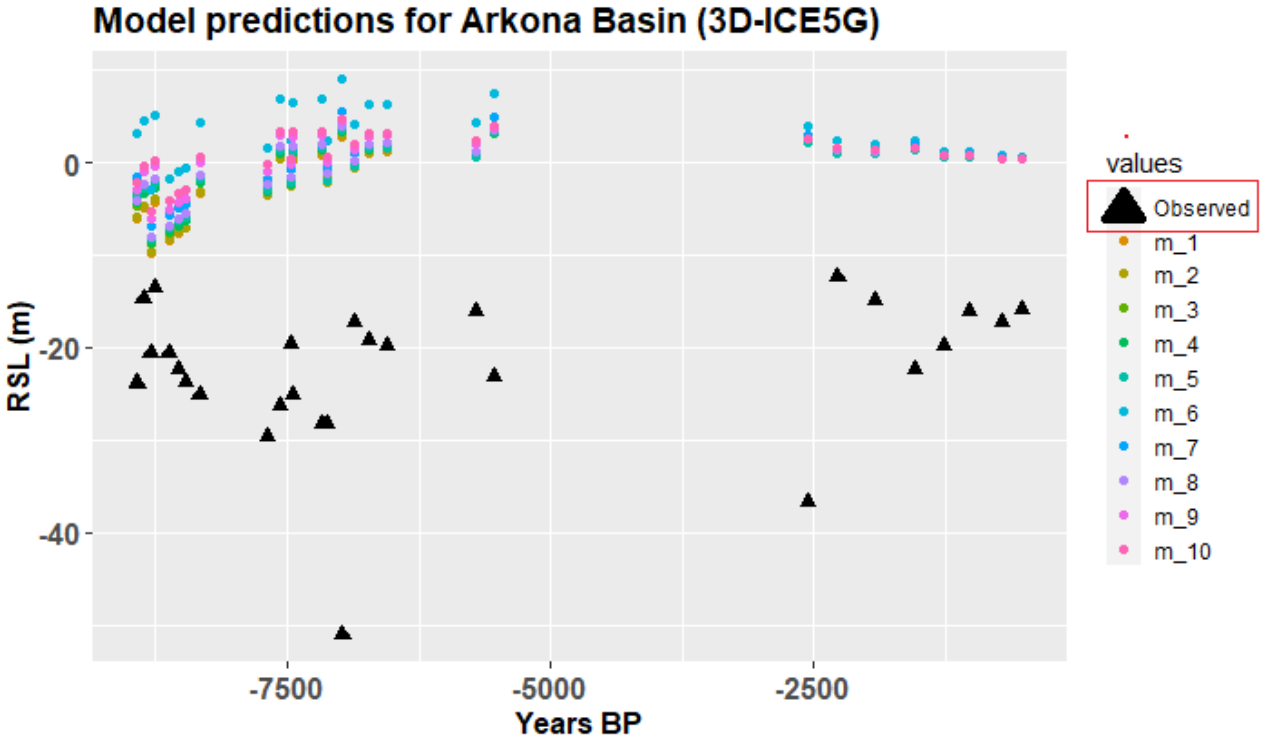

FIGURE D.5: Ten 3D models (ICE5G) in the Arkona Basin.

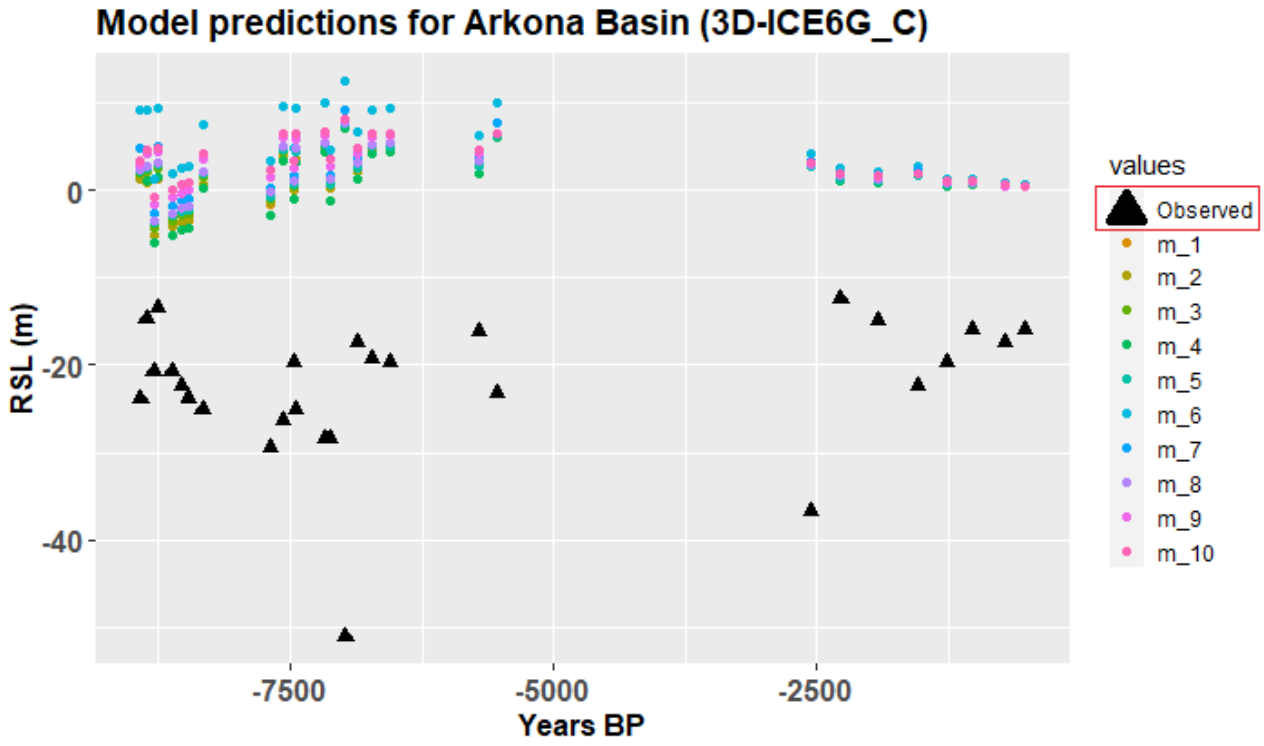

FIGURE D.6: Ten 3D models (ICE6G_C) in the Arkona Basin.

Bibliography

Allard, M., A. Fournier, E. Gahé, and M. K. Seguin (1989). Le quaternaire de la côe sud-est de la baie d'ungava, québec nordique. *Geogr. Phys. Quat. 43*, 325–326. M, RSL, Hudson Bay.

Allard, M. and G. Tremblay (1983). La dynamique littorale des îles Manitounuk durant l'Holocène. *Z. Geomorphol. suppl. 47*, 61–95. S.

Alley, R. B., P. U. Clark, P. Huybrechts, and I. Joughin (2005). Ice-sheet and sea-level changes. *Science 310*(5747), 456–460.

Analytic, B. (2019). Radiocarbon dating. web, last consulted on 10.08.2019.

Andersen, S. H. (2013). Submerged mesolithic settlements in Denmark. *Jutland arch. Soc. Publ. 77*, 1–527.

Andrews, J. T. and G. Falconer (1969). Late glacial and post-glacial history and emergence of the Ottawa Islands, Hudson Bay, Northwest Territorities: evidence on the deglaciation of Hudson Bay. *Can. J. Earth Sci. 6*, 1263–1276. D.

Bagge, M., V. Klemann, B. Steinberger, M. Latinovic, and M. Thomas (submitted 2020). Glacial-isostatic adjustment models using geodinamically 3d earth structures. Work in preparation for Geochemistry, Geophysics, Geosystems.

Bennike, O., M. S. Andreasen, J. B. Jensen, and N. Noe-Nyegaard (2012). Early Holocene sea-level changes in Øresund, Scandinavia. *Bull. Geol. Surv. Denm. Greenl. 26*, 29–32.

Bennike, O. and J. Jensen (1998, 01). Late- and postglacial shore level changes in the southwestern baltic sea. *Bulletin of the Geological Society of Denmark 45*, 27–38.

Bennike, O. and J. B. Jensen (2011). Postglacial relative shore level changes in Lillebælt, Denmark. *Bull. Geol. Surv. Denm. Greenl. 23*, 37–40.

Bennike, O., J. B. Jensen, P. Konradi, W. Lemke, and J. Heinemeier (2000). Early Holocene lagoonal deposits from Kattegat, Scandinavia. *Boreas 29*, 272–286.

Bennike, O., J. B. Jensen, W. Lemke, A. Kuijpers, and S. Lomholt (2004). Late- and postglacial history of the Great Belt, Denmark. *Boreas 33*, 18–33.

Bennike, O., P. Pantmann, and E. Aarsleff (2017, 01). Holocene development of the arresø area, north-east sjælland, denmark. *Bulletin of the Geological Society of Denmark 65*, 25–35.

Berglund, B., P. Sandgren, L. Barnekow, G. Hannon, H. Jiang, G. Skog, and S.-Y. Yu (2005). Early holocene history of the baltic sea, as reflected in coastal sediments in blekinge, southeastern sweden. *Quaternary International 130*(1), 111 – 139. Baltic Sea Science Congress 2001.

Björck, S. (1995). A review of the history of the Baltic Sea, 13.0-8.0 ka BP. *Quat. Int. 27*, 19–40. M,pdf.

Bjørtvedt, E. (2011). Geological map of Northern Europe, focusing on the Avallonian, Baltic and Sarmatian cratons and orogenies. (in norwegian. web, last consulted on 20.11.2019. Bjoertvedt [CC BY-SA 3.0 (https://creativecommons.org/licenses/by-sa/3.0)].

Bobee, B. and F. Ashkar (1991). *The Gamma Family and Derived Distributions Applied in Hydrology*. Littleton, Colorado: Water Resources Publications.

Bogdanova, S., R. Gorbatschev, M. Grad, T. Janik, A. Guterch, E. Kozlovskaya, G. Motuza, G. Skridlaite, V. Starostenko, and L. Taran (2006). Eurobridge: new insight into the geodynamic evolution of the east european craton. *Geological Society, London, Memoirs 32*(1), 599–625.

Boltwood, B. (1907). The origin of radium. *Nature 76*, 544–545.

Bradley, S. L., G. A. Milne, I. Shennan, and R. Edwards (2011). An improved glacial isostatic adjustment model for the british isles. *Journal of Quaternary Science 26*(5), 541–552.

Briggs, R. D. and L. Tarasov (2013). How to evaluate model-derived deglaciation chronologies: a case study using antarctica. *Quaternary Science Reviews 63*, 109 – 127.

Bronk Ramsey, C. (2009). Bayesian analysis of radiocarbon dates. *Radiocarbon 51*(1), 337–360.

Bruneau, D. and J. T. Gray (1991). *Preliminary Map 11-1990.* GSC Map 11-1990. Ottawa: Geological Survey of Canada. M.

Bruneau, D. and J. T. Gray (1997). Écoulements glaciaires et déglaciation hâtive (ca 11 ka bp) du nord-est de la péninsule d'ungava, québec, canada. *Can. J. Earth Sci. 34*, 1089–1100. M.

Butzin, M., P. Köhler, and G. Lohmann (2017a). Marine radiocarbon reservoir age simulations for the past 50,000 years. *Geophysical Research Letters 44*(16), 8473–8480.

Butzin, M., P. Köhler, and G. Lohmann (2017b). Marine radiocarbon reservoir ages for the past 50,000 years, links to model results in netcdf format. pangaea, supplement to: Butzin,

m et al. (2017): Marine radiocarbon reservoir age simulations for the past 50,000 years. geophysical research letters, 44(16), 8473-8480, https://doi.org/10.1002/2017gl074688v. data.

Canadian Society of Soil Science (2019). Soils of Canada. web, last consulted on 15.11.2019.

Carlson, A. E., P. U. Clark, G. M. Raisbeck, and E. J. Brook (2007). Rapid holocene deglaciation of the labrador sector of the laurentide ice sheet. *Journal of Climate 20*(20), 5126–5133.

Caron, L., E. R. Ivins, E. Larour, S. Adhikari, J. Nilsson, and G. Blewitt (2018). Gia model statistics for grace hydrology, cryosphere, and ocean science. *Geophys. Res. Lett. 45*, 2203–2212. pdf.

Cato, I. (1985). The definitive connection of the Swedish Geochronological Time Scale with the present and the new date of the zero-year in Döviken, northern Sweden. *Boreas 14*, 117–122. M.

Cato, I. (1987). On the definitive connection of the Swedish time scale with the present. *Sverig. Geol. Unders. Ca 68*, 55. M.

Cato, I. (1992). Shore displacement data based on lake isolations confirm the postglacial part of the Swedish geochronological time scale. *Sverig. Geol. Unders. Ca 81*, 75–80. M.

Cato, I. (1998). Ragnar Liden's postglacial varve chronology from the Angermanälven Valley, northern Sweden. *Sverig. Geol. Unders. 88*, 82. S.

Chamberlain, E. (2018). A bright approach to geochronology. *Physics Today 71*, 74–75.

Christensen, C. (2014). *Havniveauændringer 5500-2500 f. Kr. i Vedbæk-området, NØ-Sjælland – fortsatte geobotaniske undersøgelser i årene 1982-1990.* Number 15 in Nationalmuseets Naturvidenskabelige Undersøgelser NNU-rapport 2014.

Christensen, C., A. Fischer, and D. Mathiasen (1997). The great sea rise in the Storebælt. In L. Pedersen, A. Fischer, and B. Aaby (Eds.), *The Danish Storebælt since the Ice Age*, pp. 45–54 and 323–324. Copenhagen: A/S Storebæltsforbindelsen.

Christensen, C. and A. B. Nielsen (2008). Dating Littorina Sea shore levels in Denmark on the basis of data from a Mesolithic coastal settlement on Skagens Odde, northern Jutland. *Pol. Geol. Inst., Special Pap. 23*, 27–38.

Christensen, N. I. (1982). Seismic velocities. In R. S. Carmichael (Ed.), *Handbook of Physical Properties of Rocks, Vol. 2*, pp. 2–228. Inc: CRC Press. pdf.

Christensen, U. (1983). Convection in a variable-viscosity fluid: Newtonian versus power-law rheology. *Earth and Planetary Science Letters 64*(1), 153 – 162.

Cianetti, S., C. Giunchi, and G. Spada (2002). Mantle viscosity beneath the Hudson Bay: an inversion based on the Metropolis algorithm. *J. Geophys. Res. 107*, 2352, doi:10.1029/2001JB000585. pdf.

Clark, P. U., R. B. Alley, and D. Pollard (1999). Northern hemisphere ice-sheet influences on global climate change. *Science 286*(5442), 1104–1111.

Clarke, R. T. (1980). Bivariate gamma distributions for extending annual streamflow records from precipitation: some large sample results. *Water Resour. Res. 16*, 863–870.

Craig, B. G. (1969). Late-glacial and post-glacial history of the Hudson Bay region. In P. J. Hood (Ed.), *Earth Science Symposium on Hudson Bay*, GSC Paper 68-53, pp. 63–77. Ottawa: Geological Survey of Canada.

Davis, J. L., J. X. Mitrovica, H.-G. Scherneck, and H. Fan (1999). Investigations of fennoscandian glacial isostatic adjustment using modern sea level records. *Journal of Geophysical Research: Solid Earth 104*(B2), 2733–2747.

De Boer, B., P. Stocchi, and R. Wal (2014, 09). A fully coupled 3-d ice-sheet-sea-level model: Algorithm and applications. *Geoscientific Model Development 7*.

De Geer, G. (1884). Om möjligheten af att införa en kronologi för istiden. *Geol. Fören. Stockh. Förh 7*(3).

De Geer, G. (1940). Geochronologia suecica principles.–kva handl., tredje ser., bd 18, nr 6. *GLACIALGEOLOGI OCH ISAVSMÄLTNING I ÖSTRA BLEKINGE-173*.

Deschamps, P., N. Durand, E. Bard, B. Hamelin, G. Camoin, A. Thomas, G. Henderson, J. Okuno, and Y. Yokoyama (2012, 03). Ice-sheet collapse and sea-level rise at the b??lling warming 14,600 years ago. *Nature 483*, 559–64.

Dredge, L. A. and F. M. Nixon (1992). *Glacial and environmental geology of northeastern Manitoba*. Geological Survey of Canada, Memoir 432. Ottawa: Geological Survey of Canada. pdf.

Düsterhus, A., A. Rovere, A. E. Carlson, B. P. Horton, V. Klemann, L. Tarasov, N. L. M. Barlow, T. Bradwell, J. Clark, A. Dutton, W. R. Gehrels, F. D. Hibbert, M. P. Hijma, N. Khan, R. E. Kopp, D. Sivan, and T. E. Törnqvist (2016). Palaeo-sea-level and palaeo-ice-sheet databases: problems, strategies, and perspectives. *Climate of the Past 12*(4), 911–921.

Dziewonski, A. M. and D. L. Anderson (1981). Preliminary reference earth model. *Phys. Earth Planet. Inter. 25*, 297–356. V,pdf.

Ekman, M. (2009). *The Changing Level of the Baltic Sea During 300 Years: A Clue to Understanding the Earth*. Summer Inst. for Historical Geophysics.

Engelhart, S., W. Peltier, and B. Horton (2011, 08). Holocene relative sea-level changes and glacial isostatic adjustment of the U.S. Atlantic coast. *Geology 39*(8), 751–754.

Engelhart, S. E. and B. P. Horton (2012). Holocene sea level database for the atlantic coast of the united states. *Quat. Sci. Rev. 54*, 12–25. pdf.

England, J., A. S. Dyke, R. D. Coulthard, R. McNeely, and A. Aitken (2013). The exaggerated radiocarbon age of deposit-feeding molluscs in calcareous environments. *Boreas 42*, 362–373. pdf.

Ernst, T. (1974). Die Hohwachter Bucht. Morphologische Entwicklung einer Küstenlandschaft Ostholsteins. *Schr. Naturwiss. V. Schlesw.-Holst. 44*, 47–96. GFZ.

Eronen, M. (1983). Late Weichselian and Holocene shore displacement in Finnland. In D. E. Smith and A. L. Dawson (Eds.), *Shore lines and isostasy*, pp. 581–599. Academic Press.

Eurobridge Seismic Working Group (1999, Dec). Seismic velocity structure across the Fennoscandia-Sarmatia suture of the East European Craton beneath the EUROBRIDGE profile through Lithuania and Belarus. *Tectonophysics 314*(1-3), 193–217.

Fang, M. and B. F. Hager (2002). On the apparent exponential relaxation curves at the central regions of the last Pleistocene ice sheets. In J. X. Mitrovica and B. L. A. Vermeersen (Eds.), *Ice Sheets, Sea Level, and the Dynamic Earth*, Volume 29 of *Geodynamic Series*, pp. 201–218. Washington: American Geophysical Union. D.

Farrell, W. E. and J. A. Clark (1976). On postglacial sea level. *Geophys. J. R. Astr. Soc. 46*, 647–667. PDF.

Feldens, P. and K. Schwarzer (2012). The Ancylus Lake stage of the Baltic Sea in Fehmarn Belt: Indications of a new threshold? *Continental Shelf Research 35*, 43–52. pdf.

Fischer, A. (1993). Stenalderbopladser på bunden af Øresund. Del 1. report, Det centrale Øresund. Skov- og Naturstyrelsen.

Fischer, A. (2005). Mennesket og havet i ældre stenalder. In C. Bunte (Ed.), *Arkeologien och naturvetenskap*, pp. 227–297. Lund: Gyllenstiernska Krapperupstiftelsen.

Fjeldskaar, W. (1994). Viscosity and thickness of the asthenosphere detected from the Fennoscandian uplift. *Earth Planet. Sci. Lett. 126*, 399–410. in script,V.

Fleming, K., Z. Martinec, and D. Wolf (2003). A reinterpretation of the Fennoscandian relaxation-time spectrum for a viscoelastic lithosphere. In I. N. Tziavos (Ed.), *Gravity and Geoid 2002, 3rd Meeting of the International Gravity and Geoid Comission, Thessaloniki, Greece, August 26–30, 2002*, Thessaloniki, pp. 432–438. Ziti Publishing. V.

Gamage, S. H. P. W., G. A. Hewa, and S. Beecham (2013). Probability distributions for explaining hydrological losses in south australian catchments. *Hydrology and Earth System Sciences 17*(11), 4541–4553.

Ganopolski, A., S. Rahmstorf, V. K. Petoukhov, and M. P. Claussen (1998). Simulation of modern and glacial climates with a coupled global model of intermediate complexity. *Nature 391*, 351–356.

Geissler, W. H., F. Sodoudi, and R. Kind (2010, 05). Thickness of the central and eastern European lithosphere as seen by S receiver functions. *Geophysical Journal International 181*(2), 604–634.

Godwin, K., J. Shallenberger, D. Leopold, and B. Bedford (2002, 12). Linking landscape properties to local hydrogeologic gradients and plant species occurrence in minerotrophic fens of new york state, usa: A hydrogeologic setting (hgs) framework. *Wetlands 22*, 722–737.

Gomez, N., D. Pollard, and J. X. Mitrovica (2013). A 3-d coupled ice sheet – sea level model applied to antarctica through the last 40 ky. *Earth and Planetary Science Letters 384*, 88 – 99.

Gomez, N., D. Pollard, J. X. Mitrovica, P. Huybers, and P. U. Clark (2012). Evolution of a coupled marine ice sheet–sea level model. *J. Geophys. Res. 117*(F1).

Gowan, E. J., P. Tregoning, A. Purcell, J.-P. Montillet, and S. McClusky (2016). A model of the western laurentide ice sheet, using observations of glacial isostatic adjustment. *Quaternary Science Reviews 139*, 1 – 16.

Grad, M., T. Janik, A. Guterch, P. Sroda, W. Czuba, V. Astapenko, A. Belinsky, R. Garetsky, G. Karatayev, V. Terletsky, G. Zlotski, S. Jensen, M. Knudsen, H. Thybo, R. Sand, K. Komminaho, U. Luosto, T. Tiira, J. Yliniemi, and A. Smirnov (2006, 01). Lithospheric structure of the western part of the east european craton investigated by deep seismic profiles. *Geological Quarterly 50*, 9–22.

Grad, M., G. Keller, H. Thybo, and A. Guterch (2002). Lower lithospheric structure beneath the trans-european suture zone from polonaise'97 seismic profiles. *Tectonophysics 360*(1), 153 – 168. Geophysical Investigations og the Trans-European Suture Zone II.

Grand, S. P. (2002). Mantle shear–wave tomography and the fate of subducted slabs. *Philosophical Transactions of the Royal Society of London. Series A: Mathematical, Physical and Engineering Sciences 360*(1800), 2475–2491.

Gray, J., B. de Boutray, C. Hillaire-Marcel, and B. Lauriol (1980). Postglacial emergence of the west coast of ungava bay, quebec. *Arctic Alpine Res. 12*, 19–30. pdf.

Gray, J., B. Lauriol, D. Bruneau, and J. Ricard (1993). Postglacial emergence of ungava peninsula, and its relationship to glacial history. *Can. J. Earth Sci. 30*, 1976–1996. 0, RSL, Hudson Bay.

Gray, J. T. and B. Lauriol (1985). Dynamics of the late wisconsin ice sheet in the ungava peninsula interpreted from geomorphological evidence. *Arctic Alpine Res. 17*, 289. pdf.

Guterch, A., M. Grad, H. Thybo, and G. Keller (1999). Polonaise '97 — an international seismic experiment between precambrian and variscan europe in poland. *Tectonophysics 314*(1), 101 – 121.

Guterch, A., M. Grad, A. Špicák, E. Brückl, E. Hegedüs, R. Keller, H. Thybo, K. Aric, S. Acevedo, I. Asudeh, M. Behm, A. Belinsky, T. Bodoky, R. Brinkmann, M. Brož, W. Chwatal, R. Clowes, W. Czuba, T. Fancsik, and S. Jensen (2004, 08). Huge contrasts of the lithospheric structure revealed by new generation seismic experiments in central europe. *Przeglad Geologiczny 52*, 753–760.

Hagedoorn, J. M., D. Wolf, and Z. Martinec (2007). An estimate of global sea level rise inferred form tide gauge measurements using glacial isostatic models consistent with the relative sea level record. *Pure Appl. Geophys. 164*, 791–818. pdf.

Han, D. and J. Wahr (1995). The viscoelastic relaxation of a realistically stratified earth, and a further analysis of postglacial rebound. *Geophys. J. Int. 120*, 287–311. V, pdf.

Hansen, J. M. (1977). Dinoflagellate stratigraphy and echinoid distribution in upper maastrichtian and danian deposits from denmark. *Bull. Geol. Soc. Denmark 26*, 1–26.

Harders, R., B. Dehde, M. Diesing, M. Gelhart, and K. Schwarzer (2005). Postglacial development of neustadt bay in the western baltic sea. *Meyniana 57*, 37–60.

Hardy, B. G. (1976). *Contribution a l'etude geomprhologique de la portion Quebecoise de la Baie de James*. Ph. D. thesis, McGill University, Montreal. 0.

Hardy, L. (1977). La déglaciation et les épisodes lacustre et marin sur le versant québécois des basses terres de la baie de james. *Geogr. Phys. Quat. 31*, 261. pdf.

Haskell, N. A. (1935). The motion of a viscous fluid under a surface load. *Physics 6*, 265–369. V, pdf.

Hede, M. U., L. Sander, L. B. Clemmensen, A. Kroon, M. Pejrup, and L. Nielsen (2015). Changes in holocene relative sea-level and coastal morphology: A study of a raised beach ridge system on samsø, southwest scandinavia. *The Holocene 25*(9), 1402–1414.

Hede, S. U. (2003). Prehistoric settlements and holocene relative sea-level changes in northwest Sjælland, Denmark. *Bull. Geol. Surv. Denm. 50*, 141–149.

Heuer, B., W. H. Geissler, R. Kind, and H. Kämpf (2006). Seismic evidence for asthenospheric updoming beneath the western bohemian massif, central europe. *Geophysical Research Letters 33*(5).

Heuer, B., H. Kämpf, R. Kind, and W. H. Geissler (2007). Seismic evidence for whole lithosphere separation between saxothuringian and moldanubian tectonic units in central europe. *Geophysical Research Letters 34*(9).

Hibbert, F., E. J. Rohling, A. Dutton, F. Williams, P. M. Chutcharavan, C. Zhao, and M. E. Tamisiea (2016). Coral indicators of past sea-level change: A global repository of u-series dated benchmarks. *Quat. Sci. Rev. 145*, 1–56.

Higham, T. (2019). Radiocarbon web-info, radiocarbon laboratory, University of Waikato, New Zealand. web, last consulted on 20.10.2019.

Hijma, M. P., S. E. Engelhart, T. E. Törnqvist, B. P. Horton, P. Hu, and D. F. Hill (2015). A protocol for a geological sea-level database. In I. Shennan, A. J. Long, and B. P. Horton (Eds.), *Handbook of Sea-Level Research*, pp. 536–553. John Wiley & Sons, Ltd.

Hillaire-Marcel, C. (1976). La déglaciation el le relèvement isostatique sur la côte est de la baie d'Hudson. *Cah. Geogr. Quebec 20*, 185–220. S, M, pdf.

Hoffmann, G., N. Schmedemann, and M.-T. Schafmeister (2009). Relative sea-level curve for SE Rügen and Usedom Island (SW Baltic Sea coast, Germany) using decompacted profiles. *Z. dt. Ges. Geowiss. 160*, 69–78.

Holzhüter, W. (2012, 01). *Seasonal distribution of methane in the surface water and the water column of selected areas of the Baltic Sea*. Ph. D. thesis.

Ivins, E. R. and C. G. Sammis (1995). On lateral viscosity contrast in the mantle and the rheology of low-frequency geodynamics. *Geophys. J. Int. 123*, 305–322. V, pdf.

Jamieson, T. (1865). On the history of the last geological changes in scotland. *Quarterly Journal of the Geological Society of London 21*, 161–203.

Janutyte, I., M. Majdanski, P. H. Voss, E. Kozlovskaya, and P. W. Group (2015). Upper mantle structure around the trans-european suture zone obtained by teleseismic tomography. *Solid Earth 6*(1), 73–91.

Jensen, J. and O. Bennike (2009). Geological setting as background for methane distribution in holocene mud deposits, Århus bay, denmark. *Continental Shelf Research 29*(5), 775 – 784.

Jensen, J. B., O. Bennike, A. Witkowski, W. Lemke, and A. Kuijpers (1997). The Baltic Ice Lake in the southwestern Baltic: sequence-, chrono- and biostratigraphy. *Boreas 26*, 217–236.

Jensen, J. B. and O. Stecher (1992). Paraglacial barrier-lagoon development in the Late Pleistocene Baltic Ice Lake, southwestern Baltic. *Mar. Geol. 107*, 81–101.

Jensen, S. and H. Thybo (2002). Moho topography and lower crustal wide-angle reflectivity around the tesz in southern scandinavia and northeastern europe. *Tectonophysics 360*(1), 187 – 213. Geophysical Investigations og the Trans-European Suture Zone II.

Johansson, J. M., J. L. Davis, H.-G. Scherneck, G. A. Milne, M. Vermeer, J. X. Mitrovica, R. A. Bennett, B. Jonsson, G. Elgered, P. Elósegui, H. Koivula, M. Poutanen, B. O. Rönnäng, and I. I. Shapiro (2002). Continuous GPS measurements of postglacial adjustment in Fennoscandia 1. Geodetic results. *J. Geophys. Res. 107*, 10.1029/2001JB000400. V, pdf.

Johnson, R. W., D. V. Kliche, and P. L. Smith (2014). Maximum likelihood estimation of gamma parameters for coarsely binned and truncated raindrop size data. *Quarterly Journal of the Royal Meteorological Society 140*(681), 1245–1256.

Kass, R. E. and A. E. Raftery (1995). Bayes factors. *J. Am. Stat. Assoc. 90*, 773–795.

Kaufmann, G. and K. Lambeck (2002). Glacial isostatic adjustment and the radial viscosity profile from inverse modeling. *J. Geophys. Res. 107*, 2280, doi:10.1029/2001JB000941. pdf.

Kaufmann, G. and P. Wu (2002). Glacial isostatic adjustment in Fennoscandia with a three-dimensional viscosity structure as an inverse problem. *Earth Planet. Sci. Lett. 197*, 1–10. pdf,V,.

Kaufmann, G., P. Wu, and G. Li (2000). Glacial isostatic adjustment in Fennoscandia for a laterally heterogeneous earth. *Geophys. J. Int. 143*, 262–273. V,in script.

Kaufmann, G., P. Wu, and D. Wolf (1997). Some effects of lateral heterogeneities in the upper mantle on postglacial land uplift close to continental margins. *Geophys. J. Int. 128*, 175–187. D.

Kelsey, H. M. (2015). *Geomorphological indicators of past sea levels*, Chapter 5, pp. 66–82. John Wiley & Sons, Ltd.

Kemp, A. C. and R. J. Telford (2015). *Transfer functions*, Chapter 31, pp. 470–499. John Wiley & Sons, Ltd.

Khan, N. S., E. Ashe, T. A. Shaw, M. Vacchi, J. Walker, W. Peltier, R. E. Kopp, and B. P. Horton (2015, Dec). Holocene relative sea-level changes from near-, intermediate-, and far-field locations. *Current Climate Change Reports 1*(4), 247–262.

Khan, N. S., B. P. Horton, S. Engelhart, A. Rovere, M. Vacchi, E. L. Ashe, T. E. Törnqvist, A. Dutton, M. P. Hijma, and I. Shennan (2019). Inception of a global atlas of sea levels since the last glacial maximum. *Quaternary Science Reviews 220*, 359 – 371.

Klassen, R. W. (1986). *Surficial geology of north-central Manitoba*. Geological Survey of Canada, Memoir 419. Ottawa: Geological Survey of Canada. pdf.

Klemann, V., Z. Martinec, and E. R. Ivins (2008). Glacial isostasy and plate motions. *J. Geodyn. 46*, 95–103. V, pdf.

Klemann, V., M. Thomas, and H. Schuh (2015). Elastic and viscolestic response of the lithosphere to surface loading. In W. Freeden, M. Z. Nashed, and T. Sonar (Eds.), *Handbook of Geomathematics*, pp. 661–677. Berlin, Heidelberg: Springer-Verlag. pdf.

Klemann, V. and D. Wolf (2005). The eustatic reduction of shoreline diagrams: implications for the inference of relaxation-rate spectra and the viscosity stratification below Fennoscandia. *Geophys. J. Int. 162*, 249–256. V.

Klemann, V. and D. Wolf (2007). Using fuzzy logic for the analysis of sea-level indicators with respect to glacial isostatic adjustment: an application to the Richmond-Gulf region, Hudson Bay. *Pure Appl. Geophys. 164*, 683–696. V, pdf.

Kliche, D. V., P. L. Smith, and R. W. Johnson (2008, 12). L-Moment Estimators as Applied to Gamma Drop Size Distributions. *Journal of Applied Meteorology and Climatology 47*(12), 3117–3130.

Knapmeyer-Endrun, B., F. Krüger, and W. H. Geissler (2017). Upper mantle structure across the trans-european suture zone imaged by s-receiver functions. *Earth and Planetary Science Letters 458*, 429 – 441.

Konrad, H., M. Thoma, I. Sasgen, V. Klemann, K. Grosfeld, D. Barbi, and Z. Martinec (2014). The deformational response of a viscoelastic solid earth model coupled to a thermomechanical ice sheet model. *Surv. Geophys. 35*(6), 1441–1458. spp, pdf.

Kopp, R. E., F. J. Simons, J. X. Mitrovica, A. C. Maloof, and M. Oppenheimer (2009). Probabilistic assessment of sea level during the last interglacial stage. *Nature 462*, 863–867. pdf.

Kostecki, R. (2014). Stages of the baltic sea evolution in the geochemical record and radiocarbon dating of sediment cores from the arkona basin. *Oceanological and Hydrobiological Studies 43*(3), 237 – 246.

Koutsoyiannis, D. (2008, 01). *Probability and statistics for geophysical processes*. National Technical University of Athens.

Kristiansen, T. and E. Aas (2015). Water type quantification in the skagerrak, the kattegat and off the jutland west coast. *Oceanologia 57*(2), 177 – 195.

Krog, H. (1979). The Quaternary history of the Baltic, Denamrk. In V. Gudelis and L.-K. K"onigsson (Eds.), *The Quaternary history of the Baltic*, Volume 1, pp. 207–217. Acta Univ. Ups., Symp. Univ. Ups. Annum Quingentesimum Celebrantis, Uppsala. S.

Krog, H. and H. Tauber (1974). C-14 chronology of late- and post-glacial marine deposits in North Jutland. *Danm. Geol. Unders.*
rArbog for 1973, 93–105.

Kucera, M. (2016). *Modern Analog Techniques*, pp. 514–515. Dordrecht: Springer Netherlands.

Kuchar, J., G. Milne, and K. Latychev (2019). The importance of lateral earth structure for north american glacial isostatic adjustment. *Earth and Planetary Science Letters 512*, 236 – 245.

Lambeck, K. (1998). On the choice of timescale in glacial rebound modelling: mantle viscosity estimates and the radiocarbon timescale. *Geophys. J. Int. 134*, 647–651.

Lambeck, K., P. A., and S. Zhao (2017). The North American Late Wisconsin ice sheet and mantle viscosity from glacial rebound analyses. *Quat. Sci. Rev. 158*, 172–210.

Lambeck, K. and J. Chappell (2001). Sea level change through the last glacial cycle. *Science 292*, 679–686. V.

Lambeck, K., A. Purcell, P. Johnston, M. Nakada, and Y. Yokoyama (2003). Water-load definition in the glacio-hydro-isostatic sea-level equation. *Quat. Sci. Rev. 22*, 309–318. 0.

Lambeck, K., C. Smither, and M. Ekman (1998). Tests of glacial rebound models for Fennoscandinavia based on instrumented sea- and lake-level records. *Geophys. J. Int. 135*, 375–387. D.

Lambeck, K., C. Smither, and P. Johnston (1998). Sea-level change, glacial rebound and mantle viscosity for northern Europe. *Geophys. J. Int. 134*, 102–144. V, pdf.

Lampe, R., E. Endtmann, W. Janke, and H. Meyer (2010, 01). Relative sea-level development and isostasy along the ne german baltic sea coast during the past 9 ka. *EG Quaternary Science Journal 59*, 3–20.

Lampe, R. and W. Janke (2004, 01). The holocene sea level rise in the southern baltic as reflected in coastal peat sequences. *Polish Geological Institute Special Papers 11*, 19–30.

Lass, H. (2003, 02). On dynamics and mixing of inflowing saltwater in the arkona sea. *Journal of Geophysical Research 108*.

Latychev, K., J. X. Mitrovica, M. E. Tamisiea, J. Tromp, and R. Moucha (2005). Influence of lithospheric thickness variations on 3-D crustal velocities due to glacial isostatic adjustment. *Geophys. Res. Lett. 32*, L01304, doi:10.1029/2004GL021454. pdf, V, in script.

Lauriol, B. and J. T. Gray (1987). The decay and disappearance of the late wisconsin ice sheet in the ungava peninsula, northern quebec, canada. *Arctic Alpine Res. 19*, 109. 0.

Lemke, P., J. Ren, R. Alley, I. Allison, J. Carrasco, G. Flato, Y. Fujii, G. Kaser, P. Mote, R. Thomas, and T. Zhang (2007, 01). *IPCC, 2007. Climate Change 2007. Synthesis Report. Contribution of Working Groups I, II & III to the Fourth Assessment Report of the Intergovernmental Panel on Climate Change. Geneva.*

Libby, W. F., E. C. Anderson, and J. R. Arnold (1949). Age determination by radiocarbon content: World-wide assay of natural radiocarbon. *Science 109*(2827), 227–228.

Lidberg, M., J. M. Johansson, H.-G. Scherneck, and G. A. Milne (2010). Recent results based on continuous gps observations of the gia process in fennoscandia from bifrost. *Journal of Geodynamics 50*(1), 8 – 18. Upper Mantle Dynamics and Quaternary Climate in Cratonic Areas (DynaQlim); Understanding the Glacial Isostatic Adjustment.

Lidén, R. (1913). *Geokronologiska studier öfver det finiglaciala skedet i rAngermanland.* Sveriges geologiska Undersökning. Norstedt.

Lidén, R. (1938). Den senkvartära strandförskjutningens förlopp och kronologie i rAngermanland. *Geol. Fören. Stockholm Förh. 60*, 397–404. D.

Lorenz, S. J., J.-H. Kim, N. Rimbu, R. R. Schneider, and G. Lohmann (2006). Orbitally driven insolation forcing on holocene climate trends: Evidence from alkenone data and climate modeling. *Paleoceanography 21*(1).

Lorscheid, T. (2017, 01). *MIS 5e relative sea level indicators : new methodologies to sustain the quantitative estimate of past sea level changes.* Ph. D. thesis, University of Bremen.

Love, R., G. A. Milne, L. Tarasov, S. E. Engelhart, M. P. Hijma, K. Latychev, B. P. Horton, and T. E. Törnqvist (2016). The contribution of glacial isostatic adjustment to projections of sea-level change along the atlantic and gulf coasts of north america. *Earth's Future 4*(10), 440–464.

Lowdon, J. A., I. M. Robertson, and W. Blake Jr. (1977). *Geological Survey of Canada radiocarbon dates XVII.* Geological Survey of Canada, Paper 77-7. Ottawa: Geological Survey of Canada,. M.

Lyell, C. (1835). I. the bakerian lecture. —on the proofs of a gradual rising of the land certain parts of sweden. *Philosophical Transactions of the Royal Society of London 125*, 1–38.

Martinec, Z. (2000). Spectral–finite element approach for three-dimensional viscoelastic relaxation in a spherical earth. *Geophys. J. Int. 142*, 117–141. V, pdf.

Martinec, Z. and J. Hagedoorn (2005). Time-domain approach to linearized rotational response of a three-dimensional viscoelastic earth model induced by glacial-isostatic adjustment: I. inertia-tensor perturbations. *Geophys. J. Int. 163*, 443–462. pdf.

Martinec, Z., V. Klemann, W. van der Wal, R. E. M. Riva, G. Spada, Y. Sun, D. Melini, S. B. Kachuck, V. Barletta, K. Simon, G. A, and T. S. James (2018). A benchmark

study of numerical implementations of the sea level equation in gia modelling. *Geophys. J. Int. 215*, 389–414. pdf.

Martinec, Z. and D. Wolf (2005). Inverting the Fennoscandian relaxation-time spectrum in terms of an axisymmetric viscosity distribution with a lithospheric root. *J. Geodyn. 39*, 143–163. V.

Mathier, L., L. Perreault, B. Bobée, and F. Ashkar (1992, Dec). The use of geometric and gamma-related distributions for frequency analysis of water deficit. *Stochastic Hydrology and Hydraulics 6*(4), 239–254.

Matthews, B. (1966). Radiocarbon dated postglacial land uplift in northern Ungava, Canada. *Nature 211*, 1164–1166. pdf, RSL, Hudson Bay.

Matthews, B. (1967). Late quaternary land emergence in northern ungava, quebec. *Arctic 20*, 176–202. pdf.

Matti, K., S. H. De Moel, V. D. Gianluigi, P. Ward, and V. Olli (2016, 3). Over the hills and further away from coast: Global geospatial patterns of human and environment over the 20th-21st centuries. *Environmental Research Letters 11*(3).

McRae, A. (1998). Radiometric dating and the geological time scale: Circular reasoning or reliable tools? radiometric dating and the geological time scale. TalkOrigins Archive.

Melini, D. and G. Spada (2019, 03). Some remarks on Glacial Isostatic Adjustment modelling uncertainties. *Geophysical Journal International 218*(1), 401–413.

Milanković, M. (1969). *Canon of insolation and the ice-age problem : (Kanon der Erdbestrahlung und seine Anwendung auf das Eiszeitenproblem) Belgrade, 1941.* Jerusalem : Israel Program for Scientific Translations; [available from U.S. Dept. of Commerce, Clearinghouse for Federal Scientific and Technical Information, Springfield, Va.]. "List of the author's publications referring to the subject treated in this book": p. xx-xxiii.

Milne, G. and I. Shennan (2013). Sea level studies | isostasy: Glaciation-induced sea-level change. In S. A. Elias and C. J. Mock (Eds.), *Encyclopedia of Quaternary Science (Second Edition)* (Second Edition ed.)., pp. 452 – 459. Amsterdam: Elsevier.

Milne, G. A. (2015). *Glacial isostatic adjustment*, Chapter 28, pp. 419–437. John Wiley & Sons, Ltd.

Milne, G. A., J. L. Davis, J. X. Mitrovica, H. Scherneck, J. M. Johannson, M. Vermeer, and H. Koivula (2001). Space–geodetic constraints on glacial isostatic adjustment in Fennoschandia. *Science 291*, 2381–2384. V, suppl.

Milne, G. A., A. J. Long, and S. E. Bassett (2005). Modelling Holocene relative sea-level observations from the Caribbean and South America. *Quat. Sci. Rev. 24*, 1183–1202. S, pdf.

Milne, G. A., J. X. Mitrovica, H.-G. Scherneck, J. L. Davis, J. M. Johansson, H. Koivula, and M. Vermeer (2004). Continuous GPS measurements of postglacial

adjustment in Fennoscandia: 2. Modeling results. *J. Geophys. Res. 109*, B02412 doi:10.1029/2003JB002619. V, pdf.

Mitrovica, J. X. and A. M. Forte (2002). On the radial profile of mantle viscosity. In J. X. Mitrovica and B. L. A. Vermeersen (Eds.), *Ice Sheets, Sea Level and the Dynamic Earth*, pp. 187–200. Washington, DC: American Geophysical Union. D.

Mitrovica, J. X. and A. M. Forte (2004). A new inference of mantle viscosity based upon joint inversion of convection and glacial isostatic adjustment data. *Earth Planet. Sci. Lett. 225*, 177–189. V.

Mitrovica, J. X. and G. A. Milne (2003). On post-glacial sea level : I. General theory. *Geophys. J. Int. 154*, 253–267. V.

Mitrovica, J. X. and W. R. Peltier (1992). A comparison of methods for the inversion of viscoelastic relaxation spectra. *Geophys. J. Int. 108*, 410–414. pdf.

Mitrovica, J. X. and W. R. Peltier (1993). The inference of mantle viscosity from an inversion of the Fennoscandian relaxation spectrum. *Geophys. J. Int. 114*, 45–62. V.

Mitrovica, J. X. and W. R. Peltier (1995). Constraints on mantle viscosity based upon the inversion of post-glacial uplift data from the Hudson Bay region. *Geophys. J. Int. 122*, 353–377. V.

Moran, P. A. P. (1969). Statistical inference with bivariate gamma distributions. *Biometrika 56*, 627–634.

Morhange, C. and N. Marriner (2015). *Archeological and biological relative sea-level indicators*, Chapter 9, pp. 146–156. John Wiley & Sons, Ltd.

Nakada, M. (1983). Rheological structure of the earth's mantle derived from glacial rebound in Laurentide. *J. Phys. Earth 31*, 349–386. D.

Nakada, M. and K. Lambeck (1987, 07). Glacial rebound and relative sea-level variations: a new appraisal. *Geophysical Journal International 90*(1), 171–224.

Nakada, M. and K. Lambeck (1991). Late Pleistocene and Holocene sea-level change; evidence for lateral mantle viscosity structure? In R. Sabadini, K. Lambeck, and E. Boschi (Eds.), *Glacial Isostasy, Sea Level and Mantle Rheology*, pp. 79–94. Dordrecht: Kluwer. D.

NASA (2020). The national aeronautics and space administration (nasa), grace mission. web, last consulted on 28.08.2020.

Naumann, M. and R. Lampe (2014). The evolution of a southern baltic coastal barrier system, deduced from geostatistical based volume calculations and relative sea level rise (Darss-Zingst-Hiddensee area / NE Germany). *Ber. Röm.-Germ. Komm 2011 92*, 297–324.

Nielsen, E. and L. A. Dredge (1982). *Quaternary stratigraphy and geomorphology of a part of the lower Nelson River*. Field Trip Guide 5. Winnipeg: Ecological Association of Canada.

Nielsen, E., A. V. Morgan, A. Morgan, R. J. Mott, N. W. Rutter, and C. Causse (1986). Stratigraphy, paleoecology, and glacial history of the gillam area, manitoba. *Can. J. Earth Sci. 23*, 1641–1661. pdf.

Nielsen, L. and L. B. Clemmensen (2009). Sea-level markers identified in ground-penetrating radar data collected across a modern beach ridge system in a microtidal regime. *Terra Nova 21*(6), 474–479.

Nielsen, P. E., J. B. Jensen, M. Binderup, S. Lomholt, and A. Kuijpers (2004). Marine aggregates in the Danish sector of the Baltic Sea: geological setting, exploitation potential and environmental assessment. *Z. Ang. Geol. Sonderheft 2, 2004*, 87–109.

Ning, W., P. S. Andersson, A. Ghosh, M. Khan, and H. L. Filipsson (2017). Quantitative salinity reconstructions of the baltic sea during the mid-holocene. *Boreas 46*(1), 100–110.

Nordman, M., G. Milne, and L. Tarasov (2015, 03). Reappraisal of the Ångerman River decay time estimate and its application to determine uncertainty in Earth viscosity structure. *Geophysical Journal International 201*(2), 811–822.

OBIS (2017). Data from the Ocean Biogeographic Information System. Intergovernmental Oceano- graphic Commission of UNESCO. web, last consulted on 20.12.2017.

of Encyclopaedia Britannica, T. E. (2011). Article title: Verved deposit, website name: Encyclopædia britannica. web, Access Date: May 21, 2020.

of Encyclopaedia Britannica, T. E. (2012). Article title: Kattegat, website name: Encyclopædia britannica. web, Access Date: May 21, 2020.

Paulson, A., S. Zhong, and J. Wahr (2007). Inference of mantle viscosity from grace and relative sea level data. *Geophysical Journal International 171*(2), 497–508.

Peltier, W. and R. Fairbanks (2006). Global glacial ice volume and last glacial maximum duration from an extended barbados sea level record. *Quaternary Science Reviews 25*(23), 3322 – 3337. Critical Quaternary Stratigraphy.

Peltier, W. R. (1976). Glacial–isostatic adjustment—II. The inverse problem. *Geophys. J. R. Astr. Soc. 46*, 669–705. V, pdf.

Peltier, W. R. (1993). Time dependent topography through the glacial cycle: IGBP PAGES/World Data Center-A for paleoclimatology data contribution. Technical Report Series 93-015, NOAA/NGDC Paleoclimatology Program, Boulder. ftp://ftp.ngdc.noaa.gov/paleo/ice_topo/.

Peltier, W. R. (1998a). Global glacial isostasy and relative sea level: implications for solid earth geophysics and climate system dynamics. In P. Wu (Ed.), *Dynamics of the Ice Age Earth: A Modern Perspective*, pp. 17–53. Hetikon: Trans Tech Publications. V,book.

Peltier, W. R. (1998b). Postglacial variations in the level of the sea: implications for climate dynamics and solid-earth geophysics. *Rev. Geophys. 36*, 603–689. V.

Peltier, W. R. (1999). Global sea level rise and glacial isostatic adjustment. *Global Planet. Change 20*, 93–123.

Peltier, W. R. (2004a). Global glacial isostasy and the surface of the ice-age earth: the ICE-5G (VM2) model and GRACE. *Ann. Rev. Earth Planet. Sci. 32*, 111–149. V, pdf.

Peltier, W. R. (2004b). Global glacial isostasy and the surface of the ice-age earth: the ICE5G (VM2) model and GRACE. *Ann. Rev. Earth Planet. Sci. 32*, 111–149. V,pdf.

Peltier, W. R. and J. T. Andrews (1976). Glacial–isostatic adjustment—I. The forward problem. *Geophys. J. R. Astr. Soc. 46*, 605–646. 0.

Peltier, W. R. and J. T. Andrews (1983). Glacial geology and glacial isostasy of the Hudson Bay region. In D. E. Smith and A. G. Dawson (Eds.), *Shorelines and Isostasy*, pp. 285–319. London: Academic Press. D.

Peltier, W. R., D. F. Argus, and R. Drummond (2015). Space geodesy constrains ice age terminal deglaciation: The global ICE-6G_C (vm5a) model. *J. Geophys. Res. 120*, 450–487. pdf.

Peltier, W. R. and X. Jiang (1996). Mantle viscosity from the simultaneous inversion of multiple data sets pertaining to postglacial rebound. *Geophysical Research Letters 23*(5), 503–506.

Petersen, K. S. (1976). Om Limfjordens postglaciale marine udvikling og niveauforhold, belyst ved mollusk-faunaen og C-14 dateringer. *Danm. Geol. Unders. 1975*, 75–103. S.

Petersen, K. S. (1978). Den postglaciale transgression og molluskfaunaen i tude aa-omraadet, store baelt, danmark. *Danm. Geol. Unders. 1977*, 39–52. S.

Petersen, K. S. (1986). The Ertebølle "køkkenmødding" and the marine development of the Limfjord, with particular reference to the molluscan fauna. *J. Dan. Arch. 5*, 77–84.

Petersen, K. S. (1991). Holocene coastal and faunal development of the Skagen Odde, northern Jutland, Denmark. *Quat. Int. 9*, 53–60.

Petersen, K. S. (1993). Environmental changes recorded in the Holocene molluscan faunas from Djursland, Denmark. *Scr. Geol. 2*, 359–369.

Petersen, K. S. and K. L. Rasmussen (1995). The impact of radiocarbon datings on natural historical sciences in Denmark especially paleozoological and shore-line datings. *PACT 49,8*, 117–130.

Playfair, J. (1802). *Illustrations of the Huttonian theory of the Earth.*

Pollard, D., N. Gomez, and R. M. Deconto (2017). Variations of the antarctic ice sheet in a coupled ice sheet-earth-sea level model: Sensitivity to viscoelastic earth properties. *Journal of Geophysical Research: Earth Surface 122*(11), 2124–2138.

Rahbek, U. and K. L. Rasmussen (1994). Danske arkæologiske 14C-dateringer, København 1993. *1993*, 276–288.

Ramsey, B. C. (2017). Oxcal 4.2 manual. online, last conulted 05.12.2017.

Rasmussen, K. L. (1992). Danske arkæologiske 14C-dateringer, København 1991. *1991*, 233–251.

Rasmussen, P. (1995). Stavns fjords alder. In H. H. Hansen and B. Aaby (Eds.), *Stavns Fjord – et natur- og kulturhistorisk forskningsområde på Samsø*, pp. 23–33. København: Carlsbergfondet og Nationalmuseet.

Reimer, P. J., E. Bard, A. Bayliss, J. W. Beck, P. G. Blackwell, C. Bronk Ramsey, P. M. Grootes, T. P. Guilderson, H. Haflidason, I. Hajdas, C. Hatt, T. J. Heaton, D. L. Hoffmann, A. G. Hogg, K. A. Hughen, K. F. Kaiser, B. Kromer, S. W. Manning, M. Niu, R. W. Reimer, D. A. Richards, E. M. Scott, J. R. Southon, R. A. Staff, C. S. M. Turney, , and J. van der Plicht (2013). IntCal13 and Marine13 radiocarbon age calibration curves 0–50,000 years cal BP. *Radiocarbon 55*, 1869–1887.

Rosentau, A., V. Klemann, H. Steffen, J. Wehr, M. Latinović, A. K. Ojala, M. Berglund, G. Peterson, K. Schoning, O. E. Bennike, L. Nielsen, L. B. Clemmensen, M. U. Hede, A. Kroon, M. Pejrup, L. Sander, K. Stattegger, K. Schwarzer, R. Lampe, M. Lampe, S. Uścinowicz, A. Bitinas, I. Grudzinska, Y. A. Kublitskiy, J. Vassiljev, D. A. Subetto, and M. Bagge (2020). A holocene sea-level database for the baltic sea. *Quat. Sci. Rev. in preparation*, 80.

Rovere, A., M. E. Raymo, M. Vacchi, T. Lorscheid, P. Stocchi, L. Gómez-Pujol, D. L. Harris, E. Casella, M. J. O'Leary, and P. J. Hearty (2016). The analysis of last interglacial (mis 5e) relative sea-level indicators: Reconstructing sea-level in a warmer world. *Earth-Science Reviews 159*, 404 – 427.

Saarnisto, M. and A. E. K. Ojala (2009). *Varved Sediments*, pp. 973–975. Dordrecht: Springer Netherlands.

Sabadini, R., D. A. Yuen, and M. Portney (1986). The effects of upper-mantle lateral heterogeneities on postglacial rebound. *Geophys. Res. Lett. 13*, 337. V.

Sander, L., M. Fruergaard, J. Koch, P. N. Johannessen, and M. Pejrup (2015). Sedimentary indications and absolute chronology of Holocene relative sea-level changes retrieved from coastal lagoon deposits on Samsø, Denmark. *Boreas 44*, 706–720.

Sauramo, M. (1929). The quaternary geology of finland. *GFF 51*(4), 617–618.

Schaeffer, A. J. and S. Lebedev (2013, 04). Global shear speed structure of the upper mantle and transition zone. *Geophysical Journal International 194*(1), 417–449.

Scherneck, H.-G., J. M. Johansson, G. Elgered, J. L. Davis, B. Jonsson, G. Hedling, H. Koivula, M. Ollikainen, M. Poutanen, M. Vermeer, J. X. Mitrovica, and G. A. Milne (2002). BIFROST: observing the three-dimensional deformation of Fennoscandia. In J. X. Mitrovica and L. L. A. Vermeersen (Eds.), *Ice Sheets, Sea Level and the Dynamic Earth*, pp. 69–93. Washington: American Geophysical Union. V.

Segerström, U., I. Renberg, and J.-E. Wallin (1984). Annual sediment accumulation and land use history; investigations of varved lake sediments: With 7 figures in the text. *Internationale Vereinigung für theoretische und angewandte Limnologie: Verhandlungen 22*(3), 1396–1403.

Shennan, I. and B. Horton (2002). Holocene land- and sea-level changes in Great Britain. *J. Quat. Sci. 17*, 511–526. V, pdf.

Shennan, I., A. J. Long, and B. P. Horton (2015). *Introduction*, Chapter 1, pp. 1–2. John Wiley & Sons, Ltd.

Skaarup, J. and O. Grøn (2004). Geology and topography. In J. Skaarup and O. Grøn (Eds.), *Møllegabet II, a submerged Mesolithic settlement in southern Denmark*, Volume 1328 of *Br. Arch. Rep. Int. Ser.*, pp. 4–20.

SKB (2006). Climate and climate related issues for the safety assessment sr-can. Report TR-06-23, Swedish Nuclear Fuel and Waste Management Company, Stockholm.

Skinner, R. G. (1973). *Quaternary stratigraphy of Moose River basin, Ontario.* Bulletin 225. Ottawa: Geological Survey of Canada. M.

Spada, G. (2017, Jan). Glacial isostatic adjustment and contemporary sea level rise: An overview. *Surveys in Geophysics 38*(1), 153–185.

Steffen, H. and G. Kaufmann (2005, 11). Glacial isostatic adjustment of Scandinavia and northwestern Europe and the radial viscosity structure of the Earth's mantle. *Geophysical Journal International 163*(2), 801–812.

Steffen, H. and P. Wu (2011). Glacial isostatic adjustment in fennoscandia–a review of data and modeling. *J. Geodyn. 52*, 169–204. pdf.

Steffen, H., P. Wu, and H. Wang (2010, 09). Determination of the Earth's structure in Fennoscandia from GRACE and implications for the optimal post-processing of GRACE data. *Geophysical Journal International 182*(3), 1295–1310.

Steinberger, B. (2016, 01). Topography caused by mantle density variations: observation-based estimates and models derived from tomography and lithosphere thickness. *Geophysical Journal International 205*(1), 604–621.

Steinberger, B. and A. R. Calderwood (2006). Models of large-scale viscous flow in the Earth's mantle with constraints from mineral physics and surface observations. *Geophys. J. Int. 167*, 1461M–?–1481. pdf.

Stockamp, J., P. Bishop, Z. Li, E. Petrie, J. Hansom, and A. Rennie (2016, 10). State-of-the-art in studies of glacial isostatic adjustment for the british isles: a literature review. *Earth and Environmental Science Transactions of the Royal Society of Edinburgh 106*, 1–26.

Swedish Meteorological and Hydrological Institute (2017). Swedish meteorological and hydrological institute, https://www.smhi.se/en. web, last consulted on 20.10.2019.

Tarantola, A. (2005). *Inverse Problem Theory and Methods for Model Parameter Estimation.* Philadelphia: Society of Industry and Applied Mathematics. pdf.

Tarasov, L., A. S. Dyke, R. M. Neal, and W. R. Peltier (2012). A data-calibrated distribution of deglacial chronologies for the North American ice complex from glaciological modeling. *Earth Planet. Sci. Lett. 315–316*, 30–40. pdf.

Teller, J. T. (1980). *Radiocarbon dates in Manitoba*. Geological Report GR80-4. iManitoba: Manitoba Mineral Resources Division. 0.

Tushingham, A. M. and W. R. Peltier (1991). ICE-3G: a new global model of the late Pleistocene deglaciation based upon geophysical predictions of post-glacial relative sea level change. *J. Geophys. Res. 96*, 4497–4523. V.

Törnqvist, T. E., B. E. Rosenheim, P. Hu, and A. B. Fernandez (2015). *Radiocarbon dating and calibration*, Chapter 23, pp. 347–360. John Wiley & Sons, Ltd.

Unger, A., D. Rabe, V. Klemann, D. Eggert, and D. Dransch (2018). Slivisu: A visual analytics tool to validate simulation models against collected data. v. 1.0.

Unger, A., S. Schulte, V. Klemann, and D. Dransch (2012). Visual analytics concept for the validation of geoscientific simulation models. *IEEE Trans. Vis. Comp. Graph. 18*, 2216–2225. pdf.

USGS (2020). Us. geological survey, earthquake glossary-lithopshere. web, last consulted on 26.06.2020.

Vacchi, M., S. E. Engelhart, D. Nikitina, E. L. Ashe, W. R. Peltier, K. Roy, R. E. Kopp, and B. P. Horton (2018). Postglacial relative sea-level histories along the eastern canadian coastline. *Quaternary Science Reviews 201*, 124 – 146.

van der Plassche, O. (1986). *Sea-Level Research: A Manual for the Collection and Evaluation of Data*. Norwich: Geo Books.

van der Wal, W., A. Barnhoorn, P. Stocchi, S. Gradmann, P. Wu, M. Drury, and B. Vermeersen (2013). Glacial isostatic adjustment model with composite 3-d earth rheology for fennoscandia. *Geophys. J. Int. 194*, 61–77. pdf.

van der Wal, W., P. Whitehouse, and E. Schrama (2015). Effect of gia models with 3d mantle viscosity on grace mass balance estimates for antarctica. *Earth and Planetary Science Letters 414*(March), 134–143. Available online 28-01-2015.

Van Grieken, R. de Bruin, M. (1994). Nomenclature for radioanalytical chemistry (iupac recommendations 1994). *Pure and applied chemistry. - London 66:12*, 2513–2526.

Van Hengstum, P. J., D. A. Richards, B. P. Onac, and J. A. Dorale (2015). *Coastal caves and sinkholes*, Chapter 6, pp. 83–103. John Wiley & Sons, Ltd.

Vestøl, O., J. Ågren, H. Steffen, H. Kierulf, and L. Tarasov (2019). Nkg2016lu: a new land uplift model for fennoscandia and the baltic region. *Journal of Geodesy 93*(9), 1759–1779.

Vincent, J.-S. (1977). *Le quaternaire recent de la region du cours inferieur de la grande riviere, Quebec*. Etude 76-19. Ottawa: Geological Survey of Canada. M.

Wahr, J. M. and J. L. Davis (2013). *Geodetic Constraints on Glacial Isostatic Adjustment*, pp. 3–32. American Geophysical Union (AGU).

Walcott, R. I. (1972a). Late Quaternary vertical movements in eastern North America: quantitative evidence of glacio-isostatic rebound. *Rev. Geophys. Space Phys. 10*, 849–884. D.

Walcott, R. I. (1972b). Past sea levels, eustasy and deformation of the earth. *Quat. Res. 2*, 1–14. pdf.

Walcott, R. I. and B. G. Craig (1975). Uplift studies, southeastern hudson bay. In *Report of activities part A, April to October 1974*, Paper no. 75-1A, pp. 455–456. Ottawa: Geological Survey of Canada. pdf in PA75-1a.

Wallin, J.-E. (1996). History of the sedentary farming in Ångermanland, northern Sweden, during the Iron Age and Medieval period based on pollen analytical investigation. *Veg. Hist. Archaeobot. 5*, 301–312.

Webb, D. J. (2014). On the tides and resonances of hudson bay and hudson strait. *Ocean Science 10*(3), 411–426.

Webber, P. J., J. W. Richardson, and J. T. Andrews (1970). Post-glacial uplift and substrate age at Cape Henrietta Maria, southeastern Hudson Bay, Canada. *Can. J. Earth Sci. 7*, 317–325. M.

Whitehouse, P., K. Latychev, G. A. Milne, J. X. Mitrovica, and R. Kendall (2006). Impact of 3-D Earth structure on Fennoscandian glacial isostatic adjustment: Implications for space-geodetic estimates of present-day crustal deformations. *Geophys. Res. Lett. 33*, L13502, doi:10.1029/2006GL026568. V, pdf.

Whitehouse, P. L. (2018). Glacial isostatic adjustment modelling: historical perspectives, recent advances, and future directions. *Earth Surface Dynamics 6*(2), 401–429.

Whitehouse, P. L., M. J. Bentley, G. A. Milne, M. A. King, and I. D. Thomas (2012). A new glacial isostatic adjustment model for Antarctica: calibrated and tested using observations of relative sea-level change and present-day uplift rates. *Geophys. J. Int.*, 1464–1482.

Wieczerkowski, K., J. X. Mitrovica, and D. Wolf (1999). A revised relaxation-time spectrum for Fennoscandia. *Geophys. J. Int. 139*, 69–86. V.

Wilson, R. C. L., S. A. Drury, and J. A. Chapman (2000, November). *The Great Ice Age: Climate Change and Life*. London: Routledge The Open University.

Winn, K., F. R. Averdieck, H. Erlenkeuser, and F. Werner (1986). Holocene sea level rise in the western Baltic and the question of isostatic subsidence. *Meyniana 38*, 61–80. S.

Wolf, D., V. Klemann, J. Wünsch, and F.-p. Zhang (2006). A reanalysis and reinterpretation of geodetic and geomorphologic evidence of glacial-isostatic uplift in the Churchill region, Hudson Bay. *Surv. Geophys. 27*, 19–61. V, pdf.

Woodworth, P. L. and D. L. Blackman (2004). Evidence for systematic changes in extreme high waters since the mid-1970s. *Journal of Climate 17*(6), 1190–1197.

Wu, P., P. Johnston, and K. Lambeck (1999, 12). Postglacial rebound and fault instability in Fennoscandia. *Geophysical Journal International 139*(3), 657–670.

Wu, P., Z. Ni, and G. Kaufmann (1998a, 01). *Postglacial Rebound with Lateral Heterogeneities : from 2D to 3D modeling*, pp. 557–582.

Wu, P., Z. Ni, and G. Kaufmann (1998b). Postglacial rebound with lateral heterogeneities: from 2D to 3D modeling. In P. Wu (Ed.), *Dynamics of the Ice Age Earth: A Modern Perspective*, pp. 557–582. Hetikon: Trans Tech Publications. V,book.

Yokoyama, Y. and T. M. Esat (2015). *Coral reefs*, Chapter 7, pp. 104–124. John Wiley & Sons, Ltd.

Yue, S., T. B. M. J. Ourada, and B. Bobée (2001). A review of bivariate distributions for hydrological application. *J. Hydrol. 246*, 1–18.

Zhao, S. (2013). Lithosphere thickness and mantle viscosity estimated from joint inversion of GPS and GRACE-derived radial deformation and gravity rates in North America. *Geophys. J. Int. 194*, 1455–1472. pdf.